AN INVESTIGATION OF THE MORPHOLOGICAL AND ELECTROCHEMICAL PROPERTIES OF SPINEL CATHODE OXIDE MATERIALS USED IN LI-ION BATTERIES

BY

CHARMELLE SNYDERS
STUDENT NUMBER: 20502233

A thesis submitted to the Faculty of Science, Nelson Mandela Metropolitan University, in partial fulfillment of the requirements for the degree of

DOCTOR OF PHILOSOPHY
(CHEMISTRY)

Supervisor: Prof. E. E. Ferg

Abstract

Li-ion batteries have become the more dominant battery type used in portable electronic devices such as cell phones, computers and more recently their application in full electric vehicles (EV). Li-ion batteries have many advantages over the traditional rechargeable systems (Pb-acid and Ni-MH) such as their higher energy density, low self-discharge, long capacity cycle life and relatively maintenance free. Due to their commercial advantages, a lot of research is done in developing new novel Li-ion electrode materials, improving existing ones and to reduce manufacturing costs in order to make them more cost effective in their applications.

This study looked at the cathode material chemistry that has a typical spinel manganese oxide ($LiMn_2O_4$) type structure. For comparison the study also considered the influence of doping the phase with various metals such as Al, Mg, Co and Ni that were made as precursors using various carboxylic acids (Citric, Ascorbic, Succinic and Poly-acrylic acid) from a sol-gel process. Traditional batch methods of synthesizing the electrode material is costly and do not necessarily provide optimized electrochemical performance. Alternative continuous less energy intensive methods would help reduce the costs of the preparation of the electrode materials. This study investigated the influence of two synthesis techniques on the materials physical and electrochemical characteristics. These synthesis methods included the use of a typical batch sol-gel method and the continuous spray-drying technique.

The spinel materials were prepared and characterized by Powder X-Ray Diffraction (PXRD) to confirm the formation of various phases during the synthesis process. In addition, in-situ PXRD techniques were used to track the phase changes that occurred in the typical batch synthesis process from a sol-gel mixture to the final crystalline spinel oxide. The materials were also characterized by thermal gravimetric analysis (TGA), whereby the materials decomposition mechanisms were observed as the precursor was gradually heated to the final oxide.

These synthesized materials prepared under various conditions were then used to build suitable Li-ion coin type of cells, whereby their electrochemical properties were tested by simple capacity tests and electrochemical impedance spectroscopy (EIS). EIS measurements were done on the built cells with the various materials at various charge voltages.

TG analysis showed that the materials underwent multiple decomposition steps upon heating for the doped lithium manganese oxides, whereas the undoped oxide showed only a single decomposition step. The results showed that all the materials achieved their weight loss below 400 °C, and that the final spinel oxide had already formed.

The in-situ PXRD analysis showed the progression of the phase transitions where certain of the materials changed from a crystalline precursor to an amorphous intermediate phase and then finally to the spinel cathode oxide ($Li_{1.03}Mg_{0.2}Mn_{1.77}O_4$, and $LiCo_{1.09}Mn_{0.91}O_4$). For other materials, the precursor would start as an amorphous phase, and then upon heating, convert into an impure intermediate phase (Mn_2O_3) before forming the final spinel oxide ($Li_{1.03}Mn_{1.97}O_4$ and $LiNi_{0.5}Mn_{1.5}O_4$). The in-situ study also showed the increases in the materials respective lattice parameters of the crystalline unit cells upon heating and the significant increases in their crystallite sizes when heated above 600 °C. Hence the results implied that a type of sintering of the particles would occur at temperatures above 600 °C, thereby increasing the respective crystallite size. The study showed that the cathode active materials made by the sol-gel spray-drying method would give a material that had a significantly larger surface area and a smaller crystallite size when compared to the materials made by the batch process. The electrochemical analysis showed that there was only a slight increase in the discharge capacities of the cells made with the spray-drying technique when compared to the cells made with the materials from the batch sol-gel technique. Whereas, the EIS study showed that there were distinct differences in the charging behavior of the cells made with the various materials using different synthesis techniques. The EIS results showed that there was a general decrease in the cells charge transfer resistance (R_{ct}) as the charge potential increased regardless of the synthesis method used for the various materials. The results also showed that the lithium-ion

diffusion coefficient (D_{Li}) obtained from EIS measurements were in most of the samples higher for the cathode materials that had a larger surface area. This implied that the Li-ion could diffuse at a faster rate through the bulk material.

The study concluded that by optimizing the synthesis process in terms of the careful control of the thermal parameters, the Li-ion batteries' cathode active material of the manganese spinel type could be optimized and be manufactured by using a continuous flow micro spray process.

Acknowledgments

1. I thank my Lord and Saviour for the passion, knowledge, strength, patience and guidance to complete this study. Philippians 4.13 "I can do all things through Christ who strengthens me"

2. Prof. E. Ferg my supervisor for his contribution and granting me the opportunity to be a part of this study.

3. Prof. H. Loewe and Mr. J. Schulien from the JGU in Mainz, Germany for allowing me the opportunity to be a part of their research group and assistance within certain sections of this study.

4. Prof. D. Billing and Dr. S. Miller from the University of Witwatersrand for assistance within the in-situ PXRD analysis.

5. Mr. W. Goosen, Prof. M. Lee and Prof. J. R. Botha from NMMU for assistance and making their instruments available for SEM and AFM analysis.

6. Prof. K. Ozoemena and Mrs. C. Rossouw from CSIR, Pretoria for their utmost assistance when needed for contribution on certain sections.

7. South African National Research Foundation (NRF) and Nelson Mandela Metropolitan University for their financial contribution.

8. Mr. L. Bolo, Mr. S. Mgangato, Ms. O. Faku, Ms. B. Mletshe and Mrs. R. Neglur for their tremendous support, encouraging words and friendship throughout this study.

9. My parents (Mr. and Mrs. Snyders), Mr. I. Fisher, my siblings, extended family and friends for endless prayer, support, love and patience.

Related publications by the author

Parts of this work were presented at:

1 The Southern African Powder Diffraction Conference and Workshop in Johannesburg, January 2014

2 The 42nd International SACI Convention Conference in Durban, December 2015

A part of this work was published in an accredited journal:

1 A review of using spray pyrolysis through sol-gel materials in the synthesis of cathode materials for lithium-ion batteries; C.D. Snyders, E.E. Ferg, J. Schuelein and H. Loewe; *S. Afr. J. Chem.*, 2016, **69**, 88–97.

2 An investigation into the temperature phase transitions of synthesized materials with Al and Mg doped lithium manganese oxide spinels by in-situ powder x-ray diffraction, C.D. Snyders, E.E. Ferg and D. Billing, *Powder Diffraction, accepted, In Press*.

Declaration

I hereby declare that this thesis is my own, unaided work. It is being submitted for the degree of Doctor of Philosophy (Chemistry) at the Nelson Mandela Metropolitan University. It has not been submitted before for any degree or examination in any other University or Technikon.

C. Snyders

_____

TABLE OF CONTENTS

CHAPTER 1

PROJECT INTRODUCTION

1.1 Overview

Batteries are an important component in today's consumer electronic commodities. It is widely used in almost all portable electronic devices (laptops, mobile phones, torches and radios). This wide usage of batteries requires further new developments within the technology to meet the wide range of power demands. These developments are driven by the consumer market requirements that need the energy storage systems to have long capacity life cycle, high charge and discharge rates, non- or low-toxicity and be cost effective with relatively ease of manufacturing. With the increase in the awareness of the global "green" environmental aspects of consumer products, this has also become an important parameter in the manufacturing and use of batteries. This can be seen in the replacement of certain battery types that contained harmful or toxic chemicals such as mercuric oxide (Zn-HgO) or cadmium (Ni-Cad). In addition to the environmental and health concerns of certain consumer products, there is an increase in the demands for clean and efficient energy usage with a focus on renewable energy. This has increased the demand for electrical energy storage systems. With the diminishing trends in fossil-fuel reserves, global warming concerns, increase demands for portable electronics and grid storage systems, the demand for efficient management and the storage of energy in many forms has become of great importance and can be summarized graphically as "green ecology" (Figure 1.1)[1].

Figure 1.1: Illustration on green ecology[1]

One aspect of the green ecology is the need to decrease the CO_2 emissions from fossil fuel based vehicles which has led to the introduction of full electric vehicles (EV). These are powered by large batteries, which are predominately based on Li-ion chemistry. They need to be light-weight, intrinsically safe, inexpensive and have a long life span (Figure 1.2).

Figure 1.2: Application of a lithium-ion battery in electric vehicles[2]

Many research institutes focus on improving the various aspects of the Li-ion batteries that include its electrode materials and their synthesis, electrolyte materials and their synthesis, separators and cell construction.

In terms of the cost of the battery, the cathode material and its manufacturing contributes to about 39 % to the total cost of manufacturing the battery (Figure 1.3)[3]. This can be reduced by considering cheaper and more abundant raw materials such as Mn or Fe and to develop more efficient manufacturing processes that produce a consistent product on a large scale. Some of these aspects will be considered in this study, where a better understanding of the material's synthesis process would contribute to the optimization of the manufacturing process.
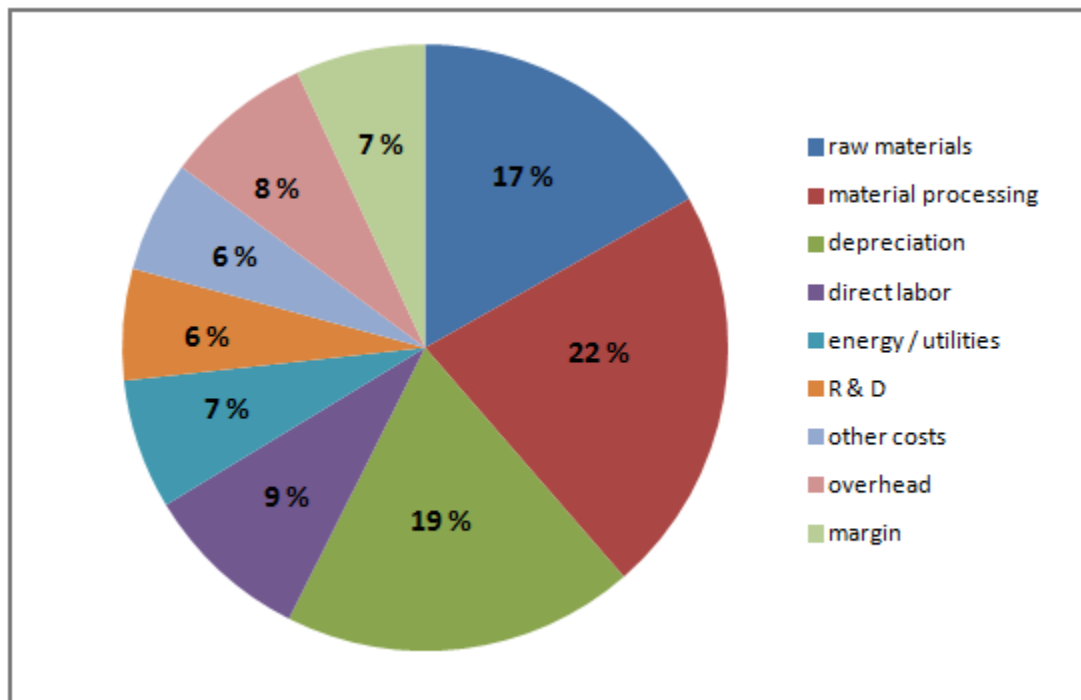
Figure 1.3: Illustration on battery cell cost breakdown, 2010[3]

1.2 Objective to the study

This project investigated the possibilities of using sol-gel chemistry combined with continuous spray-drying technologies to synthesize metal oxide materials used as the cathode in rechargeable lithium-ion batteries. The following types of synthesis methods have been explored that include solid-state reactions, softer chemistry routes (i.e. ion

exchange), composite technology, template methods and sol-gel methods[4, 5]. Solid state methods require that the precursors are thoroughly ground, mixed together and heated to high temperatures for extended periods of time. Often, this procedure has to be repeated several times until a homogeneous product is obtained. These batch methods are energy and time intensive and research is moving towards sol-gel chemistry. This study focused on the use of sol-gel chemistry in a semi-continuous process with a focus on the spinel lithium manganese oxide structure. A fair amount of research was done in improving the performance and stability of the lithium manganese oxide cathode active material by means of various dopants. This study considered typical metal dopants of Ni, Mg, Co and Al.

1.3 Aim of the study

The aim of the study was to characterize the morphological changes involved in the formation of the doped and undoped spinel lithium manganese oxide cathode material from sol-gel precursors. The study also considered the possibility of investigating a continuous spray-drying process to produce an electroactive material within a nano-scale range of particles.

1.4 Thesis outline

The outline of this study is as follows:

Chapter 2 gives an introductory background to lithium-ion batteries, their importance in a range of typical applications and its origin in various chemistries. Typical failure modes are briefly discussed with some recent developments in the electrode materials. A review is included of modern synthesis processes discussed with the focus on sol-gel pyrolysis and spray-dry techniques.

Chapter 3 gives insight to the experimental procedures of the assembled lithium-ion cells. Within this chapter the cathode active material synthesis methods would be discussed

together with the various techniques used for material characterization and electrochemical performance.

Chapter 4 discusses the results for the materials' characterization obtained by Thermal Gravimetric Analysis (TGA), Powder x-ray diffraction (PXRD) together with its microscopic analysis (Scanning electron microscopy, SEM and Atomic force microscopy, AFM). TGA investigated the changes in the materials precursor decomposition to the final spinel cathode oxide. PXRD investigated the phase composition of the final spinel cathode, where in-situ studies with changes in temperature gave insight into the phase transitions that occurred from precursor to the final product. SEM and AFM investigated the materials' microscopic morphology.

Chapter 5 discussed the electrochemical performance and characteristics of the cells made with the various synthesized materials. Within this chapter the cells' discharge capacities and their lithium-ion diffusion coefficient (D_{Li}) were evaluated. Techniques included electrochemical impedance spectroscopy (EIS) studies at various charge potentials.

REFERENCES

1. <http://www.gettyimages.com.au/detail/illustration/green-ecology-icon-royalty-free-illustration/505873969> (accessed on 13 November 2015).
2. <http://www.earthtimes.org/scitech/lithium-air-batteries-future-scientists/273/> (accessed on 13 November 2015).
3. R. Burger, Report by Global Vehicle LIB Market study, *Battery material cost study*, 2011, V2.4/Q1 (accessed on 01 December 2015).
4. V. Palomares and T. Rojo, in *Lithium Ion Batteries-New Developments,* ed. I. Belharouak, InTech Publishers, Croatia Europe, 2012.
5. L.J. Fu, H. Liu, C. Li, Y.P. Wu, E. Rahm, R. Holze and H.Q. Wu, *Progress in Materials Science*, 2005, **50**, 881–928.

CHAPTER 2

INTRODUCTION

2.1 Overview of cells

Batteries are known as energy storage devices, whereby stored chemical energy is converted to electrical energy[1]. In the year 1800, Alessandro Volta developed the first battery and referred to it as a "pile of cells"[1].

The Galvanic cell or voltaic cell as it is known today was the first battery developed which was founded by Luigi Galvani and Alessandro Volta in 1737 and 1827 respectively[2]. The well-known galvanic cell consists of a zinc electrode immersed in a zinc sulphate solution together with a copper electrode immersed in a copper sulphate solution. Within this cell, the flow of electrons is transported from the zinc electrode to the copper electrode with the aid of a salt bridge, producing electricity (Figure 2.1).
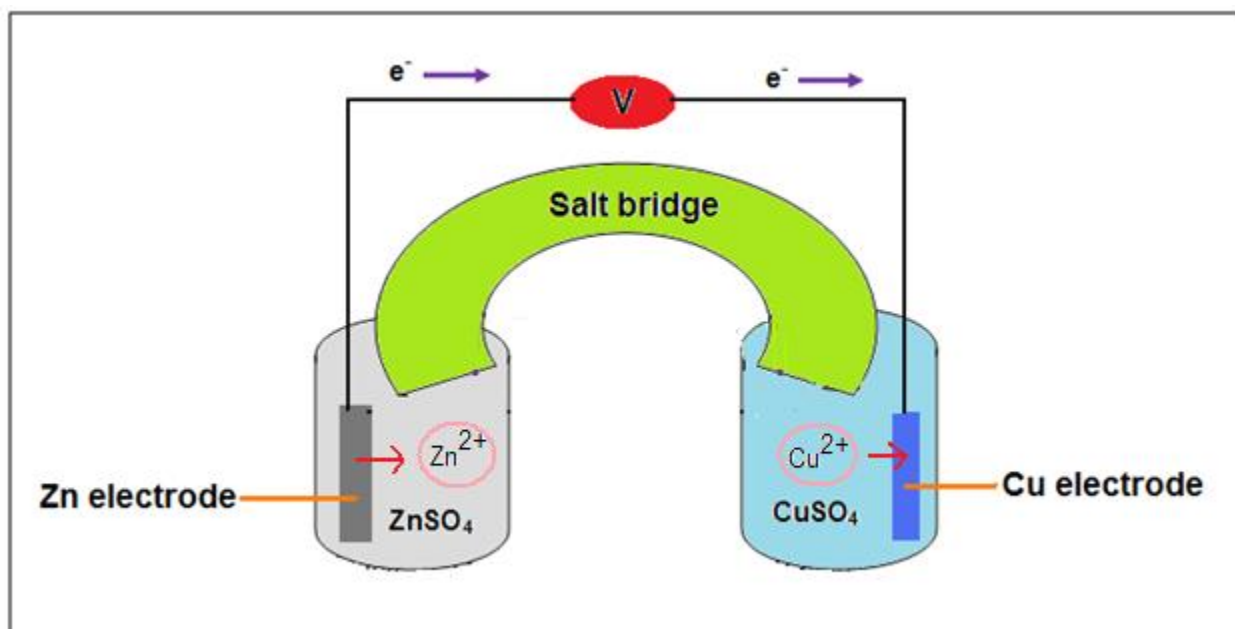

Figure 2.1: The Galvanic cell and its operation[3]

The discovery of the galvanic cell was the start of the energy industrial revolution during which a range of new developments emerged, improving the existing galvanic cell and developing various energy storage devices with their own unique chemistries.

A battery is an electrochemical system made up of a collection of cells that are connected in series, whereas a cell can be considered as the smallest repeating unit of a battery. Cells are divided into two categories; primary and secondary cells. Primary cells are used in a particular application and are replaced once consumed. Primary cells are non-rechargeable, whereas secondary cells have the ability to be restored or recharged a number of times before they are finally discarded.

The following are typical examples of primary cells[4]:

❖ <u>Alkaline cells</u> – These cells obtained their name from the use of potassium hydroxide alkaline electrolyte. They have the advantages of a relatively high energy density and use a relatively cheap active material in the form of zinc as the anode and manganese dioxide (MnO_2) as the cathode. The cells have a typical cylindrical shape and are used in applications such as portable remote controls, clocks, radios, digital cameras and hand-held games.

❖ <u>Zinc-Carbon cells</u> – These cells are the cheaper version of the manganese cell and use a mixture of carbon rods and manganese (IV) oxide (MnO_2) as the cathode, an ammonium and zinc chloride mixture as the electrolyte enclosed in a zinc container that acts as anode. These types of cells are mainly used for low-power portable electronic devices such as flashlights and toys.

❖ <u>Mercury cells</u> – These cells use mercuric oxide and manganese dioxide electrodes. Lately, these cells are rarely used due to the toxicity of mercury. They were primarily used in hearing aids, cameras and calculators.

❖ <u>Silver oxide cells</u> – These cells consist of a zinc electrode as the anode, a silver oxide electrode as the cathode and an aqueous potassium hydroxide or sodium hydroxide solution as the electrolyte. They are expensive due to their use of a silver electrode and are mainly used in military type applications.

❖ <u>Lithium cells</u> –These cells consist of a lithium metal as anode, a manganese dioxide cathode and a lithium perchlorate salt dissolved in propylene carbonate and dimethoxyethane as electrolyte. These cells are the most common type of

consumer cells and are not rechargeable. They are used in applications such as watches, clocks and cameras.

Some of the most common types of secondary cells include[4]:

- ❖ <u>Lead acid cells</u> – These cells are one of the most common secondary rechargeable cells to date. They are made up of a lead anode and a lead dioxide cathode immersed in sulphuric acid as the electrolyte. Their applications are mainly in automobile starting, lightning and ignition systems (SLI), in standby emergency power systems and electric vehicles such as fork lift trucks and golf carts.

- ❖ <u>Lithium-ion cells</u> – These cells are also secondary cells. They consist of carbon or lithium metal as anode, metal oxide as cathode and lithium salt in an organic solvent as electrolyte. This type of cell chemistry will be discussed in more detail in the sections that follow and will form part of the major section to this study.

- ❖ <u>Nickel-Metal-Hydride cells</u>[5]– These rechargeable cells consist of a mixed metal hydride negative electrode replacing the older technologies of cadmium, a nickel oxyhydroxide positive electrode in an alkaline hydroxide solution as electrolyte. These cells are similar in shape and type as the cylindrical alkaline cells and used in digital cameras, GPS units, MP3 players and other portable electronic devices.

2.2 Importance of Lithium-ion cells

There is an ever-increasing demand for smaller, lighter and cheaper cells with larger power capacity and longer life-cycle rechargeable cells. This demand can be primarily ascribed to the daily increase in the demands of small portable electronic devices such as cell phones, laptop computers, video cameras and power tools[6] (Figure 2.2) where the lithium-ion cells have become the most dominant cell chemistry technology for portable electronic applications. The chemistry of the lithium-ion cell is well-suited for these requirements due to its relatively small atomic size to fit easily into the vacancies of crystal structures of various oxide materials without destroying the crystal shape or integrity. It also has a higher energy density with an average cell voltage of 3.6 V which is twice that of standard AA-alkaline cells[6, 7].
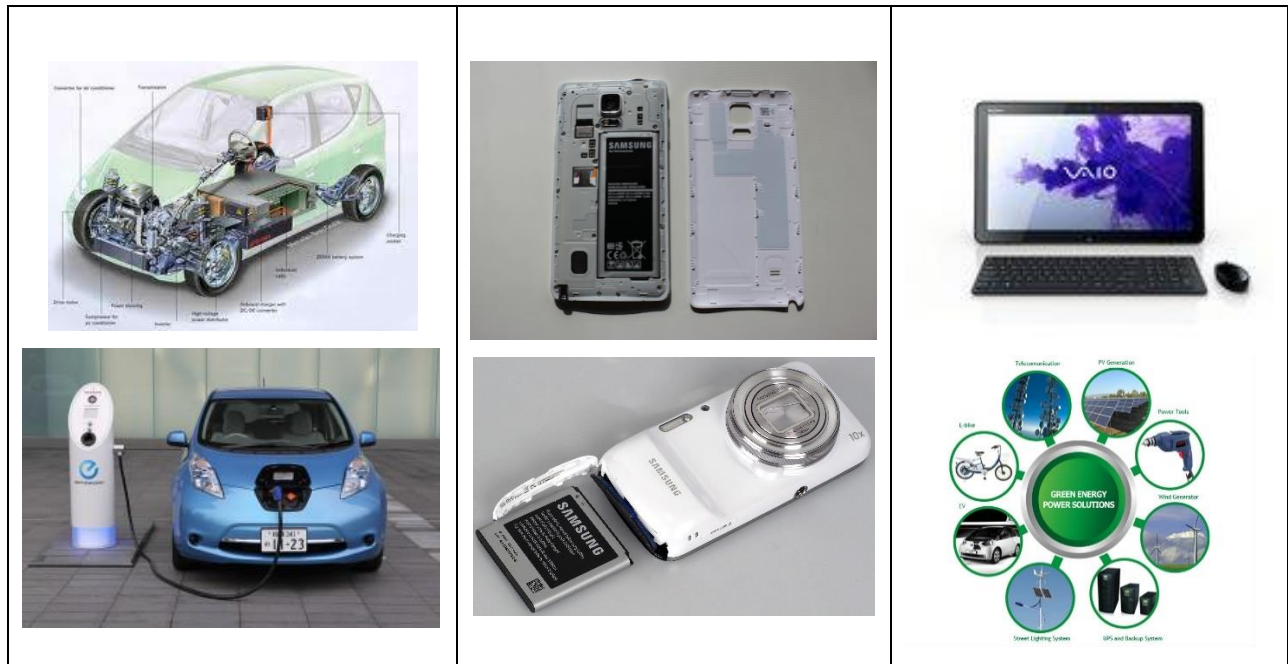
Figure 2.2: Applications of lithium-ion cells[8-13]

These cells can also be built into various designs such as, prismatic cells (used in cell phones, laptops or tablets), pouch cells (used in consumer applications, electric vehicles or military applications) coin cells (used in watches, electric clocks or remote control keys) and cylindrical cells (used in cameras, toys, power tools or medical instruments). Typical examples of these designs are shown in Figure 2.3.

| Prismatic cell | Cylindrical cell | Coin cell | Pouch cell |

Figure 2.3: Examples of various types of lithium-ion cells[14-17]

One of the most dominant energy storage applications for the lithium-ion cell over the last few decades was their use in electric vehicles (EV). Electric vehicles were already in use at the beginning of the 19th century, but were soon replaced by the internal combustion engine. It is only recently, that the full electric vehicle had gained popularity due to the

environmental concerns of excessive carbon emissions from the internal combustion engine.

EVs use battery packs for power where the electricity that is stored and subsequently used can be generated from a wide range of sources such as fossil fuels, nuclear power and renewable power such as solar and wind power.

The lithium-ion cells have a number of attractive performance advantages[18,19] and disadvantages[19] when compared to other aqueous cell chemistries such as lead-acid and nickel-metal hydride.

Advantages

> The lithium-ion cells are considered as a low maintenance battery with a good shelf life.
> The cells have no traditional memory effect merely because lithium-ion cells do not have to be completely discharged before they can be recharged.
> The cells have on average a higher cell potential due to the lithium which has a comparatively high negative reduction potential when compared to other elements.
> The cells can be considered as being fully sealed with little or no leakages during their normal use.

Disadvantages

> The cell chemistry is relatively fragile and requires a protection circuit to maintain the charge and discharge voltage during applications. This is particularly important when there are a large number of cells assembled into a battery pack in series where each cell's voltage must not drop below the discharge voltage limit.
> Transportation by air, road or sea of these cells or battery packs is restricted. As a guiding rule, cells that exceed 1.5 g of lithium per pack should be shipped as a 'hazardous material' which requires specialized packaging into flame and explosion proof containers securely separating the cells in order to prevent short-circuiting.
> Manufacturing is expensive due to a number of factors such as an on-board computer or battery management system (BMS) that is required for a large battery

pack in order to carefully manage each cell's charge and discharge state. The electrode manufacturing is usually done in separate clean rooms to prevent contamination from oxygen and moisture. The electrode alignment and cell assembly has to be very accurate where slight shifts, inaccurate assembly or contamination can lead to short circuiting and cell damage. The costs of manufacturing lithium-ion cells have decreased significantly over the last few years due to the increase in production volume. Currently, they are on average about 40 % higher in cost per kWh when compared to other rechargeable cell chemistries such as the Pb-acid, but this can change over the next few years, as the global volume and use of lithium-ion cells increase.

➢ These cells have relatively high internal resistances which would restrict the ability for high-rate discharge applications.

➢ Cells are sensitive to high temperatures and degrade significantly faster than normal when they are exposed to heat. This can result into the occurrence of cell venting and thermal runaway which eventually leads to fires.

➢ Recycling of large-scale cells such as automotive lithium-ion battery packs is currently still a commercial challenge. There are presently no specific recycling processes and policies in place. However, many countries are looking at and implementing legislation concerning the specific recycling of such battery types and companies such as Sony have started to recycle small consumer cells. For example, Toxco recycles a variety of lithium batteries which include specific large military batteries and Nippon Mining and Metals has started recycling small lithium-ion batteries[20].

2.3 History of the Lithium-ion cell

In 1912 the research on a lithium cell was first introduced by GN Lewis and these cells were only manufactured on a larger scale that made them available to the consumer market[21] in the 1970s. One of the main reasons for the limited commercialization was based on the stability of the lithium metal in a non-aqueous electrolyte. It was only in the 1950s that the lithium primary cells were made with pure metallic lithium as the anode.

These cells could not be recharged, because during the capacity cycling process, pure Li becomes unstable in terms of growing dendrites that damage the separator causing the cell to short circuit. It was only by the early 1980s that the lithium-ion cells were developed to use lithiated carbon (graphite) as the anode, or layered titanium sulfide (TiS_2) with a non-aqueous liquid electrolyte[22]. This development opened the opportunity for further research into the anode material for lithium-ion batteries. The more prominent lithium-sulfur dioxide (Li/SO_2), lithium-manganese dioxide (Li/MnO_2), lithium-polycarbon monofluoride ($Li/(CF_x)_n$) and others are still manufactured today as primary lithium cells with Li/MnO_2 as the more dominant element used typically in coin cells[6].

In the early 1980s Ballard Research Inc. (Li/SO_2 system) and Moli Energy Ltd. (Li/MoS_2 system) developed secondary cells larger than coin cells. Li/SO_2 cells were discontinued due to their limited use for consumer applications[6].

The large scale commercialization of lithium-ion cells can be dated back to the early 1990s with the development of modern portable consumer equipment, from wireless communications to mobile computing. The mentioned equipment has become reliant on the use of rechargeable lithium-ion cells for their portable power supplies[5]. In the early 1990s nickel-cadmium and lithium-ion cells emerged as the primary source of power for portable electronic devices. In 1991 the giant Japanese electronics company, Sony, used a carbon anode instead of metallic lithium to manufacture the first rechargeable Li-ion cell[5]. In 1985 MOLI Energy Inc. developed the first secondary battery with lithium metal as the anode and molybdenum sulfide as the cathode[5].

2.4 Chemistry of Lithium-ion cells

The lithium-ion cell consists of an anode electrode (lithium metal or lithiated carbon), a cathode electrode (for example $LiCoO_2$, $LiMn_2O_4$ or $LiFePO_4$)[5] immersed in non-aqueous or aprotic electrolytes consisting of lithium salts ($LiPF_6$, $LiBF_4$ or $LiClO_4$) dissolved in an organic solvent (ethylene carbonate, dimethyl carbonate, or diethyl carbonate or a mixture of them)[23]. These electrolytes are used in lithium-ion cells due to the fact that lithium is highly reactive with water and these electrolytes remain stable when working in a high cell

voltage window. The anode and cathode electrodes are separated by a separator which is made of a porous membrane to allow the ionic flow or transport of lithium-ions between the electrodes. The following types of materials are typically used as separators in lithium-ion cells: cellulose, glass fiber (non-woven materials), inorganic composite membranes (Separion®, which was developed by Evonik and used in large format lithium-ion cells) and microporous polymer membranes (polyolefines, polyethylene and polypropylene)[24, 25]. Binders are added to the cathode active material acting as an adhesive link between electrode particles which include: teflon, polyvinylidene difluoride (PVdF) or sodium carboxymethylcellulose (CMC). A typical example of a spiral wound cell with its various components is shown in Figure 2.4.
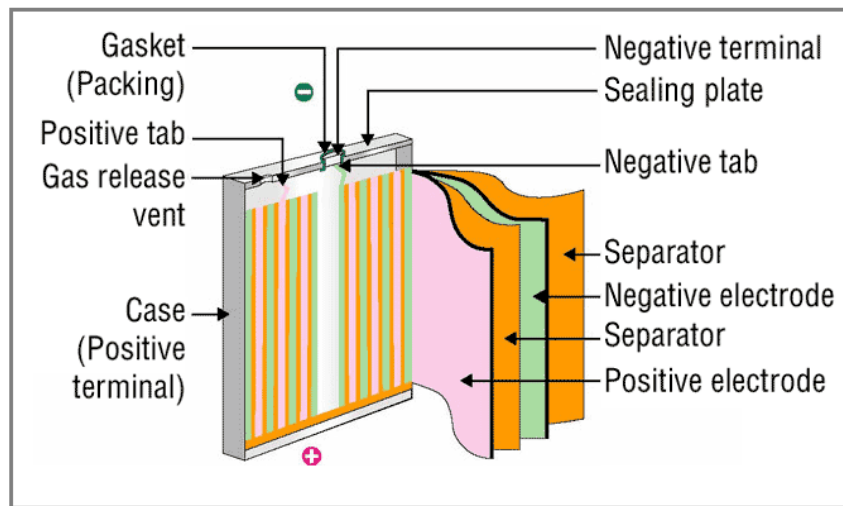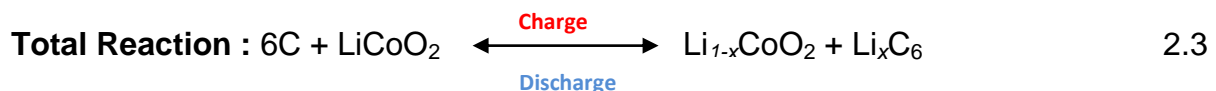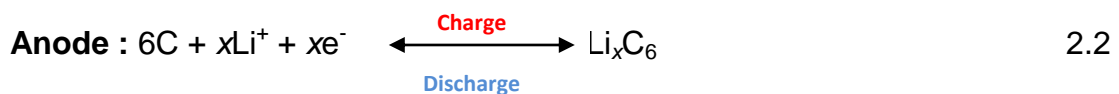

Figure 2.4: Open display on components of a lithium-ion cell[26]

In order for lithium-ion cells to be successful in their operation, two reactions take place at the electrodes upon the charge and discharge process respectively[18]:

Example:

$$\textbf{Cathode}: LiCoO_2 \xrightleftharpoons[\text{Discharge}]{\text{Charge}} Li_{1-x}CoO_2 + xLi^+ + xe^- \qquad 2.1$$

$$\textbf{Anode}: 6C + xLi^+ + xe^- \xrightleftharpoons[\text{Discharge}]{\text{Charge}} Li_xC_6 \qquad 2.2$$

$$\textbf{Total Reaction}: 6C + LiCoO_2 \xrightleftharpoons[\text{Discharge}]{\text{Charge}} Li_{1-x}CoO_2 + Li_xC_6 \qquad 2.3$$

The redox reaction is divided into two half-cell reactions that can be described by the standard reduction potentials (a measure of the energy per unit of charge) expressed by the Nernst equation:

$$E = E^\circ - \frac{RT}{nF} \ln Q \qquad\qquad 2.4$$

Where: E is total potential

E° is standard cell potential

R is the gas constant (8.314 mol.K^{-1})

T is temperature

n is the number of moles of electrons exchanged in a reaction

F is Faradays constant (96 500 C or 26.8 Ah)

Q is the reaction quotient

Temperature and redox materials are important factors for producing sufficient energy density which allow cells to be commercially viable. Therefore, a cathode material must be able to accept and release lithium-ions conducively or adequately to ensure high current recharge and discharge efficiency[27].

Lithium-ion cells are manufactured and assembled in the discharge state (the lithium-ions are in the cathode's active material structure). The cell is first charged before it is sealed and packaged for commercial use. During the charging process lithium-ions are extracted from the layered cathode structure and migrate through a porous separator with the aid of an electrolyte, into the anode active material. This process is referred to as intercalation. Whereas upon discharge the lithium-ions are extracted from the anode and embedded back into the vacant sites of the layered cathode material's crystal structure. This process of discharge is known as de-intercalation. During these two processes the lithium-ion migrates into and out of the crystalline lattice without significantly changing its structure. There is usually a slight change in the unit cell's volume associated with the process. Figure 2.5 demonstrates the intercalation and de-intercalation processes taking place in a lithium-ion cell.
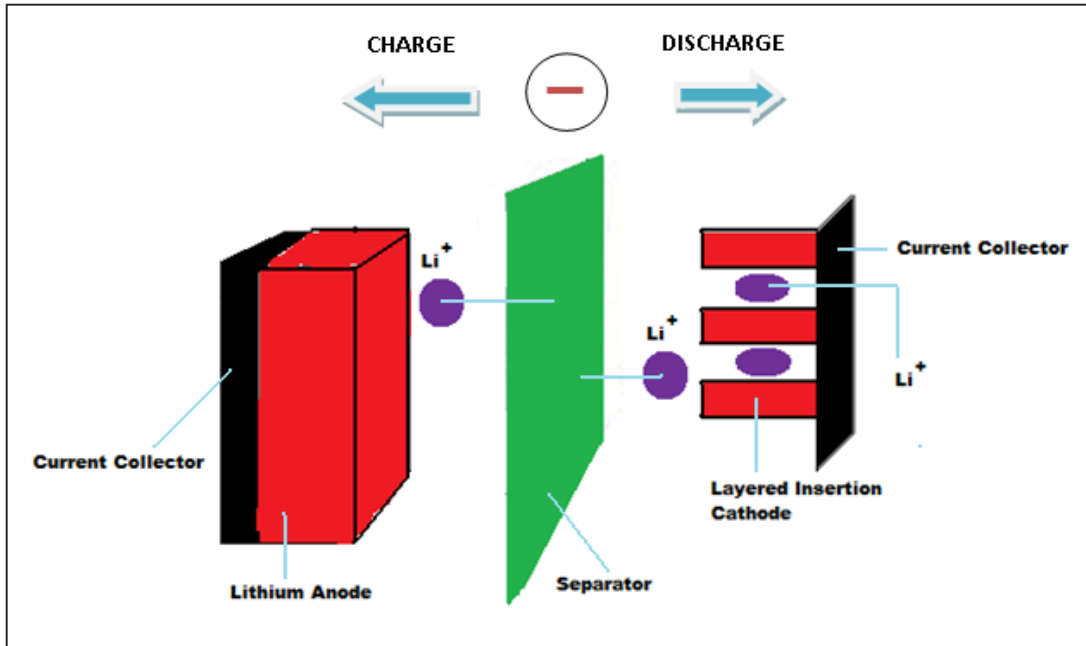
Figure 2.5: A schematic diagram on the insertion and extraction in lithium-ion cells[28]

However, there are other rechargeable cells that exist, but do not form part of this study which include the lithium-ion polymer cells, lithium iron phosphate cells and the nanowire cells[29].

2.5 Failure modes in lithium-ion cells

One of the reasons why lithium-ion cells are currently popular is because of the drive towards lower CO_2 emission passenger vehicles and the reduction of using fossil fuel. However, there are significant safety concerns in stacking a large number of cells together in order to produce a battery with sufficient power for a passenger vehicle to give a comparative speed and range to that of a regular internal combustion engine vehicle. A good understanding of the cell chemistry and its performance under vehicle conditions is required. This understanding of the cell chemistry and performance includes the thermal management, charge and discharge limits and abuse limitations where the behaviour of the battery in an accident needs to be controlled and contained. In addition, there is a significantly higher anticipation of the expected lifespan of such a large battery under a range of different environmental conditions and user applications where it would be expected to last between seven to ten years in continuous use. By comparison, lithium-ion cells for consumer applications such as laptops, cell phones and power tools, the

expected lifespan could be between three to five years with limited need of thermal management, variable charge-discharge applications and dangers due to abuse or damage from accidents. The following are some typical failure modes that can occur within lithium-ion cells[30]:

2.5.1 Solid Electrolyte Interphase (SEI) failure mode

The SEI layer is normally formed as a protective layer on the anode during its initial or first charging process. However, the excessive SEI layer that is formed by use and abuse is where the electrode loses its active material integrity due to the expansion and contraction upon charge and discharge, resulting in stress-strain evolution causing an increase in internal cell resistance. When the SEI layer becomes too thick, it reduces the lithium-ion movement across material interphase which results in capacity loss. When the SEI layer increases, especially at the anode, lithium-ions find it difficult to penetrate into the electrode's pores, resulting in cell failure[31].

2.5.2 Thermal condition failure

Thermal safety is an important parameter to consider in lithium-ion cells under various ordinary applications and possible abusive use. Upon discharge, the reaction is exothermic resulting in an increase in the temperature of the cell which will accelerate the reaction even more by increasing the cell's internal temperature. If this heat is not dispersed effectively to the environment, the temperature will rise very quickly and risk possible thermal runaway. For some cell chemistry types, thermal runaway can even occur when a cell reaches a temperature of 60 °C and higher, resulting in a continuous rapid heating that can lead to gassing and the combustion of the organic material. During thermal runaway three types of heating sources exist[32]:

- Reversible heating which is due to the cell's chemical reaction during discharge.
- Irreversible heating which is due to polarization and ohmic resistance, typically occurring during overdischarging.
- There are also side reactions that can be a source of heat generation. These side reactions include current collector corrosion, overcharging and internal short circuiting.

When lithium-ion cells are prolonging charged at potentials higher (approximately above 4.3 V) than its designated operating potentials the cells become unstable. This prolonged charging results in metallic lithium plating on the anode and the cathode becomes an oxidizing agent that can produce CO_2. The pressure in the cell would rise, causing the cell pouch or container to rupture and eventually lead to combustion when exposed to enough oxygen. This danger can also occur when a lithium-ion cell is charged at high current rates (approximately above 3 C) that can also result in a rapid temperature increase leading to thermal runaway. Thermal runaway can occur at various temperatures for different chemistries (Figure 2.6).
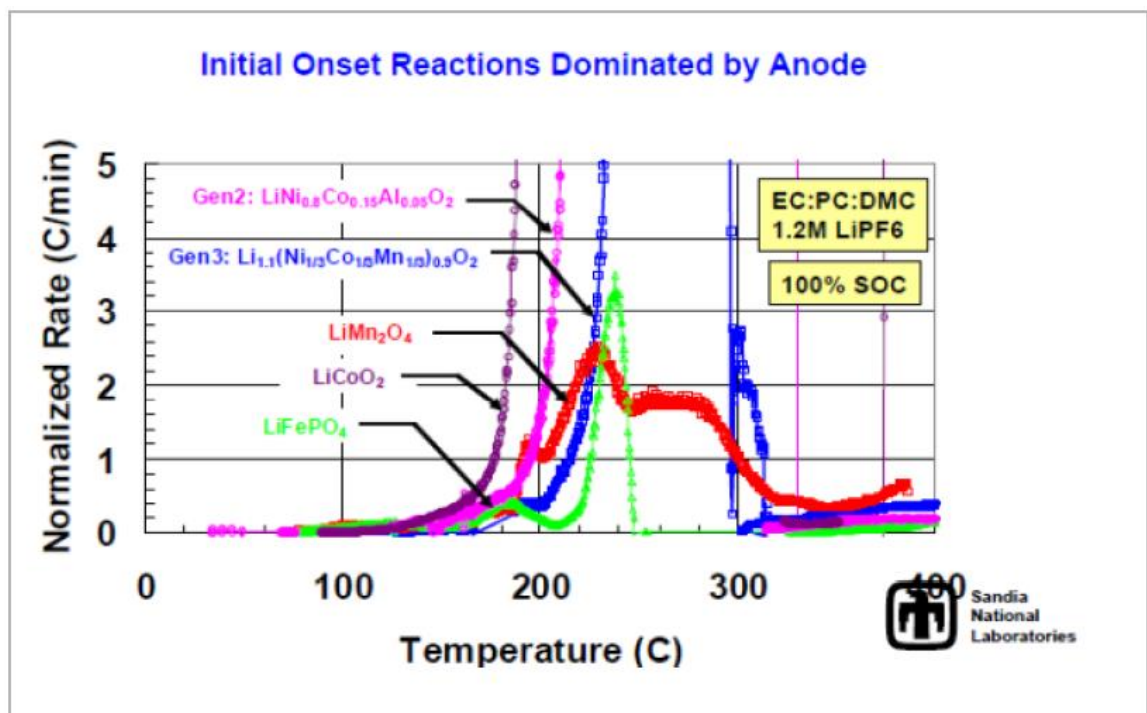

Figure 2.6: Thermal runaway graph for various chemistries[32]

2.5.3 Capacity fade or loss

Capacity fading due to calendar life or cycle life loss can also be considered as an important parameter for lithium-ion cells. The loss of active material (both primary and secondary) and rate capability differences refer to capacity fade; they consist of both reversible and irreversible components. When a cell loses its capacity due to self-discharge, it can cause reversible loss and upon recharge the loss can be recovered

again. On the other hand degradation of the cell refers to irreversible capacity and cannot be recovered. Capacity fading during cycling is normally due to the degradation of the positive material's crystalline structure. During cycling the composite electrodes' structure can experience mechanical modifications due to the crystal structure's volume change. These mechanical modifications result into the active material de-connecting or disconnecting from the conductive network. The passivation film will also accumulate on both electrodes during the process, thereby increasing the limitations of access to the active surface area and clogging the micropores.

Researchers continue to develop new materials to overcome some of these limitations and to improve the external battery management systems to effectively manage their use in large scale applications.

2.6 Elemental properties

2.6.1 The anode material

The following section discusses some of the general properties of the anode materials used and some of the research done to improve its use to date.

2.6.1.1 <u>Lithium metal</u>

Figure 2.7: The element lithium[33]

Lithium was originally discovered by José Bonifácio de Andrada e Silva in 1800 and in 1817 Arfvedson detected the presence of the new element when analyzing petalite ore[34]. This light, soft, silver-white metal (Figure 2.7) belongs to the alkali-metal group. It is found in trace amounts in natural igneous rocks and in the waters of many natural mineral

springs. It is also found in small amounts in sea water (about 0.17 ppm). The metal has a high specific heat; it is corrosive and requires special handling under normal atmospheric conditions[35].

Lithium reacts easily with water forming hydrogen gas and aqueous lithium hydroxide. Owing to this reactivity, it is usually stored in a viscous hydrocarbon. In moist air, lithium metal rapidly tarnishes to form a black coating of lithium hydroxide (LiOH and $LiOH \cdot H_2O$), lithium nitride (Li_3N) and lithium carbonate (Li_2CO_3), the result of a secondary reaction between LiOH and CO_2[36].

The use of lithium metal, besides in lithium-ion cells, includes specialty alloys. Lithium as lithium oxide is used in glasses and ceramics for the manufacturing of glazing, and in components of ovenware and ceramic parts[37]. Lithium is also used in pharmaceutics as lithium carbonate as a mood-stabilizing drug and in military applications such as rocket propellants and in nuclear reactors as a coolant[38]. The use of lithium metal as the anode in primary lithium cells (i.e. $Li-MnO_2$) was used for the first time by SANYO Inc. in the 1970s[5]. With time, the use of lithium as the anode in rechargeable cells proved to be dangerous[39,40] due to dendrite growth during repeated cycling[39]. Dendritic formation occurs on the lithium surface influenced by the electrolyte's surface tension, surface energy and the continuous deposition and dissolution process of the lithium-ion during charge-discharge processes. This dendritic formation results in poor electrochemical performance due to the formation of a non-uniform layer of solid electrolyte interphase (SEI) layers that can eventually puncture the separator causing an internal short circuit[41]. The metal anode is replaced by various types of graphitic carbons that show good reversibility of the lithium intercalation-deintercalation, high reversible capacities, excellent rate capabilities, good cycling stabilities[42], low discharge potentials[43], high lithium storage capacity, high mechanical strength, good thermal conductivity, large surface-to-mass ratio and ultra-high electronic mobility. Sony Inc. commercialized the first carbon anode with $LiCoO_2$ as the cathode in the well-known 18650 lithium-ion cell in 1991. The replacement of graphite as anode was also investigated due to graphite's cost-effective performance and its reversible lithium intercalation property. Graphite has a theoretical lithium storage capacity

of 372 mAh.g^{-1}; therefore other anode materials were also considered which consists of higher energy storage.

In spite of the effective use of graphite as the anode material for many years, there are some problems with the material that include an excessive charge build-up during repeated cycling and the material also swells during the charge process when storing Li-ions[6]. The swelling process of the active carbon breaks electrical contact points in the anode, thereby reducing overall effective conductivity[5]. This process has always been a problem in the design of high capacity lithium-ion anode materials with only a few studies that have shown an improvement of the anode material[43-47] which will be briefly discussed in the following paragraphs.

Novel graphene carbons have a theoretical capacity ranging from 500-1100 mAh.g^{-1} that may meet the requirements of a suitable active anode material that can be used to replace the traditional graphite anode material. Chakraborti *et al.*[45] looked at using small carbon clusters as possible anode material by using amine functionalized graphene (AFG) activated with lithium.

Tin IV oxide (SnO_2) has also been considered as anode material to replace graphite for lithium-ion cells because of its high theoretical capacity (782 mAh.g^{-1})[43]. However, during repeated capacity cycling, the reaction of SnO_2 and lithium results in mechanical disintegration of the active material with a loss of electrical conduction within the electrodes[43]. To overcome this problem, a carbon coating of the layered meso-porous SnO_2 spheres was prepared and sandwiched between suitable graphite layers (Gr/C-SnO_2)[44]. This approach increased the SnO_2 utilization resulting in an increased surface area that was more efficient for lithium and SnO_2 reactions. A major advantage in following this approach was that no polymer binders and conductive additives were needed as with other electrode materials with an improved overall cell energy density. From this study it was concluded that layer-by-layer assembled Gr/C-SnO_2 produced better electrochemical performance due to their low contact, low charge-transfer resistance, high reversible lithium storage capacity, improved cycling and good rate performance at high specific currents[44].

Lithium vanadate (Li_3VO_4) was also amongst other materials that showed to be suitable as an anode material for lithium-ion cells[46]. This material, combined with graphene, improved the overall electrochemical performance, resulting in lower charge transfer resistance and an enhanced lithium diffusion coefficient. Growing Li_3VO_4 onto an electric collector also improved the electrochemical performance. In this study nickel (Ni) foam was used as a deposition substrate because of its good structure stability and electronic conductivity[46].

$Li_4Ti_5O_{12}$ is another material considered for the anode because it has a comparatively low lithium insertion voltage of 1.5 V[47]. The material was also reported to have additional properties such as avoiding electrolyte reduction on the electrode surface and on the formation of the SEI layer. This material also exhibited better cycling performance. Owing to low electrical conductivity and kinetic problems, this anode material was limited in obtaining its full theoretical capacity[47]. The improvements of this material was obtained by improving the electron transfer between the current collector and the active material, cation doping of the active material, surface coating and nano-$Li_4Ti_5O_{12}$ preparation. For example, lithium lanthanum titanate ($Li_{3x}La_{(2/3)-x}TiO_3$, LLTO) was an appropriately doped material with good lithium-ion conducting properties and improved electronic conductivity when compared to $Li_4Ti_5O_{12}$[47].

2.6.2 The cathode material

2.6.2.1 <u>$LiCoO_2$</u>

Cobalt (Co) occurs naturally in a combined form such as cobalamins in minerals, in nature, in parts of vitamin B12 and is typically mined in the Democratic Republic of the Congo and Zambia. The free metal which is silver-grey in colour (Figure 2.8) is produced by reductive smelting and used extensively in glass, ceramics and paints[48]. Cobalt can have up to six oxidation states ranging from 0 to 5 of which +2 and +3 are the most common oxidation states[49]. This element has many applications in specialty alloys, catalysis, pigments, colouring, radioisotope chemistry and lithium-ion batteries[48].

Figure 2.8: The free element, Cobalt[49]

In battery or cell applications, cobalt is used in the form of lithium cobalt oxide ($LiCoO_2$) as the cathode material which was used in some of the first lithium-ion products marketed by Sony in the 1980s[5]. Significant amounts of cobalt are also used in nickel-cadmium (NiCd) and nickel metal hydride (NiMH) cells where the cobalt improves the oxidation capabilities of the nickel in the cell[50]. $LiCoO_2$ materials consist of 2D layered cobalt oxide structures (Figure2.9) in which the lithium-ions can migrate through the structure in two directions. The lithium-ions occupy the octahedral sites and upon discharge the lithium-ion de-intercalates from the anode and migrates into the layered structure[23].
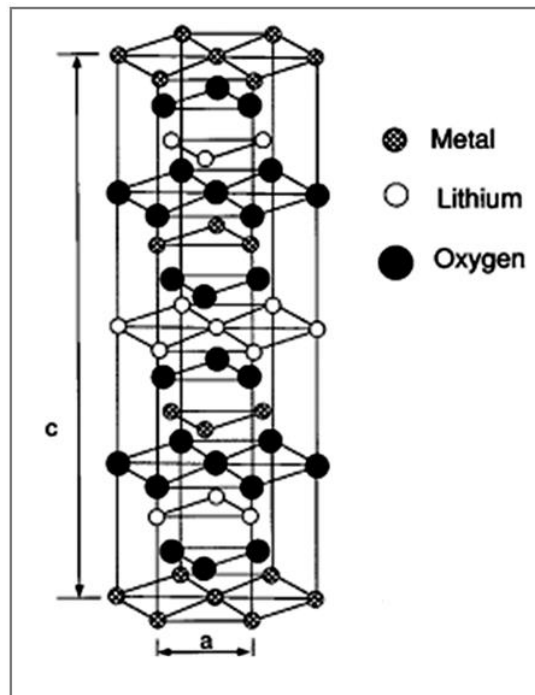
Figure 2.9: The idealized layered structure of $LiCoO_2$, Li is white, O black and Co speckled[23].

This type of oxide material produces sufficient electrochemical performance, is less hazardous and is insensitive to process variation and moisture. Apart from its excellent advantages, this material also has a number of shortcomings or disadvantages in cell chemistry such as the ability of a relatively low discharge current rate and when the discharge load is too high, overheating of the battery pack can occur relatively quickly. This shortcoming limits the material's high rate of discharge use due to safety concerns resulting in a build-up of increased internal resistance during cycling and aging.

Owing to these disadvantages, the cathode material is improved to produce a material with better electrochemical properties. The improvements include reducing the manufacturing cost, increasing the capacity cycling ability and improving material structural stability. The new developments in this layered structured material include new synthesis methods, which use doping with various transition metal elements such as Mg, Cu and Eu[51-53], to name a few and also coating with carbon and various metal oxides that include Al_2O_3, MgO, Li_2CO_3, $AlPO_4$, SnO_2[19, 54].

Some of the new developments studied by various researchers will be summarized in the next few paragraphs.

A number of investigations had been conducted into doping the cathode material with a range of elements, of which zirconium (Zr) is an element that showed a drastic improvement in the electrochemical properties of $LiCoO_2$ ($LiCo_{1-x}Zr_xO_2$)[55]. The study showed relative improvements in the rate performance (0.2 C to 3 C) when doping with Zr in comparison to the undoped $LiCoO_2$. The discharge capacity performance for Zr (at 1 mol%, 108 mAh.g^{-1} and 5 mol%, 104 mAh.g^{-1}) after 50 cycles was higher than the undoped material (23 mAh.g^{-1}). As a result the conclusion to this study was that Zr doping improves both cycling stability and rate performance[55].

Manganese and Ni doped $Li_xCo_yO_z$ cathode material forming $Li_{1.2}Mn_{0.54}Ni_{0.13}Co_{0.13}O_2$ was also proved to be a promising cathode material. The electrochemical performance of this material was significantly affected by the material's particle size which implicated that the smaller the particle sizes (230 ± 10 nm at 575 °C compare to 320 ± 10 nm at 800 °C), the better the material's electrochemical activation with an increase in capacity (206 mAh.g^{-1} at 575 °C and 172 mAh.g^{-1} at 800 °C) and cycle life (after 100 cycles)[56].

$Li_{1.2}Mn_{0.54}Ni_{0.13}Co_{0.13}O_2$ delivered excellent electrochemical performance within a wide range of process conditions.

Coating proved to be another promising technique to improve the electrochemical properties of $LiCoO_2$. The experiment entailed coating $LiCoO_2$ particles with glassy lithium boron oxide (LBO)[57]. The coating material proved the existence of a high Li^+ conductivity with good wetting properties of the $LiCoO_2$ particles at high temperatures with a relatively low viscosity. From these findings, it was concluded that coating (5 wt% glass LBO) increased the mean particle size (92 and 120 nm at 600 and 700 °C post-treatment, respectively) resulting in an improvement in the material's electrochemical properties (obtaining high initial charge-discharge capacities and good capacity cycling) and a decrease in the reactivity of the oxide with acidic electrolyte[57]. Having a capacity retention of 89 % at 600 °C (122-109 $mAh.g^{-1}$) and 98 % at 700 °C (126-123 $mAh.g^{-1}$) after 50 cycles.

Substrate Induced Coagulation (SIC) was one of the coating processes used to coat nano-sized titania onto $LiCoO_2$[58]. This technique was considered to be cheaper and can be processed with relative ease by using standard laboratory equipment. Another advantage of using the dip-coating process was the fact that it was used for any type of surface that was water insoluble and the coated particles would form a meta-stable dispersion. Researchers have used this method to produce suitable core-shell materials with a thin and dense layer of nano-sized particles. Titania reacts only with the active material at the surface, therefore having little or no effect on the electrochemical bulk capacity of the main material; thereby improving the battery's overall cycling performance[58].

Cathode materials in lithium-ion cells need to be structurally stable as well as electronically and ionically conductive for their successful use. It was shown that the use of effective carbon coating of the cathode active material can improve the electrochemical properties due to an increase in electronic conductivity[59]. Kwon *et al.*[59] showed that by using ball milling synthesis techniques, improvements in the material's homogeneity was achieved with good contact between the carbon and $LiCoO_2$ particles. The material (mixed at 5 min ball milling) proved to have good ionic conductivity (due to small particle size at 5 min milling time) with high lithium-ion diffusion (about 10^{-6} to 10^{-7} $cm^2.s^{-1}$). Too long milling

times (30 and 60 min) produced $LiCoO_2$ particles with a thick and dense layer that decreased their respective electronic conductivity[59].

Lee *et al.*[60] described the use of vanadium oxide coatings on $LiCoO_2$. They showed that the vanadium oxide coating does not negatively reduce the $LiCoO_2$ material's capacity as with other types of materials. The coated material rather showed an improvement in the cell's cycling performance (producing a capacity retention close to 100 %). The vanadium oxide coating prevented cation mixing to occur during capacity cycling, thereby reducing the negative effect of the active materials' decrease in active surface area which was in contact with the electrolyte[60].

2.6.2.2 $LiMn_2O_4$

Manganese (Mn) is found in nature in combination with iron ore and many other minerals. It is predominantly mined as oxides (pyrolusite, MnO_2 and rhodochrosite, $MnCO_3$). This metal in its pure form is silver-grey in colour (refer to Figure 2.10) and is very brittle, hard and easily oxidized[61].

Figure 2.10: The Mn oxide and pure metal[61]

Manganese has a number of oxidation states, of which +2, +3, +4, +6, +7 are the most common oxidation states[61]. This metal has a wide range of applications in industrial and metallurgical environments. It is most commonly used in the manufacture of steel and aluminium alloys for its corrosion resistant properties. It is also used in alloying copper to improve the materials' castability and mechanical strength[62]. For many years, manganese dioxide is used in alkaline primary cells[62] of which the typical Leclanchè cell is in use since 1845 and can be summarized in the following reaction equation[63]:

$$Zn_{(s)} + 2MnO_{2\,(s)} + 2(NH_4)Cl_{(aq)} + 2H_2O_{(l)} \longrightarrow ZnCl_{2\,(aq)} + 2Mn(OH)_3 + 2NH_{3\,(aq)} \qquad 2.5$$

electrolyte

Oxidized at anode   Reduced at cathode
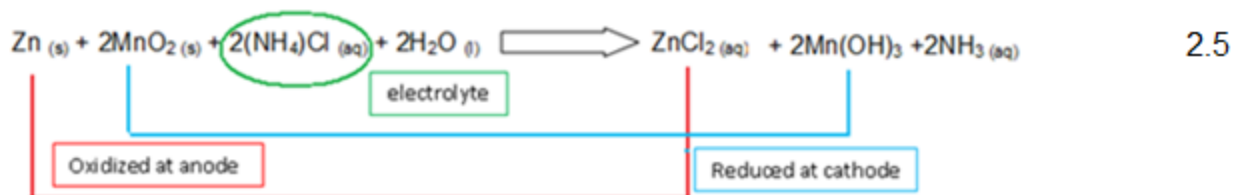
The use of manganese oxide in lithium cells was investigated by SANYO Inc. in 1962[6, 23]. The use of manganese oxide as cathode material has a number of advantages, which include its ability to operate at relative large current densities, it is relatively thermo-stable, and it is considerably lower in cost than cobalt and can operate at high potentials (4 V vs Li/Li$^+$). The manganese oxide is also environmentally friendly in terms of its low levels of toxicity when compared to cobalt which must be considered during waste disposal or recycling[64].

Lithium manganese oxide occurs in various forms, whereby the 3D structure of the spinel, $LiMn_2O_4$, is commonly used in lithium-ion cells[18, 65]. In the spinel ($LiMn_2O_4$) structure, lithium is located at the tetrahedral 8a sites, manganese at the octahedral 16d sites and oxygen on the 32e cubic close packing sites (Figure 2.11).
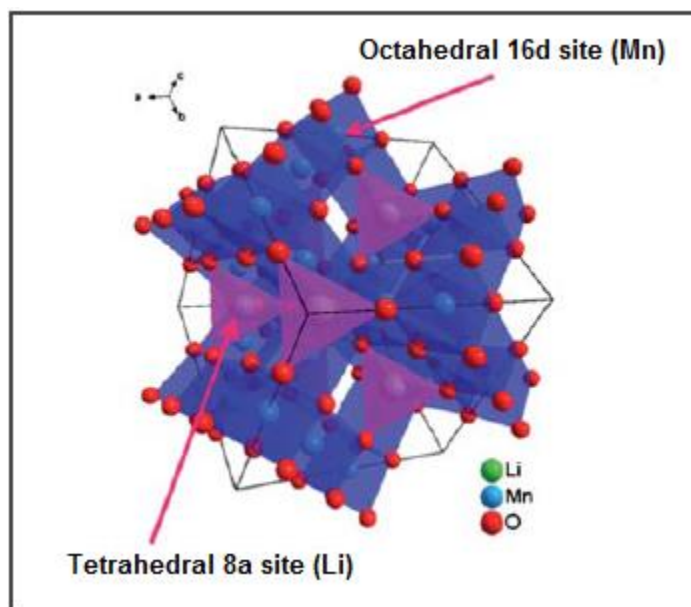
Figure 2.11*: Spinel LiMn$_2$O$_4$ structure*[66]

The spinel $LiMn_2O_4$ materials however suffers from capacity fading during cycling (at elevated temperatures) which resulted from Jahn-Teller distortion, Mn dissolution (in the electrolyte) and lattice instability and oxygen deficiency[64, 67-71].

Intercalation and de-intercalation (within $LiMn_2O_4$) occurs at the 3 and 4 V voltage plateaus. The 3 V range (whereby Li^+ is inserted into $Li_xMn_2O_4$) gave rise to Jahn-Teller distortion, leading to fast capacity fading (transformation from cubic to tetragonal symmetry)[72, 73]. The Jahn-Teller effect occurs due to the coexistence of Mn^{3+} and Mn^{4+} in the $LiMn_2O_4$ structure where the Mn^{3+} concentration is slightly higher than that of Mn^{4+}. This Mn^{3+}concentration increase the distortion effect even more causing a breakdown in the crystal lattice during capacity cycling[74]. $Li_xMn_2O_4$ is more stable to cycling within the 4 V region, however the 4 V region gave rise to slow capacity fading[72, 73].

Capacity fading during cycling is reduced by doping with various transition metals such as Co, Al, Mg, Ni, Fe, Cr, Zn and Ti[65,67,71, 72, 75], by increasing the average Mn-ion valence to 3.5[73], by coating the spinel material with various materials such as carbons or other transition metal oxides (such as $Li_2O{\cdot}2B_2O_3$ glass, MgO and Al_2O_3)[76] or by coating with doped spinel oxides[77]. Coating the spinel oxide would only be discussed on a few materials, although there are many studies on this topic.

Gummow *et al.*[73] made use of reducing the Mn^{3+} concentration within $Li_xMn_2O_4$ and increasing the average manganese-ion valence to 3.5. They investigated the effect of increasing δ in $Li_{1+\delta}Mn_{2-\delta}O_4$ (δ=0-0.33) whereby these variations resulted into a decrease in lattice constant. The investigation of replacing small Mn amounts with Li, Mg or Zn was also studied, increasing the Mn oxidation state to above 3.5[73]. Improvements within these electrodes rechargeability could be due to Jahn-Teller suppression. Using Mg^{2+}, Li^{2+}, Zn^{2+} resulted in a stable rechargeable capacity in excess of 100 mAh.g^{-1}.

Magnesium (Mg) and Iron (Fe) doping was one of the many transition metals used to dope spinel $LiMn_2O_4$[75]. Singh *et al.*[75] showed that doping with Mg and Fe had no effect on the powder X-ray diffraction pattern showing a pure cubic spinel structure. The lattice parameters increased slightly with the increase in Fe concentration (8.241 Å compared to 8.240 Å for pure $Li_{1.03}Mn_{1.97}O_4$) and decreased with an increase in Mg concentration

(8.2203 Å). The crystallinity increased in both the doped (Mg and Fe) materials. From their Scanning Electron Microscopy (SEM) analysis Singh *et al.*[75] observed that the doped material had an increase in its average particle size because the particle growth was higher. Furthermore the SEM imaging of these materials showed agglomerated particles (having truncated octahedral shapes for the doped materials), with a decrease in their average surface area, resulting in a lower surface energy and an increase in packing density with a higher bulk capacity. $Li_{1.03}Mg_{0.2}Mn_{1.77}O_4$ and $Li_{1.03}Fe_{0.2}Mn_{1.77}O_4$ showed a decrease in their initial discharge capacity (88 $mAh.g^{-1}$ and 110 $mAh.g^{-1}$ respectively) when compared to pure $LiMn_2O_4$ (126 $mAh.g^{-1}$). This decrease in capacity was due to the decrease in lithium content that occurred during de-intercalation. The doped materials showed better capacity retention (reducing from 110 to 109 $mAh.g^{-1}$ for Fe-doped and reducing from 88 to 87 $mAh.g^{-1}$ for Mg-doped) upon capacity cycling when compared to the undoped material (reduction of 126 to 118 $mAh.g^{-1}$)[75]. It can be concluded that doping improved the material's cycling performance.

de Kock *et al.*[78] also investigated the Mg^{+2} substitution together with other multivalent cations (Zn^{2+} and Al^{2+}) in $LiMn_2O_4$ with general formula, $LiMn_{2-d}M_{d/b}O_{4+\delta}$ (d=0<d≤0.15, b=M and δ=0≤δ≤0.5). These doped spinels, studied in the 4 V region, showed that a doped level of d=0.05 was appropriate optimizing stability and capacity. The Mg^{2+}, Zn^{2+} and Al^{3+} doped spinel materials observed good cycling performance with little capacity loss after 30 cycles (on average ~110 to 95 $mAh.g^{-1}$ depending on the dopant used), whereas the pure spinel ($LiMn_2O_4$) obtained a capacity loss of 10-13 % from their initial capacity[78].

Doping $LiMn_2O_4$ with Chromium (Cr) and Aluminium (Al) at various concentrations was investigated by Thirunakaran *et al.*[67]. Al-doping promoted the sintering of the spinel $LiMn_2O_4$ structure that resulted in lower structural disorder around Mn atoms and proved that the capacity retention upon cycling was improved. The doped materials had slightly higher initial discharge capacities (139 $mAh.g^{-1}$ for both 0.1 Al and 0.1 Cr) compared to the pure $LiMn_2O_4$ (135 $mAh.g^{-1}$) with coloumbic efficiencies of 96 %, 98 % and 93 % for Cr, Al and pure $LiMn_2O_4$ respectively. After approximately 10 charge-discharge cycles, capacity fading was about 34 % (for pure $LiMn_2O_4$), 12 % (for Cr-doped) and 9 % (for Al-doped). Doping with Cr showed to affect the morphology of the cathode material where a uniform

distribution of fine individual grain particles of particle size below 50 nm were observed using Scanning Electron Microscopy analysis (SEM). Whereas Al doped materials were spherical in shape with agglomeration of the grain particles with an average particle size of ~ 50 nm. Their Transmission Electron Microscopy analysis (TEM) showed that the spinel $LiMn_2O_4$ had a particle size of about 100 nm[67]. This study showed that the synthesized doped materials produced stable specific capacities, stable cycling behavior and high coloumbic efficiencies.

Zhang *et al.*[71] did a study on stabilizing spinel $LiMn_2O_4$ by modifying the oxygen stoichiometry, using $mCrO_{2.65}$ (chemically modified chromium, V-VI, oxide) as oxide. The BET results for $mCrO_x$ doped spinel ($LiCr_yMn_{2-y}O_4$ where y=0, 0.02, 0.05 and 0.1) were 2.9, 2.7, 2.8 and 2.6 $m^2.g^{-1}$ at 650 °C showing no significant change. The $mCrO_{2.65}$ doped $Li_{0.3}Cr_{0.1}Mn_{1.9}O_4$ showed the best cycle performance, where the capacity (~119 $mAh.g^{-1}$ at C/2) of the doped material remains almost the same after 200 cycles. However it was also found that this kind of cathode material had a realtively higher lithium diffusion coefficient (D_{Li}) for $mCrO_x$ doped $Li_{0.3}Cr_{0.1}Mn_{1.9}O_4$ ($3.92x10^{-8}$ to $7.42x10^{-8}$ $cm^2.s^{-1}$) compared to the standard pure spinel material $LiMn_2O_4$ ($9.65x10^{-10}$ to $5.78x10^{-10}$ $cm^2.s^{-1}$). From these findings it could be concluded that $mCrO_x$ doped improved the materials electrochemical performance[71].

$LiNi_{0.5}Mn_{1.5}O_4$ was considered as a high voltage (4.9 V) spinel structure or material[79-84] whereas $LiAl_{0.5}Mn_{1.5}O_4$ was reported as a high voltage and cyclability material[67]. Kebede *et al.*[85] have done a study on the synthesis and electrochemical properties of Ni and Al-doped spinel $LiM_{0.5}Mn_{1.5}O_4$, where it was found that the particle sizes for Ni doped cathode spinel had a distinctively narrower particle size distribution relative to the Al doped and the undoped spinel materials, the particle sized ranged from 1.5-3.0 μm for Ni doped, 0.45-0.9 μm for Al doped and relatively wider range of 0.9-3 μm for the undoped pure spinel. Powder X-ray diffraction analysis (PXRD) showed pure spectrums with space group Fd3m (for all the oxide materials studied) and showed a decrease in lattice parameter as Mn^{3+} is substituted with Ni^{2+} or Al^{3+}. $LiMn_2O_4$ obtained an initial discharge capacity of 122 $mAh.g^{-1}$ at 0.2 C (plateau at 3.8 V), $LiNi_{0.5}Mn_{1.5}O_4$ delivered a discharge capacity of 102 $mAh.g^{-1}$ (double plateaus at 4.6 and 3.8 V, due to Ni^{2+}/Ni^{4+} and Mn^{3+}/Mn^{4+} redox couples

respectively) and $LiAl_{0.5}Mn_{1.5}O_4$ gave a discharge capacity of 75 mAh.g^{-1} (plateau at 4 V). From these discharge capacities and voltage plateaus it can be observed that an increase in voltage was obtained from 3.8 V (for $LiMn_2O_4$) compared to the doped materials having higher average voltages, therefore the doped materials can be considered as high voltage cathode materials. These materials underwent capacity cycling to examine the cell performance. From these cycling results it was observed that $LiMn_2O_4$ retained 60 % of its 1st cycle capacity (after 50 cycles)[81, 85]. The Ni and Al-doped materials retained 99.8 % of its 1st cycle capacity (after 50 cycles) concluding that the doped material had a better retention[81, 85]. These observed results (enhancement in capacity retention) could possibly be due to a decrease in the Jahn-Teller distortion (by the substitution of small Ni and Al amounts for Mn) and there may be a decrease in spinel dissolution[85].

Ni-doped $LiMn_2O_4$ was also investigated by Sun *et al.*[65]. They studied the synthesis of doped and undoped spinel materials that produced particles that were sub-micron in size with a narrow size distribution with a pure phase (particle sizes of 100, 200 nm and 1 μm at 650, 750 and 800 ºC respectively). The Ni-doped oxide material studied by Sun *et al.*[65] produced powders that can be indexed with the same space group (Fd3m) as the undoped spinel oxide material. Ni-doped materials delivered a lower initial capacity (126 mAh.g^{-1}) when compared to the undoped spinel material (145 mAh.g^{-1}), but the doped material showed to have better cycling performances (120 mAh.g-1 at 100th cycle) compared to $LiMn_2O_4$ (128 mAh.g^{-1} at 90th cycle, 96 % of its initial capacity). This improved cycling performance was due to the fact that Ni-ions enhanced the octahedral site's stability in the spinel structure[65].

As mentioned previously (under this Section 2.6.2.2), spinel $LiMn_2O_4$ suffers from capacity fading during cycling, efforts had been made to improve the materials cycle life. Baochen *et al.*[86] studied Co-doped $LiCo_xMn_{2-x}O_4$ and found that this oxide material would improve a cells cycling performance. Trivalent cobalt (Co^{3+}) was added to the spinel material to partly replace the manganese in order to reduce the Mn^{3+} formation in the $LiMn_2O_4$ structure, reducing the effect of Jahn-Teller distortion[87]. Huang *et al.*[87] also showed that an over-substitution (higher than the 109:91, Co to Mn, optimized value) by the Co^{3+} led to the presence of cobalt impurities in the material which resulted in a decrease in discharge

capacity and overall performance. The PXRD pattern for this particular material were indexed to the spinel structure with a space group of F3dm, its lattice parameter was also smaller (8.0556 Å) compared to the undoped spinel material (8.2438 Å). Scanning electron microscopy analysis (SEM) showed that the material had a particle size of about 200 nm. This material also showed lower coulombic efficiencies, which was mainly due to the electrolyte decomposition at the high cell potentials (5.3 V) during charging[87].

Arora *et al.*[88] have done a study on the electrochemical performance Co doped spinel materials by varying the ratio of Co to Mn in $LiCo_yMn_{2-y}O_4$ from y=0.05-0.33, spinels. Powder X-ray diffraction results showed pure single-phase spinel materials with space group Fd3m was obtained for y=0-0.33 Co-doped spinel materials. The lattice constants decreased (8.229-8.097 Å for y=0.08-1 respectively) with increase in Co concentration and was also lower in comparison to the undoped $LiMn_2O_4$ (8.249 Å). BET results showed that increasing the Co concentration would decrease the surface area with an increase in particle size; this can be beneficial for good capacity retention properties. An increase in initial specific capacity was observed with an increase in Co concentration (~100-120 m $Ah.g^{-1}$ for y=0.05 and 0.06), which would in turn result into a decrease in capacity fading during cycling. These results can be explained by the fact that after 85 cycles the Co-doped spinel (y=0.05 and 0.06) specific capacity was 90 and 82 $mAh.g^{-1}$ respectively, being higher than the undoped spinel specific capacity of 65 $mAh.g^{-1}$. The Co-doped material had a higher estimated lithium-ion diffusion coefficient (D_{Li}) of 2.4×10^{-12}-1.4×10^{-11} $m^2.s^{-1}$ compared to the undoped material of 9.20×10^{-14}-2.6×10^{-12} $m^2.s^{-1}$ as a function of SOC[88]. The Co-doped material was further studied by Banov *et al.*[89] investigating various synthesis temperatures (400, 600 and 750 °C) producing an increase in the materials lattice parameter (8.182, 8.207 and 8.216 Å), however at 750 °C the lattice parameter was close to the undoped material (8.237 Å). The initial discharge capacity of the Co substituted material (114 $mAh.g^{-1}$) decreased slowly to 107 $mAh.g^{-1}$ at C/3 after 100 cycles in comparison to the undoped material (128-102 $mAh.g^{-1}$), thus leading to an enhanced cycling stability[89].

Hernán *et al.*[90] investigated the effect of Co, Cr and Ti dopants ($LiCo_{0.2}Mn_{1.8}O_4$, $LiCr_{0.2}Mn_{1.8}O_4$ and $LiTi_{0.19}Mn_{1.76}O_4$) to $LiMn_2O_4$ in high voltage lithium batteries. SEM

analysis showed a particle size of 1 μm in diameter (for Co and Cr-dopants) whereas Ti-doped spinel obtained a 2.5 μm particle size. The initial discharge capacity for Co-doped was 100 mAh.g^{-1}, 85 mAh.g^{-1} (for Cr-doped) and 80 mAh.g^{-1} for Ti-doped. This capacity decrease can be due to the metal-dopant having the lowest content in Mn^{3+}, different particle size and morphology as well as lattice strains. Cr and Co-doped spinel materials observed good capacity retention upon cycling[90].

During capacity fading most of the deterioration reactions take place on the surface of $LiMn_2O_4$. Coating the spinel oxide material is commonly used as an approach to reduce capacity fading. Although there is a vast study on this approach, only a few recent coating materials was discussed within this study (following the next set of paragraphs).

Chung *et al.*[91] have done a study whereby the surface of $LiMn_2O_4$ was modified by coating with doped-spinel oxide materials ($LiM_{0.05}Mn_{1.95}O_4$, M=Co and Ni). These modified coated materials resulted in a reduced capacity fade for $LiMn_2O_4$ (almost no capacity fade after 50 cycles). Showing excellent cycling performances and the Jahn-Teller distortion onset during discharge was confirmed due to Li accumulation on the surface of the spinel oxide[91].

Coating the surface of $LiMn_2O_4$ with a thin inorganic $Li_2O \cdot 2B_2O_3$ glass (LBO) layer, prevented Mn^{2+} dissolution[76, 92]. LBO-coated $LiMn_2O_4$ was considered due to its good wetting properties and low viscosity which resulted into easy processing and even coverage with minimal material. The LBO-coated $LiMn_2O_4$ also exhibited good ionic conductivity and was stable against the high oxidation potentials of the positive electrode materials that operate at 4 V. The LBO-coated $LiMn_2O_4$ material has processing temperatures consistent to those of $LiMn_2O_4$. The elevated temperature performance of $Li_{1+x}Mn_{2-x}O_4$ was improved due to a decrease in Mn^{2+} dissolution, which was developed from $LiMn_2O_4$ surface treatment[92].

Al_2O_3 coated on $LiMn_2O_4$ was studied by Lee *et al.*[93] and showed an increase in polarization and lattice parameter (ranging from 8.221 to 8.227 Å after coating, compared to 8.215 Å for uncoated $LiMn_2O_4$) because a solid solution was formed on the surface, with a smooth (angular feature) surface. These coated materials produced an improved

capacity retention at 25 and 60 °C compared to the uncoated $LiMn_2O_4$ (41 % capacity fade in 100 cycles at 60 °C). Al_2O_3 coated $LiMn_2O_4$ produced a higher capacity and capacity fade (130 mAh.g^{-1} with 16 % capacity fade) after 100 cycles at 60 °C[76, 93].

Coated Li_xCoO_2 (0<x≤1) onto the surface of $LiMn_2O_4$ improved the structural stability forming $Li_xMn_{2-x}Co_xO_4$ solid solution throughout the particle[76, 94]. This structure was referred to a core-shell structure because the coating layer ($Li_xMn_{2-x}Co_xO_4$, shell) was situated at the surface of $LiMn_2O_4$ (core)[94]. The active material was protected from Mn^{2+} dissolution (into the electrolyte solution) and maintaining the Mn^{3+} concentration due to the effectiveness of Co ions at the surface, this in turn leaded to a decreased cation disorder[76, 94]. From their material's electrochemical impedance spectroscopy (EIS) results it was observed that the 2 semicircles (of the coated material) were reduced, implying that the inter-particle contact resistance was suppressed by the passivation film (acting as an electronic insulating layer)[76]. The $LiCoO_2$-coated $LiMn_2O_4$ showed a higher capacity (120 mAh.g^{-1}) compared to the uncoated $LiMn_2O_4$ (115 mAh.g^{-1}), maintaining 50 % of its maximum capacity (@ 20 C) in comparison to 80 % ($LiCoO_2$-coated $LiMn_2O_4$)[76]. A better rate capability was obtained for $LiCoO_2$-coated $LiMn_2O_4$ (3 wt% acetylene black as conducting additive) in comparison to the uncoated $LiMn_2O_4$ (20 wt% conducting additive)[95, 96]. From their observed results it can be concluded that $LiCoO_2$-coated $LiMn_2O_4$ showed an improvement in capacity cycling performance (at room and elevated temperatures) and rate capability[76].

2.6.2.3 $LiVPO_4$ and $LiFePO_4$

John Goodenough's research group at the University of Texas[97] discovered that $LiFePO_4$ was suitable as cathode material in rechargeable lithium-ion cells in 1996. This material consists of a 1D-olivine structure, whereby the lithium-ions move through the structure in one direction only. This material showed relatively good electrochemical performances with a lower material cost and better thermal stability when compared to other types of cathode materials. This material provided significant benefits such as; tolerance to physical abuse, long cycle life, enhanced safety and environmentally friendly. The fully charged battery showed a good shelf life with the disadvantage that it has an average cell

voltage of 3.3 V/cell resulting in a decrease in the overall specific energy density when compared to the lithium manganese or lithium cobalt system[97].
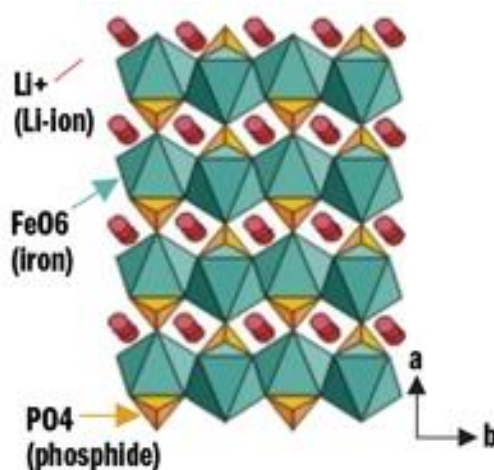

Figure 2.12: Olivine LiFePO₄ structure[98]

Iron (Fe) has the advantages of cost-effectiveness, abundancy and less toxicity than the other transition metals used as cathode material for lithium-ion cells. $LiFePO_4$ is found as the mineral triphylite, whereby the material's structure, stability and increase in redox energies ($Fe^{2+/3+}$) are improved by the phosphate-ion $[(PO_4)^{3-}]$[99]. $LiFePO_4$ as cathode material has relatively poor rate capabilities which limit the material's function in lithium-ion cells. $LiFePO_4$ is an orthorhombic olivine type structure, where the oxygen atoms are arranged in a distorted, hexagonal close-packed arrangement. The octahedral sites are occupied by Fe and lithium atoms and the tetrahedral sites are occupied by the phosphate group (Figure2.12). This material has a relatively high lithium intercalation voltage (3.4 V vs Li/Li⁺) with a high theoretical capacity (170 mAh.g⁻¹)[100].

$Li_3V_2(PO_4)_3$ was also considered as cathode material because of its high operating potential, better ion conductivity and a higher theoretical capacity when compared to $LiFePO_4$[101]. The cell using $Li_3V_2(PO_4)_3$ as cathode material's first charge is between 3.61 and 3.68 V and relates to an ordered lithium phase with an intermediate composition of $Li_{2.5}V_2(PO_4)_3$. The second step, between 3.68 and 4.1 V, relates to the lithium-ion's removal from the stable tetrahedral sites and the third step, between 4.1 and 4.5 V, is related to the change of $V^{3+/4+}$ to $V^{4+/5+}$ [102]. This material has a good thermal stability and ionic conductivity and is suitable for high power-density and large-scale battery

applications. A number of new developments are reported in literature that considers the doping and coating of the iron phosphate and vanadium phosphate cathode materials respectively[99-101 and 103-106]. Only a few considerations will be discussed in more detail.

Lee *et al.*[99] conducted a study on doping $LiFePO_4$ with Cu. The study showed that by increasing the Cu content, an increase in the capacity profile was observed. These findings concluded that Li and Cu substitution played an important role in increasing the $LiFePO_4$ battery's performance[99].

Li phospho-olivine applications in lithium-ion cells were limited due to poor electronic conductivity, resulting in an increase in electrode impedance and the rate-capacity decreased[100]. These challenges were solved by particle coating (carbon coating), co-synthesizing with carbon and doping the material with transition metals[100]. Wang *et al.*[100] investigated the addition of magnesium (Mg) to $LiFePO_4$. These doped synthesized materials produce an average crystal size of 1-2 µm with an electronic conductivity of four orders of magnitude greater than the plain $LiFePO_4$.

Xie *et al.*[103] investigated the effect of Al doped $LiFePO_4$ at various concentrations. The initial charge and discharge capacities increased with change in Al doped concentration ratios (compared to the pure $LiFePO_4$) during the investigation[103].

Nitrogen-doped (N-doped) carbon coating significantly increased the material's electronic conductivity. N-doped precursors were synthesized by using ionic liquids that allow the formation of a homogeneous N-doped carbon layer on the material's surface[104]. Zhang *et al.*[104] showed that by coating $LiFePO_4$ (LFP) with N-doped carbon (NC-LFP), particles of 100-400 nm and 50-300 nm in C-LFP and NC-LFP were formed respectively. The smaller particle size in the NC-LFP increased the contact area between the electrode and the electrolyte, resulting in a shortened Li^+ diffusion path, thereby improving the material's electrochemistry. An initial discharge capacity of NC-LFP was higher than that of C-LFP. However, after a repeated number of cycles, the capacity droped in both materials while the NC-LFP material still delivered slightly more capacity. The results showed that the $LiFePO_4$ conductivity was enhanced and an improvement in the Li intercalation ability was observed. The good electrochemical performance in the NC-LFP study showed uniform

coated N-doped carbon, thereby improving the electronic conductivity with a decrease in internal resistance and polarization[104].

The results reported by Zhang *et al.*[101] showed that the initial discharge capacity of $Li_3V_2(PO_4)_3$-Ni doped (LVPN) decreased with an increase in Ni-doping concentration. Zhang *et al.*[101] concluded that this decrease in capacity resulted from the intrinsic lithium-ion diffusion limitations of the material where Ni-doping significantly influenced the discharge capacity of $LiFePO_4$.

Chen *et al.*[105] investigated the structural and electrochemical properties of $Li_3V_2(PO_4)_3$ with partially substituted Cr in its V-sites. Cr-doping developed a stable phase and the ionic or electrical conductivity was enhanced, resulting in an improved electrochemical performance. Cr-doped lithium vanadium phosphate had a lower capacity than the undoped material and the observed improvements in the electrochemical properties were due to particle size optimization, the quality of the carbon coating and material structural stability[105].

Zinc-doped (Zn-doped)$Li_3V_2(PO_4)_3$/C was investigated by Yang *et al.*[106] at various Zn concentrations ($Li_3V_{2-x}Zn_x(PO_4)_3$/C). The results showed that the $Zn_{0.04}$ dopant amounts obtained the highest initial discharge capacity among the other dopant concentrations including the undoped $Li_3V_2(PO_4)_3$. The $Zn_{0.04}$ doped phase obtains an 89.2 % capacity retention after continuous cycling (after 100 cycles), whereas Zn_0 showed only a 60 % comparative capacity retention[106].

The $LiFePO_4$ and $Li_3V_2(PO_4)_3$ materials are not included in this study because of the relative complexity of their synthesis processes and their cell types are not that widely used. Also, their synthesis processes do not lend themselves well towards in-situ phase analysis studies. However, the $LiMn_2O_4$ phases with and without doping are considered in this study since these materials are widely used as suitable cathode material.

2.6.3 Lithium-ion cell electrolyte

The type of electrolyte used plays a significant role in the performance of lithium-ion cells. It allows for easy mobility of the lithium-ions between the anode and cathode during charging and discharging respectively. The overall cell's performance is significantly

influenced by the type of electrolyte solvent, the dissolved ions and the levels of purity[5]. Electrolytes should meet the following requirements[22, 107, 108]:

- High ionic conductivity over a wide temperature range.
- Good thermal stability.
- A wide electrochemical potential window.
- Good mechanical property (easily manufactured and non hazardous).
- Relatively low in cost.
- High thermal flashpoint.
- Environmentally benign.

The electrolytes are usually grouped into three different categories[107]:

- Liquid electrolyte (both primary and secondary lithium-ion cellsuse this electrolyte).
- Solid state electrolyte (usually only used in rechargeable cells).
- Polymer gel electrolyte (usually used in lithium-ion cells).

Liquid electrolytes consist of lithium salts such as, $LiPF_6$, $LiBF_6$, $LiClO_4$, $LiBC_4O_8$ or $Li[PF_3(C_2CF_5)_3]$ which are dissolved in non-aqueous organic alkyl carbonate solvents such as ethylene carbonate (EC), propylene carbonate (PC), diethyl carbonate (DEC), dimethyl carbonate (DMC) or ethyl methyl carbonate (EMC)[6]. $LiClO_4$ was one of the first salts used in rechargeable lithium-ion cells because of its low interfacial resistance, its relatively low cost and it can be synthesized[107] easily. This salt was replaced by $LiPF_6$ because ClO_4^- is a strong oxidizing agent which results in safety issues where cells explode[107]. Currently, $LiPF_6$ is the most common electrolyte salt that is used commercially because of its overall good electrochemical properties and stability. It also readily forms a passivation film on the aluminium current collector which enhances the conductivity. However, this salt has the disadvantage of a relatively low thermal stability and can decompose at 80 °C forming toxic gaseous decomposition compounds[5, 108].

Extensive research is done to reduce the effects of the electrolytes' instability at high cell voltages and temperatures. These effects can be solved by using solvent substitution, blending and electrolyte gelation.

For example, the addition of tris(trimethylsilyl) borate (TMSB) and tris(trimethylsilyl) phosphate (TMSP) were used as additives to the electrolyte which showed an improvement in the cycling stability of the cathode's active material[109]. TMSP showed an improvement in the capacity retention of 77-90.9 % and provided protection of the layered cathode oxide material. The expectation of the study was that tris(trimethylsilyl) phosphite (TMSPi) would be more effective than TMSP because of its preferable oxidation and lower phosphorous oxidation state. TMSPi's addition to the standard electrolyte (1M $LiPF_6$ in EC/DMC) improved the cycling stability and developed improved capacity retention of 91.2 % with an improved discharge capacity. This improvement can be credited to the reduction of the electrolyte decomposition and transition metal ion dissolution due to the formation of a protective solid electrolyte interface on the cathode electrode caused by the TMSPi additive[109].

In order for lithium-ion cells to be successful in the electric vehicle and hybrid electric vehicle (HEV) applications, cells need to operate over wide temperature ranges 243 to 333 K[110]. EC, DMC, DEC and EMC are commonly used commercial electrolytes, whereby EC is responsible for the negative electrode passivation[110]. Using the typical carbonate electrolytes (EC, DMC and others) in a cell, capacity fading and a large voltage drop at low temperatures of less than 243 K was observed. In order to minimize this effect and to allow the cells to work over a wider operating temperature, the EC content can be decreased to ensure that the blends of solvents had lower melting and higher boiling points[110].

Appropriate co-solvents can include methyl propionate, methyl butyrate and ethyl butyrate which allowed cells to work within the temperature range of 243 to 333 K[110]. Lu *et al.*[110] showed that by using 2,2,2-trifluoroethyl n-caproate (TFENH) as co-solvent, improvements in the electrochemical performance of $LiCoO_2$-graphite cells at low temperatures was observed. The electrolytes with an appropriate TFENH content improved the cells' low temperature performance without compromising the cycling performance at low and high temperatures. However, a too high TFENH content or concentration could lead to irreversible capacity loss. For improving performance over wide temperatures, the ratio must be between 17 and 25 vol% TFENH[110].

A standard lithium-ion cell consisted of a highly oxidative cathode, carbonaceous anode and an organic carbonate electrolyte. These materials in the cell make them flammable with relatively low thermal runaway temperatures. Thermal runaway occurred when this cell reached about 60 °C (and above) but continued to rapidly heat up which causes the cells in application to burn or to explode[111] and the combustion of the organic material occurred. For example, referring to $LiCoO_2$, the metal and oxygen atoms were directly covalently bonded. The oxygen atoms were easily cleaved at high temperatures because they were directly bonded to the metal which resulted in the thermal decomposition reactions.

The internal thermal safety of the cells can be improved by using overcharge protective additives, temperature-sensitive separators and thermally stable electrodes. However, these precautions do not prevent the flammable electrolyte from igniting[111]. The effect of the flammable electrolyte can be reduced by the addition of a fire-retardant electrolyte additive that can range from ionic liquids, organosilicon compounds, hydrofluoroethers (HFEs) and phosphates[112]. The phosphate molecules were a good fire-retardant electrolyte to use because it had a low viscosity and was highly soluble. Zeng *et al.*[111] used $LiFePO_4$ or $LiMn_2O_4$ as the cathode, SiO (or SiFe and Sb) as the anode and dimethyl methylphosphonate (DMMP) as the electrolyte. In this study it was noted that organic phosphates found it difficult to form a stable SEI layer on graphite electrodes, resulting in poor cycling with no reversible capacity (at the graphite electrode). Therefore, fluoroethylene carbonate (FEC) was added to DMMP electrolyte, improving the reversible capacity, but with a low or poor cycling performance[111]. In conclusion, FEC's addition suppressed DMMP's decomposition and poor electrochemical performance of the graphite electrode. SiO-C anode in DMMP provided that FEC's addition produced a stable SEI layer on SiO anode. Constructing a $SiO/LiFePO_4$ battery in DMMP electrolyte showed good cycling performances (similar to the existence of these electrodes in carbonate electrolytes) which produced safer and non-flammable cells[111].

These new developments in the make-up of the secondary lithium-ion cell improved the cells' electrochemical performance in application tremendously and extended the range of the cells' possible uses.

2.6.4 Synthesis methods

Many methods have been explored for the synthesis of cathode oxide materials used within lithium-ion cells, these techniques ranged from solid-state to sol-gel, co-precipitation, combustion, spray pyrolysis, microwave and hydrothermal methods[112].

Recent developments in these synthesis methods have remarkably improved the material's electrochemical performance such as cycle life and capacity and to make them more cost-effective and uniform in material morphology.

The most common method of synthesis was the solid-state technique. Solid state methods required that the precursors were thoroughly ground, mixed together and heated at high temperatures. This procedure had to be repeated several times until a homogeneous product was obtained. The materials had to then be transformed into the desired particle shape and size. For these methods to be successful on a large scale, operation at high furnace temperatures were required and for some materials the use of an inert atmosphere. Samples had to also be milled for lengthy periods of times in order to achieve the desired particle size.

Recent research in the field of synthesis had moved towards sol-gel chemistry[19] requiring considerably less time and energy. Many of these synthesis methods had proven to be useful in laboratory scaling, but scaling them at industrial levels was difficult. However, the spray pyrolysis method had proven to be feasible at both laboratory and industrial level[113].

Sol-gel chemistry together with spray pyrolysis would be the desired methods discussed and used throughout this study in making the cathode active materials for the lithium-ion cells.

The history of sol-gel chemistry goes back to the 18th century where it was discovered by J.J. Ebelenen in 1846[19] when he discovered that SiO_2 gels can be formed through the hydrolysing of $Si(OEt)_4$. However, it was only in 1930 that this method was developed further to find commercial applications[19]. The synthesis of silica by sol-gel method involved the hydrolysis and condensation of silicon alkoxides. During hydrolysis, reactive silanol groups are formed and bridging oxygens was formed during condensation[114]. Equations 2.6 to 2.9 indicate bonding rearrangements in sol-gel methods.

Si – OR + H_2O $\Longrightarrow$ Si – OH + ROH (hydrolysis)   2.6

Si – OH + RO – Si $\Longrightarrow$ Si – O – Si + ROH (alcohol condensation)   2.7

Si – OH + Si – OH $\Longrightarrow$ Si – O – Si + HOH (water condensation)   2.8

Si $(OR)_4$ + $2H_2O$ $\Longrightarrow$ SiO_2+ 4ROH (overall reaction)   2.9
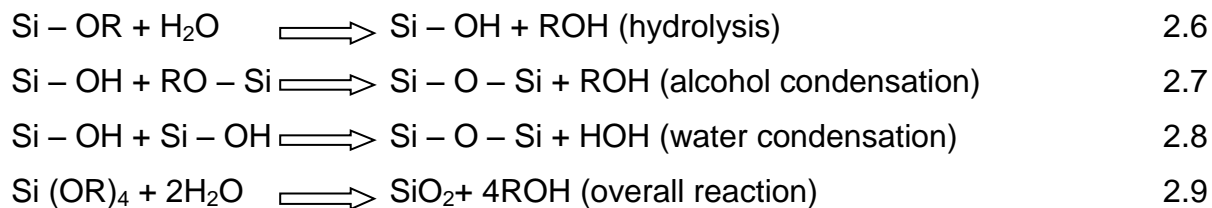
This sol-gel method was then further developed for the synthesis of a variety of glasses, ceramics, inorganic fillers and coatings[19]. In some industrial applications, the coatings were used for chemical protection (such as corrosion inhibitors) and mechanical protection (such as abrasion resistance)[115]. The sol-gel technology was also used in biomedical applications (such as biomedical sensors and coatings for metal implants)[116, 117] and is still being used daily in various chemistries such as cosmetics (including sunscreen lotion and makeup that include UV absorbers)[117]. The uniqueness of the sol-gel method was that it produced a homogeneous mixture in a solution that was almost at the atomic or molecular level. The stoichiometric amount could be controlled and the synthesis temperatures were relatively low, where short heating periods can produce a good crystalline material with uniform particle sizes that had relatively smaller diameters[19]. However, there are a number of disadvantages in using the method that include the high cost of the raw material and a comparatively large volume shrinkage that came from drying and sintering the material.

Materials can be prepared by following two different sol-gel technique routes:

- the metal-organic route with metal alkoxides in organic solvent
- the inorganic route with metal salts in aqueous solution (chloride, oxychloride, nitrate), being much cheaper and easier to handle than metal alkoxides, but their reactions were more difficult to control

Sol-gel methods were employed to prepare materials for energy conversion and storage systems. In this chemical process the "sol" (solution) would gradually be adjusted forming a gel-like system containing both a liquid and a solid phase. At this point two phases were present having the gel phase settling at the bottom with the solvent phase being on top, this was due to density differences between the gel and solvent phases. The solvent (liquid or fluid) had to be removed for the gel-like properties to be recognized. This solvent removal can be done in a number of ways. The simplest method was to allow time for

sedimentation to occur and then pour off or decant the remaining liquid. Centrifugation can also be used to accelerate the process of phase separation. Removal of the remaining liquid or solvent phase required a drying process in order to obtain a pure gel.
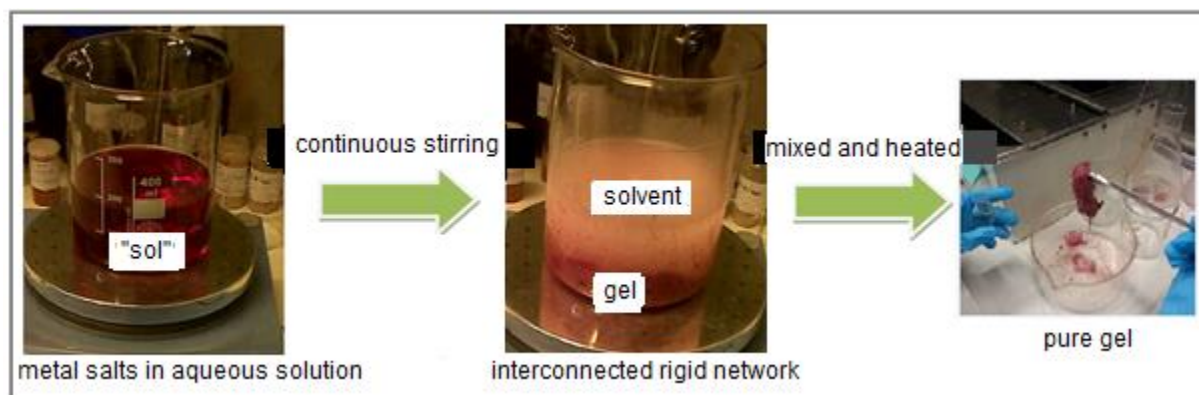
Figure 2.13: Flow diagram describing the sol-gel method

The sol-gel technique was one of the most common procedures used in the manufacturing of large scale oxide as cathode material. For most processes, the sol-gel method could be considered as continuous, where it was taken to a batch furnace process at high temperatures of approximately 600 to 800 ^{0}C for up to 15 hours[65, 75, 87, 118, 119].

Even though many of these methods in themselves had proven to be useful at the laboratory-scale synthesis, the complexity and cost implications of scaling such methods to industrial manufacturing often proved to be unfeasible. One method that had shown over the years to be successful at both the laboratory scale and industrial level of synthesising was combining spray pyrolysis with sol-gel methods. The spray pyrolysis method had shown to be versatile in its approach of incorporating a variety of chemical compositions and techniques that can, with relative ease, be scaled to industrial feasible processes.

The spray pyrolysis method can be combined with the sol-gel chemistry processes to develop or synthesise cathode active materials of good quality, low moisture and narrow particle size distribution. The technique was used for a variety of chemistry syntheses and can be adapted for either continuous or single-step preparation methods. Besides the large number of advantages this spray pyrolysis technique also had a few disadvantages. The technique was well suited for the synthesis of micro or even nano-sized particles. However, an efficient separation technique was required for the production of these fine

powders in order to avoid the loss of products and environmental pollution. Industries such as fuel cells (Pt active material), food (milk powder, coffee, or tea), pharmaceuticals (antibiotics) and consumer goods (paint pigments or ceramic materials) use this technique[120, 121]. The processes of spray pyrolysis techniques require high evaporation rates and took place in short residence times. They were ideally meant for drying heat-sensitive materials and were not suitable for easily conglomerated materials.

The powders of the desired material were produced from a liquid or slurry mixture that was pumped through a set of nozzles where it was rapidly dried with the aid of hot gases. Air was the preferred gas for use during the drying process; however, if the solvent or liquid was flammable and if the produced product was oxygen-sensitive then nitrogen gas was often used. The technique makes use of spray nozzles or atomisers that can disperse the liquid into very finely controlled droplets. The gas used during the process acted as a carrier, enabling the particles that were formed to undergo a significantly faster and uniform thermal reaction. The flow of the precursor solution was pumped, usually by a peristaltic pump, together with a constant gas flow through a nozzle into a preheated heating apparatus. At this point, solvent evaporation took place rapidly and the dried mixed precursor powder was passed through a filtering system that collected the final desired active material. The final product that was produced by using this process made powders that were either amorphous, semi crystalline or crystalline[122].
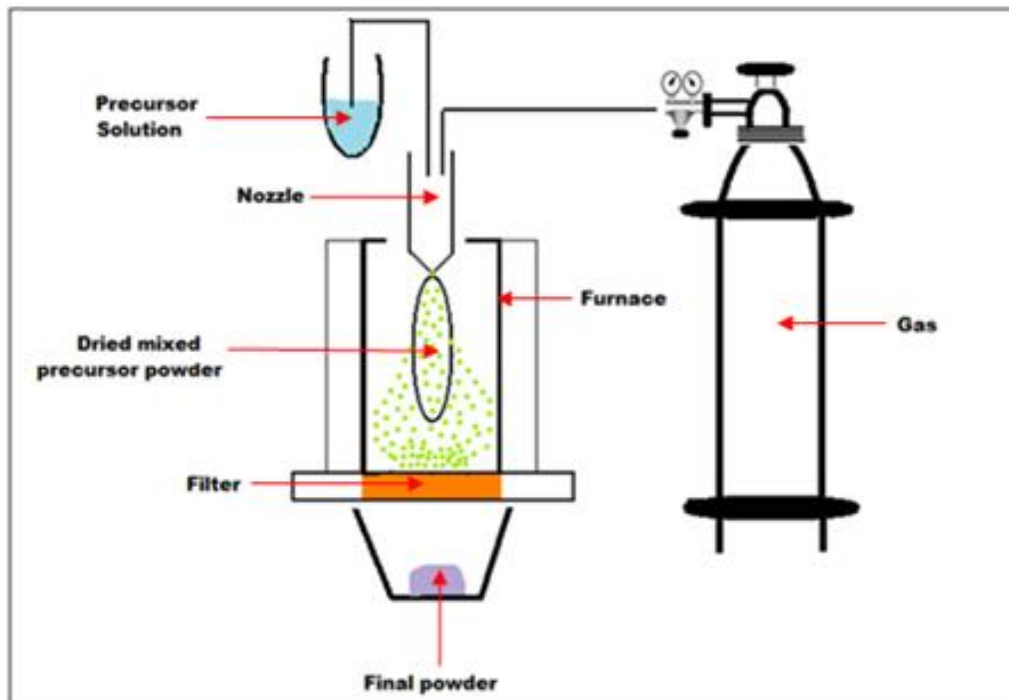
Figure 2.14: Schematic diagram on a typical spray pyrolysis process

Spray pyrolysis techniques had been used successfully to make pure cubic spinel $LiMn_2O_4$ hollow structures with a spherical shaped nanostructured particle that showed to have improved electrochemical properties[123]. The method used an aqueous reaction solution of $LiNO_3$ and $Mn(NO_3)_2 \cdot 6H_2O$ in stoichiometric ratios that went through an ultrasonic atomiser (at 100 kHz with a gas flow rate of 20 $dm^3.min^{-1}$ and residence time of 60 sec) into a heated ceramic furnace at 800 °C for 4 hours under an air atmosphere[123].

A big advantage of the technique was the small particle size that can be achieved, where the final dried solid $LiMn_2O_4$ powder made from the spray technique obtained particles that ranged between 75 and 1250 nm[124]. Taniguchi *et al.*[123] also studied the synthesis of $LiMn_2O_4$ by spray pyrolysis and drying system according to this study it was produced that X-ray diffraction analysis showed a pure crystalline material that was cubic spinel in structure, and SEM analysis showed that the particles were spherical and in some cases, hollow. The charge/discharge curves showed distinct plateaus corresponding to well defined $LiMn_2O_4$ structures, indicating the characteristics of a spinel manganese oxide structure. Their electrochemical analysis results showed that the first charge/discharge cycle capacity was 141 and 126 $mAh.g^{-1}$ (at 0.1 C) respectively. After 99 capacity cycles,

the discharge capacity was still 100 mAh.g^{-1} producing an irreversible capacity of 12 %[123]. Increase in rate also produced a slight change in discharge capacity that resulted from slow lithium ion diffusion, however still producing a relatively high discharge capacity (74 mAh.g^{-1} at 10 C). This method showed good cycle and high rate performances.

Cobalt-substituted $LiMn_2O_4$ samples were studied by heating the sample at 750 °C for various time intervals (1, 4 and 8 hours) by ultrasonic spray pyrolysis process. Their structural analysis again showed spherical single spinel-phase particles that ranged in crystallite sizes from 39.6 nm (1 hour) to 52 nm (4 hours) and 58.9 nm (8 hours) respectively[125]. This structural behaviour (crystallinity increase) resulted in an increase in the first discharge capacity (107 mAh.g^{-1} at 1 hour, 108 mAh.g^{-1} at 4 hours and 113 mAh.g^{-1} at 8 hours) together with a decrease in irreversible capacity loss over the first cycles (below 10 %). This material was also studied at various C-rates ranging from 1 C to 60 C. At higher rates (60 C), the sample that was prepared at 4 hour time intervals resulted in better capacity retention (87 %) compare to the capacity at 0.1 C rate. Following the spray pyrolysis process for this material (4 hour time intervals) showed an improvement within its electrochemical performance at high rates whereby the crystallinity were well controlled[125].

Another new development within this spinel structure was that $LiMn_2O_4$ particles are coated to improve the electrochemical performance within this cathode oxide material. These effects include the dissolution of the electrode material that was in contact with the electrolyte, together with side-reactions on the electrode surface and crystal structure instability contributing to the shortening of the battery's capacity life. The particles of $LiMn_2O_4$ (LMO) can be coated with lithium boron oxide glass (LMO-LBO) and TiO_2 (LMO-TiO_2) by a spray pyrolysis process[126]. This process involved dissolving Li, Mn and boron precursors and atomising them into droplets. These droplets were then exposed to a heated reactor, where the Li reacts with the Mn to form $LiMn_2O_4$ and upon evaporating the solvent, a reaction between Li and B occurs to produce the LBO glass phase. The preparation of a core-shell structure by the one-step spray pyrolysis method occurs where the substance with a higher melting point tends to bond together at the core, while the substance with a lower melting point would be "pushed" outwardly forming the coating layer[126] as illustrated in Figure 2.15.
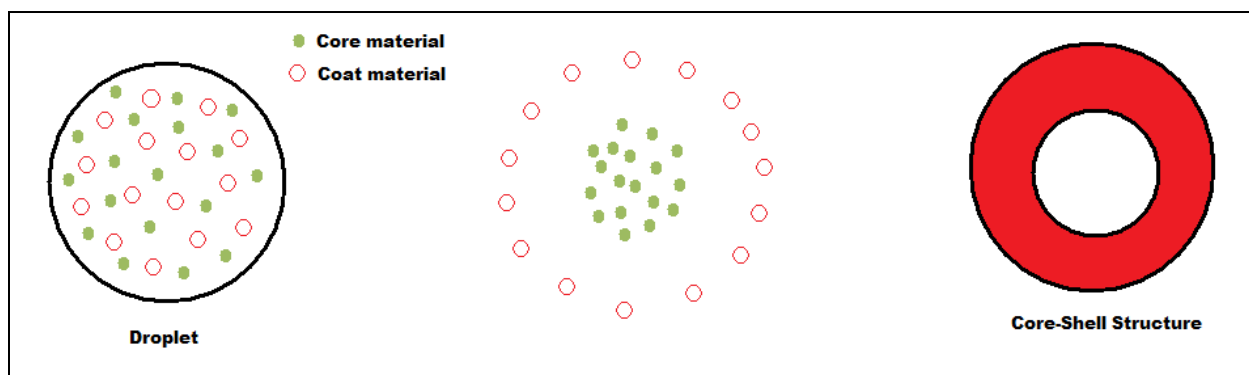
Figure 2.15: Schematic diagram on the formation of a core-shell structure

The cathode material $LiMn_2O_4$ that was coated with Li_2O-$2B_2O_3$ glass showed an improvement in its initial capacity of 131 mAh.g^{-1} with an 86 % retention after 100 cycles at the 1 C rate, in comparison to its uncoated $LiMn_2O_4$ producing a 80 % capacity retention (after 100 cycles at 1 C)[126]. $LiMn_2O_4$ that was coated by TiO_2 had an initial capacity of 126 mAh.g^{-1} also with an 86 % retention after 170 cycles at the 1 C rate[126]. Following this synthesis route enhanced or improved the materials structural stability and prevents active material dissolution during cycling.

Using this spray-pyrolysis technique reduces the use of expensive reagents, lowers solvent use, improved the temperature control and improves workplace safety. A more detailed description of explaining the processes and comparing various synthesis techniques (solid state, sol-gel and spray pyrolysis) and various cathode oxide materials (for example, $LiCoO_2$ and $LiFePO_4$) is included as a review article in Appendix D.

REFERENCES

1.   G.W. Vinal, *Storage Batteries*, John Wiley & Sons, New York, 4th edn., 1955.

2.   H. Bode, *Lead-acid batteries*, John Wiley & Sons, New York, 1977.

3.   <https://en.wikipedia.org/wiki/Galvanic_cell> (accessed 20 January 2015).

4.   U. Mirza and K. Sleight, *Types of Batteries and Their Applications*, <http://www.brighthubengineering.com/power-generation-distribution/123909-types-of-batteries-and-their-applications/> (accessed 12 February 2015).

5.   Energizer Report, Nickel Metal Hydride (NiMH), Handbook and Application Manual, 2010.

6.   K. Ozawa, *Lithium Ion Rechargeable Batteries*, Wiley-VCH Verlag GmbH & Co. KGaA, Weinheim, 2009.

7.   G. T. K. Fey, *Introduction to Lithium Ion Batteries*, Short communication, Dept. of Chemical and Materials Engineering, National Central University, Chung-Li, Taiwan

8.   <http://www.physicscentral.com/explore/action/lithium.cfm> (accessed on 24 June 2014).

9.   <http://www.kids.esdb.bg/smart_inventions.html> (accessed on 13 January 2015).

10.   <http://www.ercblogs.co.za/2013/shifting-mobility-electric-vehicles/> (accessed on 13 January 2015).

11.   <https://cdn0.vox-cdn.com/thumbor/hCpIDs5yME4p6fXW9ktkU03VbTg=/cdn0.vox-cdn.com/uploads/chorus_asset/file/2431234/Screen_Shot_2014-11-05_at_12.29.09_PM.0.png> (accessed on 04 March 2015)

12.   <http://www.ephotozine.com/articles/samsung-galaxy-s4-zoom-camera-phone-review-22655/images/highres-Samsung-Galaxy-S4-Zoom-8_1376057294.jpg> (accessed on 04 March 2015).

13.   <https://pro.sony.com/bbsc/ssr/cat-vaio/> (accessed on 13 January 2015).

14.   <http://i01.i.aliimg.com/img/pb/146/824/980/980824146_856.jpg> (accessed on 5 March 2015).

15.   <http://www.retrify.com/ten-facts-know-lithium-ion-batteries/> (accessed on 19 June 2014).

16. <http://www.cwnenergy.com/products3gonet.asp?lx=big&anid=150> (accessed on 19 June 2014).

17. <http://img.diytrade.com/cdimg/712195/5661686/0/1241830983/CR2032_lithium_coin_cell_button_cell_battery_dry_battery_primary_battery.jpg> (accessed on 10 March 2015).

18. <http://www.mtixtl.com/ProductImages/battery-equipment/polymer%20back.jpg> (accessed on 14 March 2015).

19. L.J. Fu, H. Liu, C. Li, Y.P. Wu, E. Rahm, R. Holze and H.Q. Wu, *Progress in Materials Science*, 2005, **50**, 881–928.

20. M. Oswal, J. Paul and R. Zhao, *A comparative study of Lithium-ion batteries*, University of Southern California, 2010.

21. L. Gaines and R. Cuenca, Costs of Lithium-Ion Batteries for Vehicles Annual Report by Argonne National Laboratory- Centre for Transportation Research, 2000.

22. <http://www.ehow.com/about_5454465_lithium-vs-lithium-ion-batteries.html> (accessed on 24 June 2014).

23. B.C.H. Steele, *Fast ion transport in solids: solid-state batteries and devices*, North-Holland/American Elsevier Inc., Amsterdam-London/New York, 1973.

24. J. Yamaki, in *Advances in Lithium-Ion Batteries*, ed. W.A. van Schalkwijk and B. Scrosati, Kluwer Academic/Plenum Publishers, New York, 2002, Chapter 5pp. 155-183.

25. S.S. Zhang, *Journal of Power Sources*, 2007, **164**, 351-364.

26. P. Anora and Z. Zhang, *Chem. Rev.*, 2004, **104**, 4419-4462.

27. <http://www.baj.or.jp/e/knowledge/structure.html> (accessed on 16 February 2015).

28. C. J. Allen, *Advanced cathodes and electrolytes for Lithium-ion and Li-air batteries*, Department of Chemistry and Chemical Biology, Northeastern University, 2012.

29. <http://www.enerdel.com/lithium-ion-battery-systems-training-program/> (accessed on 8 July 2012).

30. J.A. Choia, Y. Kangb, H. Shimb, D.W. Kimb, E. Chac and D.W. Kima, *Journal of Power Sources*, 2010, **195**, 6177-6181.

31. Colin A. Vincent, *Solid Sate Ionics*, 2000, **134**, 159-167.

32.   J. Venter, P. Novák, M.R. Wagner, C. Veit, K.C. Möller, J.O.Bensenhard, M. Winter, M. Wohlfahrt-Mehrens, C. Vogler and A. Hammouche, *Journal of Power Sources*, 2005, **147**, 269-281.

33.   Presentation by Walter A. Van Schalkwijk on Lithium-ion chemistry and Battery Management Systems, Cape Town, July 2010.

34.   <http://www.element-collection.com/index.html> (accessed on 22 March 2012).

35.   Iran F. Machado and Silva F. De M. Figueirôa, *Resources Policy*, 2001, **27**, 9-24.

36.   H. Vikstrom, S. Davidson and M. Hook, *Applied Energy*, 2013, **110**, 252-266.

37.   C.W. Kamienski, D.P.McDonald, M.W. Stark and J.R. Papcun, *Lithium and lithium compounds,* in Kirk-Othmer Encyclopedia of Chemical Technology, John Wiley & Sons Inc., 2004.

38.   S. E. Kesler, P. W. Gruber, P. A. Medina, G. A. Keoleian, M. P. Everson and T. J. Wallington, *Ore Geology Reviews*, 2015, **48**, 55-69.

39.   <http://www.mineralszone.com/minerals/lithium.html> (accessed on 24 March 2015).

40.   Z. Li, J. Huang, B. Y. Liaw, V. Metzler and J. Zhang, *Journal of Power Sources*, 2014, **254**, 168-182.

41.   Brian L. Ellis, Kyu Tae Lee and Linda F. Nazar, *Chem. Mater*, 2010, **22**, 691-714.

42.   Y.J. Zhang, X.Y. Lui, W.Q. Bai, H. Tang, S.J. Shi, X.L. Wang, C.D. Gu and J.P. Tu, *Journal of Powers Sources*, 2014, **266**, 43-50.

43.   Y. Yun, V. Le, H. Kim, S. Chang, S. Baek, S. Park, B.H. Kim, Y.H. Kim, K. Kang and H. Jin, *Journal of Power Sources*, 2014, **262**, 79-85.

44.   M. Shahid, N. Yesibolati, M.C. Reuter, F.M. Ross and H.N. Alshareef, *Journal of Power Sources*, 2014, **263**, 239-245.

45.   H. Chakraborti and S.K. Pal, *Chemical Physics Letter*, 2014, **600**, 118-122.

46.   S. Ni, X. Lv, J. Ma, X. Yang and L. Zhang, *Electrochimica Acta*, 2014, **130**, 800-804.

47.   T.F. Yi, S.Y.Yang, M.Tao, Y.Xie and Y.R.Zhu, *Electrochimica Acta*, 2014, **134**, 377-383.

48.   <http://www.lenntech.com/periodic/elements/co.htm> (accessed on 16 January 2015).

49.   <http://en.wikipedia.org/wiki/Cobalt> (accessed on 1 September 2014).

50.   R.D. Armstrong, G.W.D. Biggs and E.A. Charles, *Journal of Applied Electrochemistry*, 1988, **18**, 215-219.

51.   M. V. Reddy, T. W. Jie and C. J. Jafta, et.al, *Electrochimica Acta*, 2014, **128**, 192-197.

52.   P. Prahasini, M. Sivakumar, R. Subadevi and F. M. Wang, *Advanced Materials Research*, 2012, **584**, 345-349.

53.   S. Valanarasu, R. Chandramohan, R. M. Somasundaram and S. R. Srikumar, *Journal of Materials Science*, 2011, **22**, 151-157.

54.   C. Li, H. P. Zhang, L. J. Fu, H. Lui, Y. P. Wu, E. Rahm, R. Holze and H. Q. Wu, *Electrochimica Acta*, 2006, **51**, 3872-3883.

55.   S. H. Kim and C. S. Kim, *Journal of Electroceramic*, 2009, **23**, 254-257.

56.   M. Lengyel, G. Atlas, D. Elhassid, P. Y. Luo, X. Zhang, I. Belharouak and R. L. Axelbaum, *Journal of Power Sources*, 2014, **262**, 286-296.

57.   S. H. Choi, J. H. Kim, Y. N. Ko, K. M. Yang and Y. C. Kang, *Journal of Power Sources*, 2013, **244**, 129-135.

58.   A. Basch and J. H. Albering, *Journal of Power Sources*, 2011, **196**, 3290-3295.

59.   N. H. Kwon, H. Yin, P. Brodard, C. Sugnaux and K. M. Fromm, *Electrochimica Acta*, 2014, **134**, 215-221.

60.   J. W. Lee, S. M. Park and H. J. Kim, *Journal of Power Sources*, 2009, **188**, 583-587.

61.   <http://en.wikipedia.org/wiki/Manganese> (accessed on 16 January 2015).

62.   International Manganese Institute, <http://www.manganese.org/about-mn/applications> (accessed on21 January 2015).

63.   W. B. Jensen, *The Lechanchè Cell*, Museum Notes, January/February, Oesper Website, 2014.

64.   J. L. Wang, Z. H. Li, J. Yang, J. J. Tang, J. J. Yu, W. B. Nie, G. T. Lei and Q. Z. Xiao, *Electrochimica Acta*, 2012, **75**, 115-122.

65.   Y. K. Sun, D. W. Kim and Y. M. Choi, *Journal of Power Sources*, 1999, **79**, 231-237.

66. O.K. Park, Y. Cho, S. Lee, H. Yoo, H. Song and J. Cho, *Energy and Environmental Science*, 2011, **4**,1621-1633.

67. R. Thirunakaran, A. Sivashanmugam, S. Gopukumar, C. W. Dunnill and D. H. Gregory, *Journal of Materials Processing Technology*, 2008, **208**, 520-531.

68. D.H. Jang, Y.J. Shin and S.M. Oh, *Journal of Electrochemical Society*, 1996, **143**, 2204-2211.

69. T. Ohzuku, M. Kitagawa and T. Hirai, *Journal of Electrochemical Society*, 1990, **137**, 769-775.

70. Y.Y. Xia, T. Sakai, T. Fujieda, X.Q. Yang, Z.F. Ma, J. McBreen and M. Yoshio, *Journal of Electrochemical Society*, 2001, **148**, A723.

71. D. Zhang, B.N. Popov, R.E. White, *Journal of Power Sources*, 1998, **76**, 81-90.

72. L. Guohua, H. Ikuta, T. Uchida and M. Wakihara, *Journal of Electrochemical Society*, 1996, **143**, 178-182.

73. R.J. Gummow, A. de Kock and M.M. Thackeray, *Solid State Ionics*, 1994, **69**, 59-67.

74. X. Li, Y. Xu and C. Wang, *Journal of Alloys and Compounds*, 2009, **479**, 310-313.

75. P. Singh, A. Sil, M. Nath and S. Ray, *Physica B*, 2010, **405**, 649-654.

76. C. Li, H.P. Zhang, L.J. Fu, H. Liu, Y.P. Wu, E. Rahm, R. Holze and H.Q. Wu, *Electrochimica Acta*, 2006, **51**, 3872-3883.

77. K.Y. Chung, C.W. Ryu and K.B. Kim, *Journal of Electrochemical Society*, 2005, **152**, A791-A795.

78. A. de Kock, E. Ferg and R.J. Gummow, *Journal of Power Sources*, 1998, **70**, 247-252.

79. K. Amine, H. Tukamoto, H. Yasuda and Y. Fujita, *Journal of Power Sources*, 1997, **68**, 604.

80. R. Alcántara, M. Jaraba, P. Lavela and J.L. Tirado, *Electrochimica Acta*, 2002, **47**, 1829.

81. M. Kebede, N. Kunjuzwa, K. Ozoemena and M. Mathe, *ECS Transactions*, 2013, **50 (40)**, 1-14.

82. J.H. Lee, J.K. Hong, D.H. ang, Y.K. Sun and S.M. Oh, *Journal of Power Sources*, 2000, **89**, 7-14.

83. R. Santhanam and B. Rambabu, *Journal of Power Sources*, 2010, **195**, 5442-5451.

84. G.Q. Liu, Y.J. Wang, Qilu, W. Li and Chenhui, Electrochimica Acta, 2005, **50**, 1965-1968.

85. M. Kebede, K. Ozoemena and M. Mathe, *"Synthesis and electrochemical properties of cation doped spinel LiM0.5Mn1.5O4 (M=Mn, Ni and Al) cathode materials for Li-ion battery"*, Energy Materials, Materials Science and Manufacturing, CSIR, Pretoria, (Accessed by):

   http://events.saip.org.za/materialDisplay.py?contribId=279&sessionId=13&materialId=paper&confId=14.

86. W. Baochen, X. Yongyao, F. Li and Z. Dongjiang, *Journal of Power Sources*, 1993, **43-44**, 539.

87. X. Huang, M. Lin, Q. Tong, X. Li, Y. Ruan and Y. Yang, *Journal of Power Sources*, 2012, **202**, 352-356.

88. P. Arora, B. Popov and R.E. White, *Journal of Electrochemical Society*, 1998, **145**, 807-815.

89. B. Banov, Y. Todorov, A. Trifonova, A. Momchilov and V. Manev, *Journal of Power Sources*, 1997, **68**, 578-581.

90. L. Hernán, J. Morales, L. Sánchez and J. Santos, *Solid State Ionics*, 1999, **118**, 179-185.

91. K.Y. Chung, C.W. Ryu and K.B. Kim, *Journal of Electrochemical Society*, 2005, **152 (4)**, A791-A795.

92. G.G. Amatucci, A. Blyr, C. Sigala, P. Alfonse and J.M. Tarascon, *Solid State Ionics*, 1997, **104**, 13-25.

93. S.W. Lee, K.S. Kim, H.S. Moon, H.J. Kim, B.W. Cho, W.I. Cho, J.B. Ju and J.W Park, *Journal of Power Sources*, 2004, **126**, 150-155.

94. B.J. Hwang, R. Santhanam, C.P. Huang, Y.W. Tsai and J.F. Lee, *Journal of Electrochemical Society*, 2002, **149**, A694-A698.

95. S.C. Park, Y.M. Kim, Y.M. Kang, K.T. Kim, P.S. Lee and J.Y. Lee, *Journal of Power Sources*, 2001, **103**, 86-92.

96. S.C. Park, Y.S. Han, Y.S. Kang, P.S. Lee, S. Ahn, H.M. Lee and J.Y. Lee, *Journal of Electrochemical Society*, 2001, **148 (7)**, A680-A686.

---

97. <http://batteryuniversity.com/learn/article/types_of_lithium_ion> (accessed on 25 June 2014).

98. <http://i.cmpnet.com/eetimes/news/09/11/1571art_pg40.jpg> (accessed on 14 March 2015).

99. S.B. Lee, S.H. Cho, J.B. Heo, V. Aravindan, H.S. Kim and Y.S. Lee, *Journal of Alloys and Compounds*, 2009, **488**, 380-385.

100. G.X. Wang, S.L. Bewlay, K. Konstantinov, H.K. Liu, S.X. Dou and J.H. Ahn, *Electrochimica Acta*, 2004, **50**, 443-447.

101. Y. Zhang, Q. Huo, Y. Lv, L. Wang, A. Zhang, Y. Song, G. Li, H. Gao, T. Xia and H. Dong, *Journal of Alloys and Compounds*, 2012, **542**, 187-191.

102. Q. Kuang, Y. Zhao, X. An, J. Liu, Y. Dong and L. Chen, *Electrochimica Acta*, 2010, **55**, 1575-1581.

103. H. Xie and Z. Zhou, *Electrochimica Acta*, 2006, **51**, 2063-2067.

104. B. Zhang, X. Yuan, H. Li, X. Wang, J. Zhang, H. Chen and J. Zheng, *Journal of Alloys and Compounds*, 2015, **627**, 13-19.

105. Y. Chen, Y. Zhao, X. An, J. Liu, Y. Dong and L. Chen, *Electrochimica Acta*, 2009, **54**, 5844-5850.

106. Y. Yang, W. Xu, R. Guo, L. Liu, S. Wang, D. Xie and Y. Wan, *Journal of Power Sources*, 2014, **269**, 15-23.

107. R. Zhang, *Advanced gel polymer electrolyte for lithium-ion polymer batteries*, MSc Thesis, Iowa State University, 2013.

108. R.W. Schmitz, P. Murmann, R. Schimtz, R. Müller, L. Krämer, J. Kasnatscheew, P. Isken, P. Niehoff, S. Nowak, G. Röschenthaler, N. Ignatiev, P. Sartori, S. Passerini, M. Kunze, A.Lex-Balducci, C. Schreiner, I. Cekic-Laskovic and M. Winter, *Progress in Solid State Chemistry*, 2014, **42**, 65-84.

109. S. Mai, M. Xu, X. Liao, J. Hu, H. Lin, L. Xing, Y. Liao, X. Li and W. Li, *Electrochimica Acta*, 2014, **147**, 556-571.

110. W. Lu, K. Xie, Z. Chen, S. Xiong, Y. Pan and C. Zheng, *Journal of Power Sources*, 2015, **274**, 676-684.

111. Z. Zeng, B. Wu, L. Xiao, X. Jiang, Y. Chen, A. Ai, H. Yang and Y. Cao, *Journal of Power Sources*, 2015, **279**, 6-12.

112. V. Palomares and T. Rojo, in *Lithium Ion Batteries-New Developments,* ed. I. Belharouak, InTech Publishers, Croatia Europe, 2012.

113. A.J. Gröhn, S.E. Pratsinis and K. Wegner, *Computational Investigation of Nanoparticle Synthesis by Flame Spray Pyrolysis*, Particle Technology Forum Annual Meeting, 2012.

114. M.A. Aegerter, M. Mennig, *Sol-Gel Technologies for Glass Producers and Users,* Springer Science & Business Media, New York, 2004.

115. G.G. Avci, D. Abanoz, *Engineering Materials*, 2004, **264–268**, 387–390.

116. A. U-Jarza, D. Andrzejewski, K. Maruszewski, H. Podbielska, W. Strek, *Advantages of sol-gel technologies for biomedical applications,*Proceedings of SPIE, 1999, **3567**, 50-58.

117. PR Newswire Report, Sol-Gel Processing of Ceramics and Glass, July 2014.

118. G.T.K. Fey, R.F. Shiu, V. Subramanian, C.L. Chen, *Solid State Ionics*, 2002, **148**, 291-298.

119. N. Ding, X.W. Ge, C.H. Chen, *Materials Research Bulletin*, 2005, **40**, 1451-1459.

120. A. Gharsallaoui, G. Roudaut, O. Chambin, A. Voilley, R. Saurel, *Food Research International*, 2007, **40**, 1107–1121.

121. C. Arpagaus, N. Schafroth and M. Meuri, *Laboratory Scale Spray Drying of Lactose*, Buchi Report, 57, 2010, **57**.

122. T. Penovic, A,Sander and V. Grozdanic, An *International Journal*, 2013, **31:5**, 458-465

123. I. Taniguchi, N. Fukuda and M. Konarova, *Journal of Power Sources*. 2008, **181**, 228-236.

124. B. Ebin, V. Battaglia and S. Gurmen, *Ceramics International*, 2014, **40**, 7029-7035.

125. C.H. Lu, T.Y. Wu, H.C. Wu, M.H. Yang, Z.Z. Gua and I. Taniguchi, *Materials Chemistry and Physics*, 2008, **112**, 115-119.

126. D. Jung, Y. Ko, Y. Kang and S. Park, *Advance Powder Technology*, 2014, **25**, 18-31.

CHAPTER 3

EXPERIMENTAL EQUIPMENT AND METHODS

The following chapter is subdivided into three sections. The first section will briefly discuss the synthesis methods for preparing the various cathode metal oxide materials of lithium-ion cells. This is followed by the different characterization instrumentations used throughout the study. The final section will briefly discuss the preparation of the electrode making and the electrochemical cell assembly used as well as the different tests to evaluate the required electrochemical performance of the cells.

3.1 Synthesis methods

The synthesis of the spinel oxide material together with its dopants was carried out by two synthesis techniques at various temperatures. These synthesis techniques are discussed under methods 1 to 3.

Method 1: Sol-gel batch process at 800 °C

Within this study the spinel $Li_{1.03}Mn_{1.97}O_4$ together with some variations in the doped material (Al, Mg, Ni and Co) were synthesized by the conventional sol-gel method and are referred to as, for example "$LiMn_2O_4$ batch-800 °C", within the text. The sol-gel synthesis method was prepared by dissolving the manganese and lithium salts (acetates) in stoichiometric amounts together with a carrier (citric, ascorbic, succinic and poly-acrylic acid) in distilled water, forming an aqueous solution. The aqueous solution was then heated to 120 °C with continuous stirring until the gel-solid precipitate was formed. Further heating was required resulting in the solid powder precursor that was then completely dried in a drying oven at 140 °C for about 5 hours (in air). The dried precursor was further calcined at 800 °C in a tube furnace for about 15 hours in an air atmosphere producing the final spinel lithium metal oxide cathode material. The doped materials were prepared under the same conditions only with the addition of the metal acetate such as aluminium acetate, magnesium acetate, nickel acetate or cobalt acetate in the appropriate proportions to give the desired stoichiometric ratios.

Method 2: Sol-gel batch process at 600 °C

It should be noted that the sol-gel process was repeated on the spinel $Li_{1.03}Mn_{1.97}O_4$ together with the doped materials (Al, Mg, Ni and Co) at 600 °C at a later stage after obtaining the in-situ PXRD results. These results are referred to as, for example "$Li_{1.03}Mn_{1.97}O_4$ batch-600 °C", within the text. The sol-gel synthesis method for these undoped oxide materials ("$Li_{1.03}Mn_{1.97}O_4$ batch-600 °C") together with its dopants was prepared following the same procedure as in method 1. However, the only difference was that the dried precursor was further calcined at 600 °C in a tube furnace for about 15 hours in an air atmosphere producing the final spinel lithium metal oxide cathode material.

The spray pyrolysis method used within this study followed two separate preparation approaches. The first approach involved the designing of a spraying technique as shown in Figure 2.14. This however might lead to unwanted fouling and clogging with an uneven temperature distribution within the sample preparation zone. This clogging would then lead to the loss of residence time control and affect the particle size and its distribution. By adding a rotating screw conveyor with a low clearance to the reactor wall avoided the fouling problem and improved the heat distribution and uniformity.

Due to the very high heat capacity, a conventional full steel hammer drill was used as the rotating screw. Heating up the furnace and the stainless steel screw conveyor to the reaction temperature needs approximately 35 minutes. Induced heat fluctuations of the relatively cold carrier gas could be suppressed. The injection of the premixed reactant droplets was done at the upper end of the quartz glass tube, which allows the solvent to evaporate and form the gel in the ascending hot air from the furnace. After the solvent release, the rotating screw conveyor transports the dried material through the furnace and one could adjust the residence time by adjusting the turning speed. However, only with a preheated carrier gas (Ar), a constant flow was achieved. The turbulences of the released hot air influenced some of the uniformity of the spray. Also, the energy that was lost through ascending hot air by using the vertical setup (version 1) was uneconomical. Due to these facts and in order to economise the process, a horizontal setup (version 2) was used. The furnace was mounted horizontally with a slight bend (at approximately 45° angle) and the screw conveyer diameter was decreased, allowing the screw conveyor or

spray to feed the droplets deeper into the furnace while still providing the residence time control (refer to Figure 3.1).

Within the schematic diagram (Figure 3.1b) the aqueous solution was pumped (by a peristaltic pump) through the nozzle into a preheated furnace (with a preheated screw) with the aid of a carrier gas (Ar). The solvent was immediately evaporated off (by the heated furnace) allowing the powder sample to collect onto the walls of the quartz rod and screw. The screw would then rotate continuously (rotation was controlled by a step motor), removing any powder from the glass rod and systematically transport the powder toward the quartz rod outlet and finally collecting the produced cathode oxide material.

However, continuous and prolonged use of this steel screw would result in contamination of the active material and cracking of the quartz glass tube as the screw rotates within the quartz glass scrapping the tube's walls (results on using this approach is included as Appendix C). Due to these shortcomings this technique was not used and a second approach was considered (Figure 3.2). The second approach was referred to a spray-drying process which was then used throughout this study. The proof of concept was determined based on the first approach and the use of spray pyrolysis and spray-drying in literature[1-5]. This spray-drying method was chosen due to the material's positive morphological and electrochemical performance reported in literature[1-5]. The spinel manganese cathode oxide together with its dopants (in this study) was prepared by following this spray-drying technique.
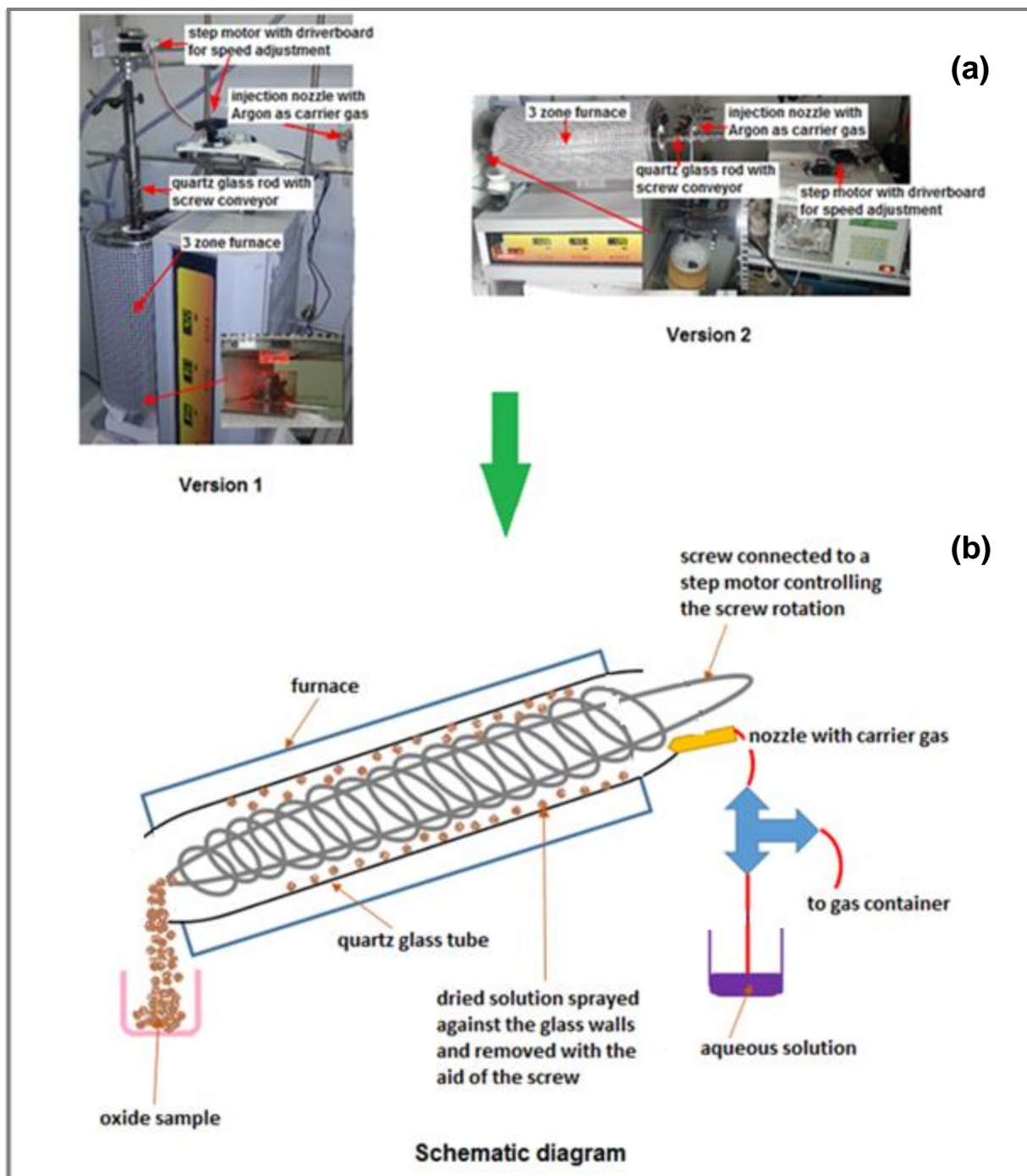
Figure 3.1: Setup for a conventional spray pyrolysis process with a high heat capacity screw conveyor (first approach) together with a schematic diagram

Method 3: Spray-drying process at 400 °C

The spray-drying process (for preparing the final oxide materials in this study) involved the preparation of an aqueous acetate solution within its correct ratio amounts (for example, 1.03:1.97 for Li to Mn acetate and 1:0.4:1.6 for Li to Al to Mn acetates together with citric acid) for the various oxide materials. The aqueous solution was then pumped (at about 7 ml.min^{-1}) by a peristaltic pump through an atomizing nozzle (from Spraytech) and sprayed onto a preheated hot surface (at 400 °C). The solvent would then instantly evaporate off, leaving behind a powder residue as the active cathode material (Figure 3.2). With this technique, the pump rate, heating surface and spray nozzle configuration could be adjusted to optimize the type of active material. These results are referred to example, "Li$_{1.03}$Mn$_{1.97}$O$_4$ spray-400 °C" within the text.
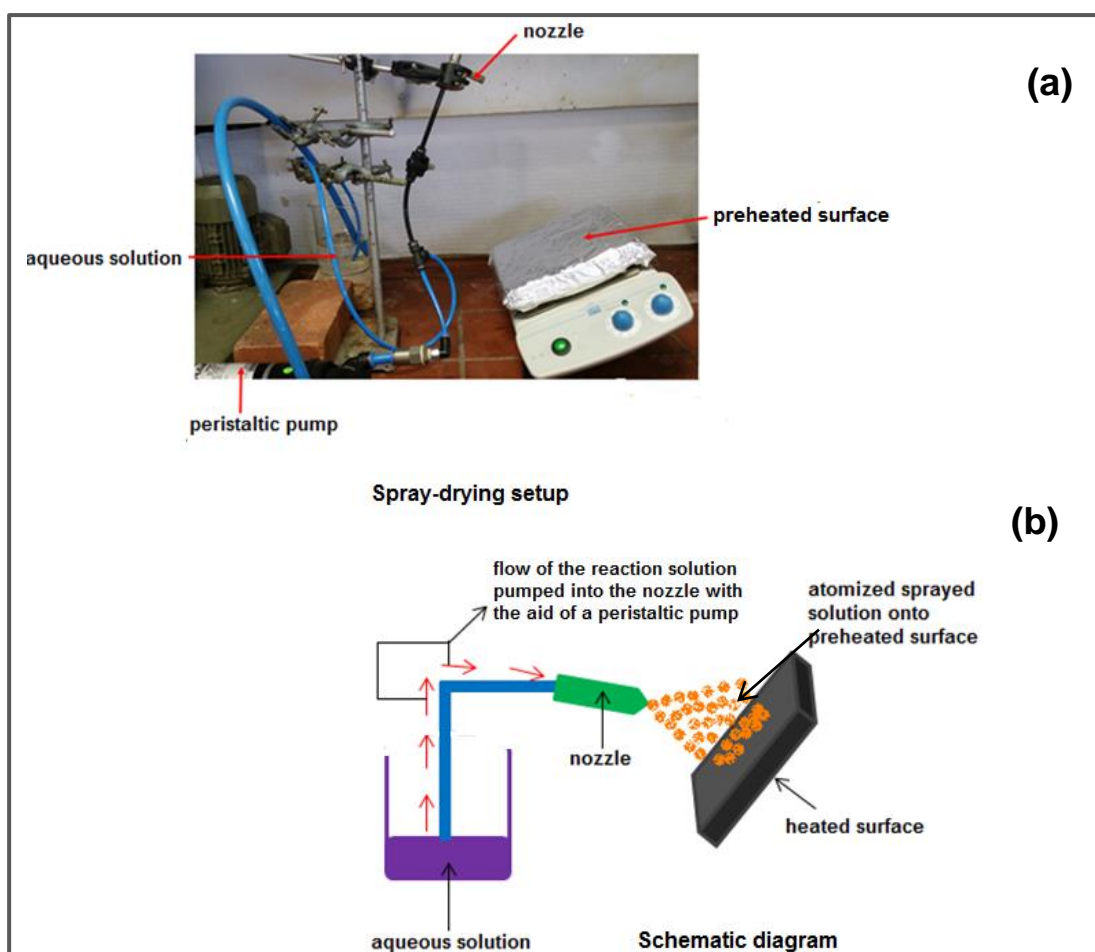
Figure 3.2: Final spray-drying setup (second approach) together with a schematic diagram

3.2 Material characterization

3.2.1 <u>Thermogravimetric Analysis</u>

Thermogravimetric analysis (TGA) is a technique that measures a material's weight loss with temperature. The specimen is heated at a predetermined rate under inert or oxygen atmosphere. The material's thermal stability is reflected in terms of the mass loss and the fractions of volatile components are carefully determined at specific temperatures.

The TGA instrument (TA Instruments, SDT Q600) (Figure 3.3) consists of a sample pan and reference pan that is supported on an accurate micro-balance enclosed within a furnace that can heat or cool the material under a continuous flow of N_2 or air.

During heating of a sample the technique can quantify any of the following parameters[6]:

- water loss
- loss of solvent
- oxidation
- decomposition
- weight % ash
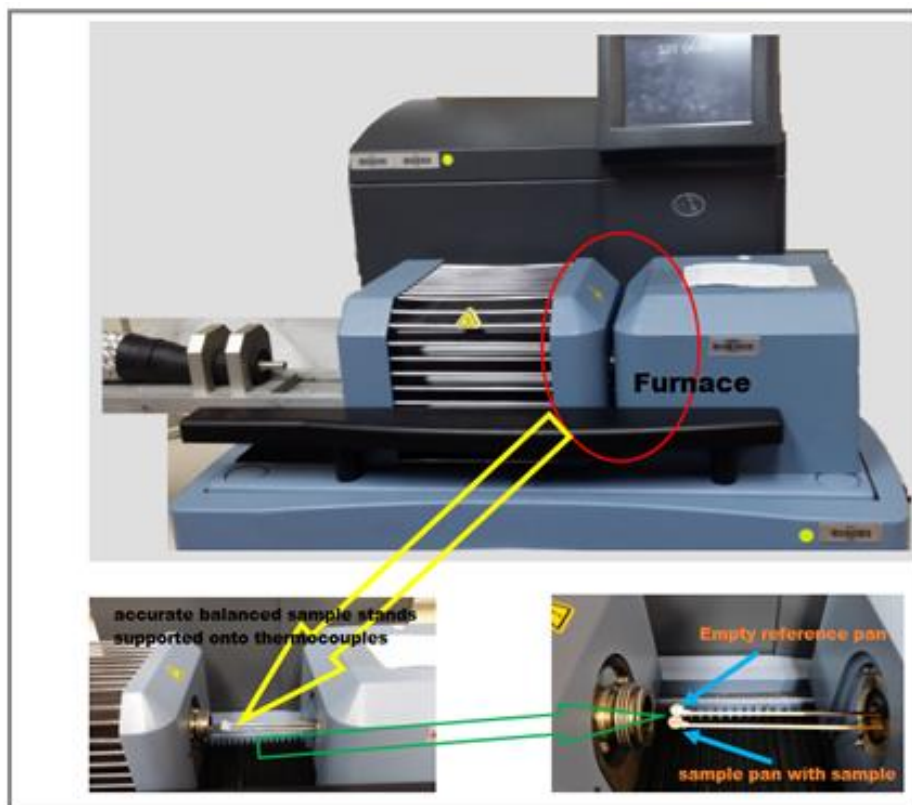
Figure 3.3: SDT Q600 TA instrument

The quantification of the various phases was done using TA Universal Analysis v4.5A software. A sample size of between 5-9 mg is usually used, but in this study, a 2 mg sample was used because the sample tended to expand upon heating and sometimes "bubble" over the sample cup and possibly damage the thermocouples. Heating was done from 25 to 800 ºC at a 1 °C.min^{-1} heating rate under an air atmosphere.

3.2.2 X-ray Diffraction Analysis

The discovery of X-rays can be dated back to 1895[7] whereby scientists were able to investigate crystalline structures at the atomic level. This is a nondestructive technique and can be used for identification of crystalline materials and information on its unit cell dimension can be determined. Powder X-ray diffraction (PXRD) can be used for qualification and quantification of phases present in a solid material. X-ray crystallography can be used to determine the crystal structure, which is usually done from single crystals of the compound. The structural information can be used in quantification on structure refining of materials under investigation. A powder X-ray diffractometer (Bruker Phaser

D2) consists of an X-ray tube (in this study Cu radiation); a sample holder and an X-ray detector (Figure 3.5). A simplistic illustration of using X-rays in determining the crystalline characteristics of a material is shown in Figure 3.4.
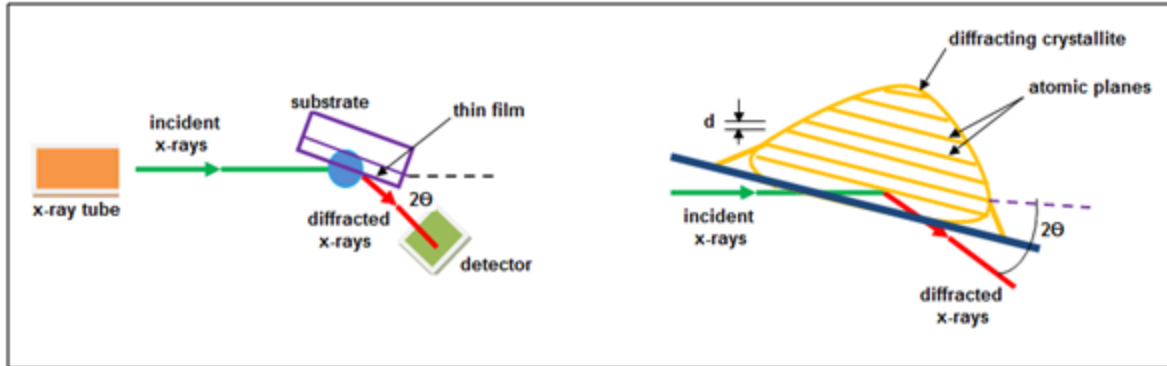
Figure 3.4: Schematic illustration on the x-ray diffraction process[8]

The following information can be obtained from PXRD:

- unit cell lattice parameters
- phase identification
- phase purity
- degree of crystallinity
- unit cell crystal structure
- % phase composition
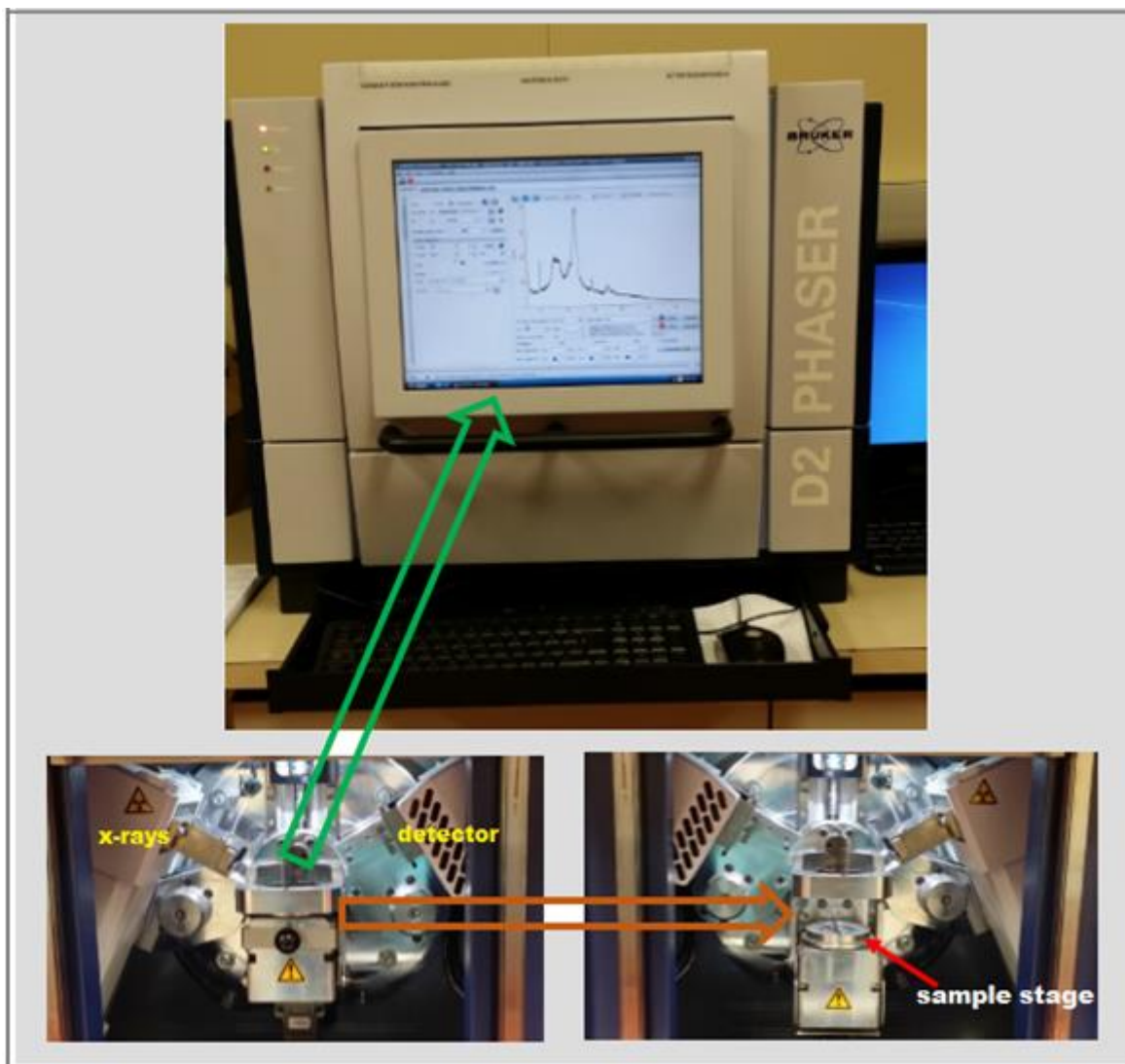
Figure 3.5: Bruker D2 phaser instrument

In this study phase identification of the cathode metal oxide materials was determined by PXRD using a Bruker D2 Phaser with a Lynxeye detector and Cu radiation. Phase quantification was done by full pattern Rietveld refinement using Topas V4.2[9]. A scan range of 5-70° was used for all PXRD analyses. The samples were pre-ground using a mortar and pestle before placing them onto a silicon low background sample holder or into standard polycarbonate sample holders.

Phase identification of the various precursors to the cathode metal oxide materials was determined by in-situ temperature PXRD. This analysis consisted of placing the precursor

sample into a ceramic sample stage which was enclosed in the heating stage, whereby the precursor was gradually heated to the materials' final oxide phase.

Figure 3.6: Bruker D8 in-situ XRD instrument

In-situ PXRD analysis was done using a Bruker D8 Advance consisting of a Vantec detector and a Cu radiation source with a Goebel mirror. Phase quantification was done by Rietveld refinement using Topas V4.2[9]. The heating chamber used for this particular instrument was an Anton Parr XRK900 with Macor® ceramic sample holders with a Pt foil insert. A scan range of 5-70° was used for all in-situ PXRD analysis. The sample was heated under an air atmosphere from 30 to 850 °C and cooled to room temperature again. A full PXRD pattern (also referred to as variable temperature scans, VT-scans) were collected every 50 °C.

3.2.3 <u>Scanning Electron Microscopic Analysis</u>

The first commercial instrument was marketed by the Cambridge Scientific Instrument Company headed by Charles Oatley in 1965 known as the "Stereoscan"[10-13]. For imaging the scanning electron microsope (SEM) scans the sample surface by a concentrated beam of electrons (5 keV to 20 keV). The electrons on the surface of the sample interact with the eletron beam via diffraction and thus a signal is produced. Samples of different surface compositions will have different interactions with the beam and therefore different morphologies are obtained. This technique allows the sample to be characterized at the nano-micrometer range due to the SEM's high spatial resolution.

The scanninng process is as follows: an electron beam is thermoionically emitted from an electron gun (normally fitted with a tungsten filament). The electron beam is then focused by two condensor lenses, the beam further passes through pairs of scanning coils in the electron column. In the x and y axes the beam is deflected by the final lens scanning the samples surface over a rectangular area.
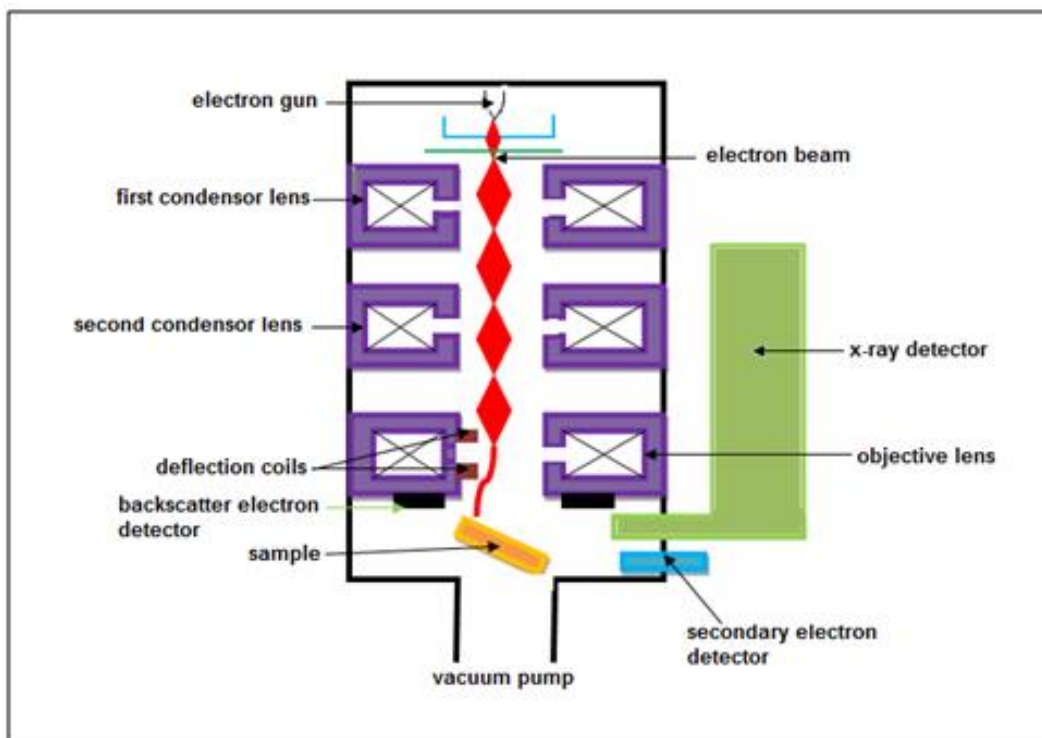
Figure 3.7: Schematic illustration on the SEM scanning process

Figure 3.8: JEOL 7001 SEM instrument

SEM analysis for this study was done using a JOEL 7001. Samples were prepared by placing a small amount of active material onto a carbon tape sample holder and subsequently gold sputter coated to increase for the conductivity for an improvement in image resolution.

3.2.4 <u>BET surface area Analysis</u>

BET analysis is a measure of a powder's specific surface area by physical adsorption of a gas on the surface of the solid. The analysis is usually carried out at the temperature of liquid nitrogen whereby the materials' precise surface area is evaluated by a measure of nitrogen multilayer adsorption as a function of relative pressure. BET analysis can be determined by multi-point or single point measurements. The typical BET equation would be[14]:

$$\frac{P}{V_a(P_0 - P)} = \frac{1}{V_m C} + \frac{C-1}{V_m C}\left(\frac{P}{P_0}\right)$$

<div align="right">3.1</div>

Where P is referred to the partial vapour pressure of the adsorbate gas in equilibrium with the surface, P_0 is referred to the saturated pressure of the adsorbate gas, V_a is the volume of gas adsorbed at standard temperature and pressure (STP), C is referred to the dimensionless constant (BET C constant) that is related to the enthalpy of adsorption of

the adsorbate gas on the powder sample and V_m is the volume of gas adsorbed at STP to produce an apparent monolayer on the sample surface.

A typical BET linear plot would be:

$$\frac{P}{V_a(P_0 - P)} \text{ vs} \left(\frac{P}{P_0}\right) \text{ with a y-intercept equal to } \frac{1}{V_m C} \text{ and a slope of } \frac{C-1}{V_m C} \qquad 3.2$$

Where V_a is referred to as the adsorbed weight and P/P_o is referred to as the sample pressure relative to atmospheric pressure. In BET theory uniformed surface coverage is assumed, as well as the assumption that the gas would be strongly attracted to the surface of the solid rather than to other gas molecules.
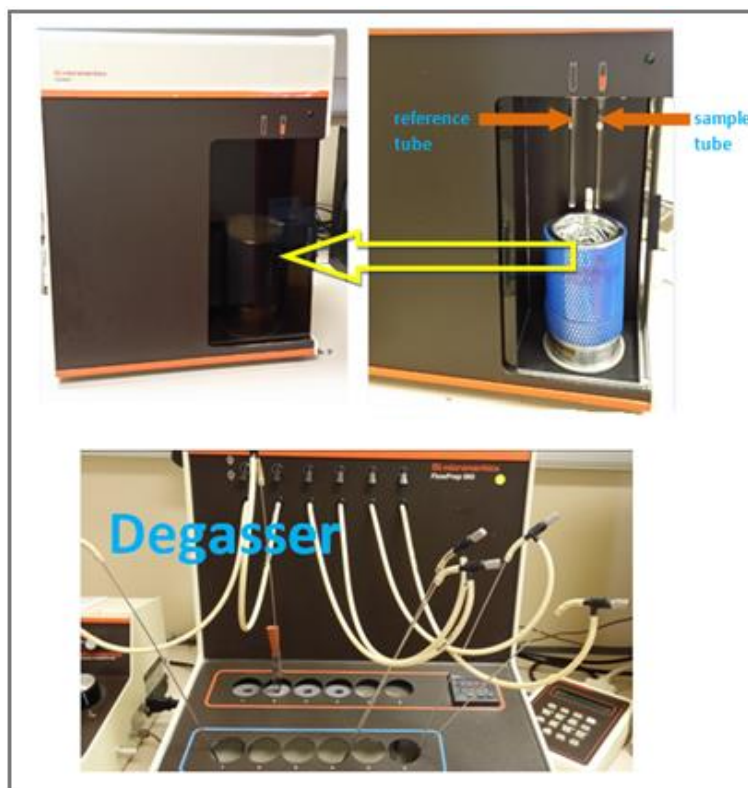
Figure 3.9: Micromeritics BET surface area instrument

BET analysis for this study was done on a Micromeritics Gemini 2375 instrument (Figure 3.9) and the quantification of the various phases was done using StarDriver v2.03 software. Samples were degassed for 1 hour under nitrogen at 300 °C.

3.2.5 <u>Atomic Force Microscopy (AFM)</u>

Atomic Force Microscopy (AFM) is a technique used to determine surface topography, 3D imaging and other properties such as surface conductivity by means of current sensing AFM just to mention a few. The ideas of AFM (using an ultra-small probe tip at the end of a cantilever) were first demonstrated in 1986 by Binnig *et al.*[15]. The AFM setup with a vibrating cantilever technique, which used the light-lever mechanism, was developed by Wickramasinghe *et al.*[16] in 1987.

This technique produces the surface on a nanoscale in a 3D profile, measuring the force between a sharp probe and surface within a short distance, this probe is supported on a flexible cantilever. This tip of the AFM touches the samples surface, recording the small force between the surface and the probe. A force is measured by placing the probe at the end of a cantilever. The force amount between the sample and probe is dependent on the spring constant or stiffness of the cantilever and the distance between the sample surface and the probe. The probe motion across the surface is controlled by piezoelectronic scanners. When this spring constant is less than the surface hardness or adhesion, the cantilever would bend, monitoring the deflection. This cantilever deflection generates a map of the surface topography.

This technique consists of three types of imaging modes such as; contact mode AFM, intermittent mode (tapping) and non-contact mode. The technique consists of a number of advantages as well as disadvantages. The advantages of using AFM include;

- easy sample preparation
- produces accurate height information
- the technique can work under vacuum, air and liquid environments
- living systems can be studied by this technique

The disadvantages associated by following this technique include;

- a limited vertical range
- magnification range is limited
- the obtained data is not independent of the tip

- the sample or tip can be damaged
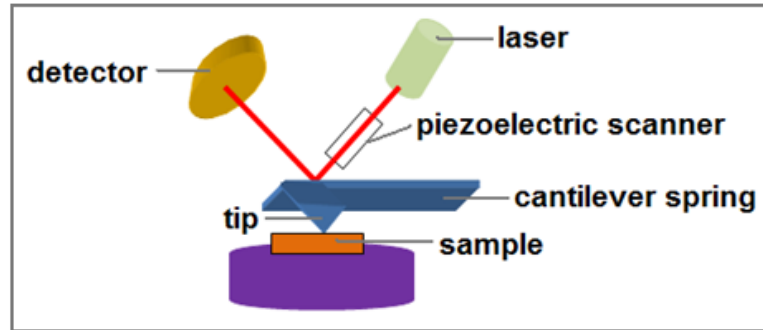
Figure 3.10: Illustration of the AFM setup

Figure 3.11: Bruker SPM instrument

AFM imaging analysis for this study was done using a Bruker Dimension SPM microscope (Figure 3.11). Imaging analyses were carried out by PeakForce QNM AFM mode, with Scan Assyst in Air tips, the scan rates were set to 1.0 Hz over a 1 µm scan range and even lower magnification. These analyses were operated by the NanoScope software.

3.3 Electrode fabrication and electrochemical methods

3.3.1 <u>Electrode fabrication</u>

The lithium-ion 2032 coin cells were fabricated by using the cathode oxide material (discussed in Section 3.1) as active material together with polyvinylidene fluoride (PVDF) as binder and carbon black as a conductive material in a weight ratio of 80:10:10 respectively. N-Methyl-2-pyrrolidone (NMP) was used as solvent. PVDF, carbon black and the active material was grounded into a fine powder with a mortar and pestle, to which NMP was added to make a suitable slurry. The slurry was then coated onto the aluminium foil current collector which was then placed into a vacuum oven at 110 °C for 24 hours. Thereafter the coated foil was punched into discs acting as the cathode electrode.

Coin cell assembly was done in an Ar filled glovebox (Saffron Anaerobic glove box) with the oxygen and moisture levels being less than 5 ppm. Lithium metal was used as anode and the electrolyte consisted of a 1 M lithium hexafluorophosphate ($LiPF_6$) in 1:1:1 (v/v) EC:DMC:DEC together with a polypropylene film (Cellgard 2300) as separator.

Before any measurements were carried out, after assembly, the coin cells were left to settle overnight ensuring proper wetting of the electrodes.

3.3.2 <u>Electrochemical methods</u>

All electrochemical tests were done on the assembled coin cells using a Gamry Reference 3000 Potentiostat (Figure 3.12). The analysis was controlled by the Gamry Instrument Framework software and interpretation was done on the Gamry Echem Analyst version 6.23 software.

Figure 3.12: Gamry Potentiostat

3.3.2.1 <u>Cyclic Voltammetry Analysis</u>

Cyclic voltammetry (CV) is a potentiodynamic electrochemical technique used by electro, organic and inorganic chemists. CV is normally used to study the electrochemical properties of an analyte in solution. The potential is applied between the working and reference electrodes, while measuring the current between the working and counter electrodes. This technique gives information on the electron transfer reactions and also on the thermodynamics of the redox reactions taking place. Within this technique the electrode's potential is linearly ramped versus time at a specific scan rate. The experiments within this technique consists of scanning the potential of the working electrode using a triangular waveform (refer to Figure 3.13).

During this study CV analysis was done on the assembled coin cells, whereby the lithium metal represented both the counter and reference electrodes. Each cell was scanned over a potential range of 3.0 to 5.0 V with a scan rate of 0.1 mV.s^{-1}.
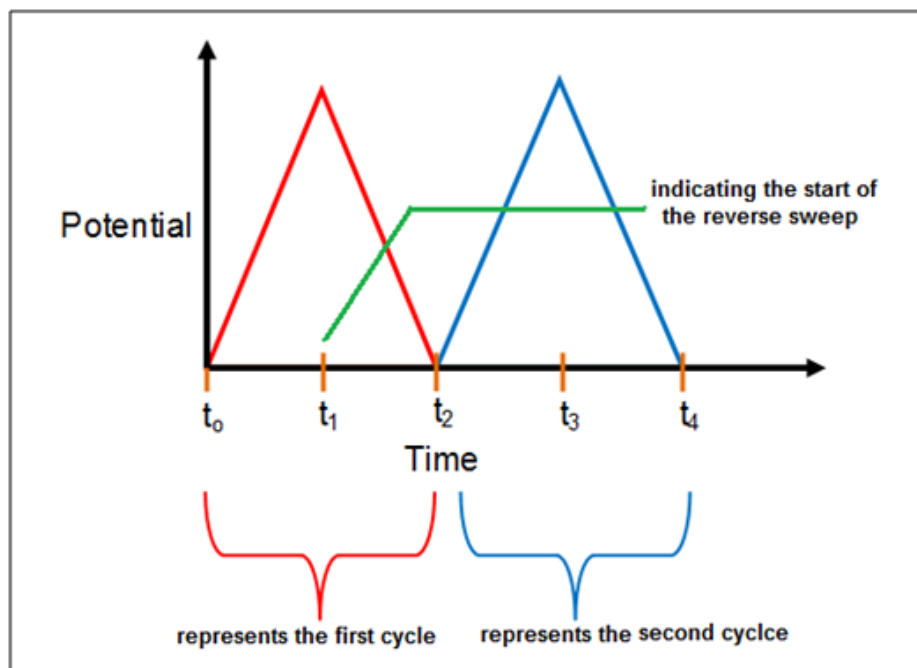
Figure 3.13: Schematic illustration on the CV process

3.3.2.2 <u>Electrochemical Impedance Spectroscopy Analysis</u>

This method is a very important electrochemical characterization technique. The electrochemically active sample is subjected to a small alternating current or voltage that is varied over a large frequency range. The system's response to the signal, either the voltage or current is then recorded. With this technique a large amount of information can be obtained over a short analysis period. The interpretation of the information is then modeled according to an equivalent circuit model. Electrochemical impedance spectroscopy (EIS) has the advantage of characterizing a wide range of the physical and chemical phenomena by a single experimental analysis over a wide frequency range. While the electrochemical system remains intact with a suitable reference electrode, various subcomponent properties are measured and the electrochemical properties of one electrode can be evaluated. The response obtained from these results is described as impedance (Z) which is a ratio or transfer function of the voltage to the current. The systems response is regarded as being linear due to the small signal response. Some processes relate to time derivatives of potential and concentration rather than upon the magnitude of the variables themselves, part of the system will be in phase with the

perturbation (a real component), whereas other parts will be out of phase with the applied signal (imaginary component) summarized as[17]:

$$Z(\omega) = Z'(\omega) + j \cdot Z''(\underline{\omega}) \qquad\qquad 3.3$$

total impedance ↗   real component ↑   imaginary component ↖

The results or data of this technique after analysis can be displayed by either a Bode or Nyquist plot (Figures 3.14 and 3.15)[18]. Information on the impedance change and phase shift with frequency can be obtained by the Bode plot. The Nyquist plot provides information on the mixture of resistance and capacitance at high and low frequencies.
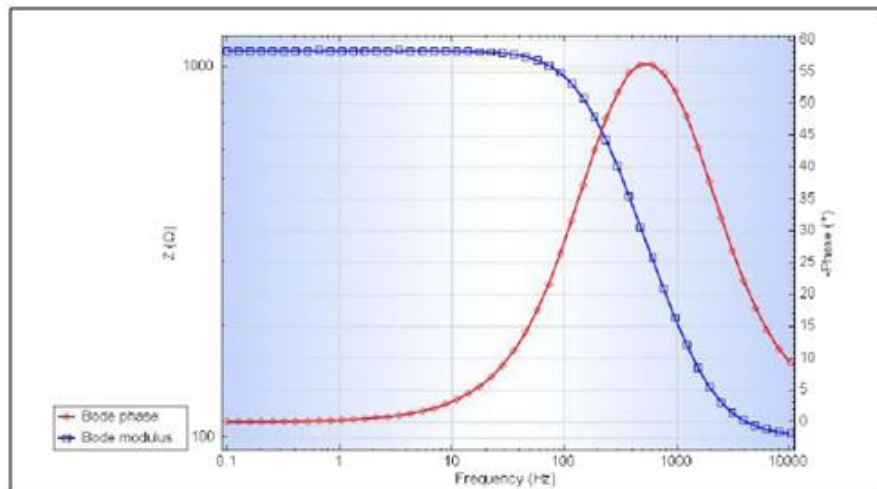
Figure 3.14: Example of a typical Bode plot
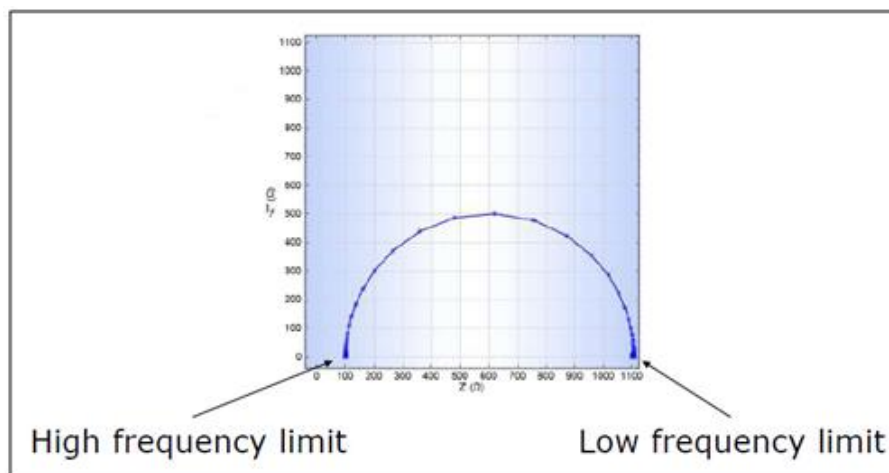
Figure 3.15: Example of a typical Nyquist plot[19]

Both of these plots have their own charge transfer processes, which are resolved by an equivalent circuit model (Figure 3.16).
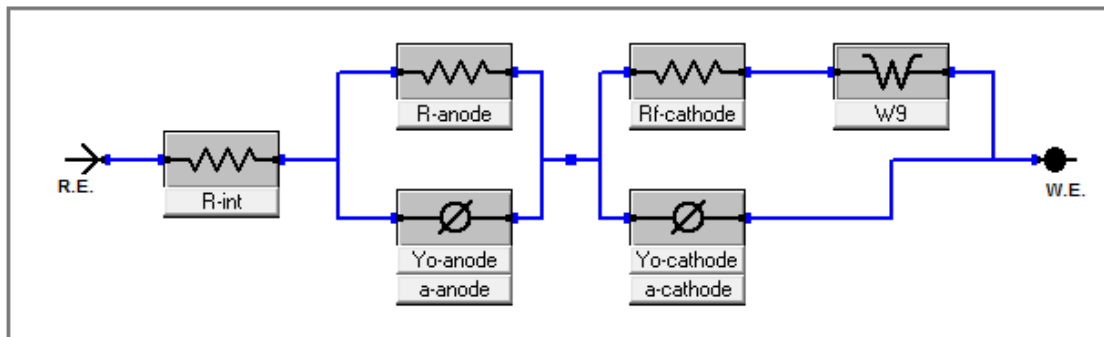
Figure 3.16: Electrical equivalent circuit (EEC) model used in this study

From the EEC model the internal resistance (R-int) is a representation of the resistance buildup within the full lithium-ion cell. This resistance can be caused by the cell assembling, electrolyte and separators. Y_o-anode and a-anode represents the constant phase element within the anode, whereas R-anode contributes to the resistance buildup within the lithium metal (anode) electrode which can be caused by the standard electrolyte interphase (SEI) layer. Y_o-cathode and a-cathode represents the constant phase element within the cathode, whereas R-cathode contributes to the resistance buildup within the spinel lithium metal oxide (cathode) electrode. This resistance could be caused by the expansion and contraction of the spinel structure during intercalation and de-intercalation. W represents the Warburg function whereby the lithium-ion diffuses between the anode and cathode.

Within the Nyquist plot small impedances can be swamped by large impedances, whereas the Bode plot provides information on both small and large impedances. EIS is a very sensitive technique and result reproducibility is often difficult due to:

➢ instrumental variations
➢ cell connection
➢ sample composition

The Nyquist plot for a battery chemistry system provides certain information described in Figure 3.17[20].
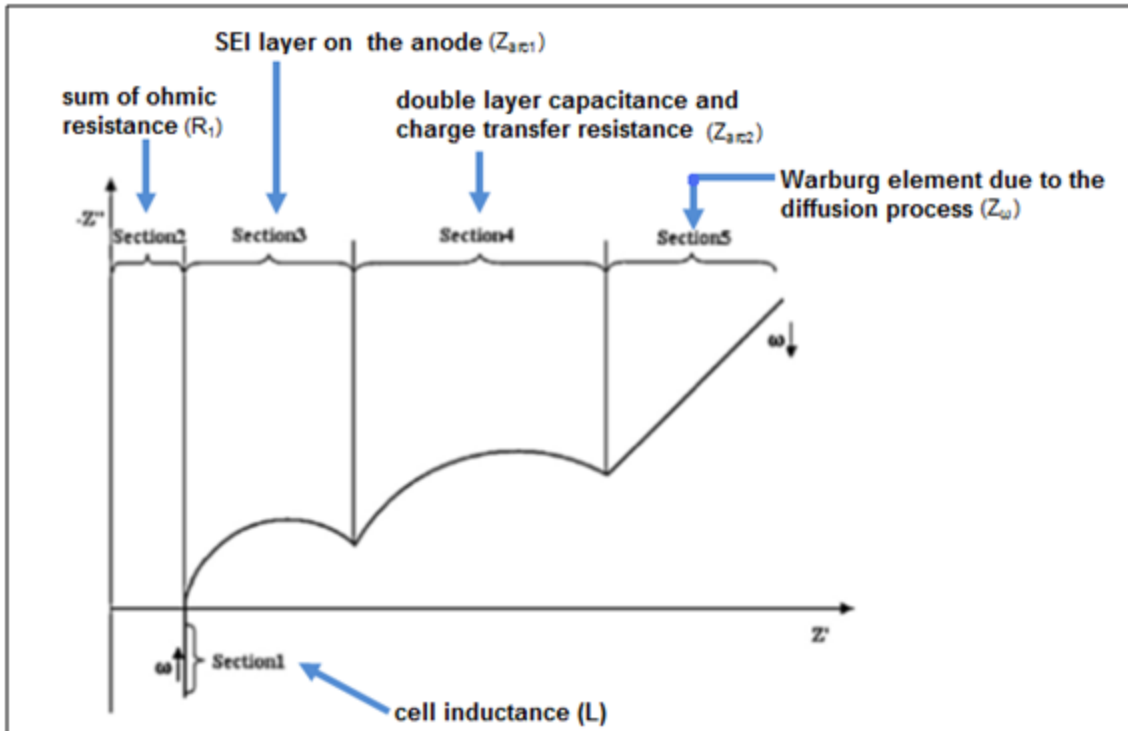
Figure 3.17: Different sections of an ideal EIS Nyquist spectrum for a battery system

During this study, an initial EIS measurement was done on the coin cells after a complete charge at 0.1 C (formation) to 4.5 V. The cells with the different cathode material compositions were then completely discharged to 3 V at 0.1 C and recharged at various recharge limiting potentials (3.9, 4.2, 4.5 V) respectively. The cells were potentiostatically held at a particular potential until the current dropped to 0.001 mA. This was then followed by an EIS measurement after each charging potential step.

3.3.2.3 <u>Lithium-ion diffusion</u>
For many years it was believed that lithium-ion batteries were unable to achieve high power outputs due to the slow Li-ion mobility in the organic electrolyte solvent. Ozawa[21] discussed this effect and found that if the organic electrolyte was the limiting component, the lithium-ion diffusion through the electrolyte should then be the principal rate determining factor. In 1993 a theoretical study was done on reducing the internal resistance and various mathematical equations were developed and investigated and showed that the Li-ion diffusion is limited by the ability for the ion to move in and out of the cathodes active material[21].

After numerous studies on the subject in literature[22-25] the following diffusion coefficient equation was considered to be suitable to describe the diffusion ability of the Li-ion through the bulk cathode material[26]:

$$D_{Li} = \frac{2R^2 T^2}{C_{Li}^2 n^4 F^4 A^2 \sigma^2}$$

3.4

where D_{Li} represents the lithium diffusion coefficient ($cm^2.sec^{-1}$), R is the gas constant (8.314 $J.K^{-1}mol^{-1}$), T is the absolute temperature (K), C_{Li} is the lithium concentration ($mol.cm^{-3}$) in the cathode material at a particular cell voltage (refer to Figure 5.14), n is the number of electrons transferred per Li^+ molecule, F is the Faraday's constant (96486 C), A is the electrode surface area (cm^2) and σ is the Warburg factor ($\Omega.s^{-1/2}$) which is associated with the Warburg (infinite) impedance[27]:

$$Z_w = \sigma/\omega^{-1/2} (1-j)$$

3.5

Where: Z_w is the Warburg (infinite) diffusion impedance

ω is the radial frequency

j is $\sqrt{-1}$

σ is the Warburg factor obtained from the slope by plotting the Z_{re} (real impedance) vs $\omega^{-1/2}$ (the reciprocal square root of the frequency in the low frequency region (Figures 5.15 to 5.25 and summarized in Appendix B) which can alternatively also be obtained from the following equation[28]:

$$\sigma_D = \frac{RT}{Z^2 F^2 A\sqrt{2}} \left(\frac{1}{C_{ox}^* \sqrt{D_{ox}}} + \frac{1}{C_{red}^* \sqrt{D_{red}}} \right)$$

3.6

where: R is the gas constant

T is the absolute temperature

Z is the number of transferred electron charges per diffusing species

F is Faradays constant

A is the electrodes surface area

$C_{ox/red}$ is the concentrations of the diffusing species

$D_{ox/red}$ is the diffusion coefficients of the oxidant and reductant

3.3.2.4 Charge-Discharge Capacity Analysis

The charge-discharge technique is the most important characteristic tool for lithium-ion cells. From this technique or test the charge and discharge capacity parameters can be obtained. The capacity of a battery measures the charge amount stored by the battery, which is determined by the weight of the active materials contained within the battery. This parameter is a representation of the maximum amount of energy available to be extracted from the battery under certain conditions. Within this method or technique a constant current is applied, while monitoring the working electrodes potential (with respect to the reference electrode) with time, setting limits to the upper and lower potentials for the working electrode. When reaching one of these limits the test (charge or discharge) is stopped and the current is reversed, thereafter cycling is determined.

During this study the Gamry Reference 3000 Potentiostat was used for capacity measurements on the assembled two electrode coin cells for the various cathode oxide materials. Charging and discharging was done at 0.1 C (charge/discharge rates) with a charge voltage limit of 4.5 V and a discharging voltage limit of 3 V.

REFERENCES

1 Y. Li, N.P. Haigh, C. Wan, Y. Wu, C. Jiang and Y. Zhu, *Journal of Power Sources*, 2000, **85**, 294-298.

2 I. Taniguchi, N. Fukuda and M. Konarova, *Journal of Power Sources*, 2008, **181**, 228-236.

3 S. Hirose, T. Kodera and T. Ogihara, *Journal of Alloys and Compounds*, 2010, **506**, 883-887.

4 D. Jung, Y. Ko, Y. Kang and S. Park, *Advance Powder Technology*, 2014, **25**, 18-31.

5 G.X. Wang, S.L. Bewlay, K. Konstantinov, H.K. Liu, S.X. Dou and J.H. Ahn, *Electrochimica Acta*, 2004, **50**, 443-447.

6 PerkinElmer notes, Thermogravimetric Analysis (TGA) – A Beginner's Guide, 2010, 1-19.

7 H. Loye, *X-Ray Diffraction, How it works, What it can and What it cannot tell us*, X-ray tutorial, University of South Carolina, 2015.

8 B. Fultz, J. Howe, *Transmission Electron Microscopy and Diffractometry of Materials*, Springer, 2013, Chapter 1, 1-57.

9 Bruker AXS, Topas Manual, Version 4.2, West Germany, 2009.

10 C.W. Oatley, W.C. Nixon, *Advance Electronics Electron Phys*, 1965, **21**, 181–247.

11 K.C.A. Smith, C.W. Oatley, *British Journal of Applied Physics,* 1955*,* **6** (11), 391.

12 D. McMullan, *An improved scanning electron microscope for opaque specimens*,Proceedings of the IEE, 1953, **100**, 245-256.

13 O.C. Wells,*The construction of a scanning electron microscope and its application to the study of fibers,* PhD Dissertation, Cambridge University, 1957.

14 G. Fagerlund, *Materials and Structures*, 1973, **6**, 239-245.

15 G. Binnig, C.F. Quate, C. Gerber, *Phy. Rev. Letters*, 1986, **56**, 930.

16 H.K. Wickramasinghe, Y. Martin, C.C. Williams, *J. Appl. Phys.*, 1987, **61**, 4723.

17 M. van Dyck, *Presentation on Metrohm Instruments*, EIS conference PE, South Africa, 2011.

18 Gamry Instrument Application Notes, *Basics of Electrochemical Impedance Spectroscopy*, 2015.

19 J. Ketter, *Presentation on Gamry Instruments*, EIS conference PE, South Africa, 2011.

20 D. Andre, M. Meiler, K. Steiner, H. Walz, T. Soczka-Guth, D.U. Sauer, *Journal of Power Sources*, 2011,**196**, 5341-5348.

21 K. Ozawa, *Lithium Ion Rechargeable Batteries*, Wiley-VCH Verlag GmbH & Co., Weinheim, 2009.

22 C. Heubner, M. Schneider, A. Michaelis, *Journal of Power Sources*, 2015, **288**, 115-120.

23 Y. Zhou, J. Wang, Y. Hu, R. O'Hayre, Z. Shao, *Chemistry Communication*, 2010, **46**, 7151.

24 X. Zhang, A. Mauger, Q. Lu, H. Groult, L. Perrigaud, F. Gendron, C.M. Julien, *Electrochimica Acta*, 2010, **55**, 6440-6449.

25 X. Fang, J. Li, K. Huang, S. Liu, C. Huang, S. Zhuang, J. Zhang, *Journal of Solid State Electrochemistry*, 2012, **16**, 767.

26 C.O. Ikpo, C.J. Jafta, K.I. Ozoemena, N. West, N. Njomo, N. Jahed, P.G. Baker, E.I. Iwuoha, *International Journal of Electrochemical Science*, 2013, **8**, 753-772.

27 Gamry Instruments Application notes, *Basics of Electrochemical Impedance Spectroscopy*, Rev 1, 2010.

28 J. Bisquert, *Journal of Chemical Physics B*, 2002, **106**, 325-333.

CHAPTER 4

RESULTS AND DISCUSSION

Material characterization

This chapter is subdivided into three sections consisting of thermal, X-ray and morphology analysis, which is used to characterize the spinel cathode oxide materials.

4.1 **Thermogravimetric results**

Thermal Gravimetric analysis (TGA) is a simulation of the batch sol-gel process (at 800 °C), understanding how the material decomposes (from starting precursor materials) to form its final metal oxide material and also how much of the final material is present with respect to the starting material. TGA was done in air (from room temperature to 800 °C) on the following precursor materials (Table 4.1):

Table 4.1: Summary on precursors analyzed, acids and synthesis methods used.

Precursor	Acid	Synthesis method
$Li_{1.03}Mn_{1.97}O_4$	Citric acid	The batch sol-gel method (method 1 in Chapter 3) was used, whereby the appropriate acetates were dissolved in water together with the appropriate acid. This aqueous solution was stirred and heated at 120 °C, producing a gel. The gel was dried at 140 °C for 5 hrs, producing a precursor. This precursor was then used for TGA.
	Succinic acid	
	Ascorbic acid	
	Poly-acrylic acid	
$LiAl_{0.4}Mn_{1.6}O_4$	Citric acid	
$Li_{1.03}Mg_{0.2}Mn_{1.77}O_4$	Citric acid	
$LiCo_{1.09}Mn_{0.91}O_4$	Citric acid	
$LiNi_{0.5}Mn_{1.5}O_4$	Citric acid	

Acids within the synthesis process functions as a chelating agent and also provides the requirement for heat of combustion. This in turn would lead to an increase in crystallinity

and surface area for the $LiMn_2O_4$ and its various doped derivative powders with an increase in acid quantity[1]. Y.K. Sun[2] described the importance of the chelating agent on the physicochemical properties of the oxide powders used in sol-gel methods. Having a low acid to metal ion ratio at high calcination temperatures can result in impure phases. It was therefore decided to use a higher acid to metal ion ratio that would form relatively pure phases of $LiMn_2O_4$ at lower temperatures. Also, increasing the temperature would result in a more crystalline pure spinel oxide phase[1, 2]. Various acids were used (within this study) in making the $Li_{1.03}Mn_{1.97}O_4$. It was of interest to investigate the materials weight decomposition at a specific temperature and possibly correlate this finding to the phase composition results obtained from PXRD. Citric acid was then considered as the preferred chelating agent for further studies due to the following findings from its TGA results:

- small water residual amount
- precursor material was easier to work with and not hygroscopic (like the other acids)
- this acid was cheaper in comparison to the other acids used in the study
- experimental residual weight % was closer to its theoretical residual weight %
- from literature, it seemed to be a common material used for sol-gel synthesis
- no complex intermediate phases formed when considering only the $Li_{1.03}Mn_{1.97}O_4$

The stoichiometric ratios used for the spinel cathode oxide materials (in this study) were chosen so that the substituted metal ion ratio together with the ratio of the undoped spinel material would still add up to the cationic stochiometric ratio (Li to Mn = 1:2). The partial substitution of Mn by various cations was well described in literature to reduce the Jahn-Teller effect that occurs during capacity cycling[3-5]. The Cobalt doping consisted of a 1:1 ratio (Co to Mn) based on the work done by Huang *et al.*[6]. They showed that at the cell potential of 4.0 V, a plateau was observed which related to the Jahn-Teller effect (Mn^{3+} in the impurity phase of $LiMn_2O_4$) that causes capacity fading during cycling. They found that a 1:1 ratio of Co to Mn reduced this effect and the plateau at 4.0 V was not observed. The 0.4:1.6 (Al to Mn) doping ratio was used as described by Myung *et al.*[7]. They did a study by investigating the Al doping effect in $LiAl_xMn_{2-x}O_4$, where x was between 0.1 to 0.6. They concluded that having a small amount of Al concentration ratio between 0.3 to 0.5 would

result in no 4.0 V plateau (associated with the Jahn-Teller effect), thereby improving the materials cycle ability. The 0.2:1.77 (Mg to Mn) ratio was similarly studied as described by Singh *et al.*[4]. According to their work, this particular doped ratio cathode material showed better capacity retention upon capacity cycling when compared to the undoped samples they studied. The standard ratio for the high voltage cathode material of the Ni doped material, $LiNi_{0.5}Mn_{1.5}O_4$ at 0.5:1.5 (Ni to Mn) was also considered in this study[8].

The TGA results for the above mentioned materials ($Li_{1.03}Mn_{1.97}O_4$, $LiAl_{0.4}Mn_{1.6}O_4$, $LiMg_{0.2}Mn_{1.77}O_4$, $LiCo_{1.09}Mn_{0.91}O_4$ and $LiNi_{0.5}Mn_{1.5}O_4$) are shown in the following Figures 4.1 to 4.8, where the mass loss and derivative mass loss with temperature are shown graphically. The percentage mass loss at various significant mass loss steps are shown as well as the residual mass of the final product when compared to the starting precursor. In addition, room temperature powder X-ray diffraction (PXRD) patterns of the respective sample's precursor material (material before calcination) and after it was heated to 300 °C and 400 °C respectively are shown as inserts in the Figures 4.1 to 4.8. These PXRD patterns are inserted to visibly show the various phase changes that occurred during the heating stages and will be discussed in more detail in Section 4.3.
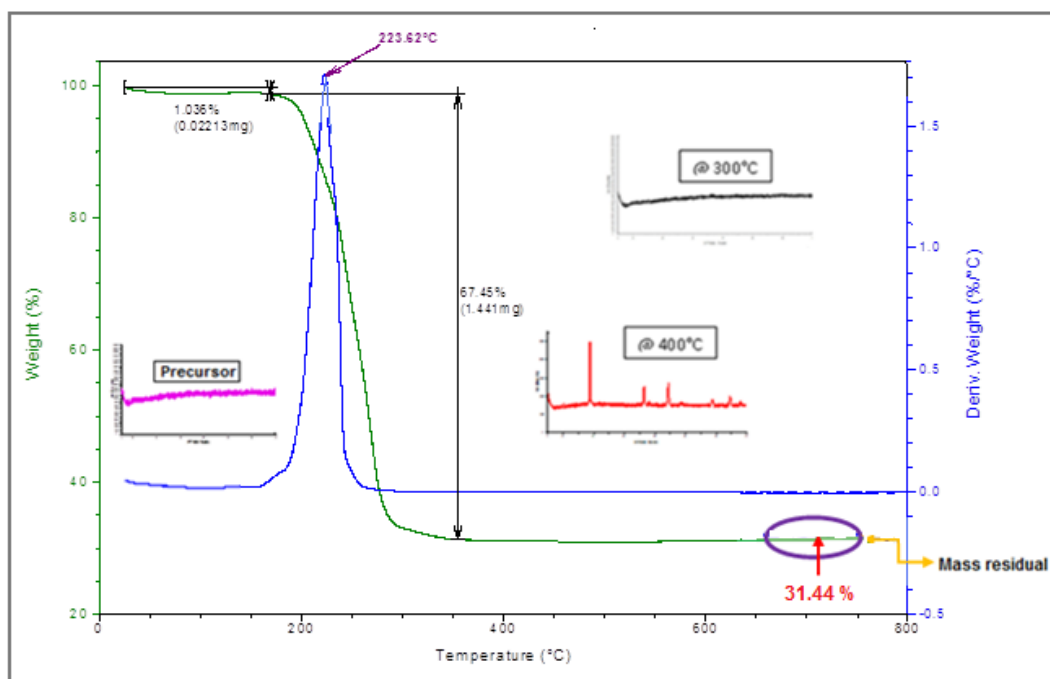
Figure 4.1: TGA curve of Li$_{1.03}$Mn$_{1.97}$O$_4$ in citric acid.

By considering the mole amounts of the starting materials, the following thermal reaction equation could be considered to take place, assuming that the decomposition of the organic materials would convert completely to CO_2 and H_2O respectively. This assumption would apply to all the spinel oxide materials considered in this study (Figures 4.1 to 4.5, oxides in citric acid and Figures 4.6 to 4.8, undoped oxide in various acids).

Reaction equation

$1.03Li(C_2H_3OO) + 1.97Mn(C_2H_3OO)_2 + 0.92C_6H_8O_7 + 14.81O_2 \rightarrow Li_{1.03}Mn_{1.97}O_4(s) +$
$15.42CO_2(g) + 11.11H_2O(g)$ 4.1
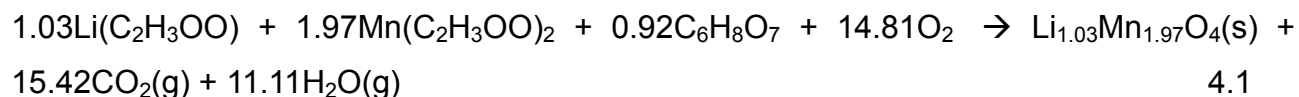
This would give a theoretical mass loss of 69 % or a residue (product) of 30.70 %. When compared to the TGA mass residual that remained, excluding the small amount of residual water that was in the starting materials, the product should amount to 30.40 % when compared to the starting material.

These results are in reasonable good agreement where the TGA curve showed a weight loss of 1.036 % below 200 °C that was due to some water still trapped within the precursor powder during material preparation (Figure 4.1). Thereafter the curve showed a single weight loss decomposition which correlated to a single phase change between the amorphous precursor (at room temperature) and the final oxide phase that had started to form at 400 °C. The derivative weight loss curve showed a single distinct weight change at 224 °C which can be related to the acid and acetate decomposition (67 % weight change). The TGA results obtained within this study was similar to those reported by Bao *et al.*[9] and Thirunakaran *et al.*[10]. There were however slight differences (between literature results and results in this study) in the respective decomposition weight loss and residual weight. There were also slight shifts in the respective decomposition temperatures. Bao *et al.*[9] observed a 4.8 % weight decomposition at 200 °C and 56.7 % at 300 °C with a residual of about 35 %, whereas Thirunakaran *et al.*[10] observed a 5 % weight decomposition at 100 °C and 45 % at about 327 °C with a residual of about 50 %. These differences could possibly be explained by the fact that there were slight changes in the preparation method,

with different stoichiometric amounts of the starting material and different chelating agents (Thirunakaran *et al.*[10] used myristic acid).

The inserted room temperature PXRD pattern (Figure 4.1) of the material that was heated to 300 °C showed that it was still amorphous in character, whereas the diffraction pattern at 400 °C corresponded to the diffraction pattern of the final spinel oxide. More detail on the exact formation of the final spinel over the temperature range will be discussed under Section 4.3 concerning the in-situ powder X-ray diffraction study of the material.
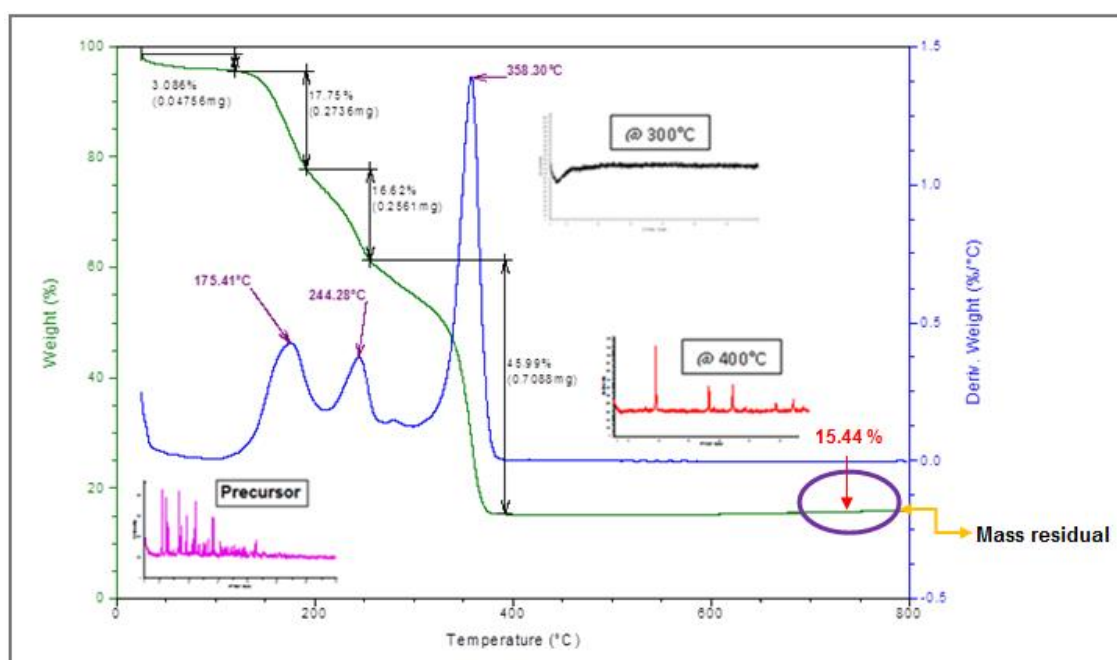
Figure 4.2: TGA curve of Li$_{1.03}$Mg$_{0.2}$Mn$_{1.77}$O$_4$ in citric acid.

Similar to the previous sample the following thermal reaction equation (4.2) could be considered.

Reaction equation

$1.03Li(C_2H_3OO) + 0.16Mg(C_2H_3OO)_2 + 1.77Mn(C_2H_3OO)_2 + 0.92C_6H_8O_7 + 14.68O_2 \rightarrow$
$Li_{1.03}Mg_{0.2}Mn_{1.77}O_4 + 15.27CO_2 + 11H_2O$ 4.2
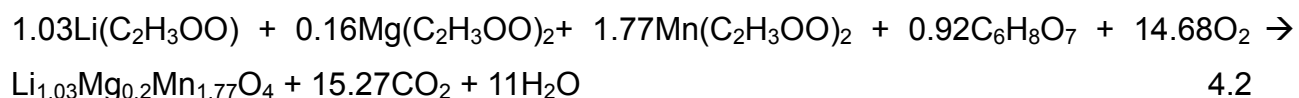
This would give a theoretical mass loss of about 76 % or a residual (product) of 23.79%, when compared to the TGA mass loss curve of 81 % (excluding water).

For the $Li_{1.03}Mg_{0.2}Mn_{1.77}O_4$ sample, the TGA mass loss curve together with the derivative weight curve (Figure 4.2) showed multiple decomposition steps that took place upon heating the material. A 3.1 % weight loss was observed below 100 °C that would relate to some residual water left within the precursor sample. The 2nd and 3rd smaller weight loss decompositions of about 18 % and 17 % were observed around 175 °C and 244 °C (from the derivative weight curve) respectively. This would relate to the loss of the crystalline material whereby the citrate precursor phase would convert into an amorphous phase. This was shown by PXRD patterns of a sample that was heated to 300 °C only. Heating the sample further to 360 °C, another decomposition step occurred with a major weight loss of 46 %. This would relate to the complete decomposition of any acetate precursors that would result in a crystalline material corresponding to the typical lithiated manganese oxide spinel structure. The sample was further heated to 800 °C with little or no change in the respective weight loss on the TGA curve. By comparison, the final formed oxide accounted for about 15 % of the final material when compared to the original precursor.

These TGA results were similar to literature reported results[11]. Suryakala et al.[11] showed a 1st decomposition of about 15 % between 150 to 200 °C, a 2nd decomposition of about 55 % between 200 to 400 °C and a residual of about 30 %. The slight differences could be accounted for the slightly lower Mn ratio (0.5:1.5, Mg to Mn) used. There were also slight differences in the respective decomposition temperatures, and the reported residual weight losses. These slight differences could be due to the differences in precursor preparation conditions.
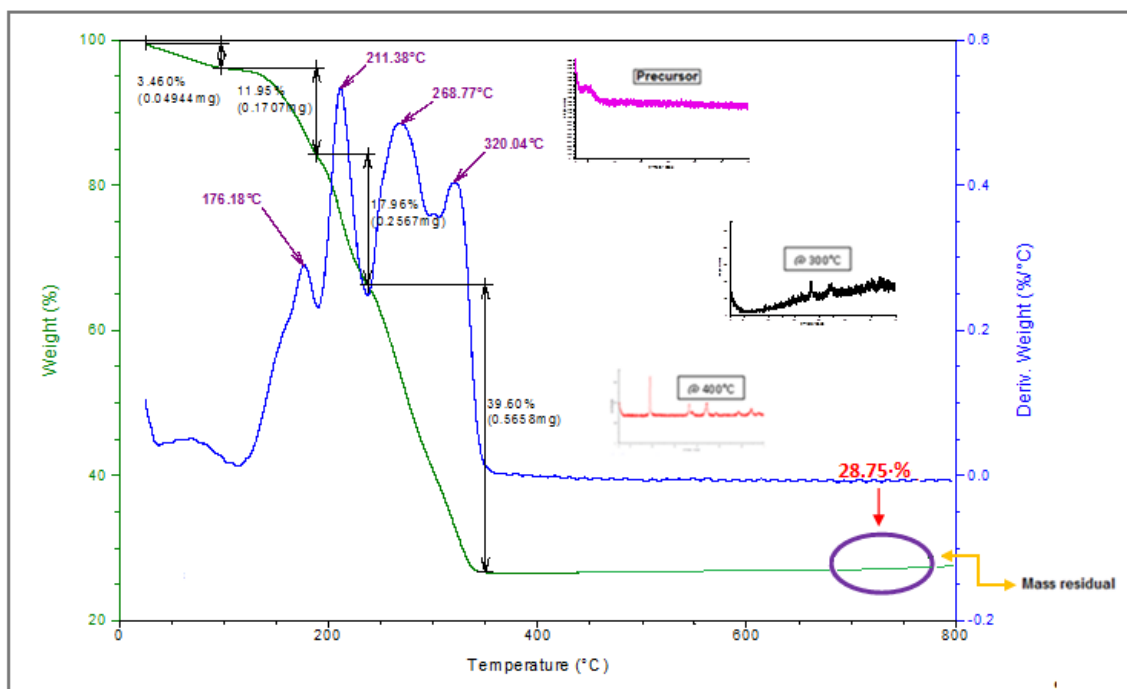
Figure 4.3: TGA curve of $LiNi_{0.5}Mn_{1.5}O_4$ in citric acid.

<u>*Reaction equation*</u>

$1.05Li(C_2H_3OO) + 0.48Ni(C_2H_3OO)_2 + 1.45Mn(C_2H_3OO)_2 + 0.92C_6H_8O_7 + 14.71O_2 \rightarrow LiNi_{0.5}Mn_{1.5}O_4 + 15.31CO_2 + 11.03H_2O$ 4.3
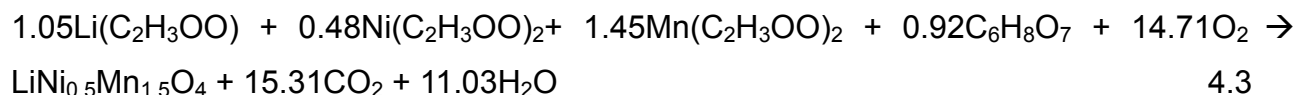
The results showed that the theoretical mass loss should be about 69 %, whereas the TGA mass loss curve showed a mass loss of about 68 % (excluding the water loss).

The TGA curve and the derivative weight curve for the Ni doped lithium manganese precursor showed multiple decomposition steps that were similar to the Mg doped sample (Figure 4.2). A notable difference in the TGA curves between the two samples was that the final decomposition peak was comparatively lower in temperature for the Ni doped sample. The first relatively small decomposition peaks was at about 176 °C, followed by a 2nd decomposition peak at 211 °C (from the derivative weight curve). The 3rd and 4th peaks were 268 °C and 320 °C respectively. The corresponding PXRD pattern of the sample that was heated to 300 °C only, showed the formation of some crystalline phase, when comparing the diffraction pattern to that of the precursor material, which was amorphous in

character. These small peaks could correspond to the MnO_2-Mn_2O_3 intermediate phase. At 400 °C (from the derivative weight and TGA curves) no further weight losses were observed and the PXRD pattern also showed no further significant material phase changes of the room temperature analyzed samples. The diffraction patterns would correspond to the typical Ni doped lithiated manganese oxide spinel structure[12]. In this case, the final cathode oxide material was about 29 % by weight comparison of the starting material.
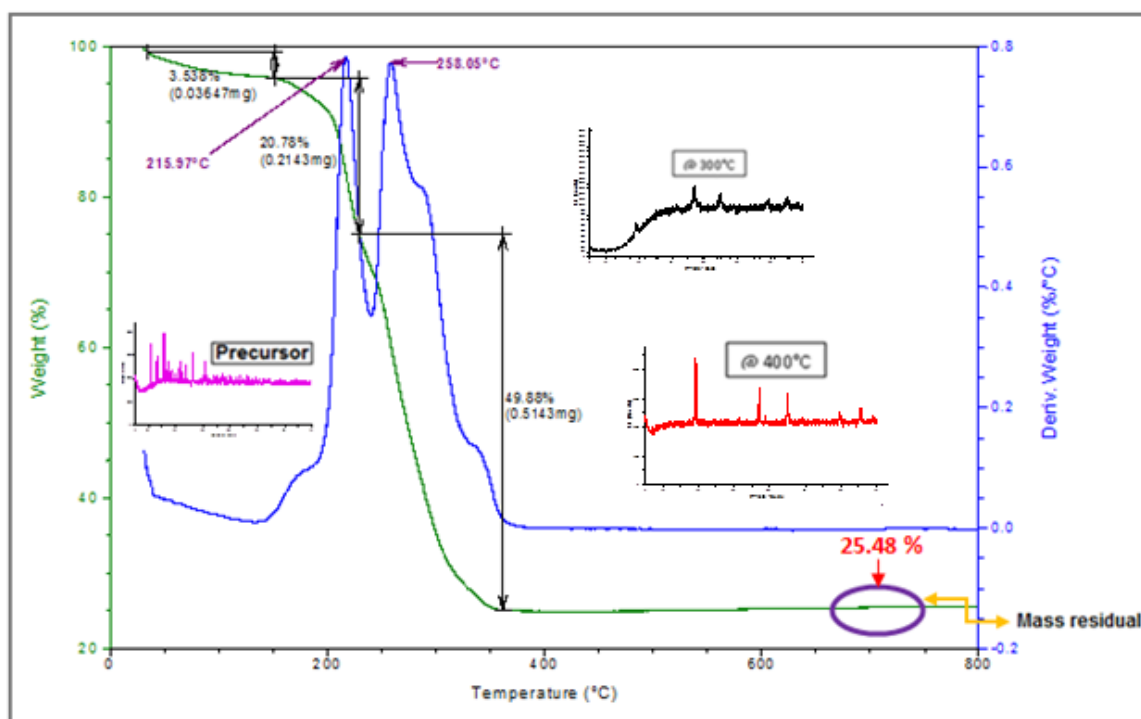
Figure 4.4: TGA curve of $LiCo_{1.09}Mn_{0.91}O_4$ in citric acid.

Reaction equation

$Li(C_2H_3OO)$ + $1.09Co(C_2H_3OO)_2$+ $0.92Mn(C_2H_3OO)_2$ + $1.01C_6H_8O_7$ + $15.23O_2$ →
$LiCo_{1.09}Mn_{0.91}O_4$ + $16CO_2$ + $11.57H_2O$ 4.4
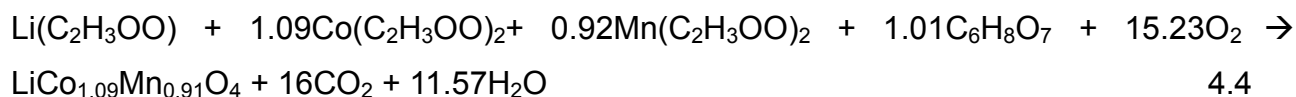
This gives a theoretical mass loss of about 70 % or a residual (product) of 30.25 % when compared to the TGA mass loss curve of 25.48 %.

The TGA curve and the derivative weight curve for the Co doped lithium manganese precursor showed again multiple decompositions (Figure 4.4) that were similar to the previous two samples. The initial 4 % weight loss below 150 °C could be ascribed to some residual water that was left in the precursor sample. There were two distinct decomposition peaks at 216 °C and 258 °C respectively (from the derivative weight curve). Notably in the sample, the decomposition temperatures were slightly lower than the previous doped samples. The crystalline precursor initially decomposed into another phase before 300 °C (which will be discussed in greater detail under Section 4.3 where the in-situ PXRD of the material was studied). The decomposition would be typically attributed to the loss and decomposition of the citrate and acetate in the sample material. Only by heating the sample to 300 °C and higher, the material formed the typical spinel crystalline material.

The Co doped TGA results were similar to those reported in literature[13, 14]. Huang *et al.*[13] showed a 1st decomposition of about 15 % between 130 to 200 °C, a 2nd decomposition of about 40 % between 270 to 380 °C and a residual of about 45 %. Whereas, Amdouni *et al.*[14] observed a 1st decomposition of about 10 % below 250 °C, a 2nd decomposition of 65.4 % at about 300 °C with a residual of about 30 %. The differences (such as the slight shift in decomposition temperature and weight loss compared) could relate to the variation in differences in metal-ion ratios used (0.16:1.84 and 0.4:1.6, Co to Mn, for Huang *et al.*[13] and Amdouni *et al.*[14] respectively), chelating agent (Huang *et al.*[13] made use of oxalic acid) and precursor preparation (solid state coordination method[13]).
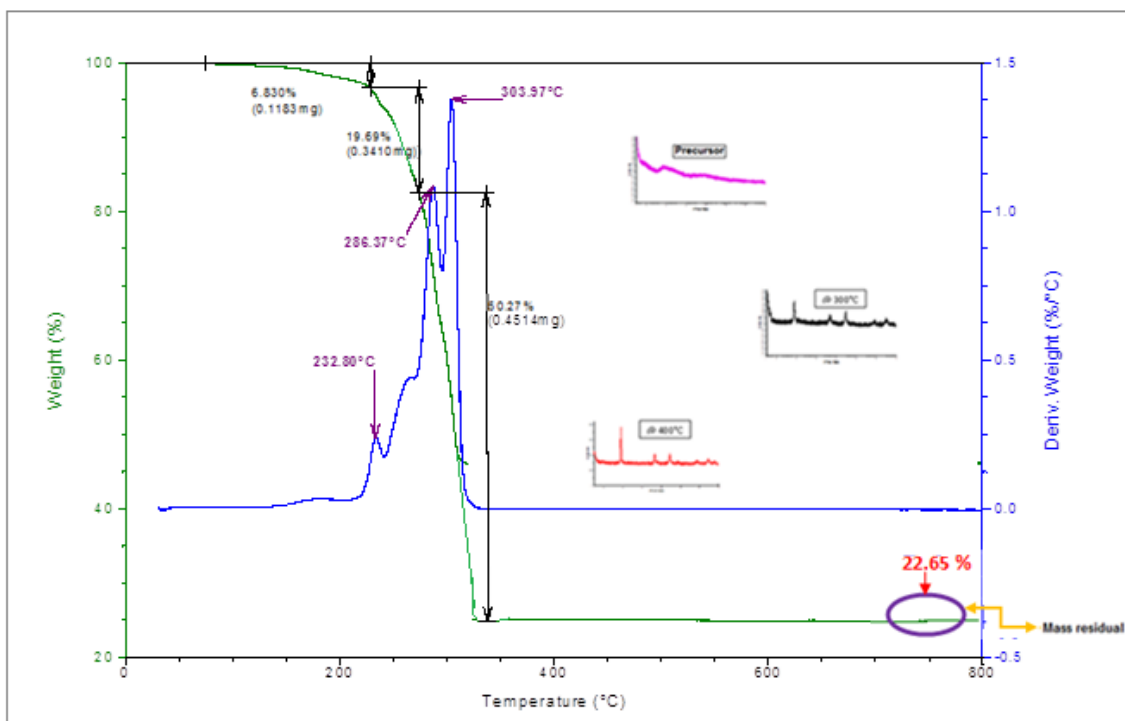
Figure 4.5: TGA curve of $LiAl_{0.4}Mn_{1.6}O_4$ in citric acid.

Reaction equation

$1.05Li(C_2H_3OO) + 0.37Al(C_2H_3OO)_3 + 1.55Mn(C_2H_3OO)_2 + 0.92C_6H_8O_7 + 15.31O_2 \rightarrow LiAl_{0.4}Mn_{1.6}O_4 + 16CO_2 + 11.55H_2O$ 4.5
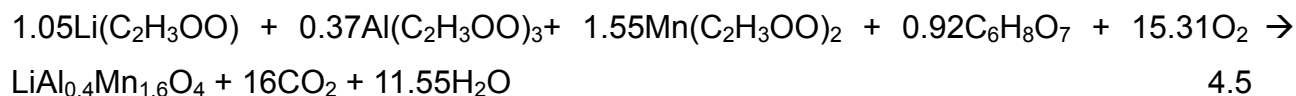
This would give a theoretical mass loss of about 76 % or a residual (product) of 24.19 % when compared to the TGA mass loss curve of 22.65 %.

For the $LiAl_{0.4}Mn_{1.6}O_4$ sample, the TGA curve (Figure 4.5) showed multiple decomposition steps during heating together with the occurrence of multiple-phase changes that were observed from their respective PXRD analysis. The TGA curve showed a water mass loss of 6 % below 200 °C. Within these results the derivative weight curve showed a double peak at 290 and 300 °C with weight losses of 20 and 50 % respectively, relating to complete acetate decomposition and the formation of a slightly incomplete final crystalline phase. At 400 °C and above no weight loss was observed, concluding that the final pure oxide phase was obtained, this also correlated well to the PXRD analysis done on these

samples that are shown as inserted patterns on the TGA curve. The final product would account for only 23 % by mass when compared to the initial starting material.

The TGA results within this study were similar to the literature results reported[15]. Bao *et al.*[15] showed a 1st decomposition of about 9.5 % around 141 °C, a 2nd decomposition of about 9.6 % around 213 °C, a 3rd decomposition of 49.9 % around 300 °C and a residual of about 30 %. The slight difference between these two results (in this study and that of literature) could be due to variations in Al to Mn ratio (0.1:1.9) and the use of Al-nitrate instead of Al-acetate (which was used in this study).

The results of the TGA decomposition curves of the cathode precursor material's decomposition process and phase changes prepared in citric acid (Figure 4.1 to 4.5) showed that there were similar trends in that most of the decomposition process would have occurred below 400 °C. Notably, there were distinctively different decomposition patterns below 400 °C for the various doped materials when compared to the standard lithium manganese oxide spinel material ($Li_{1.03}Mn_{1.97}O_4$). The cathode materials that contained metal dopants all showed multiple decomposition steps with some of them showing multiple phase changes at the different temperatures which were confirmed by obtaining a PXRD pattern of the material that was heated to just below the indicated temperatures (see inserts in Figures 4.2 to 4.5). A more detailed in-situ temperature phase transition study of the different materials will be discussed in Section 4.3.

Table 4.2 summarizes the calculated theoretical weight loss and the actual experimental residual weight loss for the various oxide materials studied.

Table 4.2: Summary on actual and theoretical residual weight loss.

Sample	Residual weight (%) [from TGA graph]	Theoretical residual weight (%) from decomposition reaction equations 4.1-4.5
$Li_{1.03}Mn_{1.97}O_4$	31.44	30.70
$Li_{1.03}Mg_{0.2}Mn_{1.77}O_4$	15.44	23.79
$LiNi_{0.5}Mn_{1.5}O_4$	28.75	31.46
$LiCo_{1.09}Mn_{0.91}O_4$	25.48	30.25
$LiAl_{0.4}Mn_{1.6}O_4$	22.65	24.19

Table 4.2 showed that $Li_{1.03}Mn_{1.97}O_4$ had a slightly higher experimental residue amount when compared to the other doped precursor materials. The undoped oxide material together with the nickel and cobalt doped materials obtained similar total decompositions (from its TGA graphs) of around 70 % and obtained higher experimental residual weights. This observation could be explained by the fact that the Ni and Co dopants had higher metal-ion ratios and the decomposition reaction was completed at approximately 350 °C (for Ni and Co) and approximately 300 °C (for undoped). Whereas the Mg and Al doped oxides produced a total decomposition of 80 %, due to a lower metal to manganese ion ratio and the decomposition reactions are completed either after 350 °C (for Mg dopant) or between 300 to 350 °C (for Al-dopant). Overall, the differences between the experimental and theoretical residual weight is of negligible error range (<10 %).

The following set of TGA studies, looked at the influence of different organic acids on the decomposition of the undoped manganese oxide spinel. Figures 4.6 to 4.8 represent the thermal gravimetric analysis of $Li_{1.03}Mn_{1.97}O_4$ that was synthesized using ascorbic, succinic and poly-acrylic acid respectively.
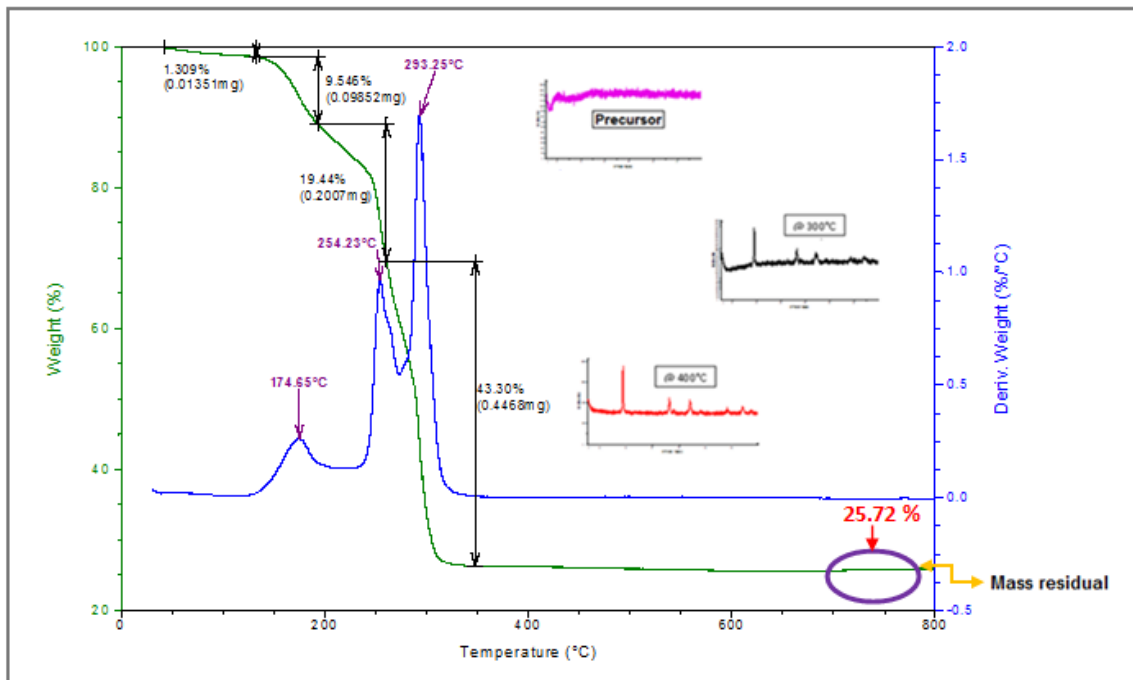
Figure 4.6: TGA curve of Li$_{1.03}$Mn$_{1.97}$O$_4$ in ascorbic acid.
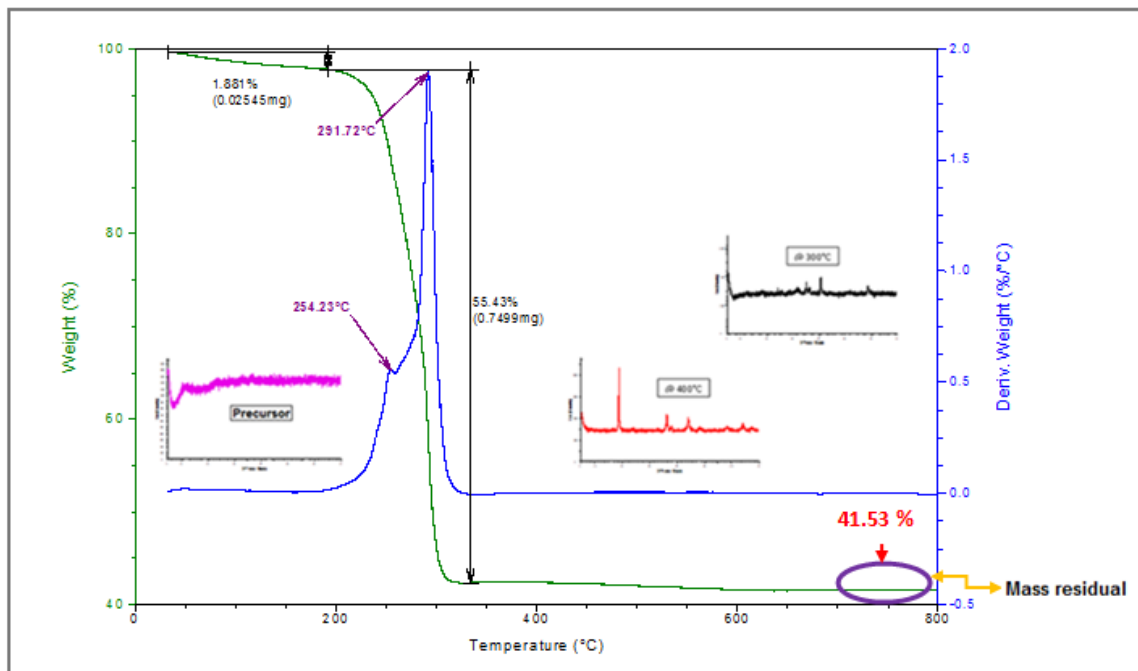
Figure 4.7: TGA curve of Li$_{1.03}$Mn$_{1.97}$O$_4$ in succinic acid.
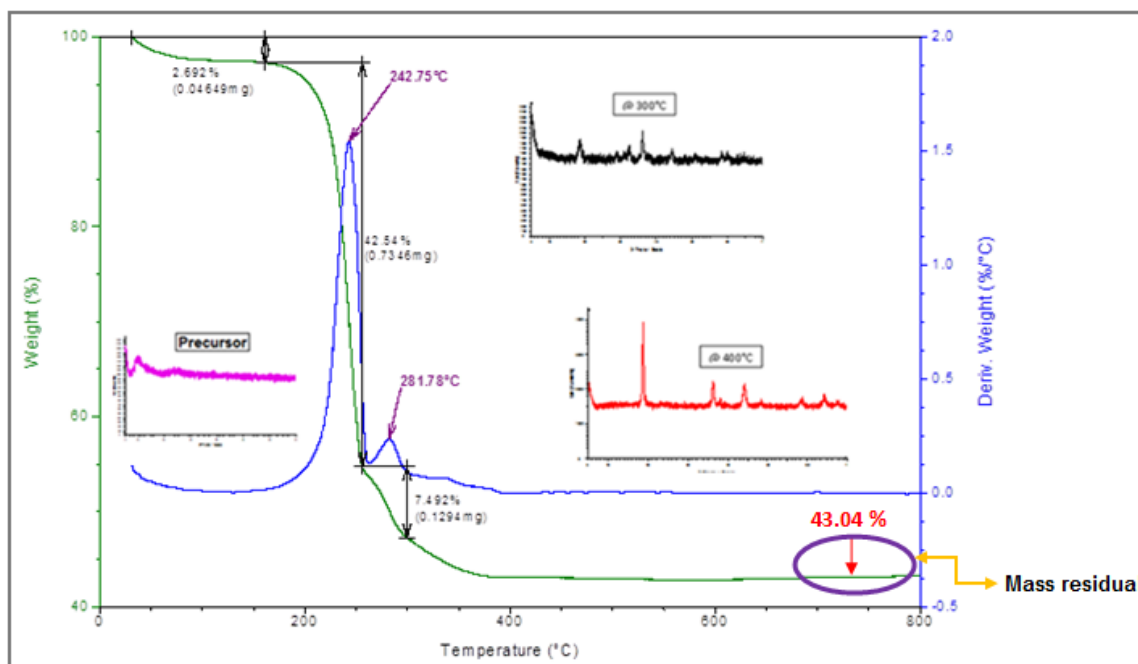
Figure 4.8: TGA curve of $Li_{1.03}Mn_{1.97}O_4$ in poly-acrylic acid.

The following thermal reaction equations would describe the processes observed for the undoped spinel material in various acids.

Reaction equation for $Li_{1.03}Mn_{1.97}O_4$ in ascorbic acid

$1.03Li(C_2H_3OO) + 1.97Mn(C_2H_3OO)_2 + C_6H_8O_7 + 15.66O_2 \rightarrow Li_{1.03}Mn_{1.97}O_4 + 15.9CO_2 + 11.45H_2O$
         4.6
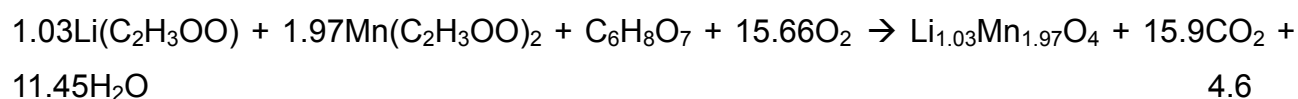
This gives a theoretical mass loss of about 75 % or a residue (product) of 24.69 % when compared to the TGA mass loss of about 73 % (excluding the water loss).

Reaction equation for $Li_{1.03}Mn_{1.97}O_4$ in succinic acid

$1.03Li(C_2H_3OO) + 1.97Mn(C_2H_3OO)_2 + C_4H_6O_4 + 14.19O_2 \rightarrow Li_{1.03}Mn_{1.97}O_4 + 13.93CO_2 + 10.45H_2O$
         4.7
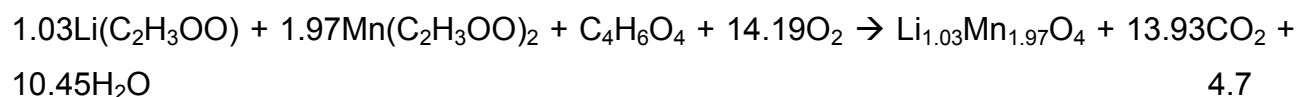
It should be noted that $Li_{1.03}Mn_{1.97}O_4$ in poly-acrylic acid was synthesized using the same weight quantities (for the chelating agent) as that of succinic acid, merely because n within the molecular formula (for poly-acrylic acid) is unknown.

Reaction equation for Li$_{1.03}$Mn$_{1.97}$O$_4$ in poly-acrylic acid

1.03Li(C$_2$H$_3$OO) + 1.97Mn(C$_2$H$_3$OO)$_2$ + (C$_3$H$_4$O$_2$)$_n$ + 14.19O$_2$ → Li$_{1.03}$Mn$_{1.97}$O$_4$ + 13.93CO$_2$ + 10.45H$_2$O   4.8
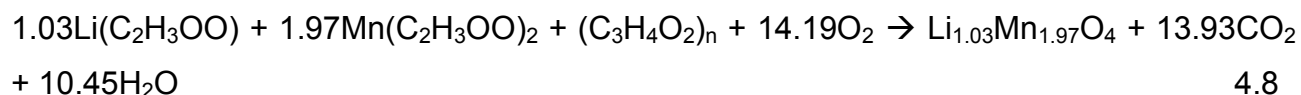
Although n is unknown (within the formula) the moles for CO_2 and H_2O (within the reaction equation) can be roughly calculated, if assuming, **n=4 (because it is a poly acid)**, the reaction equation would then be as follows:

1.03Li(C$_2$H$_3$OO) + 1.97Mn(C$_2$H$_3$OO)$_2$ + (C$_3$H$_4$O$_2$)$_n$ + 34.5O$_2$ → Li$_{1.03}$Mn$_{1.97}$O$_4$ + 18CO$_2$ + 12.5H$_2$O   4.9
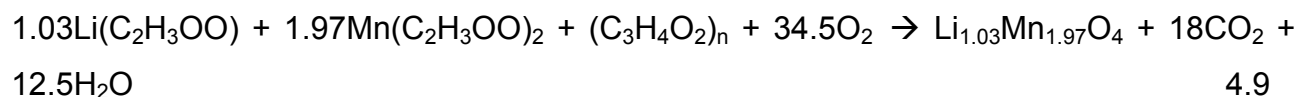
For both materials (Li$_{1.03}$Mn$_{1.97}$O$_4$ in succinic and poly-acrylic acids) a theoretical mass loss of 66 % or a residue (product) of 34.06 % was obtained when compared to the TGA mass loss curve of about 57 % (succinic acid) and 54 % (poly-acrylic acid) respectively excluding the water loss.

The TGA curves (Figures 4.6 to 4.8) for these materials showed an initial water weight loss of approximately 2 % below 150 °C. The precursor for Li$_{1.03}$Mn$_{1.97}$O$_4$ in ascorbic acid (Figure 4.6) was the only material that showed a typical three step weight loss change within the TGA and weight derivative curves compared to Li$_{1.03}$Mn$_{1.97}$O$_4$ synthesized in the other acids (citric, succinic and poly-acrylic acids). Figure 4.6 showed the first decomposition peak occurred at 175 °C and a final decomposition was obtained at 280 to 293 °C.

The precursor in poly-acrylic acid showed a large 1st decomposition step at 243 °C, followed by a smaller decomposition peak at about 282 °C. These results were similar to those reported by Sun *et al.*[16], whereby they reported weight losses between 60 to 230 °C and at 230 to 340 °C respectively. They also obtained a slightly smaller or lower residual of about 35 % compared to this study (43 %). The differences could be due to flow rate (5 °C.min^{-1}), acid ratio (1.67 molar ratio) and sample preparation; whereby Sun *et al.*[16] preheated the sample by vacuum drying at 80 °C before TGA was done.

$Li_{1.03}Mn_{1.97}O_4$ synthesized in succinic acid showed the main decomposition peak to be at 291 °C with a smaller preceding decomposition peak at 254 °C. Amdouni *et al.*[14] did a study on the synthesis of $LiCo_{0.4}Mn_{1.6}O_4$ with citric and succinic acids as chelating agents. From their results, they observed that the succinate material underwent a three decomposition step (below 200 °C, around 250 °C and between 250 to 350 °C) whereas the citrate material had only one decomposition step (between 200 to 300 °C). A similar trend was observed within this study whereby $Li_{1.03}Mn_{1.97}O_4$ synthesized in succinic acid obtained two decomposition steps and $Li_{1.03}Mn_{1.97}O_4$ synthesized in citric acid had one decomposition step.

These materials (Figures 4.6 to 4.8) all started off with an amorphous precursor which would then be converted into an impure intermediate phase at 300 °C and finally formed the crystalline spinel oxide at 400 °C and higher.

Table 4.3: Summary on the actual and theoretical residual weight for $Li_{1.03}Mn_{1.97}O_4$ in various acids.

Sample	Residual weight (%) [from TGA graph]	Theoretical residual weight (%) from decomposition reaction equations 4.6-4.8
$Li_{1.03}Mn_{1.97}O_4$ in citric acid	31.44	30.70
$Li_{1.03}Mn_{1.97}O_4$ in ascorbic acid	25.72	30.68
$Li_{1.03}Mn_{1.97}O_4$ in succinic acid	41.53	34.06
$Li_{1.03}Mn_{1.97}O_4$ in poly-acrylic acid	43.04	34.06

The results (Table 4.3) showed that $Li_{1.03}Mn_{1.97}O_4$ synthesized in ascorbic acid was the only material that observed a lower experimental residual weight loss in comparison to its theoretical weight loss. This could be reasoned by the fact that this material was the only material that produced three decomposition steps within its thermal gravimetric analysis compared to the other acids.

The thermogravimetric study of the precursor decomposition to the final spinel manganese based cathode material showed that the doped oxide materials formed its final product at a slightly higher temperature when compared to the undoped spinel oxide. This could be due to the fact that the doped materials were forming intermediate phase(s) (discussed in Section 4.3 in more detail). The results also showed that the thermal synthesis of the cathode material was already complete at temperatures around 400 °C for all the oxide materials studied and that there was no further thermal decomposition or mass loss of the material. However, this does not imply that the phases formed at this temperature would be ideally crystalline and necessarily electrochemically active. This will be discussed in more detail in Chapter 5.

4.2 <u>Powder x-ray diffraction</u>

Powder X-ray diffraction (PXRD) analysis were done on the various cathode oxide materials that were synthesized by using the sol-gel as the precursor to obtain the final oxide via the traditional "batch" sol-gel process and the spray-drying method, respectively. The samples made by the spray-drying technique were synthesized by using citric acid in the aqueous precursor only. The final spinel oxides that were synthesized by the batch sol-gel process were made from the precursor samples that were heated to 800 °C in air for 15 hours in a tube furnace using four different acids. These included citric, ascorbic, succinic and poly-acrylic acid respectively. The respective PXRD patterns were analysed for their levels of phase purity, their crystallite size and changes in lattice parameters.

The overlayed PXRD patterns of the $Li_{1.03}Mn_{1.97}O_4$ together with the doped metals ($Li_{1.03}Mg_{0.2}Mn_{1.77}O_4$, $LiAl_{0.4}Mn_{1.6}O_4$, $LiCo_{1.09}Mn_{0.91}O_4$, and $LiNi_{0.5}Mn_{1.5}O_4$) synthesized in various acids are shown in Figures 4.9 to 4.13. The patterns in each of the figures are shown by offsetting the actual raw data along the y-axis in order to provide for better visual comparison. Indexing (Table 4.4) of each spinel oxide was done and compared to the standard reference pattern obtained from the ICDD Powder Diffraction reference File (PDF).
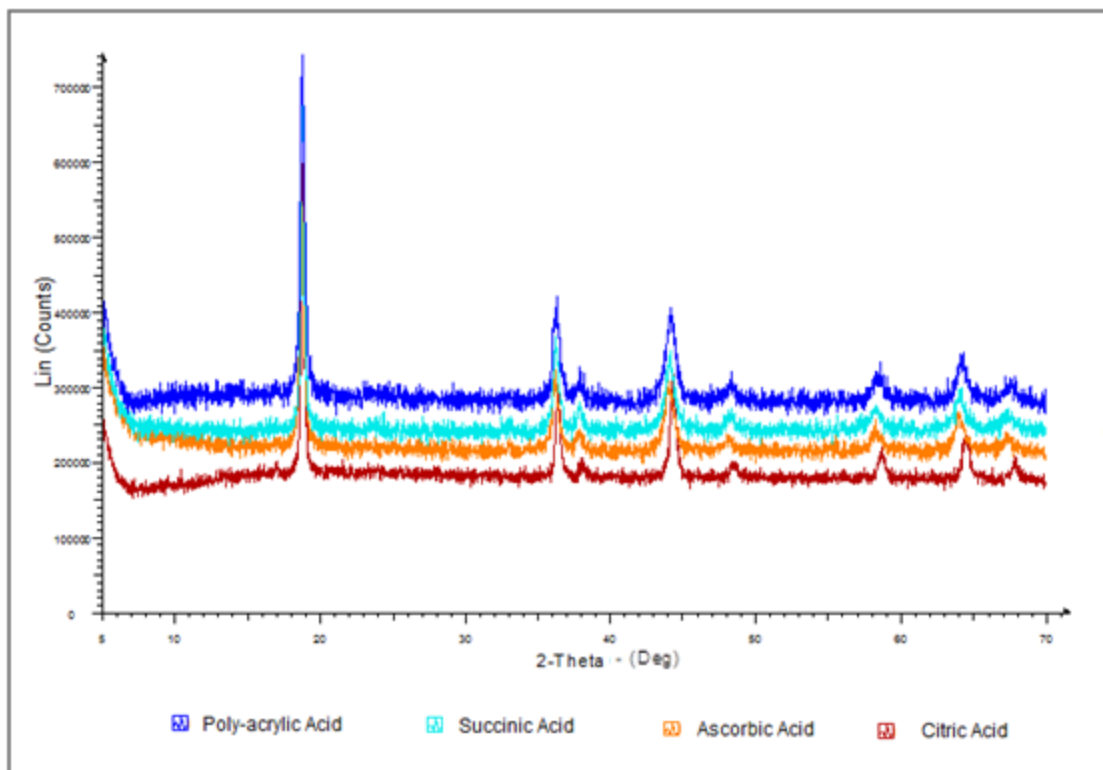
Figure 4.9: PXRD patterns of $Li_{1.03}Mn_{1.97}O_4$ in various acids.
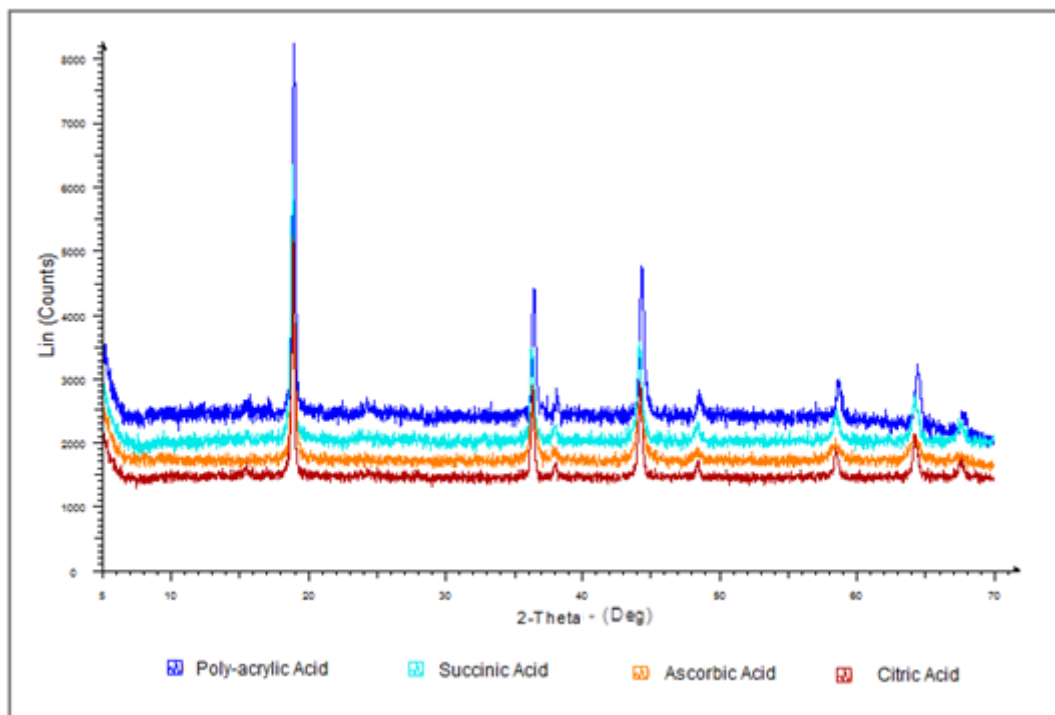
Figure 4.10: PXRD patterns of $Li_{1.03}Mg_{0.2}Mn_{1.77}O_4$ in various acids.
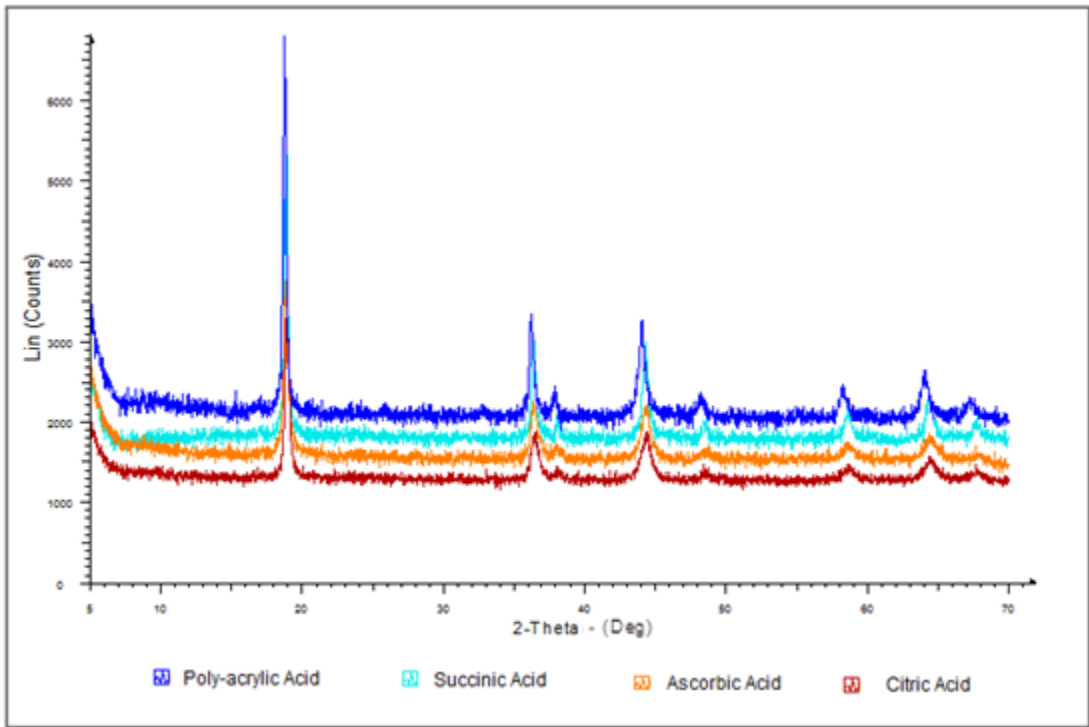
Figure 4.11: PXRD patterns of LiAl$_{0.4}$Mn$_{1.6}$O$_4$ in various acids.
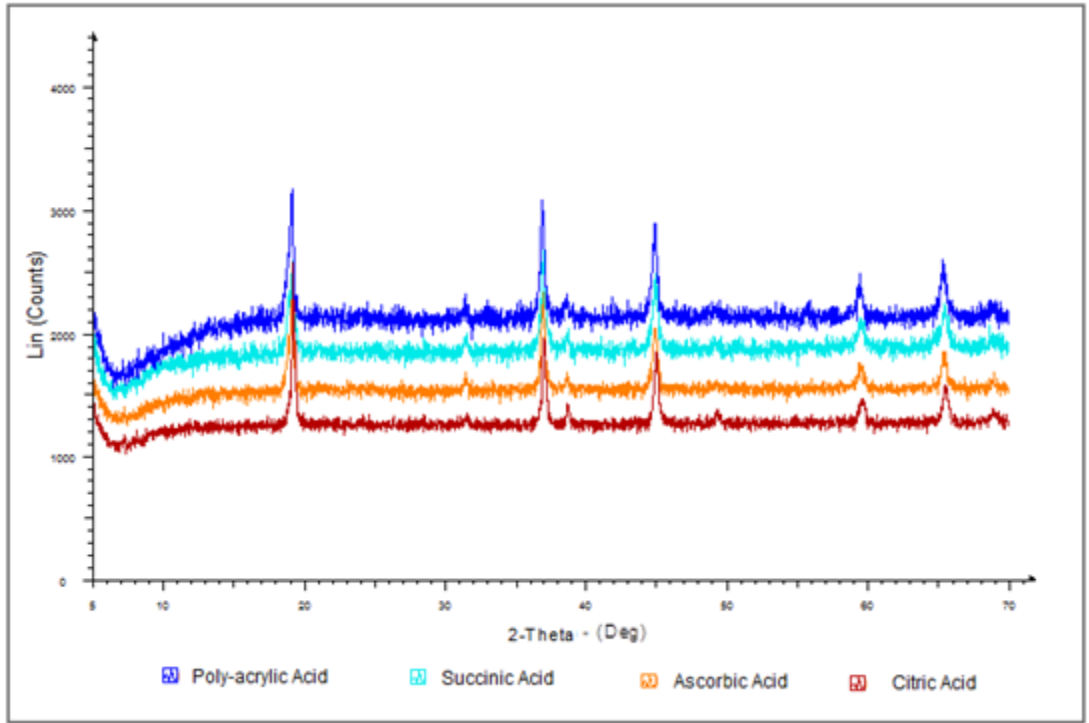
Figure 4.12: PXRD patterns of LiCo$_{1.09}$Mn$_{0.91}$O$_4$ in various acids.
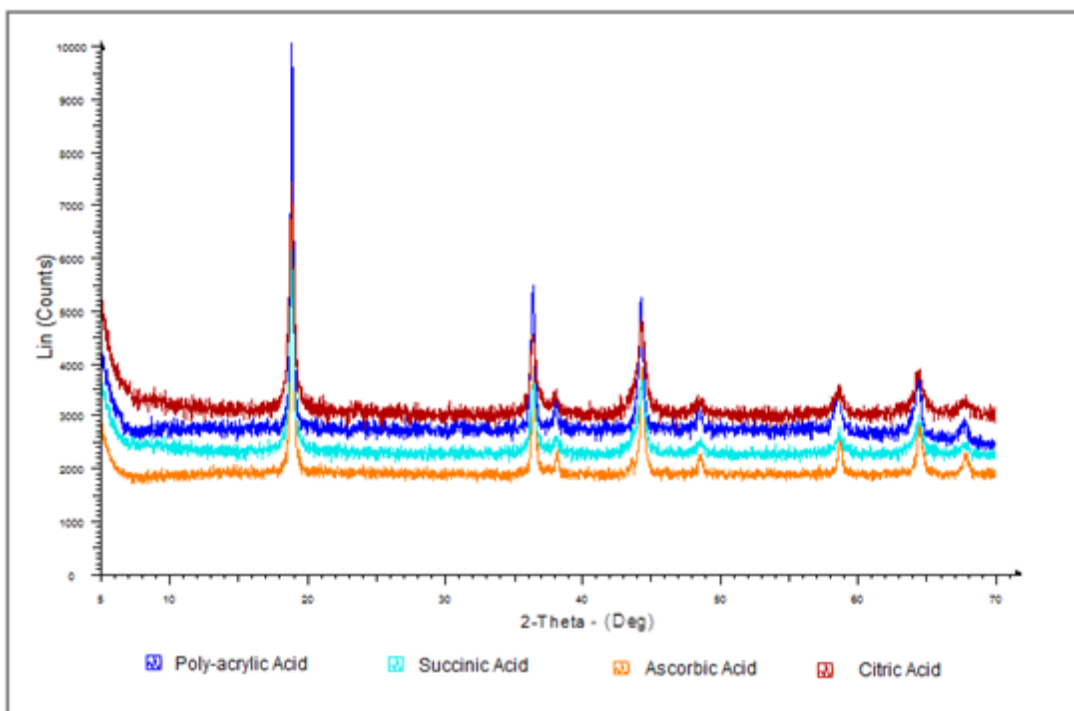
Figure 4.13: PXRD patterns of $LiNi_{0.5}Mn_{1.5}O_4$ in various acids.

Rietveld refinement was done on all the diffraction patterns that showed crystalline peaks allowing the respective lattice parameter (a) and the crystallite size parameter (LVol-IB) to refine. The background correction and zero offset was also allowed to refine. A summary of the refined data is shown in Table 4.5. All of the samples analyzed showed a relatively pure single phase of the cubic spinel structure with Fd3m as the space group. Within these structures Li-ions occupied the 8a sites, Mn and the other doped transition metal ions (Mg, Al, Co or Ni) occupied the 16d sites and the O-ions would occupy the 32e sites within the unit cell (see Figure 2.11). Within the Topas® refinement software, the site occupancy of the Mn-ion and the respective doped ion were set at the ratio 1-x and x respectively, where x would be the mole amount of the doped species in the sample.

The results of the cathode materials crystallite size (LVol–IB (nm)) and the lattice parameter (a (Å)) are summarized in Table 4.5. For all the samples analyzed by the Topas® Rietveld refinement software, the refinement parameter Rw which was an indication of the goodness of the refinement fit would vary between 2.3 and 3.1. The goodness of the refinement fit indicates the precision between the experimental data and

the calculated data and is also shown in Table 4.5 for completeness. Graphical representations of the results are shown in Figures 4.20 to 4.24 respectively.

Figure 4.14 and Table 4.4 show a typical result obtained from the Topas® Rietveld refinement software. Description of the various sub windows of the graphic user interphase of the software are shown within the figure.
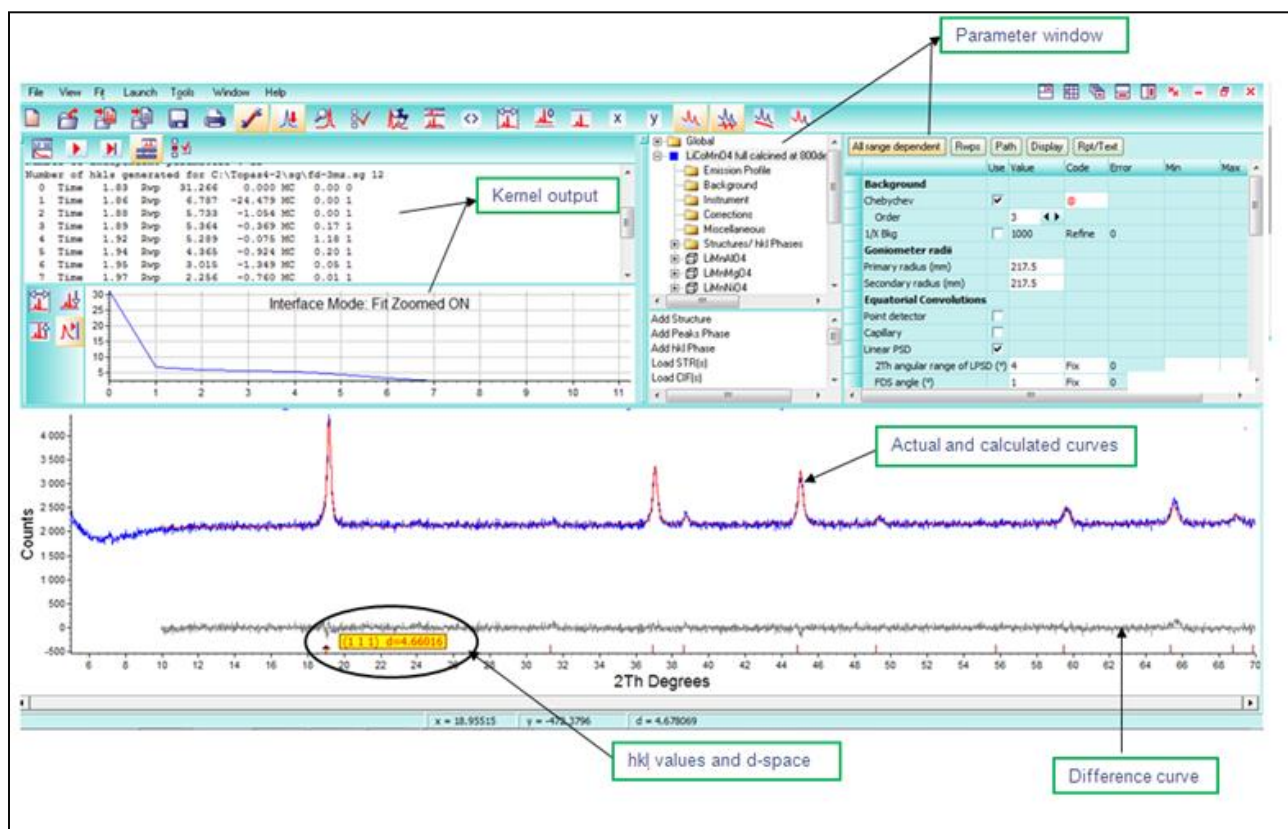
Figure 4.14: Typical example of Topas Rietveld refinement for LiCo$_{1.09}$Mn$_{0.91}$O$_4$.

Table 4.4: Summary of the unit cell d spacing and indexing (hkl) of the various oxide materials (in citric acid) synthesized by batch sol-gel process at 800 °C.

$Li_{1.03}Mn_{1.97}O_4$								
d	4.70	2.46	2.35	2.04	1.87	1.57	1.44	1.38
hkl	1 1 1	3 1 1	2 2 2	0 0 4	3 3 1	5 1 1/3 3 3	0 4 4	5 3 1

$Li_{1.03}Mg_{0.2}Mn_{1.77}O_4$								
d	4.73	2.47	2.36	2.05	1.88	1.58	1.45	1.38
hkl	1 1 1	3 1 1	2 2 2	0 0 4	3 3 1	5 1 1/3 3 3	0 4 4	5 3 1

$LiAl_{0.4}Mn_{1.6}O_4$								
d	4.71	2.46	2.36	2.04	1.87	1.57	1.44	1.36
hkl	1 1 1	3 1 1	2 2 2	0 0 4	3 3 1	5 1 1/3 3 3	0 4 4	5 3 1

$LiNi_{0.5}Mn_{1.5}O_4$								
d	4.71	2.46	2.35	2.04	1.87	1.57	1.44	1.38
hkl	1 1 1	3 1 1	2 2 2	0 0 4	3 3 1	5 1 1/3 3 3	0 4 4	5 3 1

$LiCo_{1.09}Mn_{0.91}O_4$									
d	4.66	2.85	2.43	2.33	2.02	1.85	1.55	1.43	1.36
hkl	1 1 1	0 2 2	3 1 1	2 2 2	0 0 4	3 3 1	5 1 1/ 3 3 3	0 4 4	5 3 1
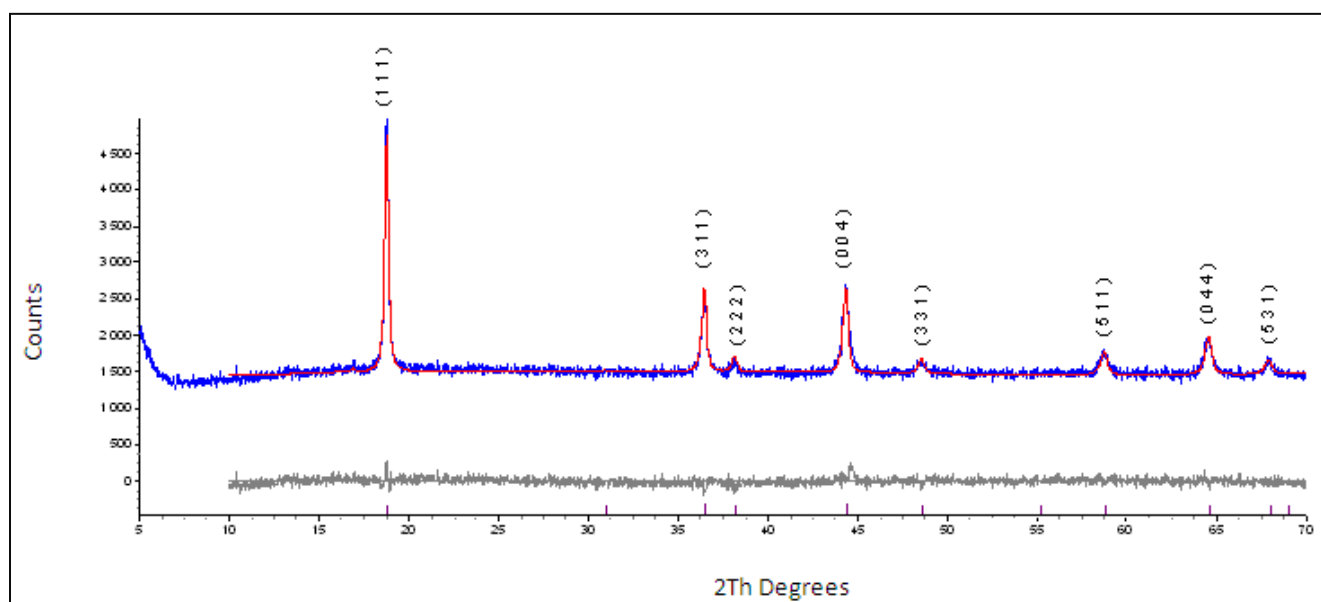
Figure 4.15: Topas Rietveld refined PXRD spectrum of $Li_{1.03}Mn_{1.97}O_4$ synthesized by sol-gel batch process at 800 °C.
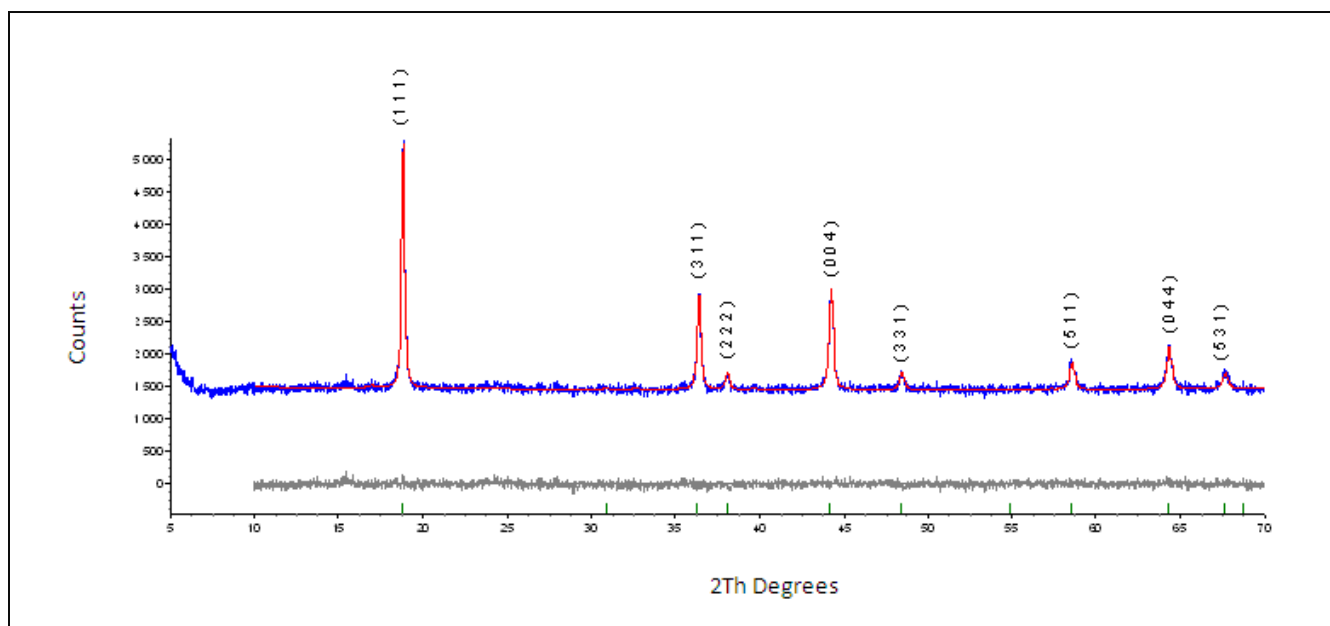
Figure 4.16: Topas Rietveld refined PXRD spectrum of $Li_{1.03}Mg_{0.2}Mn_{1.77}O_4$ synthesized by sol-gel batch process at 800 °C.
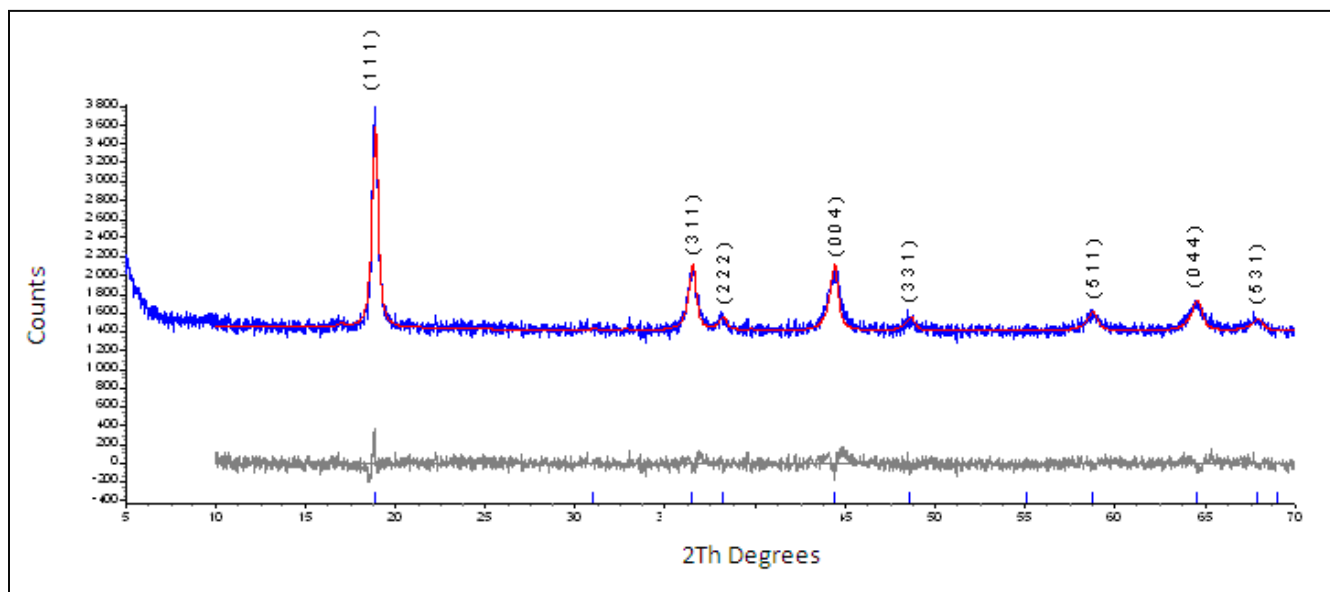
Figure 4.17: Topas Rietveld refined PXRD spectrum of $LiAl_{0.4}Mn_{1.6}O_4$ synthesized by sol-gel batch process at 800 °C.
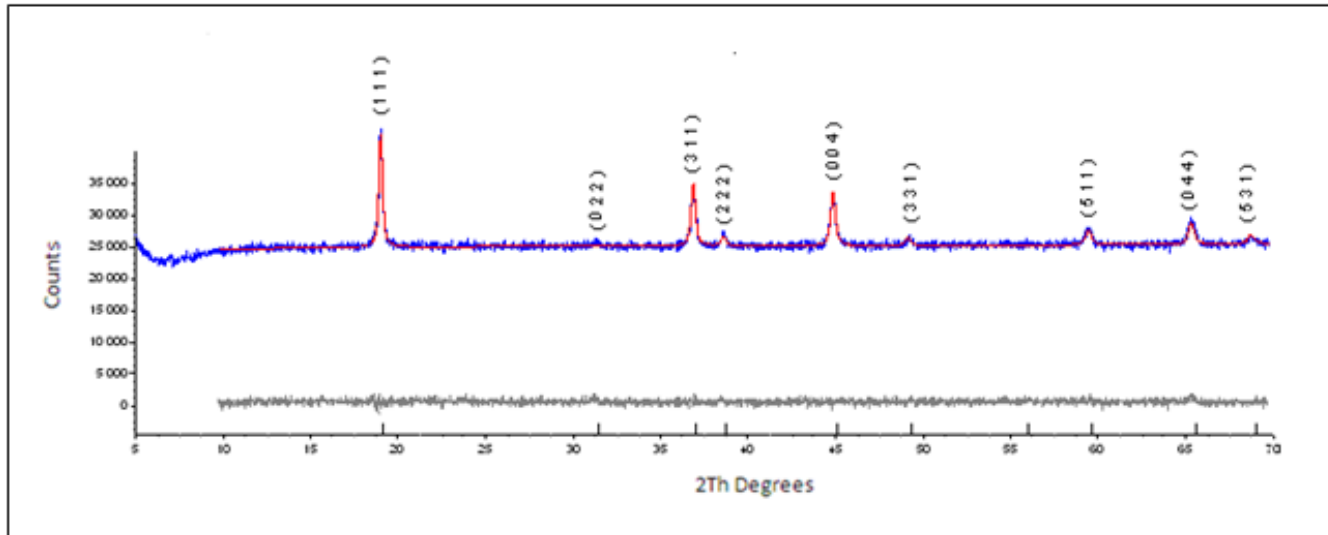
Figure 4.18: Topas Rietveld refined PXRD spectrum of LiCo$_{1.09}$Mn$_{0.91}$O$_4$ synthesized by sol-gel batch process at 800 °C.
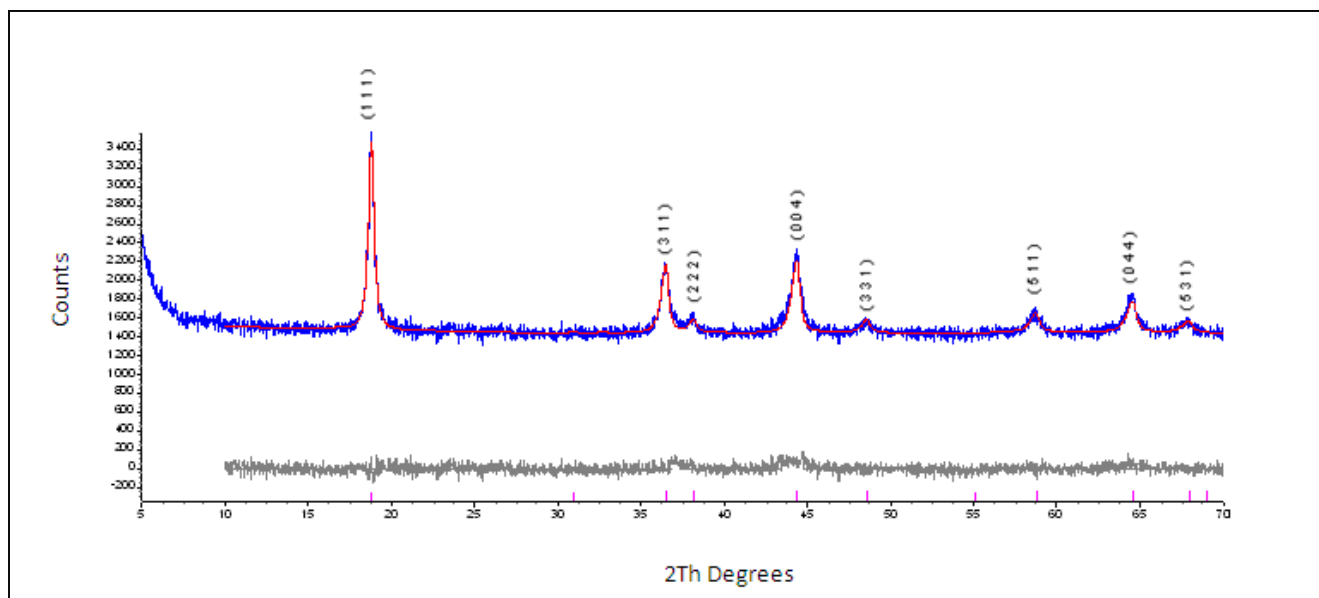
Figure 4.19: Topas Rietveld refined PXRD spectrum of LiNi$_{0.5}$Mn$_{1.5}$O$_4$ synthesized by sol-gel batch process at 800 °C.

The PXRD results showed that the $LiCo_{1.09}Mn_{0.91}O_4$ spinel material showed a slightly smaller unit cell when compared to the other spinel materials studied. The slightly higher background diffraction observed in the Co doped materials would be due to the fluorescence of Co that occurs when using Cu X-ray radiation (Figures 4.12 and 4.18).

The calculated lattice parameter (Table 4.5) for the various oxide spinel materials (in citric acid) varied slightly when compared to literature reported results. On average, the lattice parameters results in this study were slightly lower when compared to the values reported in literature. These variations could be explained by the slight experimental error of the sample loading in the sample holder and slight changes within the average oxidation state of manganese, causing deviations in the materials composition.

Table 4.5: Rietveld refinement results on samples prepared by the batch sol-gel process (800 °C).

$Li_{1.03}Mn_{1.97}O_4$	Citric acid	Succinic acid	Poly-acrylic acid	Ascorbic acid	Average (Std deviation)
LVol - IB (nm)	33.984	30.774	21.54	21.403	
a (Å) - experimental	8.201	8.206	8.179	8.199	8.196 (0.012)
Rw(GoF)	3.03 (1.19)	3.10 (1.19)	2.85 (1.13)	2.82 (1.11)	
a (Å) - literature	8.23-8.24[2, 4, 16]				
$LiAl_{0.4}Mn_{1.6}O_4$	Citric acid	Succinic acid	Poly-acrylic acid	Ascorbic acid	Average (Std deviation)
LVol - IB (nm)	21.596	27.052	29.190	16.970	
a (Å) - experimental	8.159	8.171	8.206	8.145	8.170 (0.026)
Rw(GoF)	2.95 (1.14)	2.85 (1.10)	3.01 (1.16)	2.88 (1.10)	
a (Å) - literature	8.20[17]				
$LiNi_{0.5}Mn_{1.5}O_4$	Citric acid	Succinic acid	Poly-acrylic acid	Ascorbic acid	Average (Std deviation)
LVol - IB (nm)	18.117	22.06	43.167	35.065	
a (Å) - experimental	8.158	8.161	8.177	8.163	8.165 (0.008)
Rw(GoF)	2.86 (1.12)	2.85 (1.10)	3.03 (1.17)	3.15 (1.23)	
a (Å) - literature	8.18[18]				
$Li_{1.03}Mg_{0.2}Mn_{1.77}O_4$	Citric acid	Succinic acid	Poly-acrylic acid	Ascorbic acid	Average (Std deviation)
LVol - IB (nm)	43.157	30.976	38.471	23.179	
a (Å) - experimental	8.193	8.186	8.174	8.194	8.187 (0.009)
Rw(GoF)	2.69 (1.05)	2.72 (1.07)	3.04 (1.16)	2.86 (1.10)	
a (Å) - literature	8.22[4, 11]				
$LiCo_{1.09}Mn_{0.91}O_4$	Citric acid	Succinic acid	Poly-acrylic acid	Ascorbic acid	Average (Std deviation)
LVol - IB (nm)	28.564	15.511	18.038	20.867	
a (Å) - experimental	8.070	8.064	8.062	8.066	8.066 (0.003)
Rw(GoF)	2.48 (1.16)	2.43 (1.19)	2.41 (1.15)	2.35 (1.17)	
a (Å) - literature	8.06-8.07[6, 19]				

The following graphs (Figures 4.20 to 4.24) summarize and compared the Rietveld refinements lattice parameter, a (Å) and crystallite size, LVol-IB (nm) for the various spinel oxide materials which were synthesized in different chelating agents.
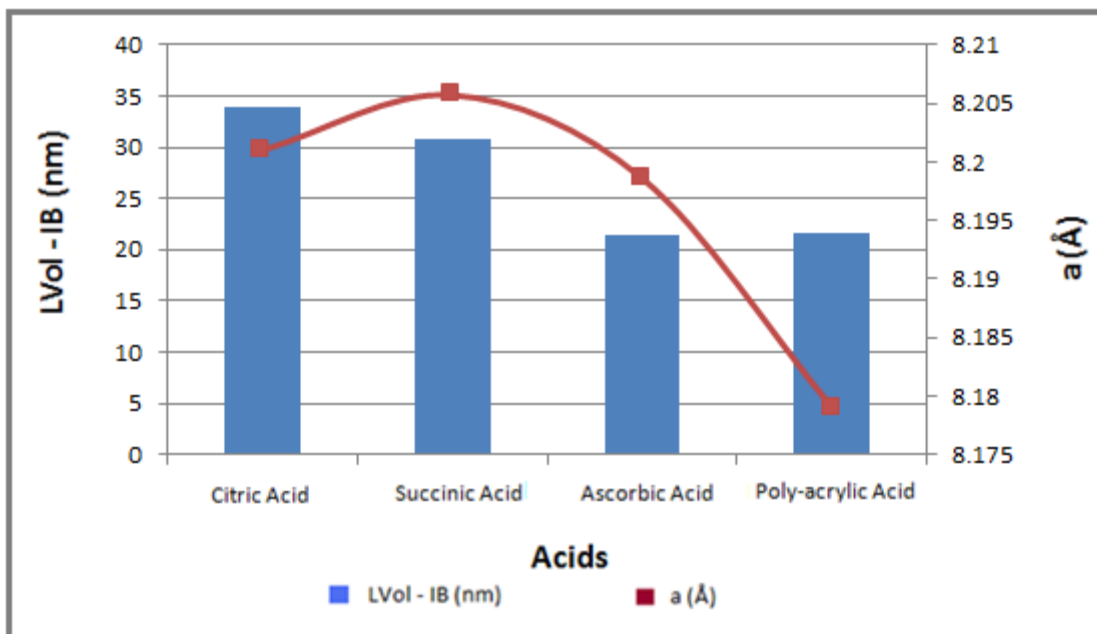
Figure 4.20: Comparison of the changes in lattice parameters and crystallite size for $Li_{1.03}Mn_{1.97}O_4$ in various acids using Rietveld refinement.
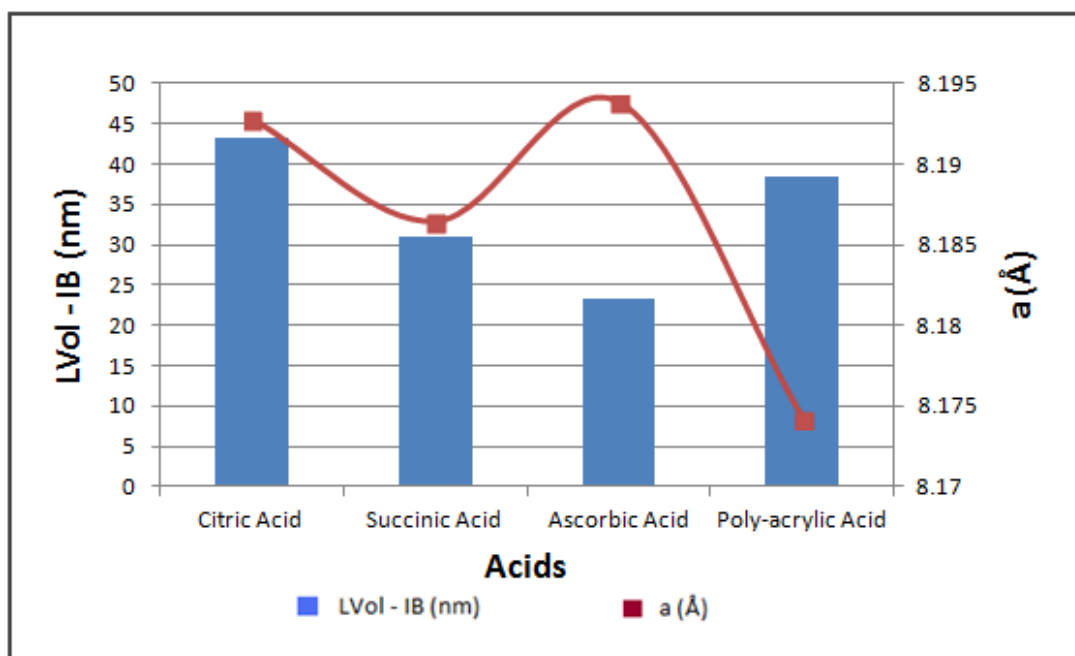
Figure 4.21: Comparison of the changes in lattice parameters and crystallite size for $Li_{1.03}Mg_{0.2}Mn_{1.77}O_4$ in various acids using Rietveld refinement.
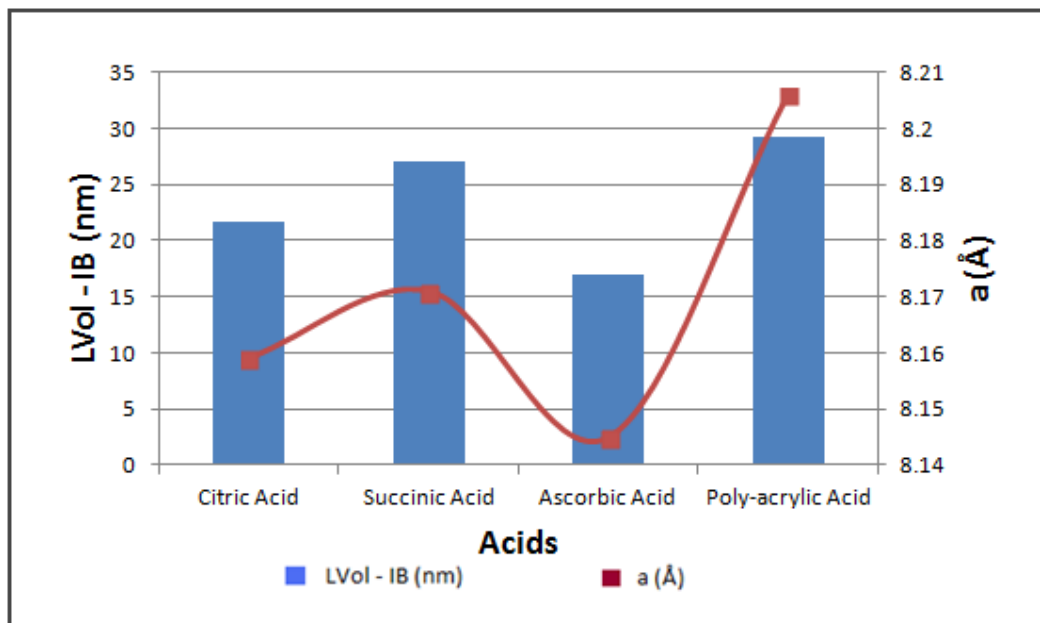
Figure 4.22: Comparison of the changes in lattice parameters and crystallite size for LiAl$_{0.4}$Mn$_{1.6}$O$_4$ in various acids using Rietveld refinement.
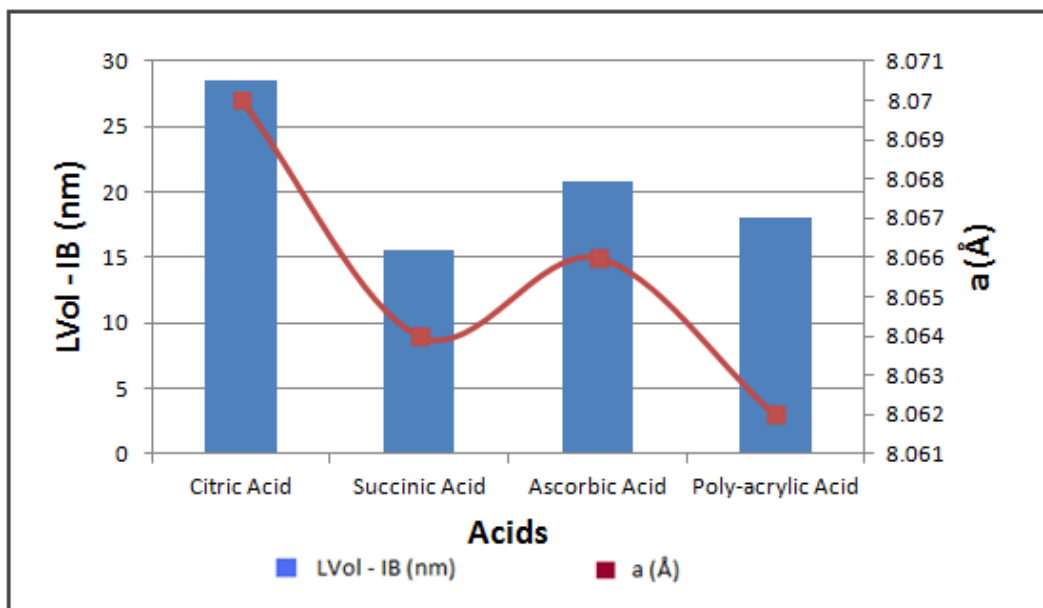
Figure 4.23: Comparison of the changes in lattice parameters and crystallite size for LiCo$_{1.09}$Mn$_{0.91}$O$_4$ in various acids using Rietveld refinement.
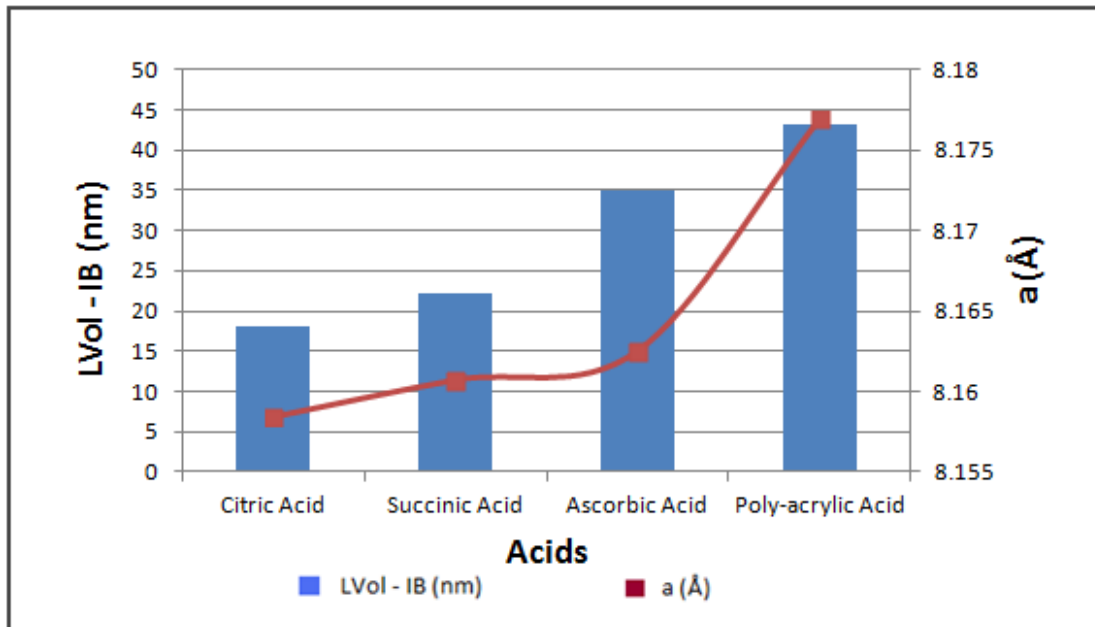
Figure 4.24: Comparison of the changes in lattice parameters and crystallite size for LiNi$_{0.5}$Mn$_{1.5}$O$_4$ in various acids using Rietveld refinement.

In summary (Figures 4.20 to 4.24), the results showed that there were only slight variations in the lattice parameter for one type of spinel oxide material that was made with different acids in the precursor material where the averages with their standard deviation are shown in Table 4.5. The respective lattice parameters of the Ni, Al and Mg doped spinels when compared to the undoped material (Table 4.5) were also similar in magnitude, whereas the spinel doped with the Co had a slightly smaller average lattice parameter. These results are similar to those reported by Huang *et al.*[6] that reported lattice parameters of the Co doped material to be 8.056 Å.

However, the type of acid used in the precursor had a slight influence on the determined crystallite size. For the Ni doped spinel material, the synthesis with citric acid seemed to have resulted in a cathode material with a slightly smaller crystallite size, whereas for Co, Mg and the undoped samples, with the citric acid resulted in a comparatively larger crystallite size. For the sample made with Al as the dopant in the spinel, the various organic acids in the precursor had little influence on the respective crystallite size.

Using the information from the TGA study and the preceding PXRD, the spray-drying technique was used to synthesize the following spinel cathode materials using only citric acid as the chelating reagent as was described in Section 3.1. The materials considered were: $Li_{1.03}Mn_{1.97}O_4$, $LiAl_{0.4}Mn_{1.6}O_4$, $Li_{1.03}Mg_{0.2}Mn_{1.77}O_4$, $LiCo_{1.09}Mn_{0.91}O_4$ and $LiNi_{0.5}Mn_{1.5}O_4$ respectively. The analysis was done at 400 °C, the lowest observable temperature from the TGA that showed the completion of the reaction and the resulting crystalline PXRD patterns are shown in Figures 4.25 to 4.29.
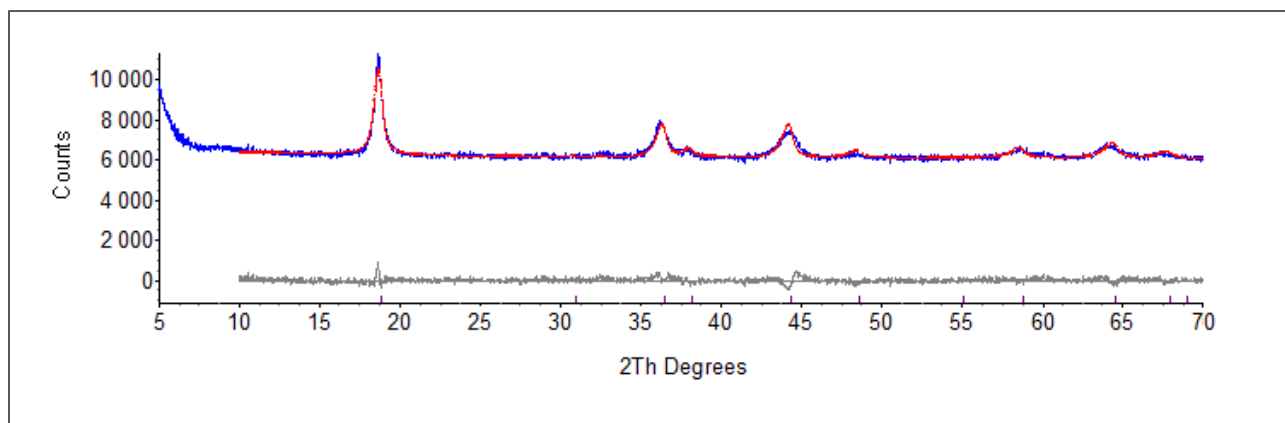
Figure 4.25: Topas Rietveld refined PXRD spectrum of $Li_{1.03}Mn_{1.97}O_4$ synthesized by spray-drying process at 400 °C.
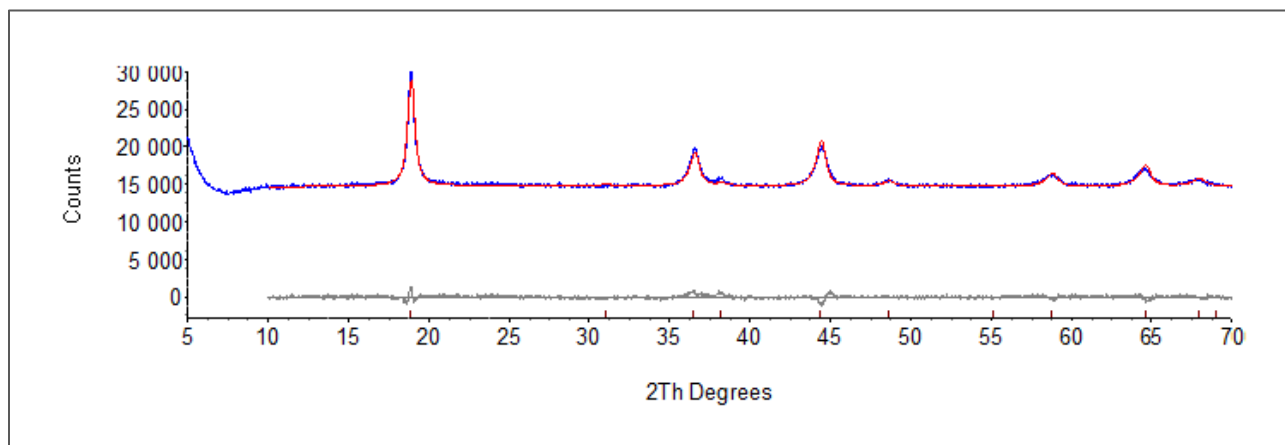
Figure 4.26: Topas Rietveld refined PXRD spectrum of $Li_{1.03}Mg_{0.2}Mn_{1.77}O_4$ synthesized by spray-drying process at 400 °C.
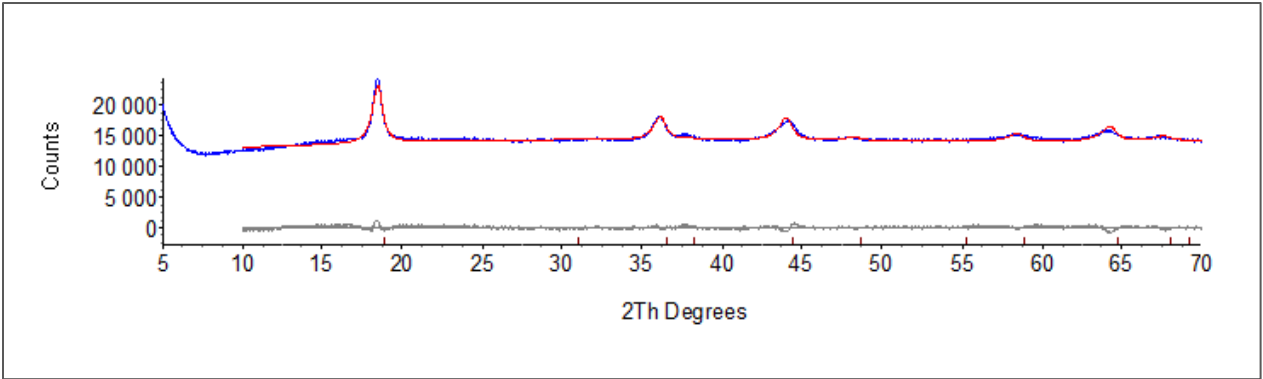
Figure 4.27: Topas Rietveld refined PXRD spectrum of LiAl$_{0.4}$Mn$_{1.6}$O$_4$ synthesized by spray-drying process at 400 °C.
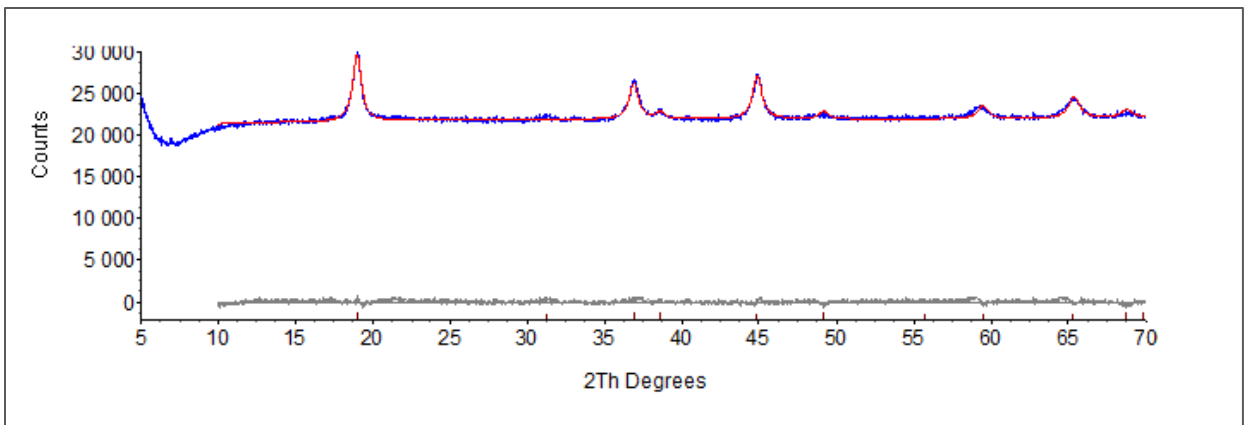
Figure 4.28: Topas Rietveld refined PXRD spectrum of LiCo$_{1.09}$Mn$_{0.91}$O$_4$ synthesized by spray-drying process at 400 °C.
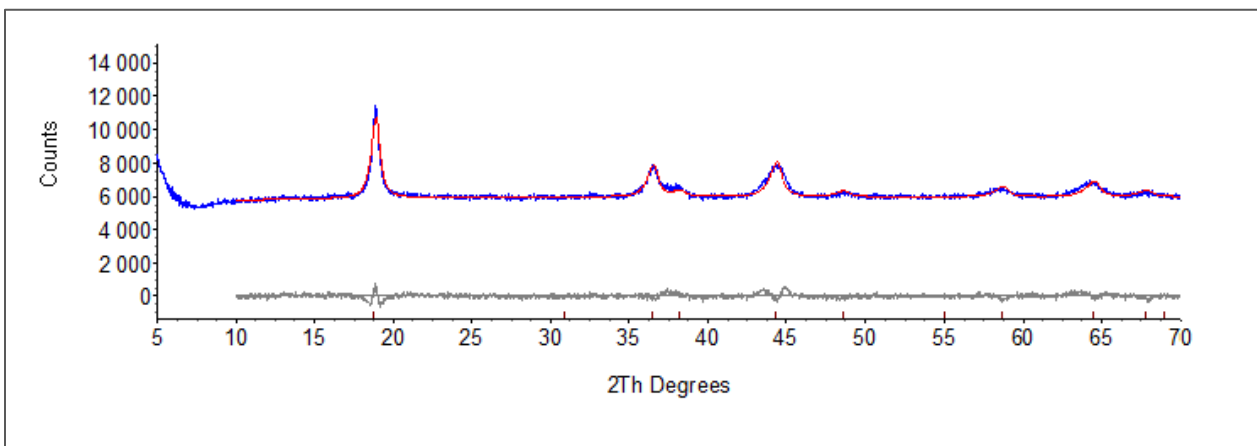
Figure 4.29: Topas Rietveld refined PXRD spectrum of LiNi$_{0.5}$Mn$_{1.5}$O$_4$ synthesized by spray-drying process at 400 °C.

The results showed that there were slight differences in the materials lattice parameters (a (Å)) between the batch process and spray pyrolysis method (Table 4.6). However, there were significant differences in the determined crystallite size (LVol–IB (nm)) of the same materials synthesized by the two different methods (Table 4.6 and Figure 4.30). For all the samples analysed by the Topas® Rietveld refinement software, the refinement parameter, Rw, which was an indication of the goodness of the refinement fit varied between 1.25 and 1.95 for the various diffraction patterns analysed. For comparison purposes, the BET surface area of the various samples studied are also shown.

Table 4.6: Rietveld refinement results on comparing batch with spray-drying process.

	Batch Process			Spray Process		
	LVol–IB (nm)	a (Å)	BET Surface area ($m^2.g^{-1}$)	LVol–IB (nm)	a (Å)	BET Surface area ($m^2.g^{-1}$)
$Li_{1.03}Mn_{1.97}O_4$	33.984	8.201	8.67	13.380	8.165	14.11
$LiAl_{0.4}Mn_{1.6}O_4$	21.596	8.159	18.15	9.379	8.144	29.80
$Li_{1.03}Mg_{0.2}Mn_{1.77}O_4$	43.157	8.193	9.68	12.726	8.161	19.91
$LiCo_{1.09}Mn_{0.91}O_4$	28.564	8.070	12.25	9.112	8.075	26.15
$LiNi_{0.5}Mn_{1.5}O_4$	18.117	8.159	6.12	11.228	8.166	19.48

The lattice parameter in Table 4.6 again showed very small differences between the doped and undoped spinel oxide materials. A decrease in lattice parameter for the doped material compare to the undoped material could possibly be a result from the oxidation of the larger Mn^{3+} ions (atomic radius of 0.72 Å) into smaller Mn^{4+} ions (atomic radius of 0.67 Å). This would then optimize the space occupation in the lattice through an increased degree of cation ordering in the 16d sites. Whereas, an increase in lattice parameter results from the doped metal-ion replacing Mn^{4+} that in turn results into an increased Mn^{3+} concentration. These lattice parameter differences would most probably also be due to experimental error.
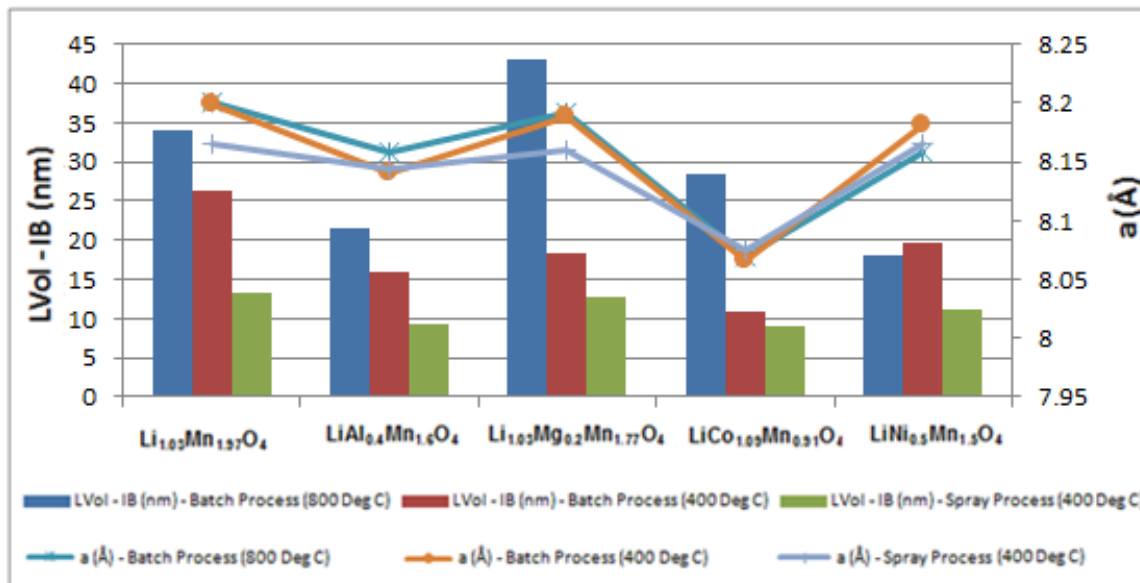
Figure 4.30: Comparison for $Li_{1.03}Mn_{1.97}O_4$ on Rietveld refinement results by various synthesis processes using citric acid only

The results showed that the materials synthesized by the spray-drying process produced particles that had significantly smaller crystallite sizes as determined by PXRD and larger surface areas when compared to the batch process materials. The results confirmed that spinel oxide materials can be made to have a finer crystallite size with a larger material surface area, thereby giving the possibility of improving the electrochemical performances of the material. Large surface areas are normally associated with Mn dissolution; therefore metal dopants are added to reduce this effect. Future work would be required to investigate Mn dissolution within these oxide materials, in order to observe the efficiency of the prepared oxide materials. A material with a larger surface area is an advantage in terms of the lithium-ion diffusion ability (electrochemical property), where a larger particle area would in principle allow for an easier movement for the lithium-ions, with a higher utilisation and possible higher rate.

A variable temperature study was also done on the batch synthesis cathode oxide materials ($Li_{1.03}Mn_{1.97}O_4$, $LiAl_{0.4}Mn_{1.6}O_4$, $Li_{1.03}Mg_{0.2}Mn_{1.77}O_4$, $LiCo_{1.09}Mn_{0.91}O_4$ and $LiNi_{0.5}Mn_{1.5}O_4$) in various acids (citric, ascorbic, succinic and poly-acrylic acids) respectively. The various phase changes that occur within a specific oxide material are

shown in Figures 4.31 to 4.50 together with its calculated Rietveld refinement results (Tables 4.7 to 4.11). The resepctive diffraction patterns within a group, were "off-set" along the y-axis on one graph for comparision purposes. This analysis started off with the precursor powder that was gradually heated from room temperature to 300 °C and further up to 600 °C over four hours. The precursor material was mounted onto a stainless steel PXRD sample holder and placed into a tube furnace with controlled temperature and time parameters. The sample would be heated up to 300 °C, over 1 hour, thereafter the sample holder containing the sample was removed from the furnace, allowed to cool and a room temperature PXRD analysis was then done. This process was repeated at 400, 500 and 600 °C. For comparison purposes, direct in-situ temperature PXRD was done on samples that were made using the citric acid precursor only.
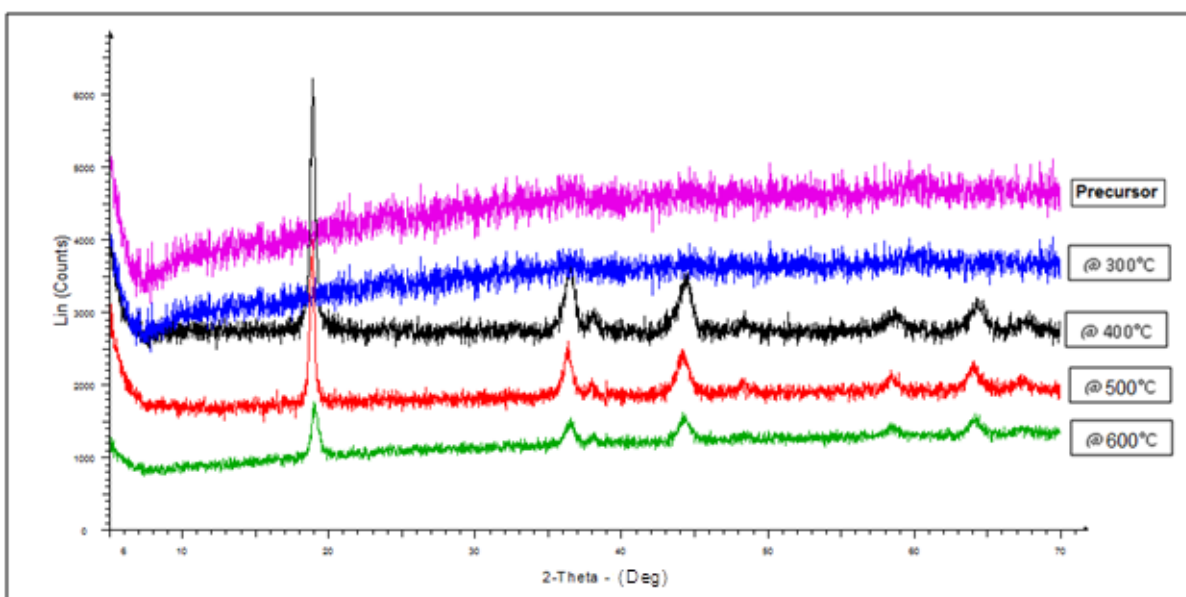
Figure 4.31: Typical PXRD patterns of the sample heated to various temperatures for Li$_{1.03}$Mn$_{1.97}$O$_4$ in citric acid.

The results (Figure 4.31) showed that the material underwent a single phase change from the amorphous precursor to a crystalline phase between 300 to 400 °C and above. The final phase corresponded to the typical spinel oxide of Li$_{1.03}$Mn$_{1.97}$O$_4$. The results from this study correlated reasonably well with the in-situ temperature PXRD study (discussed in

Section 4.3). A difference observed was that of an impure intermediate phase (relating to Mn_2O_3) for some of the samples at 250 to 350 °C from the in-situ results (Figures 4.51 and 4.42) which was not visible in Figure 4.31. This could be due to the heating time used between sample analysis. The in-situ PXRD technique sampled every 50 °C producing PXRD patterns in shorter time intervals (35 min). Whereas the furnace variable temperature study sampled after every 100 °C over longer time periods (1 hour). However, the final metal oxide materials were similar in characterisitcs once heated to the final temperature of 600 °C for both techniques (furance variable temperature and in-situ PXRD). Another difference to observe between these two techniques is that at a specific temperature the analysis (following the in-situ method) was allowed to be kept isothermal producing a PXRD pattern, being a true reflection of the materials' characterization at that temperature. However, the furnace variable temperature study allowed the sample holder (with the sample) to first cool down before the PXRD pattern was produced, therefore, slight changes to the materials' characterization is possible to occur.
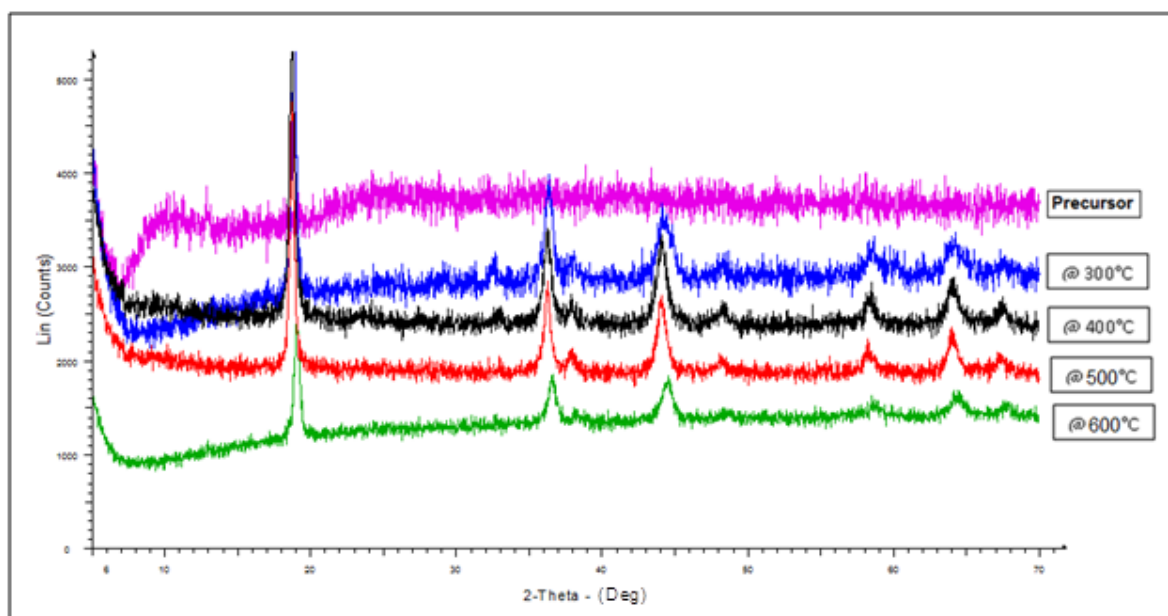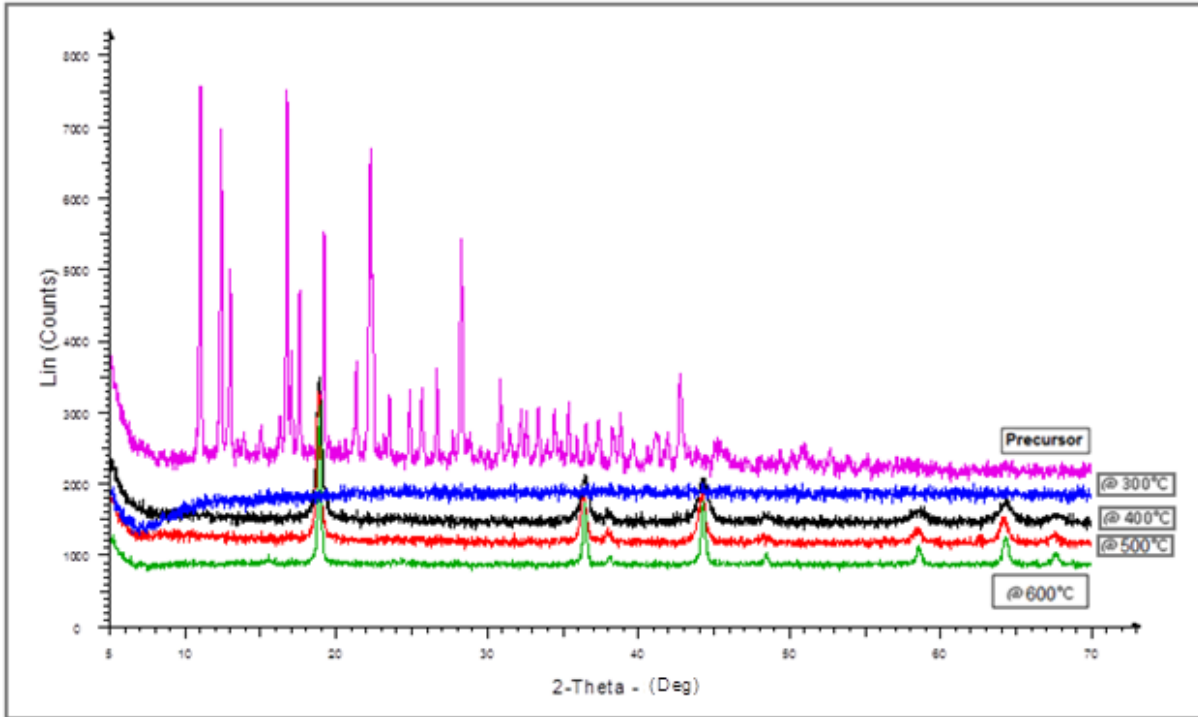

Figure 4.32: Typical PXRD patterns of the sample heated to various temperatures for $Li_{1.03}Mn_{1.97}O_4$ in ascorbic acid.
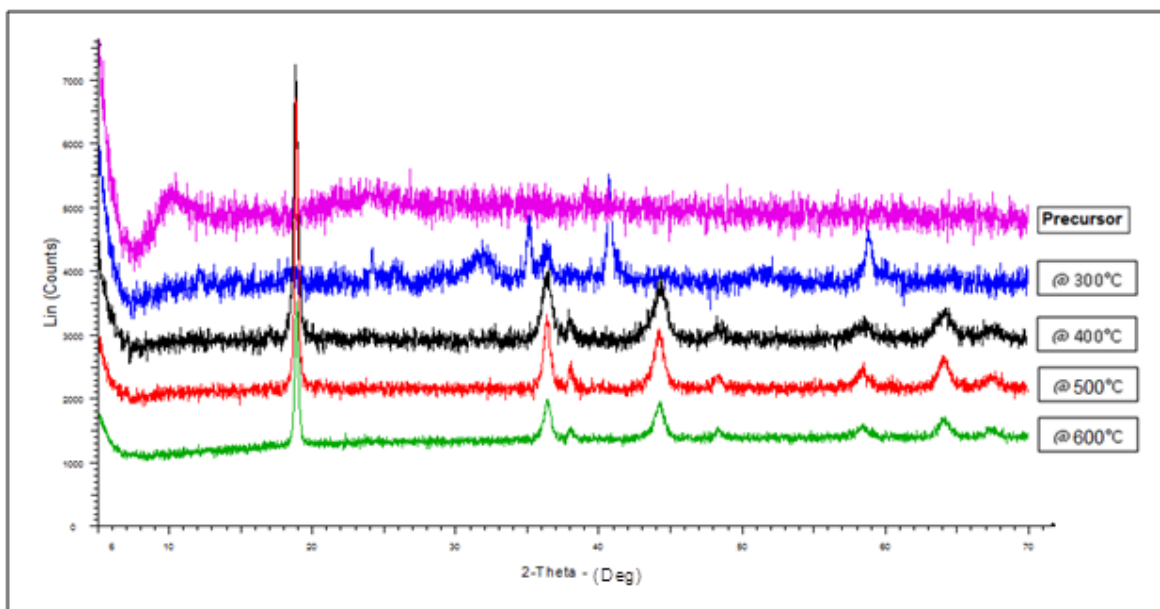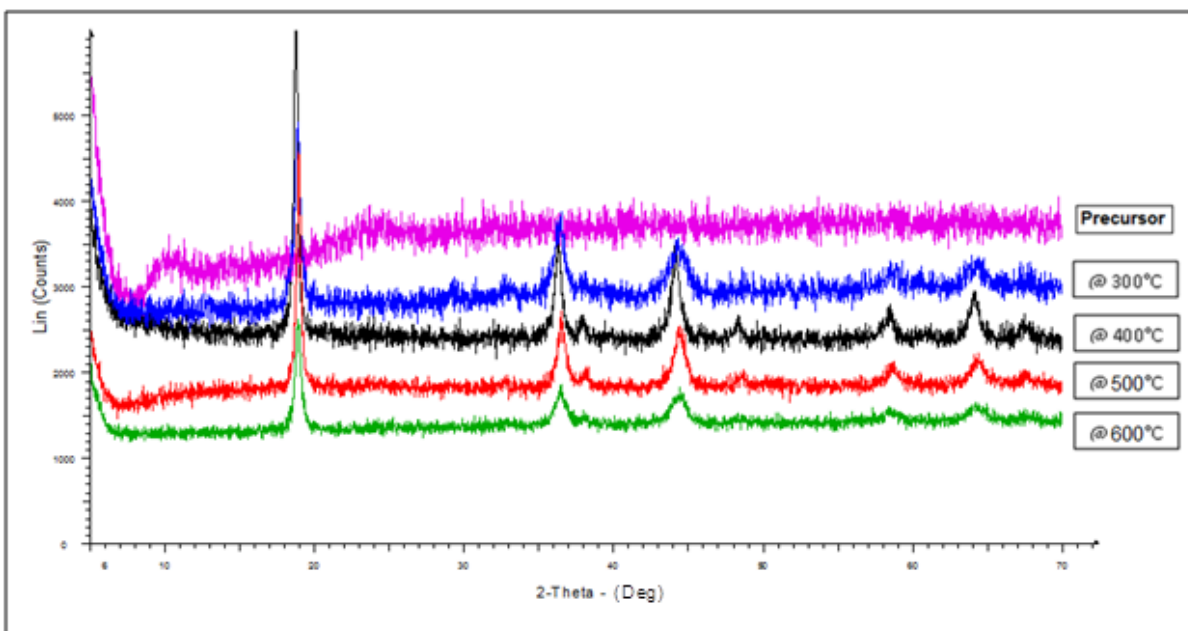
Figure 4.33: Typical PXRD patterns of the sample heated to various temperatures for Li$_{1.03}$Mn$_{1.97}$O$_4$ in succinic acid.
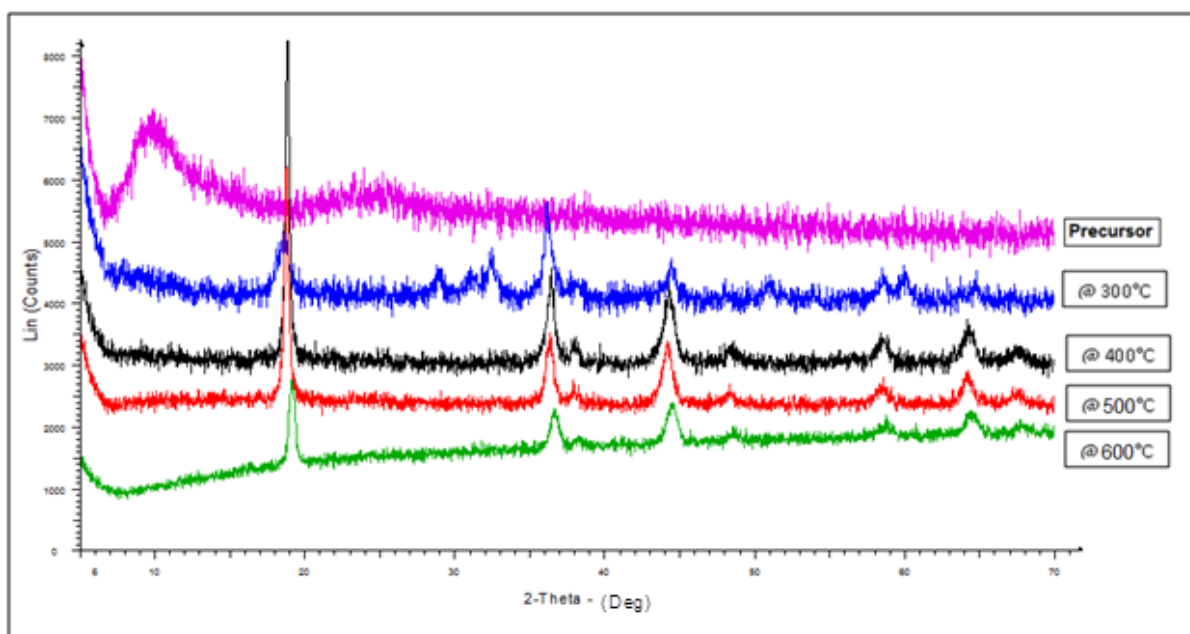
Figure 4.34: Typical PXRD patterns of the sample heated to various temperatures for Li$_{1.03}$Mn$_{1.97}$O$_4$ in poly-acrylic acid.

The spinel oxide materials summarized in Figures 4.32 to 4.34 are a representation of studying the phase changes that occur when thermally synthesizing Li$_{1.03}$Mn$_{1.97}$O$_4$ using various chelating acids. The results showed that the materials had an amorphous

precursor phase that when heated up to 300 °C would form an intermediate crystalline phase, which can be related to manganese oxide (Mn_2O_3) (for the material synthesized in ascorbic and succinic acids); whereas when the material was synthesized in poly-acrylic acid the occurrence of an alpha-MnO_2 and gamma-Mn_2O_3 intermediate phase would be shown. These intermediate trends that occurred at different temperatures were also observed in the respective TGA results (Figure 4.8). Thereafter, upon further heating the materials to 400 °C the pure spinel oxide phase was observed for all the materials studied.

Table 4.7 summarizes the calculated Rietveld refinement results for $Li_{1.03}Mn_{1.97}O_4$ synthesized in various acids (citric, succinic, ascorbic and poly-acrylic acids) at 400, 500 and 600 °C.

Table 4.7: Rietveld refinement results of $Li_{1.03}Mn_{1.97}O_4$ prepared in various acids by batch sol-gel process under different temperature conditions.

$Li_{1.03}Mn_{1.97}O_4$	Citric acid		
	400 °C	**500 °C**	**600 °C**
LVol - IB (nm)	19.222	22.090	28.094
a (Å) - experimental	8.179	8.201	8.210
Rw(GoF)	2.90 (1.13)	3.07 (1.15)	2.99 (1.16)
a (Å) - literature	8.23-8.24[2, 4, 16]		
	Succinic acid		
LVol - IB (nm)	24.560	29.717	31.070
a (Å) - experimental	8.168	8.185	8.205
Rw(GoF)	3.18 (1.24)	3.13 (1.24)	3.16 (1.17)
	Poly-acrylic acid		
LVol - IB (nm)	27.085	29.026	34.221
a (Å) - experimental	8.170	8.187	8.206
Rw(GoF)	2.99 (1.17)	2.94 (1.16)	2.78 (1.10)
	Ascorbic acid		
LVol - IB (nm)	14.625	16.851	19.670
a (Å) - experimental	8.167	8.194	8.209
Rw(GoF)	2.72 (1.08)	2.64 (1.05)	2.78 (1.10)

Figure 4.35: Typical PXRD patterns of the sample heated to various temperatures for $Li_{1.03}Mg_{0.2}Mn_{1.77}O_4$ in citric acid.
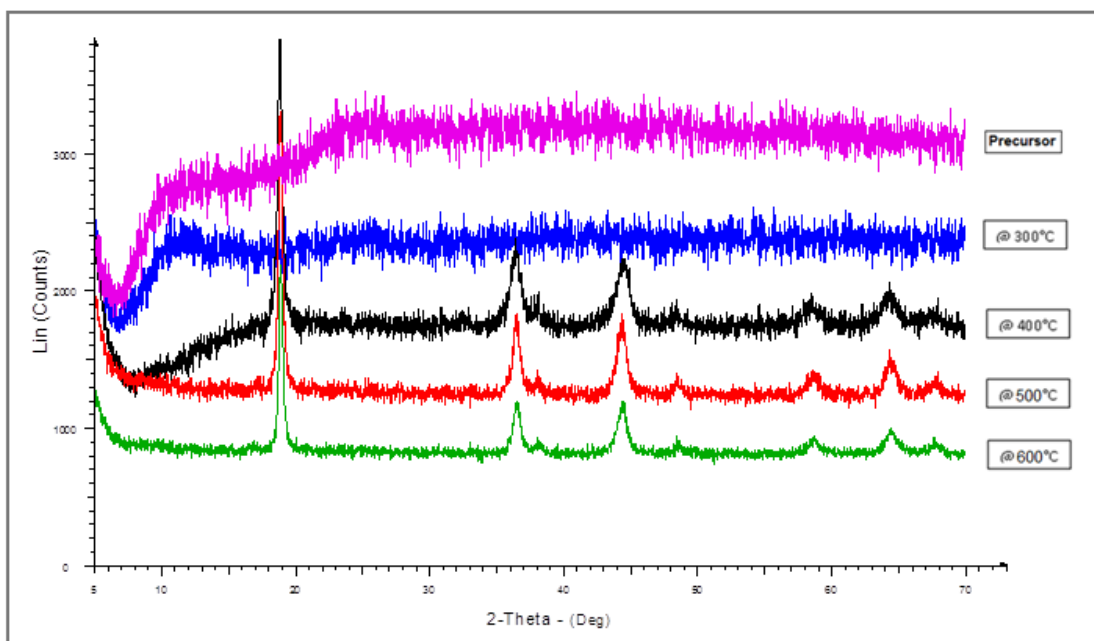
The results of doping the precursor with Mg showed that it was crystalline which corresponded to a mixed Mg-Mn citrate phase. Upon heating, the material became amorphous around 300 °C. Upon further heating to 400 ºC the material showed the typical spinel type diffraction pattern with no other intermediate crystalline phases. This would typically correspond to the doped $Li_{1.03}Mg_{0.2}Mn_{1.77}O_4$ spinel oxide phase (Figure 4.35).

By doping the precursor material with Mg using different acids, the results showed that the room temperature precursor phase was amorphous (Figures 4.36 to 4.38).
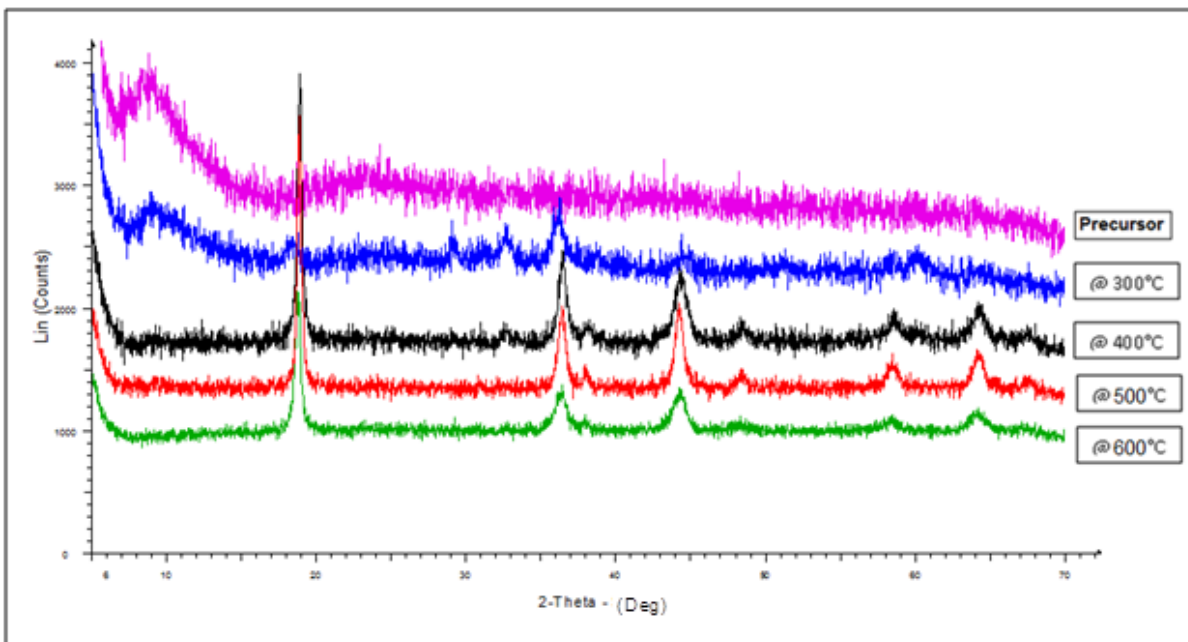
Figure 4.36: Typical PXRD patterns of the sample heated to various temperatures for Li$_{1.03}$Mg$_{0.2}$Mn$_{1.77}$O$_4$ in ascorbic acid.

Figure 4.37: Typical PXRD patterns of the sample heated to various temperatures for Li$_{1.03}$Mg$_{0.2}$Mn$_{1.77}$O$_4$ in succinic acid.
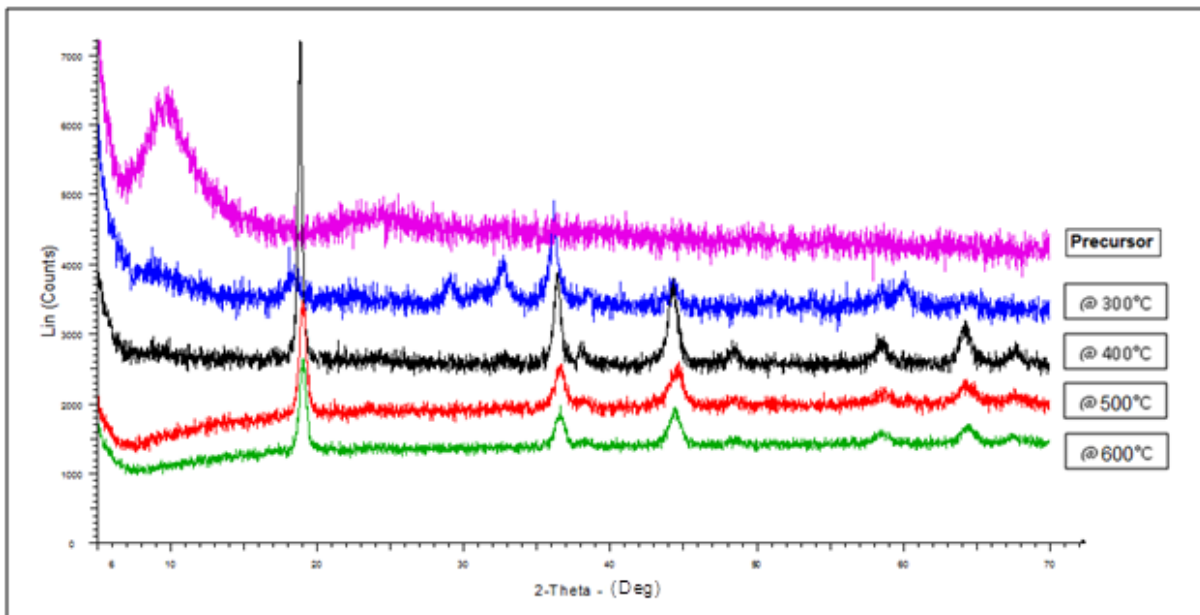
Figure 4.38: Typical PXRD patterns of the sample heated to various temperatures for Li$_{1.03}$Mg$_{0.2}$Mn$_{1.77}$O$_4$ in poly-acrylic acid.

The PXRD results showed that the samples started as an amorphous material, that upon heating to 300 °C they changed to a mixed amorphous-crystalline phase that contained Mn$_2$O$_3$, in the material with some of the spinel phase in ascorbic acid. A mixed crystalline intermediate phase, alpha-MnO$_2$ and gamma-Mn$_2$O$_3$ were observed in the samples that were prepared in poly-acrylic acid respectively. Upon further heating, the material changed to the pure spinel oxide at 400 °C and higher (Figures 4.36 to 4.38).

Table 4.8 summarizes the calculated Rietveld refinement results for Li$_{1.03}$Mg$_{0.2}$Mn$_{1.77}$O$_4$ synthesized in various acids (citric, succinic, ascorbic and poly-acrylic acids) at 400, 500 and 600 °C.

Table 4.8: Rietveld refinement results of $Li_{1.03}Mg_{0.2}Mn_{1.77}O_4$ prepared in various acids by batch sol-gel process under different temperature conditions.

$Li_{1.03}Mg_{0.2}Mn_{1.77}O_4$	Citric acid		
	400 °C	**500 °C**	**600 °C**
LVol - IB (nm)	16.430	18.952	25.121
a (Å) - experimental	8.163	8.170	8.189
Rw(GoF)	2.86(1.11)	2.76(1.09)	2.73(1.07)
a (Å) - literature	8.22[4, 11]		
	Succinic acid		
LVol - IB (nm)	14.490	21.834	29.137
a (Å) - experimental	8.171	8.180	8.197
Rw(GoF)	3.07(1.18)	2.85(1.16)	3.01(1.14)
	Poly-acrylic acid		
LVol - IB (nm)	28.173	31.896	37.560
a (Å) - experimental	8.177	8.180	8.194
Rw(GoF)	2.98(1.12)	2.88(1.11)	2.75(1.08)
	Ascorbic acid		
LVol - IB (nm)	20.569	22.720	31.100
a (Å) - experimental	8.175	8.178	8.192
Rw(GoF)	3.01(1.15)	2.97(1.14)	2.88(1.12)

Figure 4.39: Typical PXRD patterns of the sample heated to various temperatures for $LiAl_{0.4}Mn_{1.6}O_4$ in citric acid.

The results of doping the precursor with Al (in citric acid) showed a single phase change occurrence, from these PXRD patterns it should be explained that the material observed no phase change from its amorphous precursor to 300 °C and upon further heating up to 400 °C and above the final metal oxide was immediately obtained (Figure 4.39).
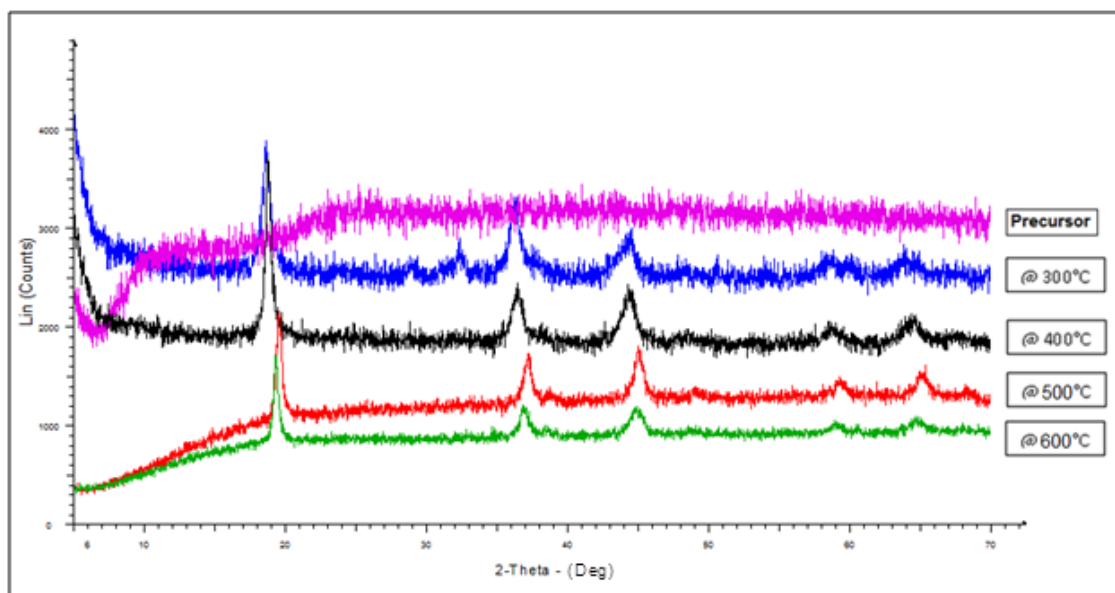
Figure 4.40: Typical PXRD patterns of the sample heated to various temperatures for $LiAl_{0.4}Mn_{1.6}O_4$ in ascorbic acid.
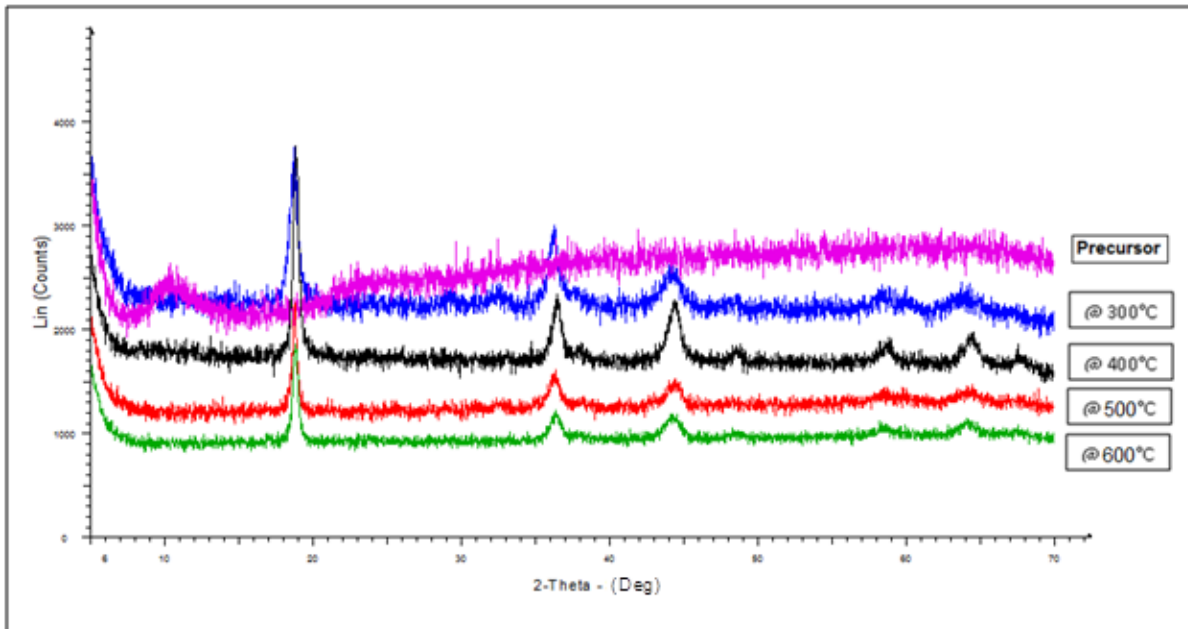
Figure 4.41: Typical PXRD patterns of the sample heated to various temperatures for LiAl$_{0.4}$Mn$_{1.6}$O$_4$ in succinic acid.
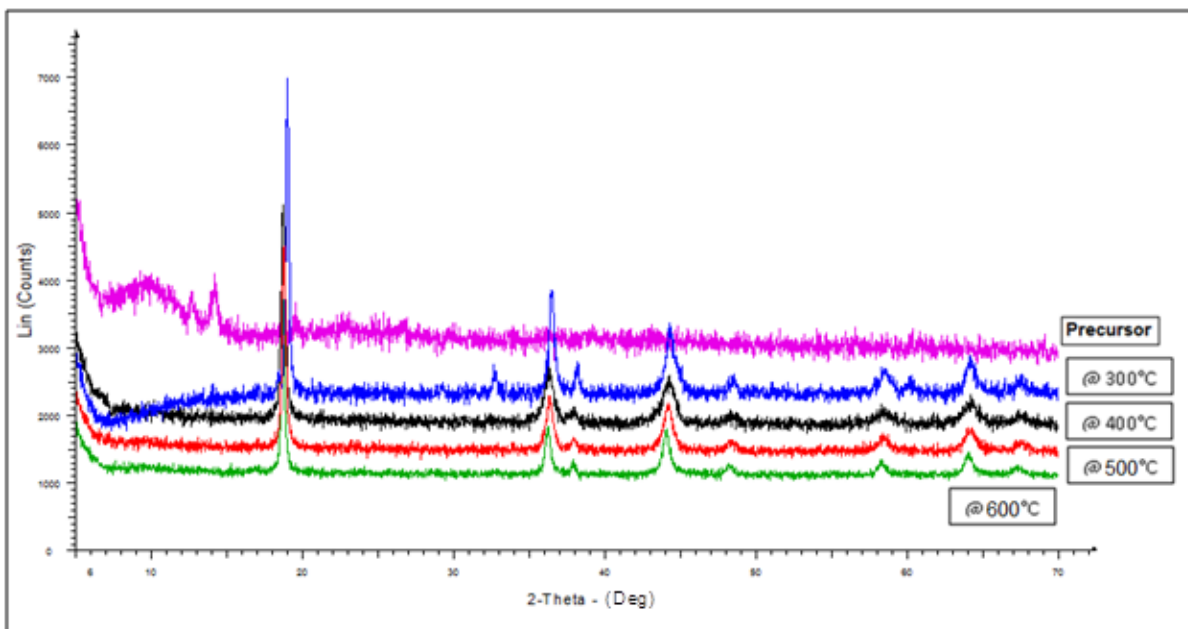
Figure 4.42: Typical PXRD patterns of the sample heated to various temperatures for LiAl$_{0.4}$Mn$_{1.6}$O$_4$ in poly-acrylic acid.

The precursors of doping the various materials with Al (Figures 4.40 to 4.42) were all amorphous; all underwent similar multiple-phase changes regardless of the chelating

acids used. The samples synthesized by using ascorbic and succinic acid in the precursor, showed to form a crystalline intermediate phase, gamma-Mn_2O_3, after heating it to 300 °C. Whereas the $LiAl_{0.4}Mn_{1.6}O_4$ synthesized with poly-acrylic acid in the precursor showed to contain Mn_2O_3 as an intermediate phase at 300 °C. All materials showed that the final pure spinel oxide phases were formed when heated to 400 °C and above.

The calculated Rietveld refinement results (obtained from Figures 4.39 to 4.42) for $Li_{1.03}Al_{0.4}Mn_{1.6}O_4$ at 400, 500 and 600 °C are summarized in Table 4.9.

Table 4.9: Rietveld refinement results of LiAl$_{0.4}$Mn$_{1.6}$O$_4$ prepared in various acids by batch sol-gel process under different temperature conditions.

$LiAl_{0.4}Mn_{1.6}O_4$	Citric acid		
	400 °C	**500 °C**	**600 °C**
LVol - IB (nm)	15.802	20.074	21.424
a (Å) - experimental	8.144	8.156	8.159
Rw(GoF)	2.95(1.13)	2.93(1.13)	2.95(1.14)
a (Å) - literature	8.20[17]		
	Succinic acid		
LVol - IB (nm)	17.132	17.943	21.983
a (Å) - experimental	8.151	8.159	8.184
Rw(GoF)	2.89(1.10)	2.86 (1.09)	2.90(1.10)
	Poly-acrylic acid		
LVol - IB (nm)	25.149	28.385	29.286
a (Å) - experimental	8.161	8.184	8.206
Rw(GoF)	3.20(1.23)	3.03(1.17)	3.01(1.16)
	Ascorbic acid		
LVol - IB (nm)	13.480	13.749	15.696
a (Å) - experimental	8.132	8.155	8.157
Rw(GoF)	2.88(1.11)	2.83(1.09)	2.91(1.11)
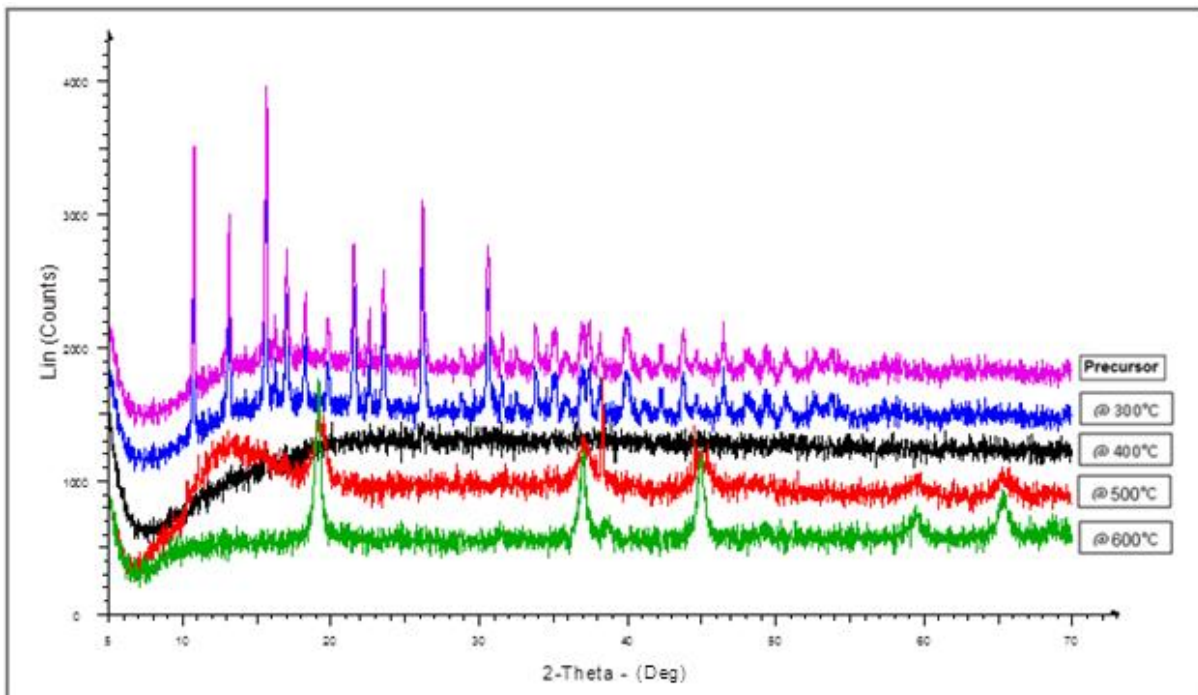
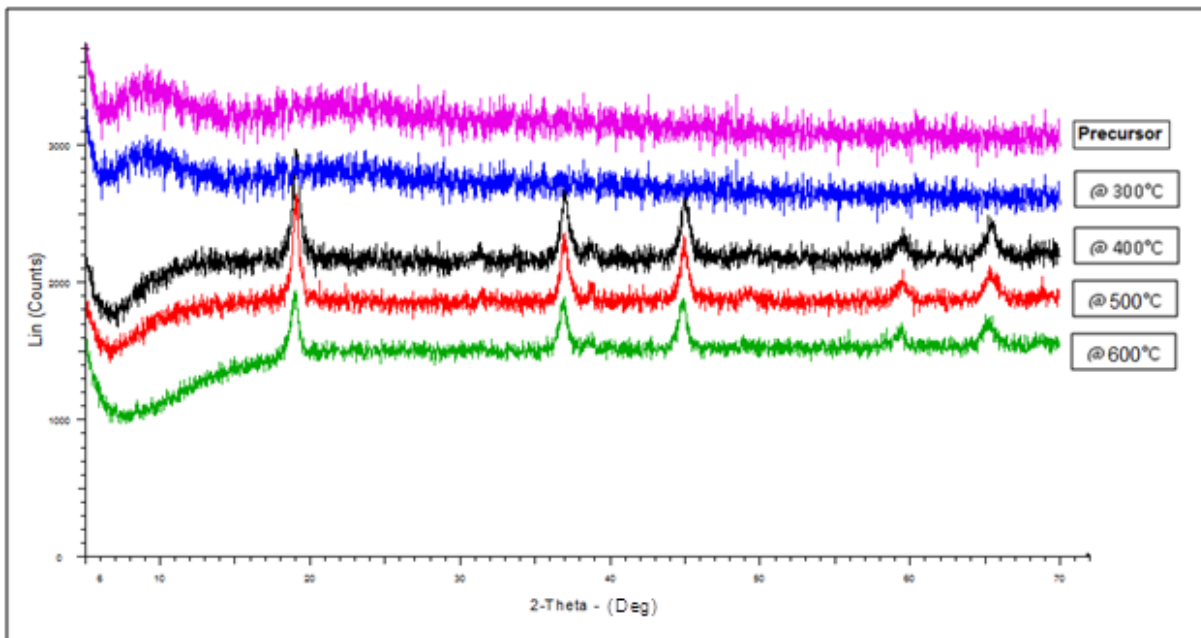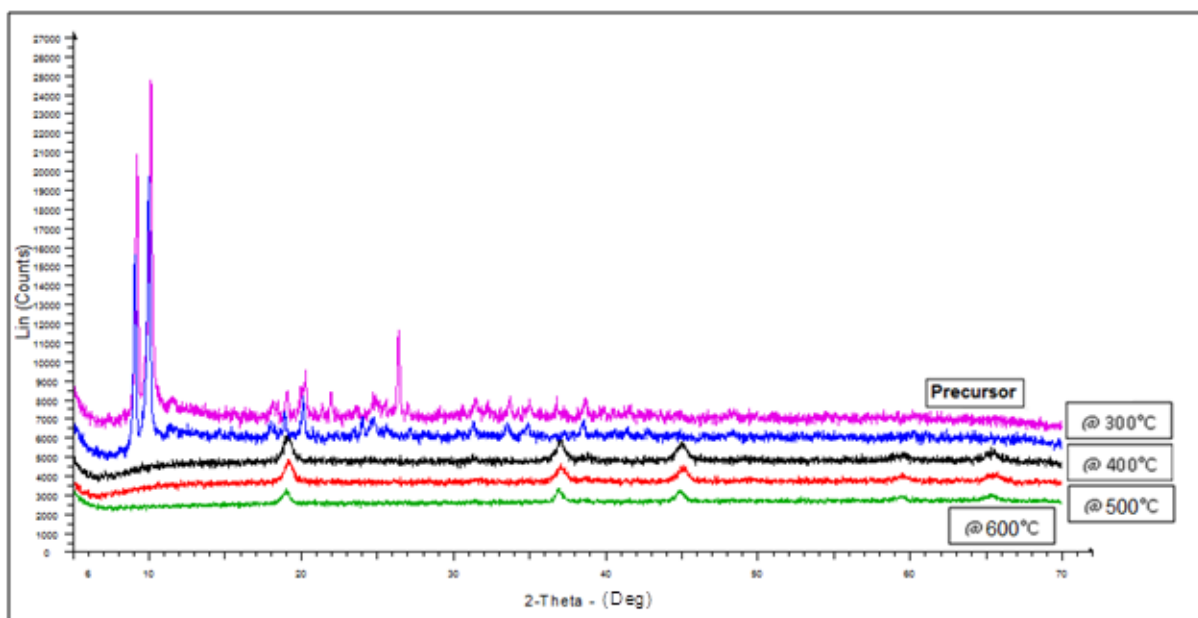*Figure 4.43: Typical PXRD patterns of the sample heated to various temperatures for LiCo$_{1.09}$Mn$_{0.91}$O$_4$ in citric acid.*

The results of using citric acid in the precursor with Co showed the material at room temperature to be crystalline. It was not possible to identify the crystalline phases clearly, but showed to comprise of a mixture of crystalline citric acid and a Co complex (Figure 4.43). Upon heating the sample to 300 °C, no phase change was observed, where upon heating further to 400 °C, the material's crystal structure collapsed and formed an amorphous phase. Heating the sample to 500 °C, the material showed an intermediate phase being a mix amorphous-crystalline phase, where upon heating further to 600 °C, the typical crystal structure of the spinel cathode oxide was observed in the respective diffraction pattern. The results observed in this study were slightly different to that obtained by the in-situ temperature technique, and will be discussed under Section 4.3. These differences would be due to the different heating times used and the fact that the samples were allowed to cool to room temperature before PXRD analysis.

Figure 4.44: Typical PXRD patterns of the sample heated to various temperatures for LiCo$_{1.09}$Mn$_{0.91}$O$_4$ in ascorbic acid.

Figure 4.45: Typical PXRD patterns of the sample heated to various temperatures for LiCo$_{1.09}$Mn$_{0.91}$O$_4$ in succinic acid.
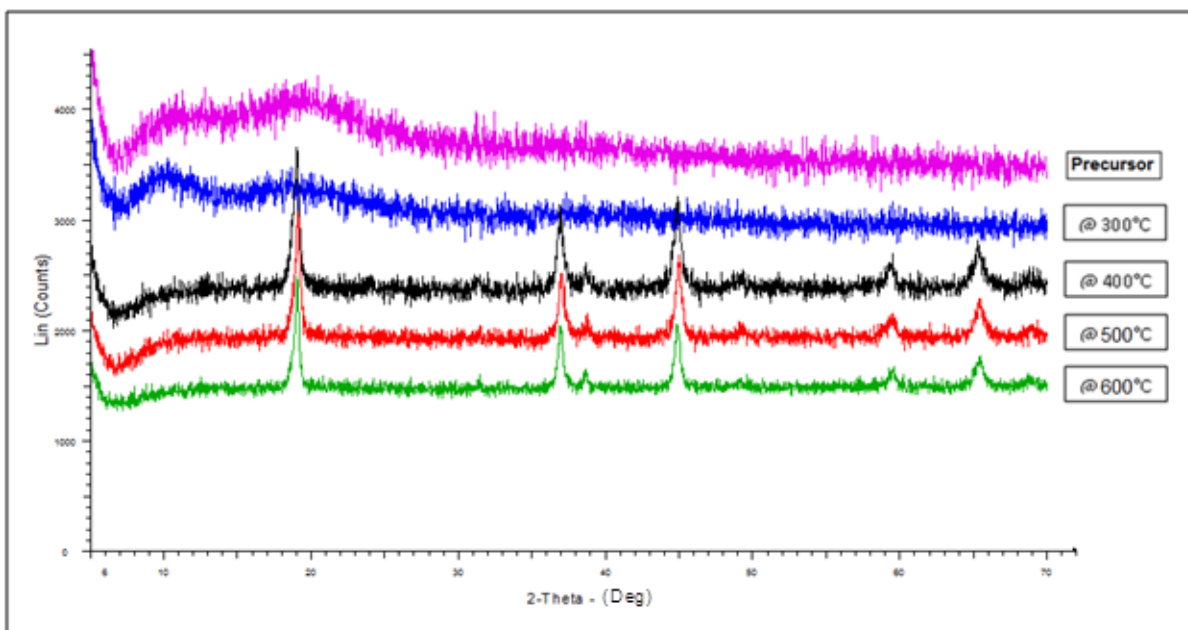
Figure 4.46: Typical PXRD patterns of the sample heated to various temperatures for
LiCo$_{1.09}$Mn$_{0.91}$O$_4$ in poly-acrylic acid.

The results showed that doping the precursor with Co using ascorbic and poly-acrylic acids showed that the phase at room temperature was amorphous (Figures 4.44 and 4.46), whereas the precursor with succinic acid was crystalline. It was not possible to clearly identify the crystalline precursor material from the powder diffraction data base, but would probably relate to some Co-Mn complex with succinic acid (Figure 4.45). Similar to the previous materials studied, the ones that were amorphous at room temperature, showed no phase changes up to 300 °C. From 400 °C and higher, the typical spinel type crystalline structure was then observed to form. Similar to the material made with succinic acid, only small changes in the diffraction pattern of the material that was heated to 300 °C was observed. Noticeably, it did not go through an amorphous intermediate as was observed with the material that was made with citric acid upon heating to 400 °C, but showed to form the typical spinel type diffraction pattern.

The calculated Rietveld refinement results for the Co doped oxide material (from Figures 4.43 to 4.46) are summarized in Table 4.10.

Table 4.10: Rietveld refinement results of $LiCo_{1.09}Mn_{0.91}O_4$ prepared in various acids by batch sol-gel process under different temperature controls.

| $LiCo_{1.09}Mn_{0.91}O_4$	Citric acid		
	400 °C	**500 °C**	**600 °C**
LVol - IB (nm)	5.866	10.097	11.408
a (Å) - experimental	8.068	8.072	8.079
Rw(GoF)	3.09(1.29)	2.87(1.25)	2.97(1.27)
a (Å) - literature	8.06-8.07[6, 18]		
	Succinic acid		
LVol - IB (nm)	9.051	9.386	10.00
a (Å) - experimental	8.066	8.067	8.068
Rw(GoF)	2.20 (1.09)	2.25 (1.12)	2.27 (1.12)
	Poly-acrylic acid		
LVol - IB (nm)	13.108	14.206	16.307
a (Å) - experimental	8.064	8.066	8.066
Rw(GoF)	2.22 (1.05)	2.20 (1.05)	2.27 (1.08)
	Ascorbic acid		
LVol - IB (nm)	10.596	11.034	11.437
a (Å) - experimental	8.062	8.063	8.072
Rw(GoF)	2.08 (1.05)	2.12 (1.07)	2.20 (1.10)
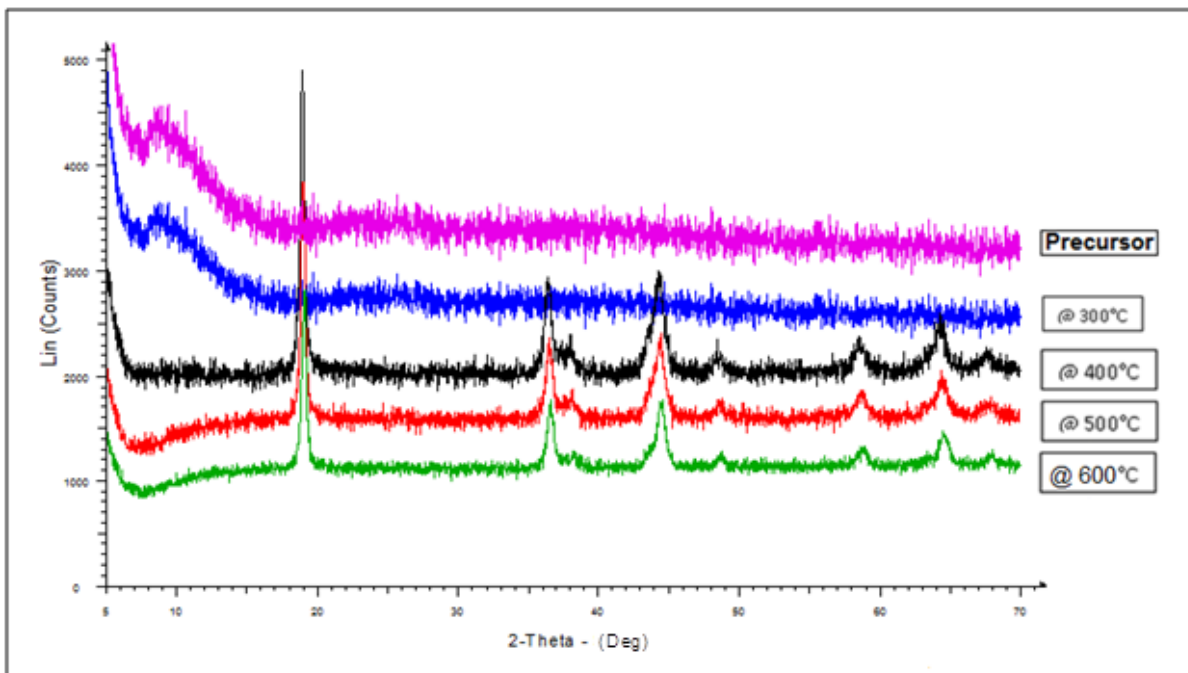
Figure 4.47: Typical PXRD patterns of the sample heated to various temperatures for LiNi$_{0.5}$Mn$_{1.5}$O$_4$ in citric acid.

The results of doping the precursor with Ni showed that the material was amorphous at room temperature and only showed the appearance of the spinel type structure when heated to 400 °C and higher (Figure 4.47). However, when comparing the results to the in-situ temperature study (Section 4.3, Figures 4.63 and 4.64 respectively), a large amorphous halo was observed at the start of the in-situ analysis and the intermediate phase that could relate to alpha-MnO$_2$ and gamma-Mn$_2$O$_3$ were observed at 250 to 350 °C (Figures 4.63 and 4.64). This could imply that the intermediate phases would probably disappear if left at the 400 ºC for longer periods of time (Figure 4.47). The final typical LiNi$_{0.5}$Mn$_{1.5}$O$_4$ spinel type structure was observed from both techniques when heated to 600 °C and higher.
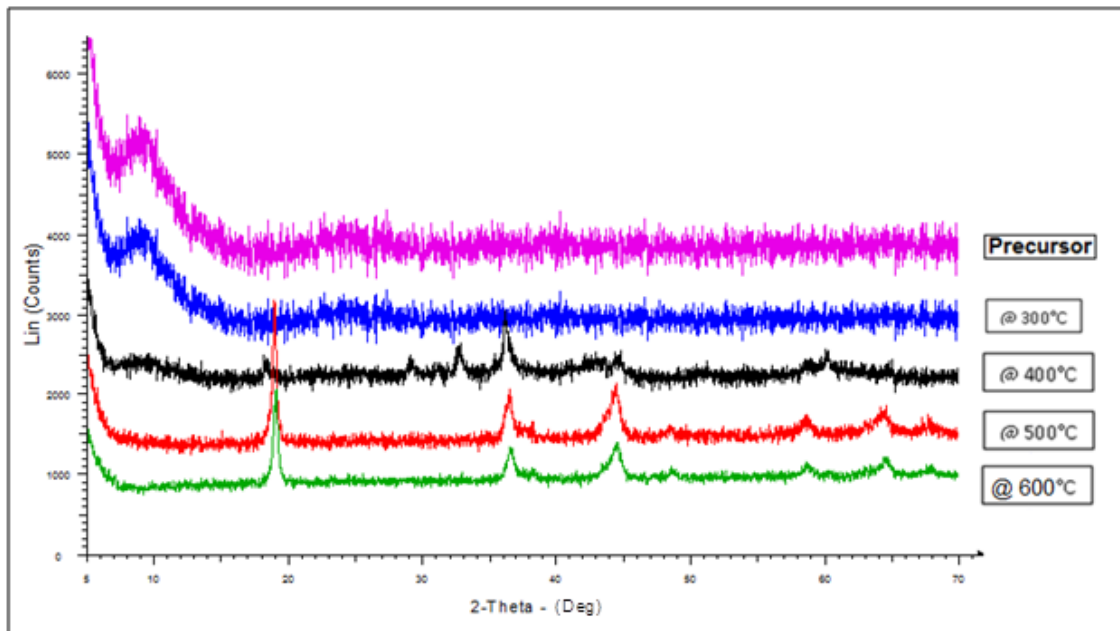
Figure 4.48: Typical PXRD patterns of the sample heated to various temperatures for $LiNi_{0.5}Mn_{1.5}O_4$ in ascorbic acid.
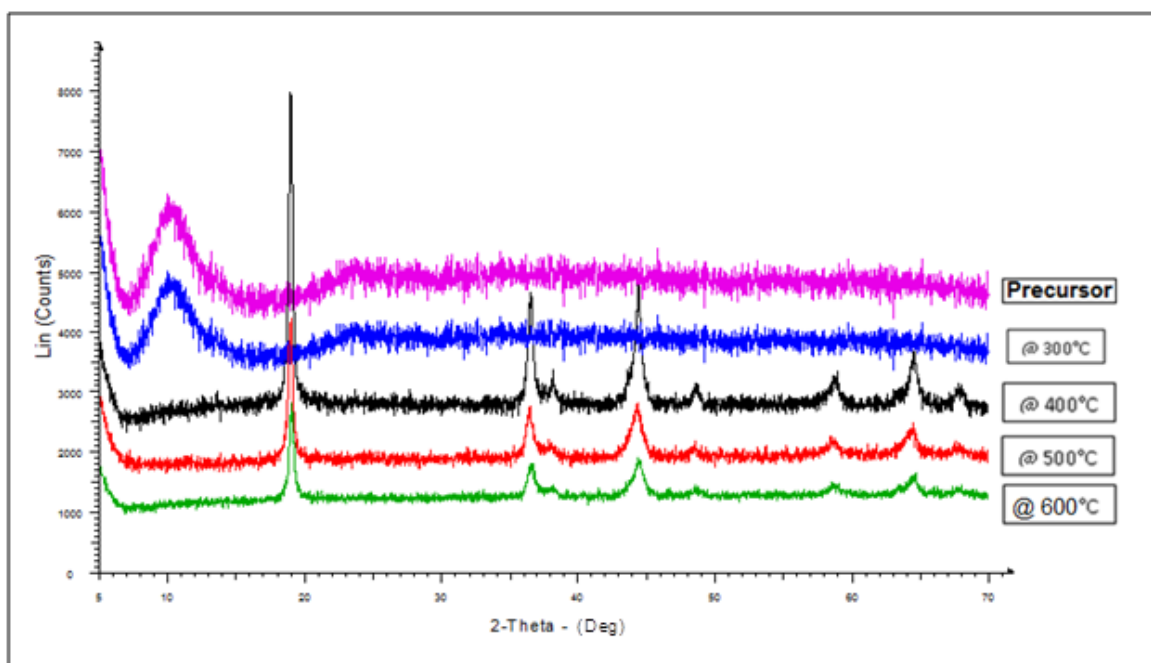
Figure 4.49: Typical PXRD patterns of the sample heated to various temperatures for $LiNi_{0.5}Mn_{1.5}O_4$ in succinic acid.
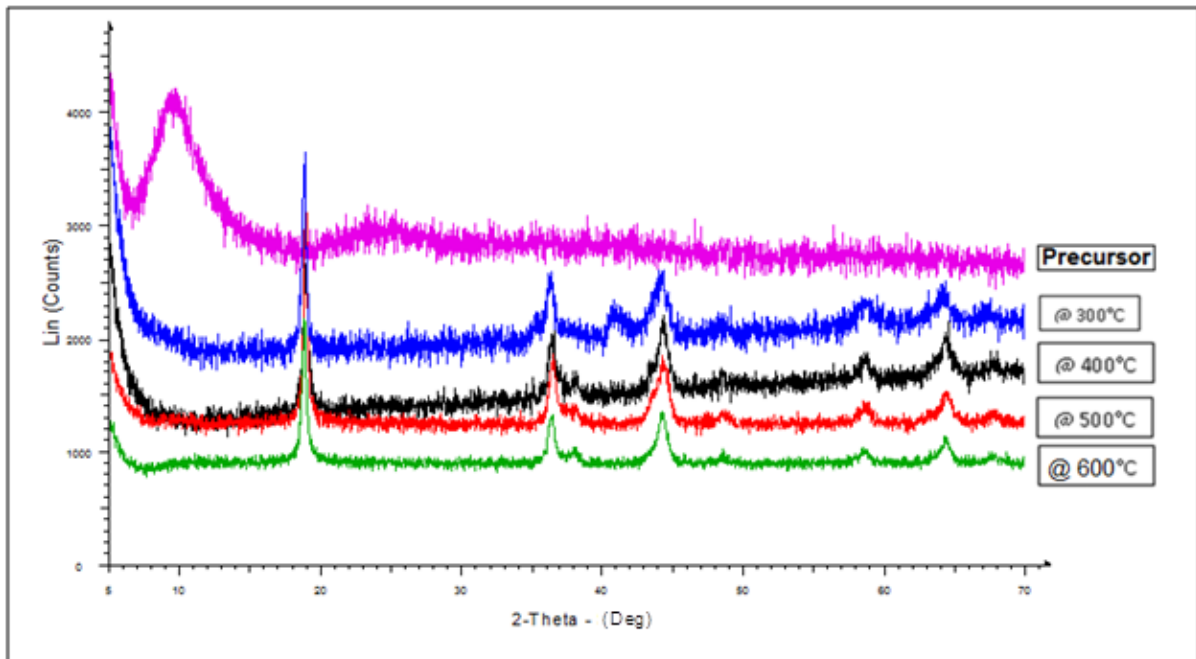
Figure 4.50: Typical PXRD patterns of the sample heated to various temperatures for LiNi$_{0.5}$Mn$_{1.5}$O$_4$ in poly-acrylic acid.

LiNi$_{0.5}$Mn$_{1.5}$O$_4$ synthesized from ascorbic acid (Figure 4.48) showed that the precursor at room temperature and heated up to 300 °C was amorphous. At 400 °C, the intermediate phase of a mixed alpha-MnO$_2$, gamma-Mn$_2$O$_3$ and the typical spinel LiNi$_{0.5}$Mn$_{1.5}$O$_4$ phases were observed. Where upon heating further to 600 °C, only then was the spinel phase observed. The PXRD results for the material synthesized in succinic acid (Figure 4.49) showed the material to be amorphous at room temperature and when heated to 300 °C. Further heating the sample then showed the formation of the typical crystalline spinel type diffraction pattern of LiNi$_{0.5}$Mn$_{1.5}$O$_4$. The material that was synthesized in poly-acrylic acid (Figure 4.50) was amorphous at room temperature and already showed the formation of the intermediate phase, alpha-MnO$_2$, at 300 °C. Upon further heating to 400, 500 and 600 °C, the typical, LiNi$_{0.5}$Mn$_{1.5}$O$_4$ spinel type phase was observed to predominantly form.

Table 4.11 summarizes the calculated Rietveld refinement results for LiNi$_{0.5}$Mn$_{1.5}$O$_4$ synthesized in various acids (citric, succinic, ascorbic and poly-acrylic acids) at 400, 500 and 600 °C.

Table 4.11: Rietveld refinement results of $LiNi_{0.5}Mn_{1.5}O_4$ prepared in various acids by batch sol-gel process under different temperature conditions.

$LiNi_{0.5}Mn_{1.5}O_4$	Citric acid		
	400 °C	**500 °C**	**600 °C**
LVol - IB (nm)	13.765	17.659	17.770
a (Å) - experimental	8.161	8.171	8.180
Rw(GoF)	2.95 (1.15)	3.01 (1.17)	2.89 (1.13)
a (Å) - literature	8.18[18]		
	Succinic acid		
LVol - IB (nm)	26.611	27.189	29.495
a (Å) - experimental	8.164	8.164	8.168
Rw(GoF)	3.01 (1.18)	3.01 (1.17)	2.97 (1.15)
	Poly-acrylic acid		
LVol - IB (nm)	17.946	25.187	28.788
a (Å) - experimental	8.152	8.154	8.155
Rw(GoF)	3.07 (1.20)	3.09 (1.21)	3.11 (1.22)
	Ascorbic acid		
LVol - IB (nm)	10.476	13.397	14.217
a (Å) - experimental	8.155	8.163	8.167
Rw(GoF)	3.12 (1.26)	3.08 (1.22)	3.00 (1.17)

In summary within Tables 4.7 to 4.11, it should be noted that as the various spinel oxide materials (in different acids) are heated the crystallite size, LVol-IB (nm) and lattice parameter, a (Å) increases, similar trends are observed for studies done by Lee *et al.*[1] and Y.K. Sun[9]. The crystallite size increases because the materials crystallinity increases at higher temperatures. With respect to the lattice parameter, the average oxidation state of Mn in a spinel structure, closely relates to this variable (the lattice parameter). At lower temperatures a smaller lattice parameter was obtained resulting in the formation of a higher Mn oxidation state. It should be noted that the Mg doped material had a slightly higher lattice parameter (for succinic, poly-acrylic and ascorbic acids) in the low calcination temperature compare to the undoped material. The lattice parameter for the doped spinel materials, throughout the different calcination temperatures, was lower than that of the

undoped spinel material regardless of the chelating agent used concluding that the doped metal ion partially replaces the Mn sites and increases the degree of cation ordering.

4.3 <u>In-situ temperature powder x-ray diffraction</u>

In-situ temperature PXRD analysis of the precursor materials using citric acid was done on the undoped spinel ($Li_{1.03}Mn_{1.97}O_4$) and the doped spinel ($LiAl_{0.4}Mn_{1.6}O_4$, $Li_{1.03}Mg_{0.2}Mn_{1.77}O_4$, $LiCo_{1.09}Mn_{0.91}O_4$ and $LiNi_{0.5}Mn_{1.5}O_4$) cathode oxide materials. This analysis consisted of placing the precursor sample into a ceramic sample stage with a Pt foil insert, which was enclosed in the heating stage. The sample was heated (6 $°C.min^{-1}$) under an air atmosphere from 30 to 850 °C and cooled immediately to room temperature again. A full PXRD pattern (also referred to as variable temperature, VT-scans) was collected from 30 to 50 °C and then in 50 °C steps up to 850 °C.

4.3.1 <u>$Li_{1.03}Mn_{1.97}O_4$</u>

The in-situ PXRD scan of the precursor material as it changed with temperature (heating and cooling) to form the final $Li_{1.03}Mn_{1.97}O_4$ is shown in Figure 4.51. Selected diffraction patterns of interest at certain temperatures are shown in a staggered format in Figure 4.52.
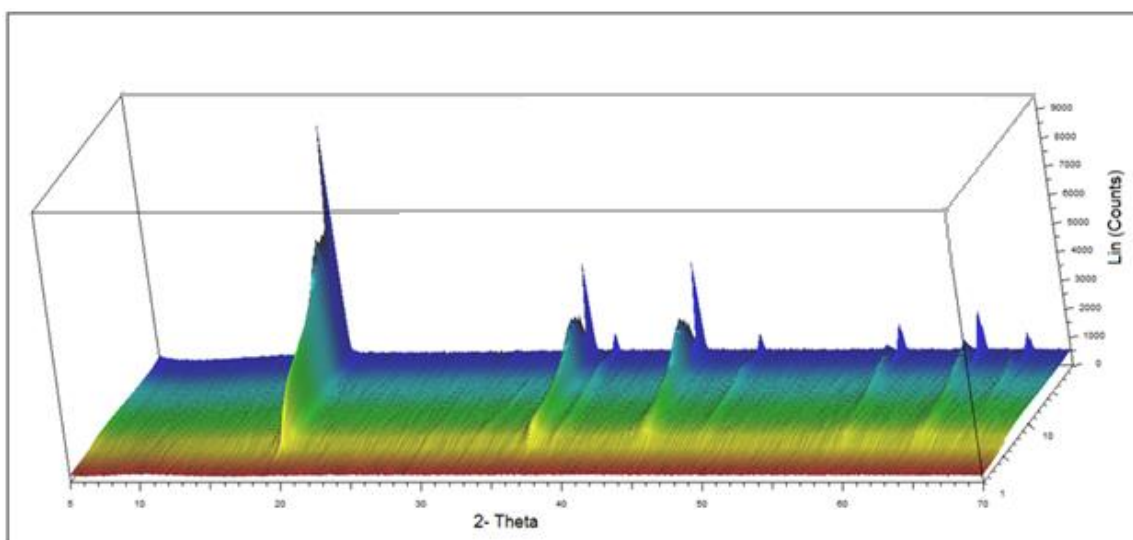
Figure 4.51: In-situ PXRD VT-scan of $Li_{1.03}Mn_{1.97}O_4$ made from the citric acid precursor. The temperature scale is shown in arbitary units .

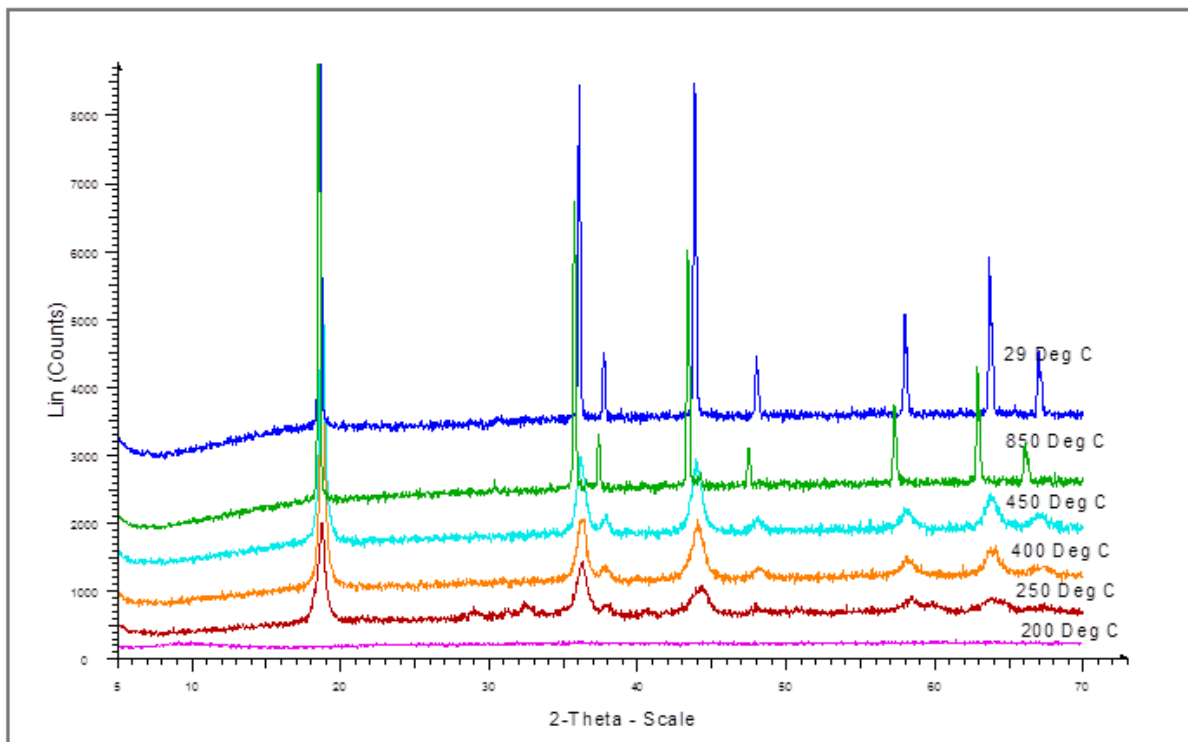*Figure 4.52: Staggered PXRD patterns of $Li_{1.03}Mn_{1.97}O_4$ at specfic temperatures of interest from the in-situ set of results.*

The results showed that the precursor material was amorphous at room temperature up to about 200 °C. At 250 °C the formation of an impure crystalline intermediate phase was observed up to about 350 °C which could relate to Mn_2O_3. At 400 °C the formation of the typical spinel crystalline phase ($Li_{1.03}Mn_{1.97}O_4$) was seen to form with the respective diffraction peaks being still relatively broad up to about 600 °C. As the temperature increased up to 850 °C, the diffraction peaks became significantly sharper, implying a growth in the crystallite size. The change in the crystal unit cell parameter (a) and the crystallite size (LVol-IB) from 350 to 850 °C are shown in Table 4.12 and Figure 4.53. For comparison purposes, the unit cell parameter and crystallite size at room temperature are also shown.

Table 4.12: Rietveld results of in-situ $Li_{1.03}Mn_{1.97}O_4$ analysis at specific temperatures.

Temperature (°C)	Unit cell lattice (Å)	Crystallite size parameter LVol-IB (nm)
350	8.19	15.8
400	8.22	16.3
450	8.24	16.9
500	8.25	18.5
550	8.27	21.0
600	8.28	24.8
650	8.29	31.8
700	8.31	45.9
750	8.32	72.2
800	8.34	85.3
850	8.37	104.8
29	8.24	137.8
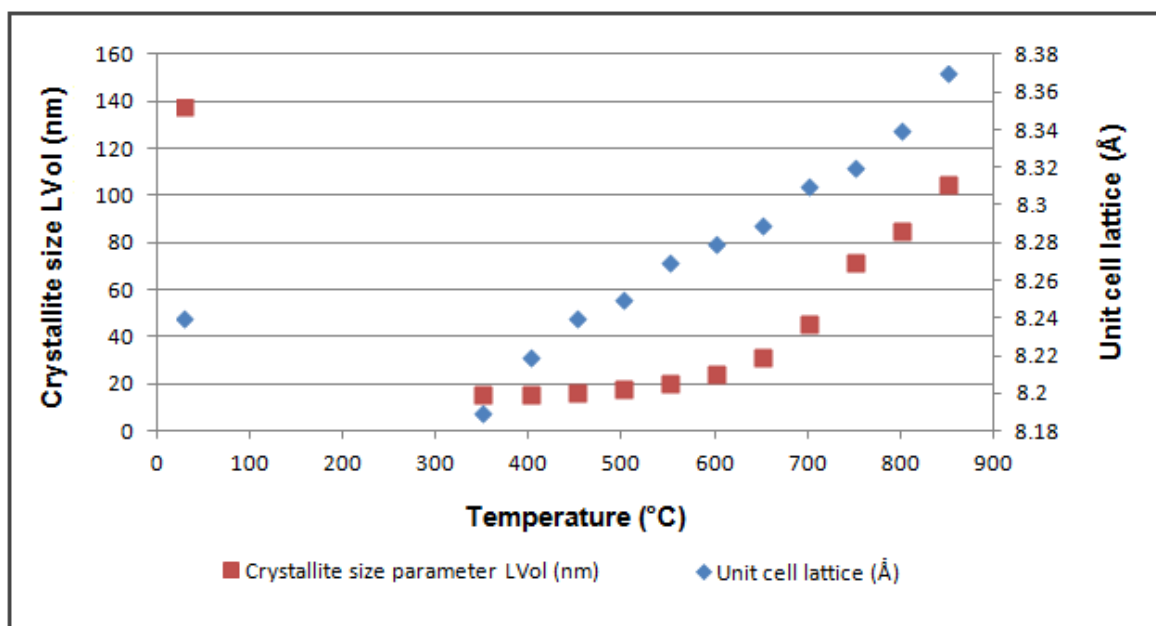
Figure 4.53: Graphical display of in-situ $Li_{1.03}Mn_{1.97}O_4$ Rietveld results.

The results showed that there was a noticable increase in unit cell lattice expansion of about 0.32×10^{-3} Å.°C^{-1} as the temperature increased from 300 to 850 °C. When the sample was cooled back to room temperature, the unit cell lattice decreased to 8.24 Å, which was slightly higher to what was previously reported (Table 4.6). The crystallite size only started to increase signficantly at about 600 °C, where there was almost 323 % increase in the crystallite size from 600 to 850 °C based on the LVol-IB (nm) calculation from Rietveld refinement. This relates to about 0.34 nm.°C^{-1} change in crystallite size. When the sample was allowed to cool to room temperature from 850 °C, the crystallites continued to grow, where the room temperature sample showed a crystallite size of 137.8 nm, which was a further growth of about 31 % in crystallite size.

These results are in agreement with the TGA results (Figure 4.1) that showed between 200 to 300 °C, a weight loss was observed that related to the impure intermediate phase at 250 °C within these in-situ results. At 400 °C the TGA results obtained no further weight decomposition concluding final phase formation which was supported by these in-situ results.

4.3.2 $Li_{1.03}Mg_{0.2}Mn_{1.77}O_4$

The in-situ PXRD scan of the precursor material as it changed with temperature to form the final $Li_{1.03}Mg_{0.2}Mn_{1.77}O_4$ is shown in Figure 4.54. Selected diffraction patterns of interest at certain temperatures are shown in a staggered format in Figure 4.55.

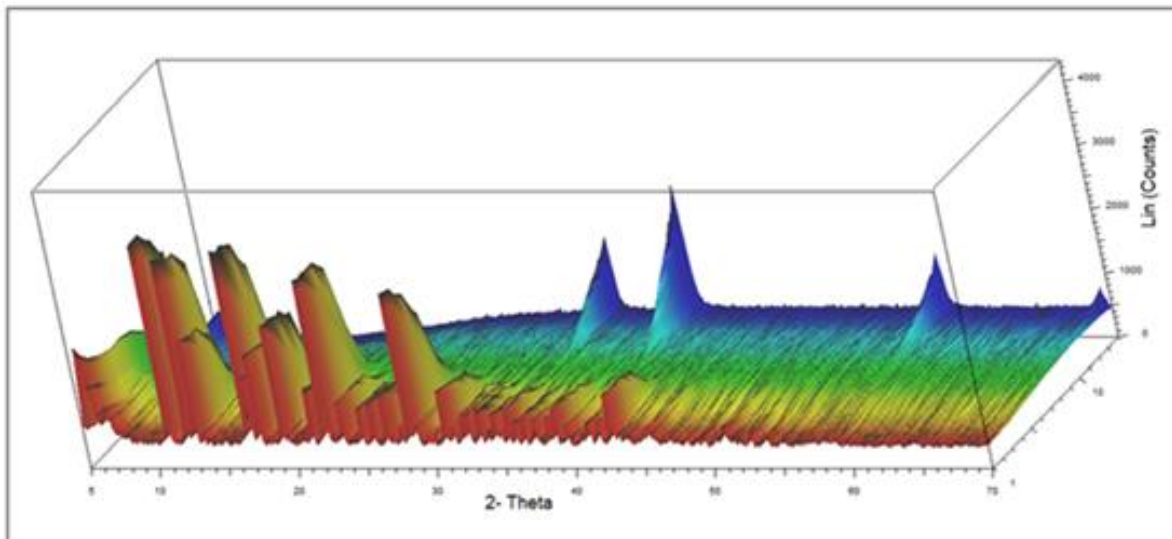*Figure 4.54: In-situ PXRD VT-scan of Li$_{1.03}$Mg$_{0.2}$Mn$_{1.77}$O$_4$ made from the citric acid precursor. The temperature scale is shown in arbitary units.*
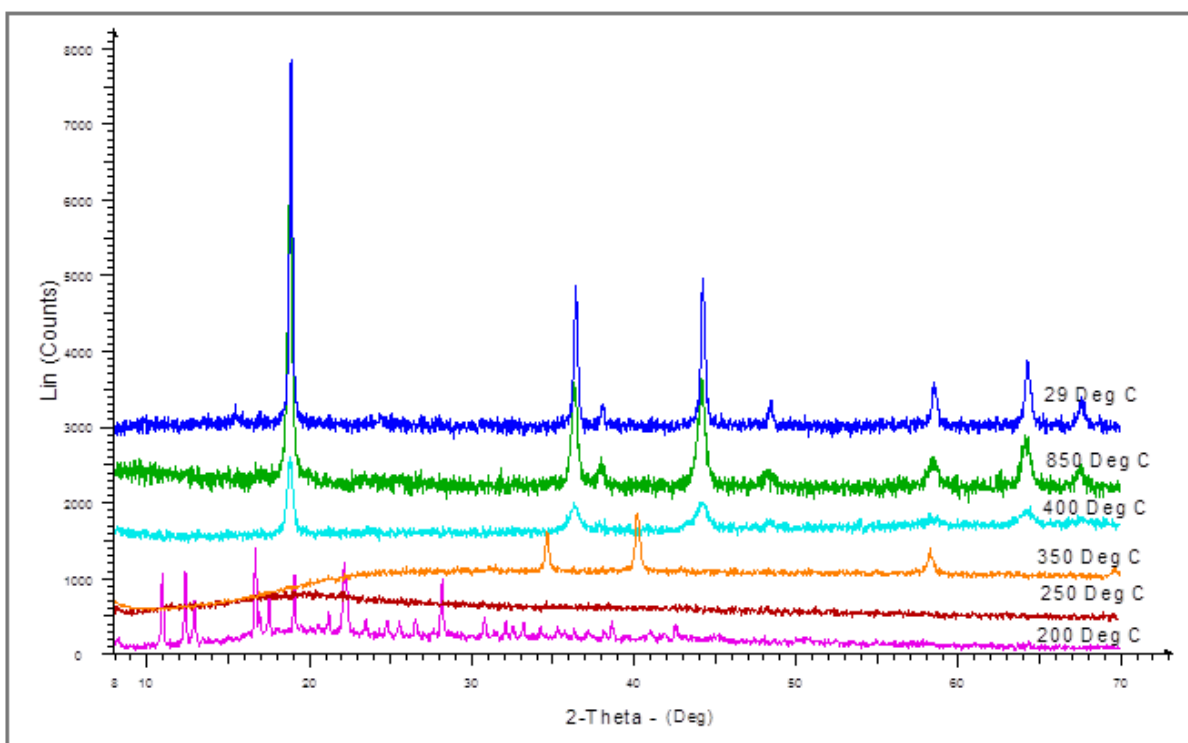

Figure 4.55: Staggered PXRD patterns of Li$_{1.03}$Mg$_{0.2}$Mn$_{1.77}$O$_4$ at specfic temperatures of interest from the in-situ set of results.

The results showed the precursor material was crystalline at room temperature up to about 200 °C. At 250 °C the material's crystalline structure collapsed to form an amorphous

intermediate phase up to about 300 °C. At 350 °C the formation of another crystalline intermediate phase was observed, before the formation of the typical spinel crystalline phase ($Li_{1.03}Mg_{0.2}Mn_{1.77}O_4$) was seen to start forming at about 400 °C. As the temperature increased to 850 °C, the diffraction peaks became significantly sharper and more defined, implying a growth in the crystallite size of the material. The change in the crystal unit cell parameter (a) and the crystallite size (LVol) from 350 to 850 °C are shown in Table 4.13 and Figure 4.56. For comparison purposes, the unit cell parameter and crystallite size at room temperature are also shown.

Table 4.13: Rietveld results of in-situ $Li_{1.03}Mg_{0.2}Mn_{1.77}O_4$ analysis at specific temperatures.

Temperature (°C)	Unit cell lattice (Å)	Crystallite size parameter LVol-IB (nm)
400	8.18	11.8
450	8.13	9.02
500	8.16	10.6
550	8.15	13.6
600	8.17	19.9
650	8.17	16.2
700	8.19	20.5
750	8.21	42.8
800	8.24	34.9
850	8.24	53.9
29	8.22	44.7
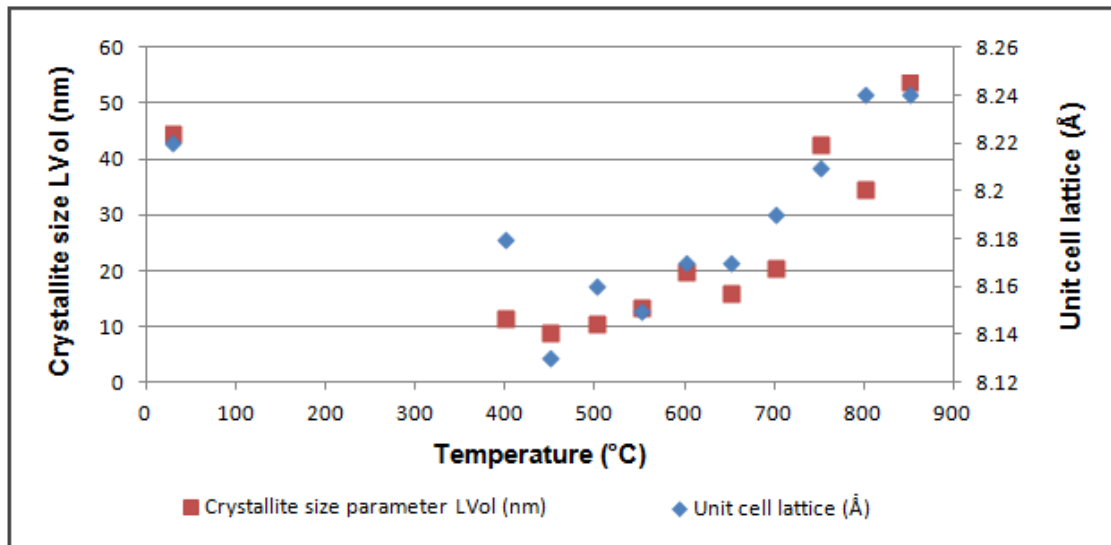
Figure 4.56: Graphical display of in-situ Li$_{1.03}$Mg$_{0.2}$Mn$_{1.77}$O$_4$ Rietveld results.

The results showed that there was a noticable increase in unit cell lattice expansion of about 0.27×10^{-3} Å.°C^{-1} as the temperature increased from 450 to 850 °C. When the sample was cooled back to room temperature, the unit cell lattice decreased to 8.22 Å, which was again slightly larger to what was previously reported (Table 4.6). The crystallite size based on the full Rietveld refinement of the diffraction pattern started to increase signficantly from about 550 °C, where there was about a 296 % increase in the crystallite size from 550 to 850 °C based on the LVol-IB (nm) calculation. This relates to about 0.15 nm.°C^{-1} change in crystallite size over that temperature range. When compared to the results of the previous sample, as the sample was allowed to cool to room temperature from 850 °C, the crystallite size did not change significantly (about 17 %) which could be within experimental error.

The results show that the doping of the managanese spinel with a small amount of Mg allowed for the formation of smaller crystalites at high temperatures. These results correlate with the TGA analysis (Figure 4.2) that showed multiple weight loss steps that can relate to the various phase changes (from precursor to final oxide) within these in-situ results. At 250 °C the TGA results showed a weight decomposition that related to the amorphous phase change by these in-situ results (also at 250 °C). However at 400 °C the in-situ results produced the final oxide formation and the TGA results showed no further weight loss.

4.3.3 $LiAl_{0.4}Mn_{1.6}O_4$

The in-situ PXRD scan of the precursor material as it changed with temperature to form the final $LiAl_{0.4}Mn_{1.6}O_4$ is shown in Figure 4.57. Selected diffraction patterns of interest at certain temperatures are shown in a staggered format in Figure 4.58.
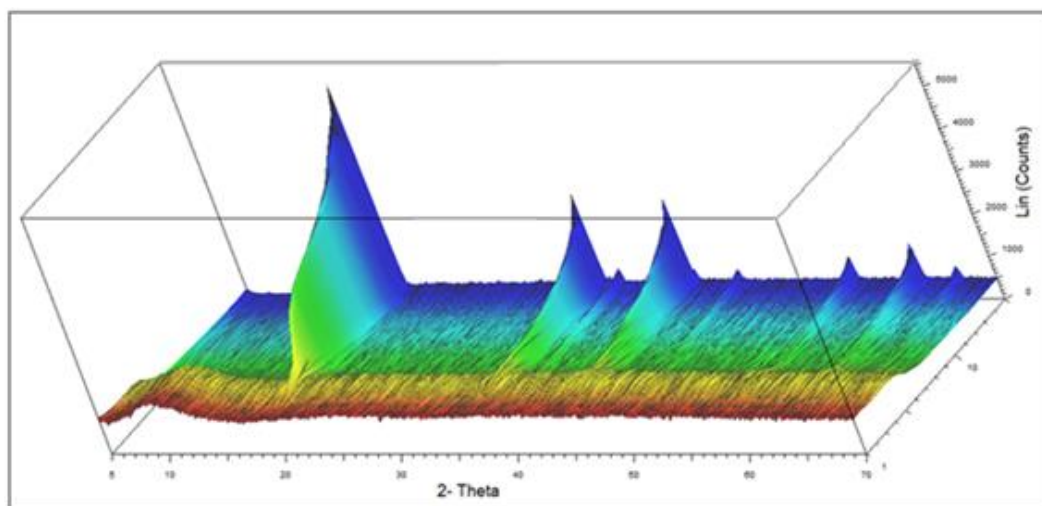

Figure 4.57: In-situ PXRD VT-scan of $LiAl_{0.4}Mn_{1.6}O_4$ made from the citric acid precursor. The temperature scale is shown in arbitary units.
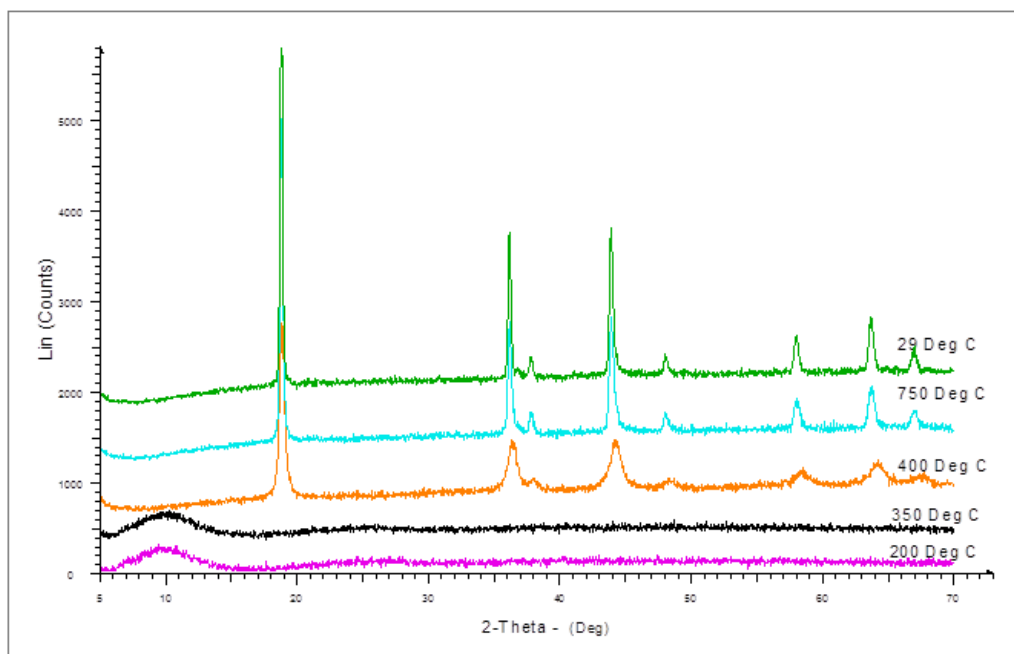

Figure 4.58: Staggered PXRD patterns of $LiAl_{0.4}Mn_{1.6}O_4$ at specfic temperatures of interest from the in-situ set of results.

The results showed the precursor material was amorphous at room temperature up to about 350 °C. At 400 °C the formation of the typical spinel crystalline phase ($LiAl_{0.4}Mn_{1.6}O_4$) was seen to form with the diffraction peaks being relatively broad up to about 700 °C. As the temperature increased up to 750 °C, the diffraction peaks became significantly sharper, implying a growth in the crystallite size. The change in the crystal unit cell parameter (a) and the crystallite size (LVol-IB) from 400 to 850 °C are shown in Table 4.14 and Figure 4.59. For comparison purposes, the unit cell parameter and crystallite size at room temperature are also shown.

Table 4.14: Rietveld results of in-situ $LiAl_{0.4}Mn_{1.6}O_4$ analysis at specific temperatures.

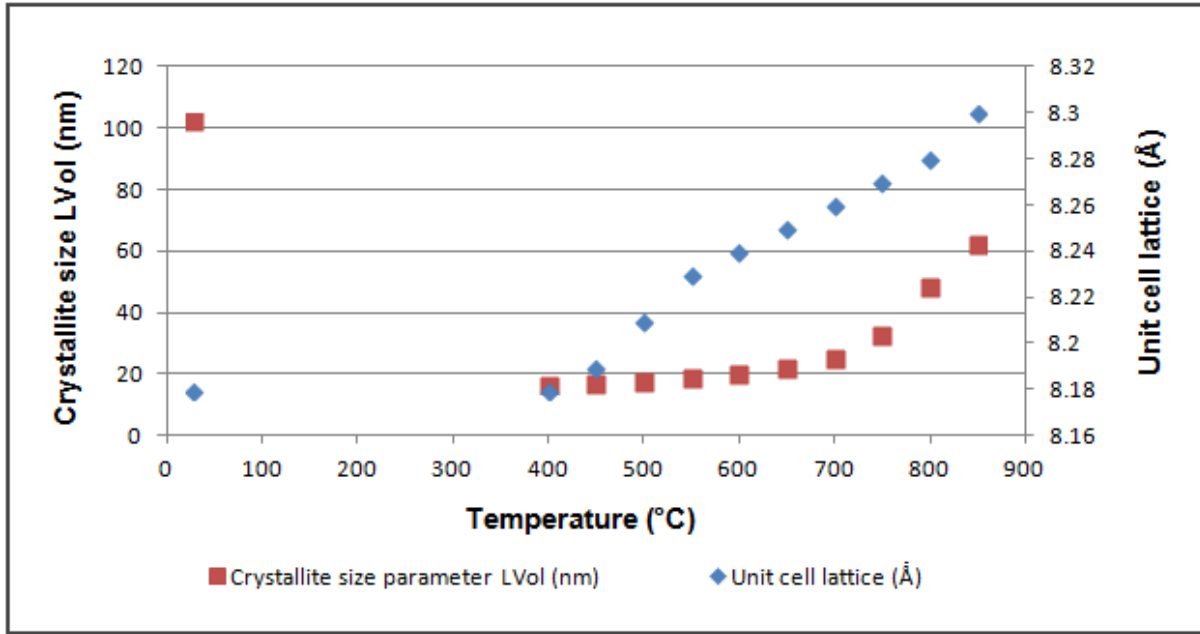| Temperature (°C)	Unit cell lattice (Å)	Crystallite size parameter LVol-IB (nm)
400	8.18	16.3
450	8.19	16.7
500	8.21	17.3
550	8.23	18.5
600	8.24	19.8
650	8.25	21.9
700	8.26	25.1
750	8.27	32.7
800	8.28	48.3
850	8.30	62.0
29	8.18	102.0

Figure 4.59: Graphical display of in-situ LiAl$_{0.4}$Mn$_{1.6}$O$_4$ Rietveld results.

The results showed that there was a noticable linear increase in unit cell lattice expansion of about 0.25×10^{-3} Á.°C^{-1} as the temperature increased from 400 to 850 °C. When the sample was cooled back to room temperature, the unit cell lattice decreased to 8.18 Á, which was only slightly higher to the previously reported value (Table 4.6). The crystallite size based on the full Rietveld refinement of the diffraction pattern started to increase signficantly from about 700 °C, where there was about a 147 % increase in the crystallite size from 700 to 850 °C based on the LVol-IB (nm) calculation. This relates to about 0.25 nm.°C^{-1} changes in crystallite size over that temperature range. On cooling the sample back to room temperature, a similar increase in the crystallite size was observed to that of Li$_{1.03}$Mn$_{1.97}$O$_4$ (Figure 4.51) where the calculated LVol-IB parameter at room temperature was 102 nm, a 65 % increase when compared to the LVol-IB parameter at 850 ^{o}C.

The results showed that the doping of the manganese spinel with a small amount of Al allows for the formation of smaller crystallites of around 20 nm up to the high temperature of 700 °C. These in-situ results are in agreement with the TGA results (Figure 4.5) that showed complete formation of the final spinel oxide at 400 °C.

4.3.4 $LiCo_{1.09}Mn_{0.91}O_4$

The in-situ PXRD scan of the precursor material as it changed with temperature to form the final $LiCo_{1.09}Mn_{0.91}O_4$ is shown in Figure 4.60. Selected diffraction patterns of interest at certain temperatures are shown in a staggered format in Figure 4.61.
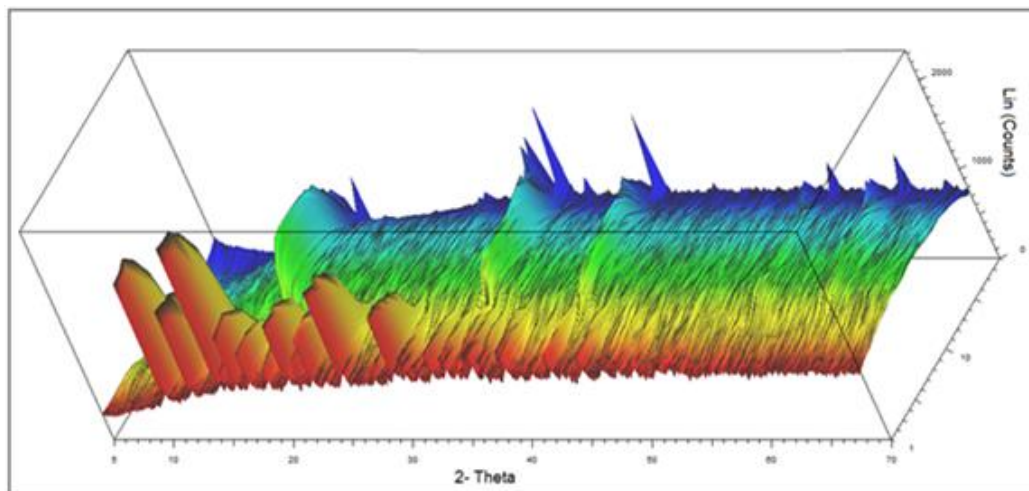

Figure 4.60: *In-situ PXRD VT-scan of LiCo₁.₀₉Mn₀.₉₁O₄ made from the citric acid precursor. The temperature scale is shown in arbitary units.*
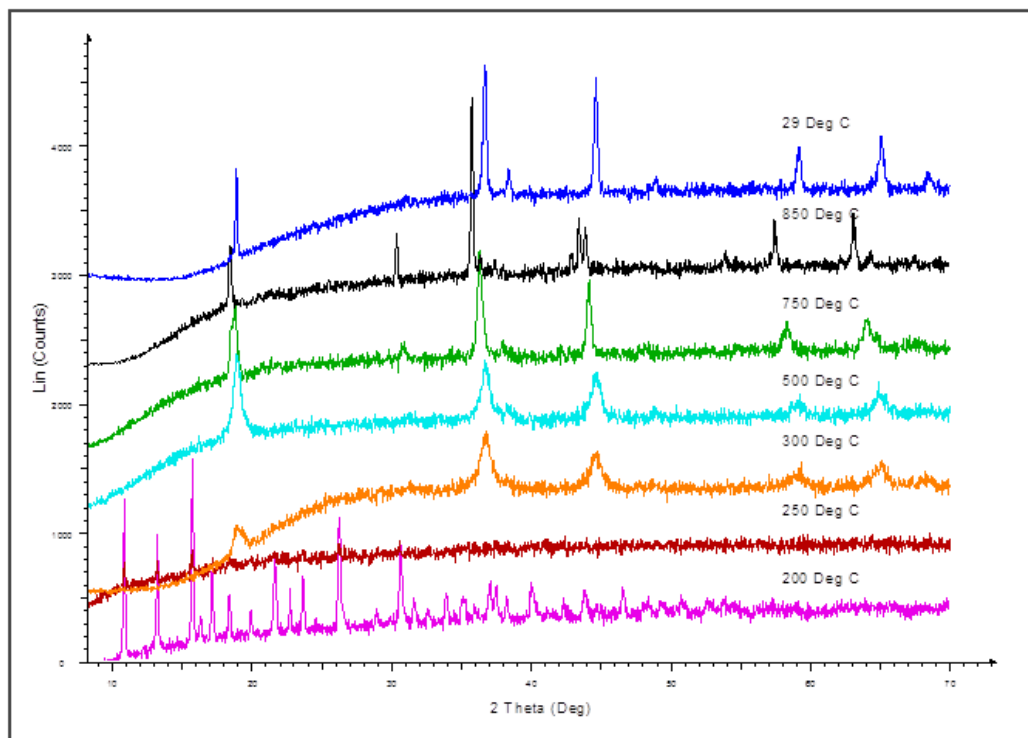
Figure 4.61: *Staggered PXRD patterns of LiCo₁.₀₉Mn₀.₉₁O₄ at specfic temperatures of interest from the in-situ set of results.*

The results showed that the precursor material was crystalline at room temperature up to about 250 °C. At 250 °C the crystal structure collapsed to form an amorphous phase until the sample reached 300 °C where the formation of the typical spinel crystalline phase ($LiCo_{1.09}Mn_{0.91}O_4$) was seen with the diffraction peaks being relatively broad, implying very small crystallites. As the temperature increased up to 850 °C, the diffraction peaks became significantly sharper, implying a growth in the crystallite size. A second disordered phase was observed to form at around 750 °C which became more distinctive at 850 °C. Peaks could be seen at 30.4, 42.8, 43.9, 53.9 and 64.3 °2θ. It was not possible to positively identify the phase, but could relate to a disordered spinel, which noticeably would change back to the single spinel structure when cooled to room temperature. The change in the crystal unit cell parameter (a) and the crystallite size (LVol-IB) from 300 to 850 °C is shown in Table 4.15 and Figure 4.62. For comparison purposes, the unit cell parameter and crystallite size at room temperature are also shown.

Table 4.10: Rietveld results of in-situ $LiCo_{1.09}Mn_{0.91}O_4$ analysis at specific temperatures.

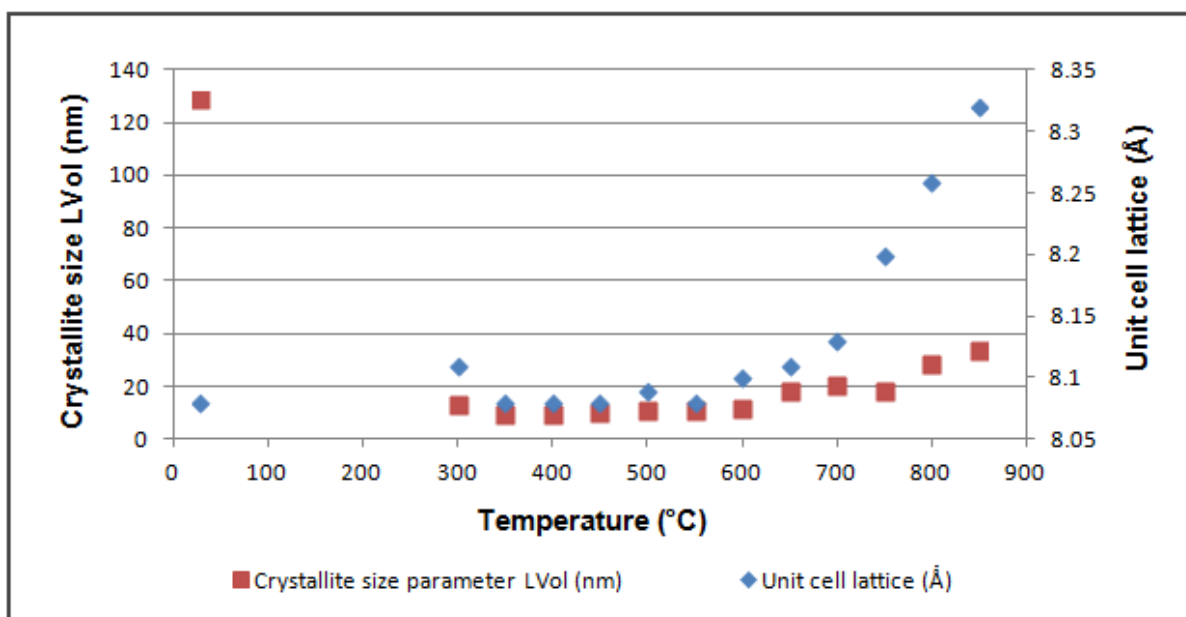| Temperature (°C)	Unit cell lattice (Å)	Crystallite size parameter LVol-IB (nm)
300	8.11	13.4
350	8.08	10.0
400	8.08	9.8
450	8.08	10.5
500	8.09	11.6
550	8.08	11.7
600	8.10	12.0
650	8.11	18.4
700	8.13	20.6
750	8.20	18.8
800	8.26	29.0
850	8.32	33.9
29	8.08	129.1

Figure 4.62: Graphical display of in-situ LiCo$_{1.09}$Mn$_{0.91}$O$_4$ Rietveld results.

The results showed that there was a noticable region from 300 to 550 °C where the unit cell lattice parameter did not change with an increase in temperature. A linear increase in the unit cell lattice expansion was determined to be about 0.93x10^{-3} Å.°C^{-1} as the temperature increased from 600 to 850 °C. This was signficantly higher than the previous three samples studied. When the sample was cooled back to room temperature, the unit cell lattice decreased to 8.08 Å, which was similar to the previously reported value (Table 4.6). The crystallite size based on the full Rietveld refinement of the diffraction pattern showed no signficant change in the crystallite size parameter (LVol-IB) up to 600 °C. From 650 to 850 °C the crystalite size changed only about 0.08 nm.°C^{-1} over that specific temperature range. It must be remembered that there was a second phase forming at 750 to 850 °C and that the crystallite size determination and lattice parameter were only determined for the predominant spinel phase. On cooling the sample to room temperature, the material changed to consist of only the single spinel LiCo$_{1.09}$Mn$_{0.91}$O$_4$ phase (Figures 4.50 and 4.51) where the calculated LVol-IB parameter at room temperature was 129 nm, a 183 % increase when compared to the LVol-IB parameter at 850 °C. This large increase in crystallite size could be attributed to the phase transition that occurred during the cooling stage of the material, where the crystallites are allowed to conglomerate into larger groups during the phase transition. This could be confirmed by repeating the in-situ

analysis of the sample, and allowing for a stepwise diffraction scan to be done at certain cooling temperature intervals.

The results showed that the doping of the manganese spinel with an almost 1:1 ratio of Co to Mn allowed for the formation of smaller crystallites to occur of around 12 nm up to the temperature of 600 °C. The TGA results (Figure 4.4) for this material showed a decomposition at 250 °C which related to the amorphous phase change (from in-situ results at 250 °C). Thereafter at 300 °C and above, the spinel oxide was formed, where the TGA results showed no further mass loss to occur during heating.

4.3.3 $LiNi_{0.5}Mn_{1.5}O_4$

The in-situ PXRD scan of the precursor material as it changed with temperature to form the final $LiNi_{0.5}Mn_{1.5}O_4$ is shown in Figure 4.63. Selected diffraction patterns of interest at certain temperatures are shown in a staggered format in Figure 4.64.
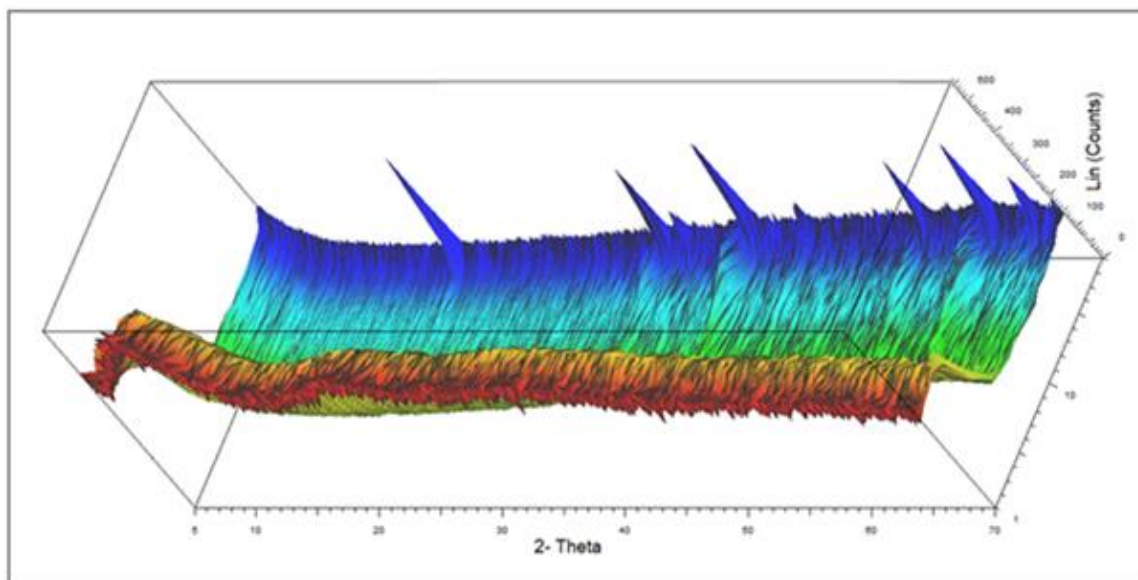

Figure 4.63: *In-situ PXRD VT-scan of $LiNi_{0.5}Mn_{1.5}O_4$ made from the citric acid precursor. The temperature scale is shown in arbitary units.*
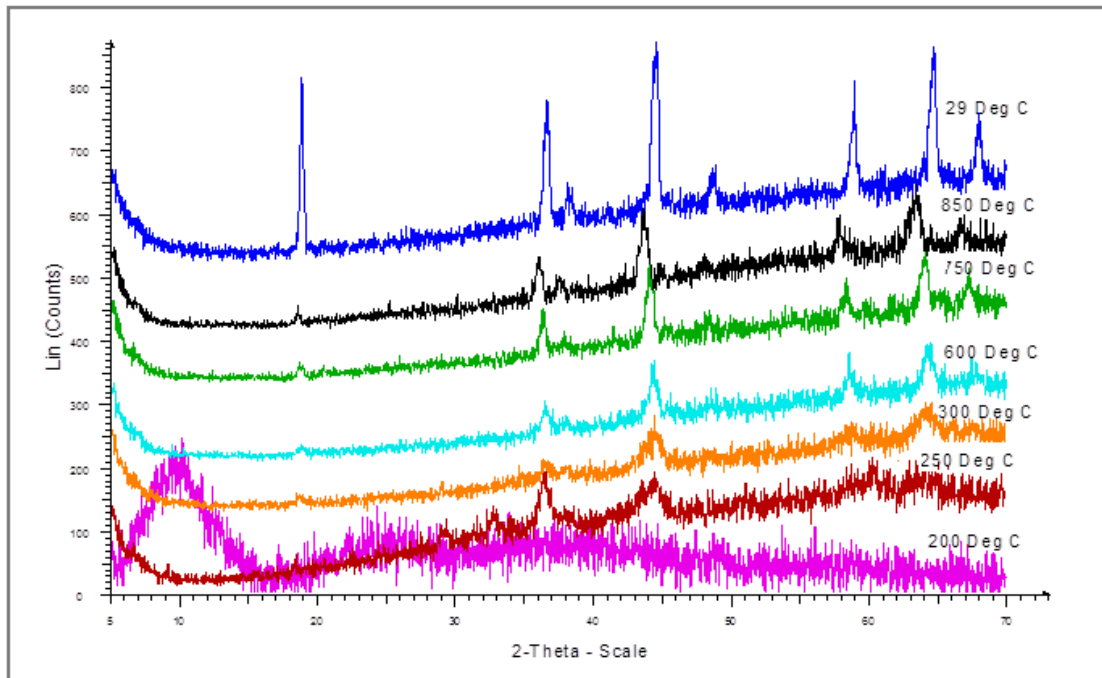
Figure 4.64: *Staggered PXRD patterns of LiNi$_{0.5}$Mn$_{1.5}$O$_4$ at specfic temperatures of interest from the in-situ set of results.*

The results of the in-situ analysis showed that there was an unusually large amorphous halo from room temperature to about 200 °C. The analysis was repeated on the same sample and showed the same unusually large diffraction halo. At about 250 °C the formation of the crystalline material could be seen, where the diffraction pattern at 250 °C would show some additional diffraction peaks (29, 33 and 60 °2θ) that would imply the formation of a second phase besides the typical spinel crystalline phase (LiNi$_{0.5}$Mn$_{1.5}$O$_4$). As the temperature increased to 850 °C, the second phase disappeared and the peaks for the spinel phase became more distinctive and sharper at the higher temperatures implying a growth in sample's crystallite size. The change in the crystal unit cell parameter (a) and the crystallite size (LVol-IB) from 300 to 850 °C are shown in Table 4.16 and Figure 4.65. For comparison purposes, the unit cell parameter and crystallite size at room temperature are also shown.

Table 4.16: Rietveld results of in-situ $LiNi_{0.5}Mn_{1.5}O_4$ analysis at specific temperatures.

Temperature (°C)	Unit cell lattice (Å)	Crystallite size parameter LVol-IB (nm)
300	8.20	4.92
350	8.22	5.33
400	8.18	5.52
450	8.17	6.75
500	8.16	7.48
550	8.19	7.73
600	8.18	9.95
650	8.20	10.55
700	8.19	12.16
750	8.22	18.89
800	8.24	19.54
850	8.28	20.00
29	8.12	28.72

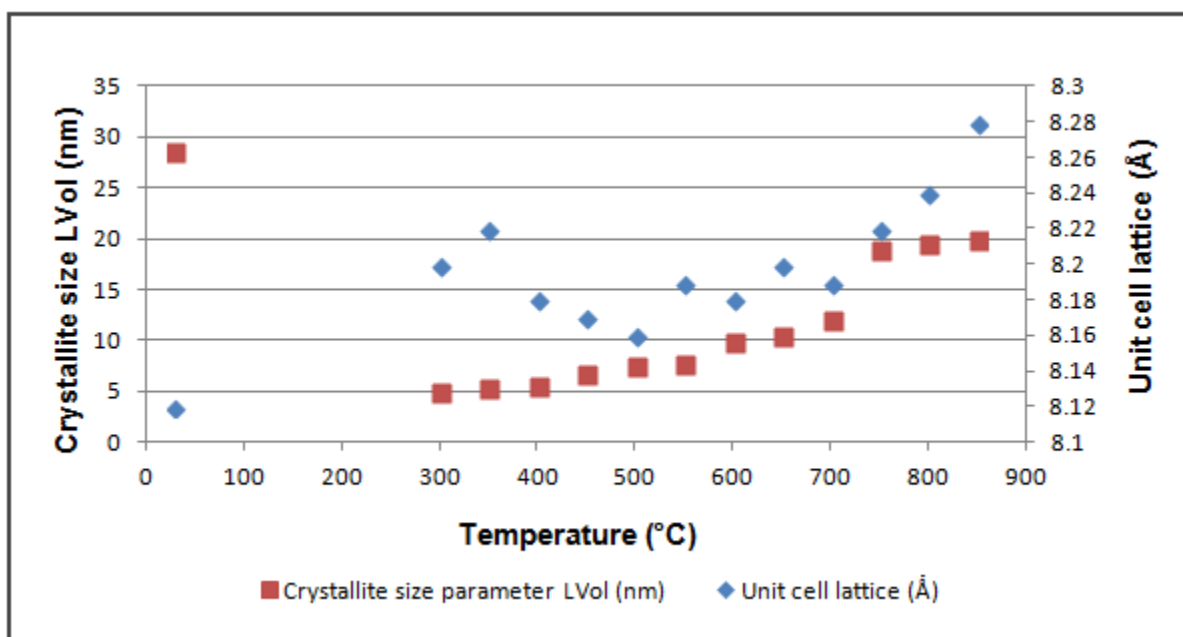*Figure 4.65: Graphical display of in-situ $LiNi_{0.5}Mn_{1.5}O_4$ Rietveld results.*

Due to the poor quality of the diffraction patterns obtained from the in-situ analysis, the determined unit cell lattice (a) and crystallite size (LVol-IB) parameters would not have been that accurate for samples analyzed up to 600 °C. The degree of crystallinity and diffraction peaks became more distinquishable at the higher temperatures. The results showed that there was a linear increase in unit cell lattice expansion of about 0.37×10^{-3} $\text{Å}.°C^{-1}$ as the temperature increased from 600 to 850 °C. When the sample was cooled to room temperature, the unit cell lattice decreased to 8.12 Å, which was slightly lower to the previously reported value (Table 4.6). The crystallite size of the material based on the full Rietveld refinement of the diffraction pattern showed that it remained relatively the same up to about 700 °C (~10 nm). There was a slight increase in the crystallite size at 750 °C to about 19 nm, after further heating to 850 °C, the LVol-IB only increased to 20 nm. Upon cooling the sample back to room temperature, a slight increase in LVol-IB was observed for the final $LiNi_{0.5}Mn_{1.5}O_4$ phase of about 29 nm (Figures 4.63 and 4.64).

The results showed that the doping of the manganese spinel with a small amount of Ni allowed for the formation of smaller crystallites around 20 nm up to the high temperature of 850 °C. These crystallite sizes remained relatively stable upon cooling to give a room temperature crystalline phase with a crystallite size of 28 nm. These results are in agreement with the TGA results (Figure 4.3) that showed multiple weight loss decomposition steps, relating to the various phase changes (from precursor to final oxide) within these in-situ results. At 250 °C (from the in-situ results) an intermediate phase change was obtained correlating to the weight decomposition between 200 to 300 °C from its TGA results. The final spinel oxide was formed at 350 °C (from the in-situ results) and correlated to the observation of no weight loss (from the TGA analysis) at 400 °C.

Table 4.17 summarizes the various calculated results obtained from the in-situ PXRD analysis. The unit cell lattice parameter (a) together with its crystallite size parameter (LVol-IB) at room temperature and 850 °C are shown together with the relative changes observed over the temperature ranges.

Table 4.17: Summary of the spinel oxide materials studied by in-situ PXRD .

Sample	$Li_{1.03}Mn_{1.97}O_4$	$LiAl_{0.4}Mn_{1.6}O_4$	$Li_{1.03}Mg_{0.2}Mn_{1.77}O_4$	$LiCo_{1.09}Mn_{0.91}O_4$	$LiNi_{0.5}Mn_{1.5}O_4$
Unit cell lattice parameter - literature (Å)	8.23 – 8.24	8.20	8.22	8.06 – 8.07	8.18
Unit cell lattice parameter at 800 ºC-batch sol-gel process(Å)	8.20	8.16	8.19	8.07	8.16
Unit cell lattice parameter after cooling to room temperature (Å)	8.24	8.18	8.22	8.08	8.12
Crystallite size parameter LVol-IB after cooling to room temperature (nm)	137.8	102	44.7	129.1	28.72
Unit cell lattice parameter at 850 °C (Å)	8.37	8.30	8.24	8.32	8.28
Crystallite size parameter LVol-IB at 850 °C (nm)	104.8	62.0	53.9	33.9	20.0
Slope of the change in the unit cell lattice with temperature from 600 to 850 °C(Å.°C^{-1})	0.32×10^{-3}	0.25×10^{-3}	0.27×10^{-3}	0.93×10^{-3}	0.37×10^{-3}
Slope on change in crystallite size (nm.°C^{-1})	0.34	0.25	0.15	0.08	0.05
% change in crystallite size from 600 to 850 °C	323	147	296	183	64

The unit cell lattice parameter, a, (Å) and crystallite size parameter, LVol-IB, (nm) of the doped spinel materials were comparatively slightly smaller at room temperature and 850

°C when compared to the undoped $Li_{1.03}Mn_{1.97}O_4$ spinel oxide material. This decrease would be due to the fact that the doped metals (Al, Ni, Co and Mg) partially substituted Mn within the crystal unit cell of the spinel oxide. The change in the unit cell lattice parameter when heated from 600 to 850 °C showed similar increases for the Ni, Mg and Al doped materials when compared to the undoped $Li_{1.03}Mn_{1.97}O_4$. Except for the Co doped material, there was a significant bigger change in the spinel lattice parameter upon heating. The room temperature lattice parameter for all materials was slightly higher to those synthesized by batch process and similar to that reported in literature (however, slightly lower for $LiAl_{0.4}Mn_{1.6}O_4$), except for the Ni doped oxide (poor quality of the diffraction patterns as discussed under Section 4.3.3); however these difference is within negligible error range. These differences observed could be due to minor variations within the material composition, changes within the manganese oxidation and experimental error.

A significant change was observed in the crystallite size, LVol-IB, of the various samples analysed upon heating from 600 °C to 850 °C. This study showed that upon heating to around 400 °C, all the spinel crystalline phase material would have formed for both the doped and undoped $Li_{1.03}Mn_{1.97}O_4$. Upon heating to 600 °C, the spinel phase in most of the samples studied showed a spinel phase composition with a relatively consistent small crystallite size, which would change significantly when heated to 850 °C. This implied that the crystallites would start to "fuse" together to form larger crystals at these temperatures. These results are in agreement with the BET surface area analysis of the spinel materials made by the spray-drying technique at 400 °C (Table 4.6). Even though the process is considerably different to the batch method of heating a sample within a sample holder of a furnace or in-situ stage, it does imply that samples heated to lower temperatures could result in samples with significantly larger surface area, where the particles are significantly smaller. BET surface area analysis of a batch sample made at 600 °C confirmed this where the area was 13.75 $m^2.g^{-1}$ when compared to a $Li_{1.03}Mn_{1.97}O_4$ (8.67 $m^2.g^{-1}$) sample made at 800 °C. This implies that the particles should be significantly smaller of the material made at the lower temperature (refer to Table 4.18).

Table 4.18 summarizes the BET surface area for the various oxide materials synthesized at 400 (method 3), 600 (method 2) and 800 °C (method 1) respectively. Based on the results from the TGA and PXRD study, a batch of material (at 600 °C) of the various doped Mn spinel oxides were synthesized (by batch sol-gel technique) and their respective BET surface areas and crystallite sizes by PXRD room temperature were determined and compared. The temperature at 600 °C was chosen since the crystallite size for all the oxides would significantly increase at temperatures above (refer to its in-situ results Section 4.3).

Table 4.18: Summary of the spinel oxide materials BET surface area and crystallite sizes at various temperatures.

	BET Surface area at 800 °C ($m^2.g^{-1}$)	Crystallite size at 800 °C (nm)	BET Surface area at 600 °C ($m^2.g^{-1}$)	Crystallite size at 600 °C (nm)	BET Surface area at 400 °C ($m^2.g^{-1}$)	Crystallite size at 400 °C (nm)
$Li_{1.03}Mn_{1.97}O_4$	8.67	33.984	13.75	26.958	14.11	13.380
$LiAl_{0.4}Mn_{1.6}O_4$	18.15	21.596	23.64	19.301	29.80	9.379
$Li_{1.03}Mg_{0.2}Mn_{1.77}O_4$	9.68	43.157	11.85	20.698	19.91	12.726
$LiCo_{1.09}Mn_{0.91}O_4$	12.25	28.564	22.46	12.686	26.15	9.112
$LiNi_{0.5}Mn_{1.5}O_4$	6.12	18.117	17.72	15.105	19.48	11.228

The materials' BET surface area (refer to Table 4.18) at 800 °C (by batch sol-gel) were lower when compared to the surface area of the materials synthesised at 400 °C by the spray technique and at 600 °C (using batch sol-gel). Comparatively, the Al doped manganese oxide spinel was shown to have the higher material BET surface area, followed by the Co doped material. Noticeably, the Ni doped oxide made at 800 °C showed to have a relatively small BET surface area of 6.12 $m^2.g^{-1}$.

Of interest was also to compare the differences in the BET surface areas to the crystallite size parameter LVol-IB (nm) (refer to Table 4.18). The results showed that there was a correlation between the materials BET surface area and the crystallite size parameter

LVol-IB of the crystalline phase. Noticeably, the material with the higher surface area as determined by BET gas adsorption also showed to have smaller crystallites.

However, care should be taken not to confuse the crystal or particle sizes of materials that can infer a larger bulk material surface area that has smaller particles as it would be determined by other methods such as laser diffraction. In this study, laser diffraction particle size determination was not done and the average crystallite sizes of the material's particles were determined based on the broadening of the diffraction peak of a powder diffraction pattern. In this case a correlation was observed between the bulk materials' average crystallite size and the respective BET surface area. This factor would then become important to study the electrochemical properties of the materials, where a cathode active material with a larger surface area and a smaller crystallite size would be desired to increase the materials capacity utilisation.

In summary, the study showed that the room temperature precursor materials consisted either of an amorphous phase or a crystalline citrate type phase. Some of the intermediate phases that formed upon heating were shown to either collapse to an amorphous or semi-crystalline Mn_2O_3 phase. Within this study a reasonably pure cathode oxide material was obtained at 400 °C, where the TGA study showed on average, that no other decomposition products formed above this temperature. In-situ PXRD results showed that as the materials that were heated would undergo phase changes up to 400 °C after which the crystallite size and lattice parameter of the formed spinel phase would change with further increase in temperature. The Co doped spinel material showed to form a secondary phase at 800 °C, which then disappeared when the material was cooled to room temperature.

4.4 <u>Microscopy analysis</u>

Atomic Force Microscopy (AFM) and Scanning Electron Microscopy (SEM) analysis were done on all the oxide materials synthesized by both the batch sol-gel technique at 800 °C (method 1 in Chapter 3) and by the spray-drying technique at 400 °C (method 2 in Chapter 3) respectively. This was done in order to give insight into the particle size and shape and to compliment the results obtained from the BET surface area and crystallite size parameter determined by PXRD (Chapter 4. 2 Table 4.6).

4.4.1 Li$_{1.03}$Mn$_{1.97}$O$_4$

The SEM micrographs of pure Li$_{1.03}$Mn$_{1.97}$O$_4$ by batch sol-gel synthesis technique at 800 °C (a, c and e) and spray-drying synthesis technique at 400 °C (b and d) are shown in Figure 4.66. The micrographs of the two synthesis techniques at the same magnification are displayed following each other. Whereas the AFM scans of the pure oxide were shown in Figure 4.67.

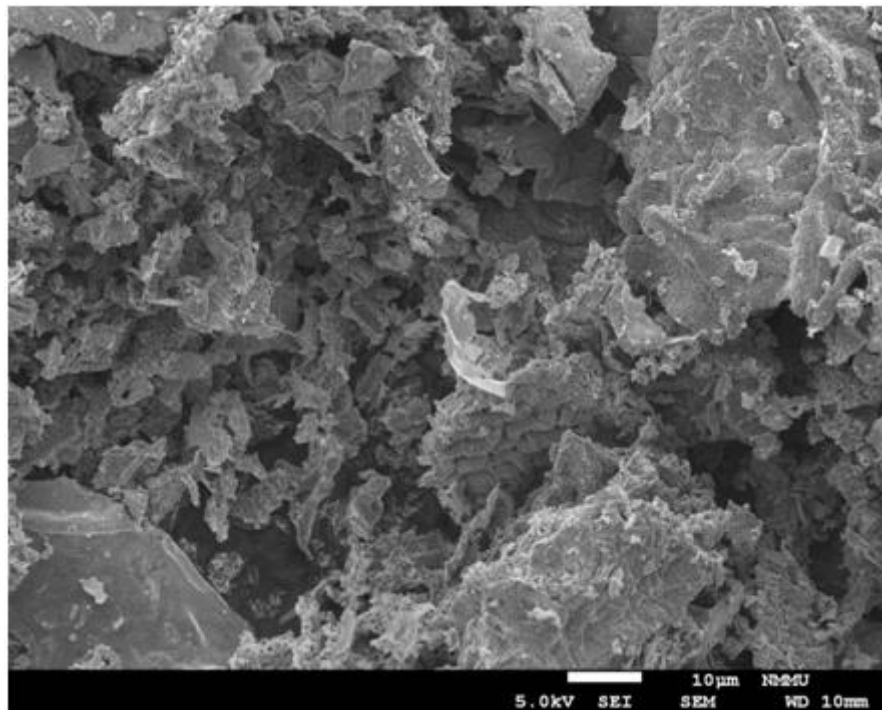**Figure 4.66 (a): Li$_{1.03}$Mn$_{1.97}$O$_4$ by batch sol-gel at 800 °C**

Figure 4.66 (b): $Li_{1.03}Mn_{1.97}O_4$ by spray-drying at 400 °C
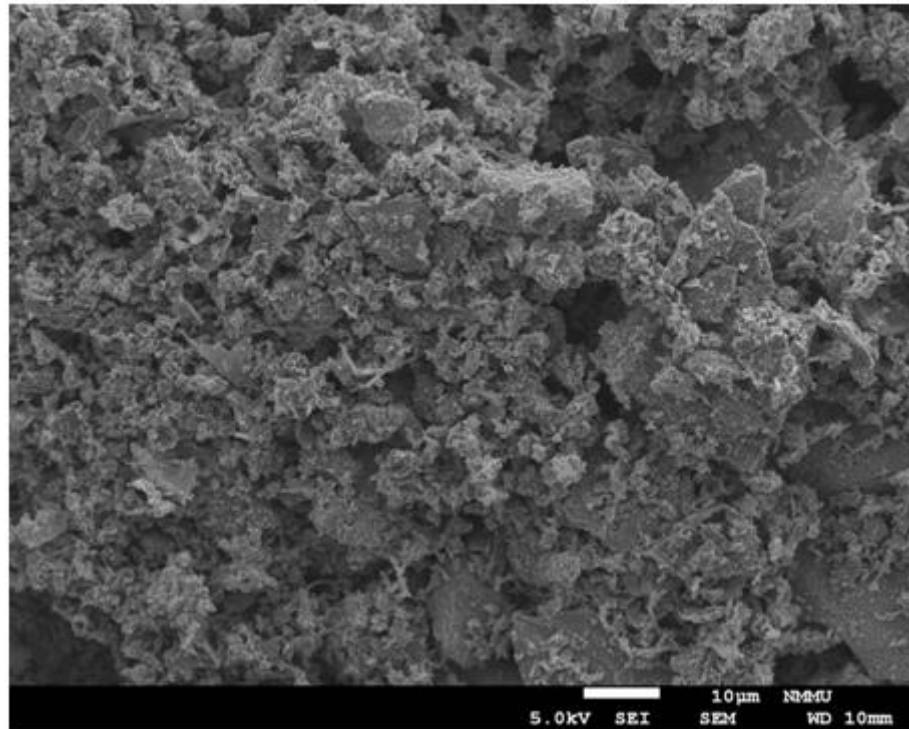
Figure 4.66 (c): $Li_{1.03}Mn_{1.97}O_4$ by batch sol-gel at 800 °C
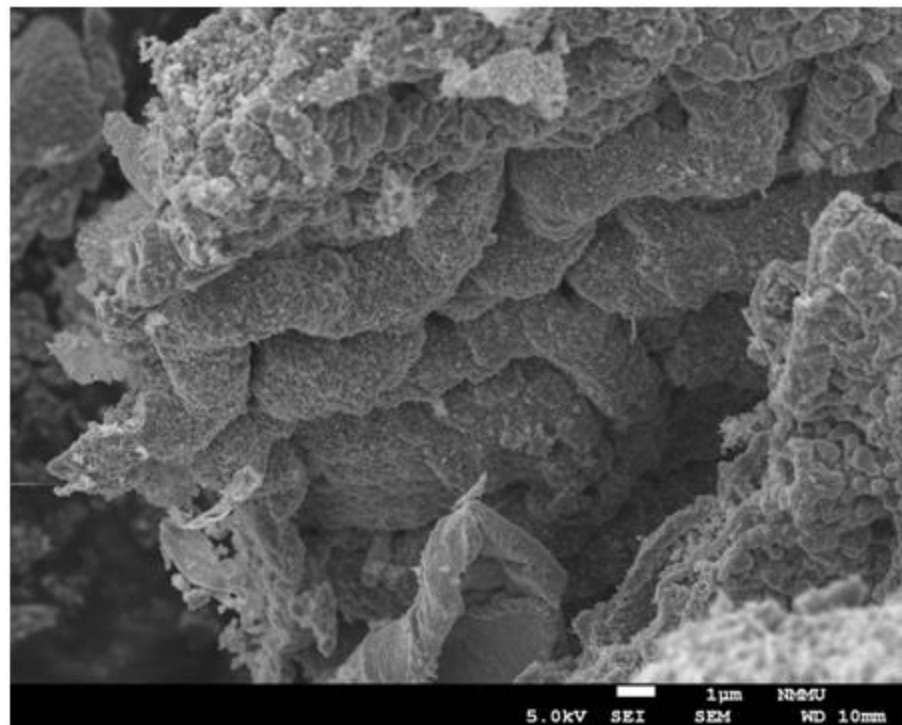
Figure 4.66 (d): Li$_{1.03}$Mn$_{1.97}$O$_4$ by spray-drying at 400 °C
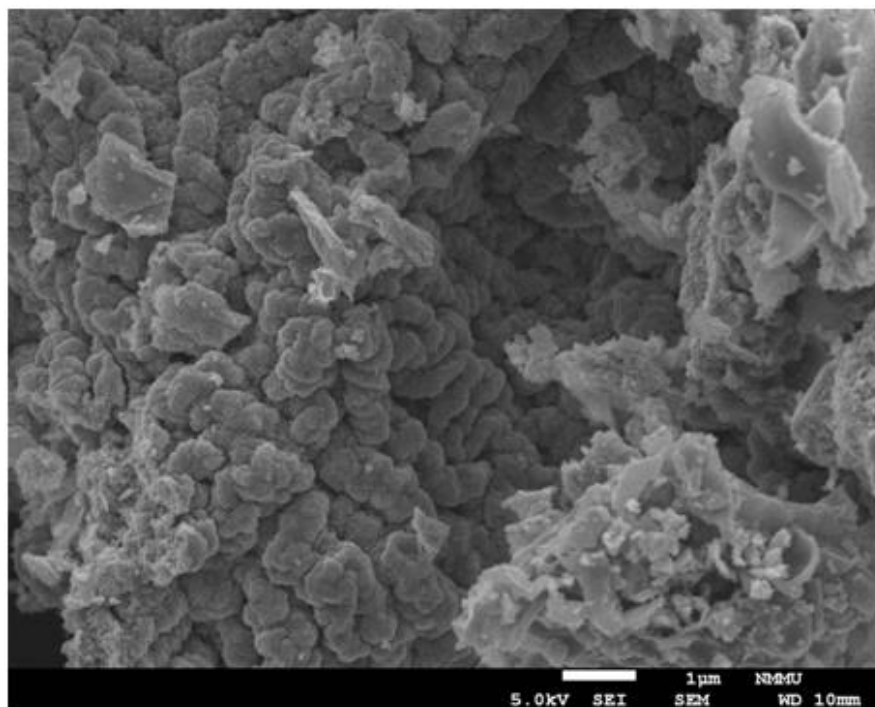
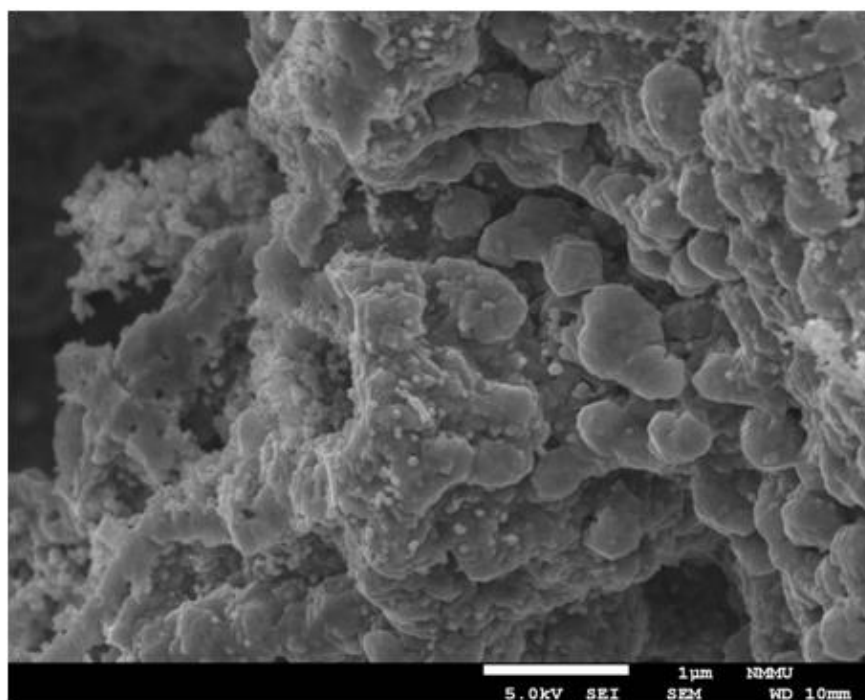**Figure 4.66 (e): Li$_{1.03}$Mn$_{1.97}$O$_4$ by batch sol-gel at 800 °C**

Figure 4.66: SEM micrographs of Li$_{1.03}$Mn$_{1.97}$O$_4$ synthesized by batch sol-gel and spray-drying techniques at various magnifications.

The SEM images (Figure 4.66 a) showed that the material consisted of irregular shaped crystals of various shapes and sizes. At higher magnification (Figures 4.66 c and e) some smaller clustered type regions that were made up of smaller almost spherical crystals should be seen.
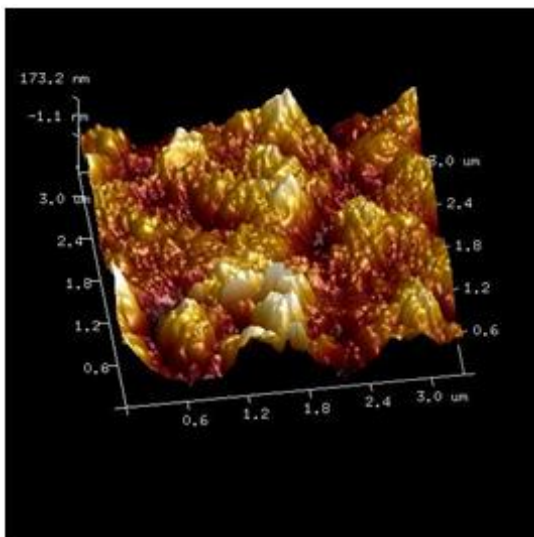
The oxide material synthesized by the spray-drying method showed a slightly different morphology (Figures 4.66 b and d) with respect to batch sol-gel synthesized $Li_{1.03}Mn_{1.97}O_4$ material. The spray-dried material was less clustered with loser network packing of particles.

With respect to the AFM scans reported at the different magnifications, where possible a magnification scale down to 100 nm was used. Some results showed poor resolution at the lower magnification, where the higher magnification of 300 nm was preferentially used (Figure 4.67).

The AFM imaging (Figure 4.67), which is a surface topology indication of the material, showed that the spheres formed a network of conglomerates with ridges or passages between them (Figures 4.67 images a and b). The individual spherical particles were shown to be about 25 to 50 nm (Figure 4.67 image d at 100 nm scale).

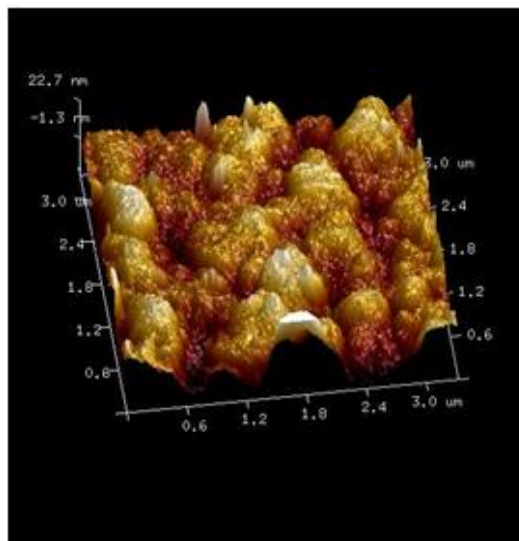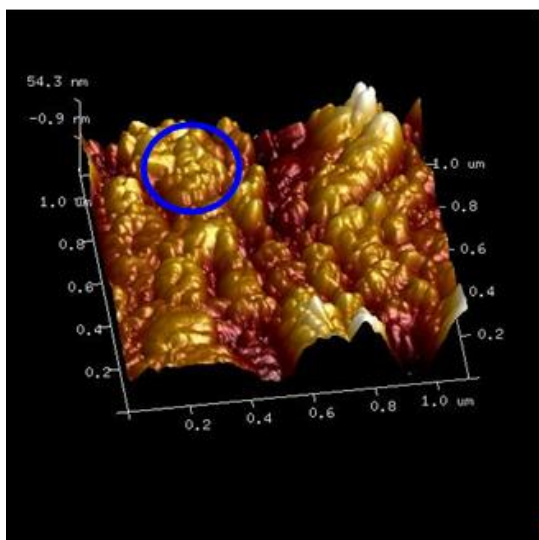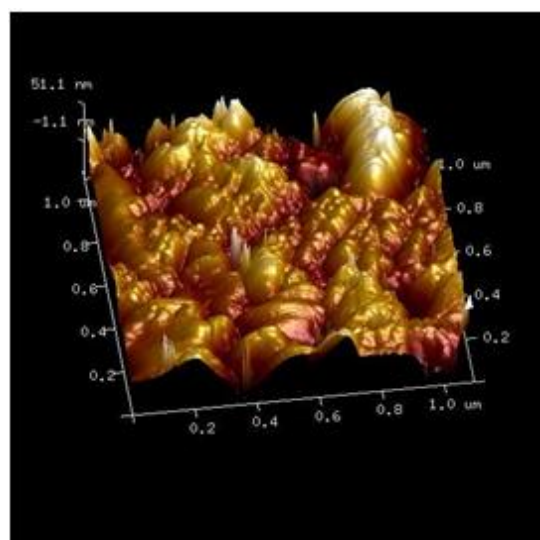| Li$_{1.03}$Mn$_{1.97}$O$_4$ prepared by batch sol-gel at 800 °C	Li$_{1.03}$Mn$_{1.97}$O$_4$ prepared by spray-drying at 400 °C
(a)	**(e)**
3.0 μm scale	3.0 μm scale
(b)	**(f)**
1.0 μm scale	1.0 μm scale

Figure 4.67: AFM scans of Li$_{1.03}$Mn$_{1.97}$O$_4$ synthesized by batch sol-gel (a and b) and spray-drying (e and f) techniques at various magnifications.

$Li_{1.03}Mn_{1.97}O_4$ prepared by batch sol-gel at 800 °C	$Li_{1.03}Mn_{1.97}O_4$ prepared by spray-drying at 400 °C
(c) 300 nm scale	**(g)** 300 nm scale
(d) 100 nm scale	**(h)** 100 nm scale

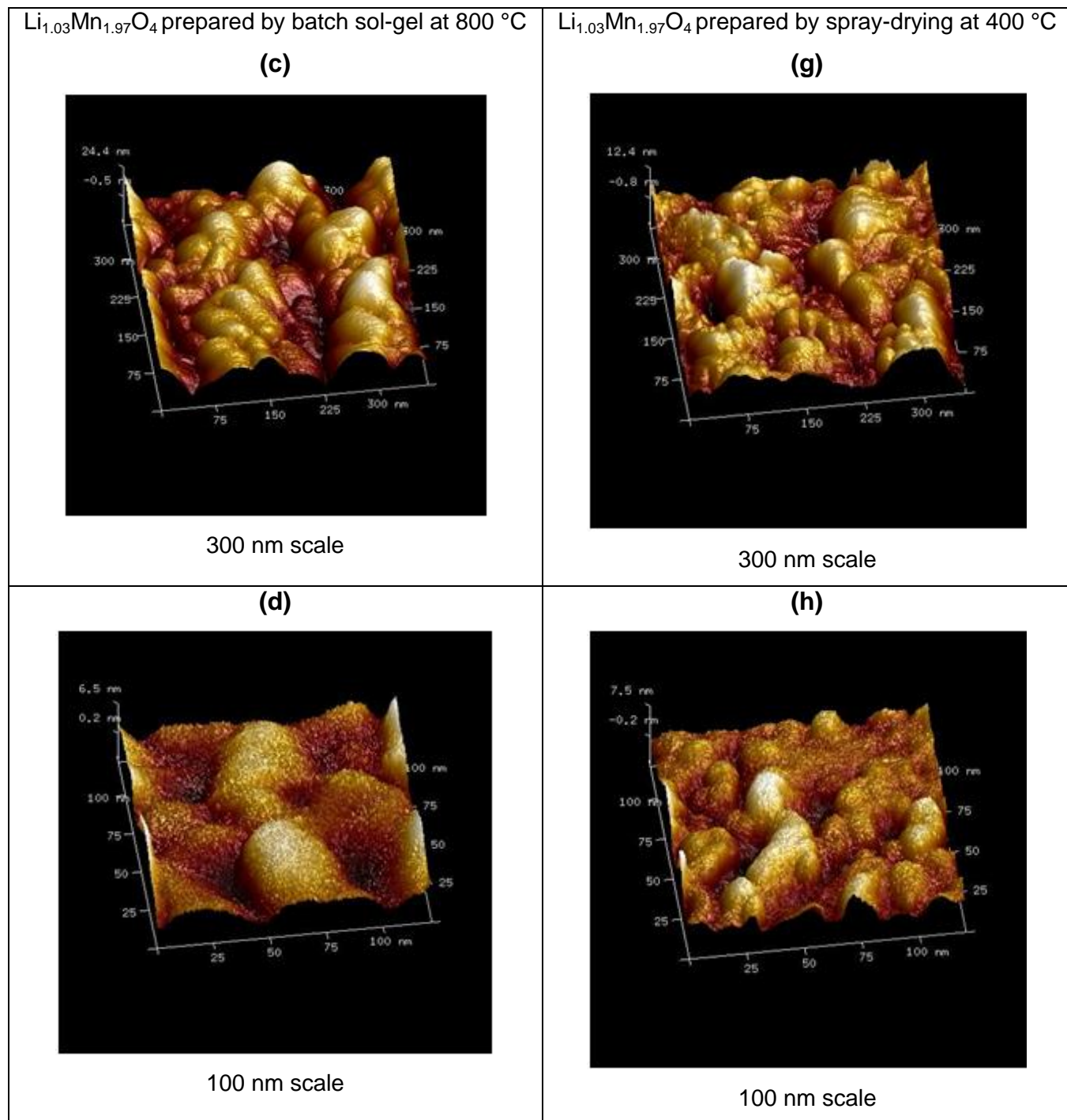*Figure 4.67 continued: AFM scans of $Li_{1.03}Mn_{1.97}O_4$ synthesized by batch-sol-gel (c and d) and spray-drying (g and h) techniques at various magnifications.*

The AFM images of the spray-dried material showed also to contain much smaller and finer particles. At the higher magnifications (Figures 4.67 g and h) the spray-drying

technique produced small spherical particles between 10 to 15 nm when compared to the batch produced $Li_{1.03}Mn_{1.97}O_4$.

4.4.2 $\underline{LiAl_{0.4}Mn_{1.6}O_4}$

The SEM micrographs in Figure 4.68 are a representation of $LiAl_{0.4}Mn_{1.6}O_4$ synthesized by both the batch sol-gel at 800 °C (a and c) and spray-drying at 400 °C (b and d) techniques.

The results in Figure 4.68 showed that the particles with Al as dopant showed a more "flaky", or courser particle. However, at higher magnification (c) there were sections in the material that comprised of small clustered groups of spherical particles, which implies that the material synthesized as a batch at 800 °C did not result in homogenous shaped particles. This could also be seen on the spray-dried samples (b and d in Figure 4.68), where there were distinctive regions of very small particles within the larger "flaky" regions. These larger "flaky" shaped particles could also be seen by the AFM analysis (b and c in Figure 4.69) between the smaller rounder shaped particles at the lower magnification.

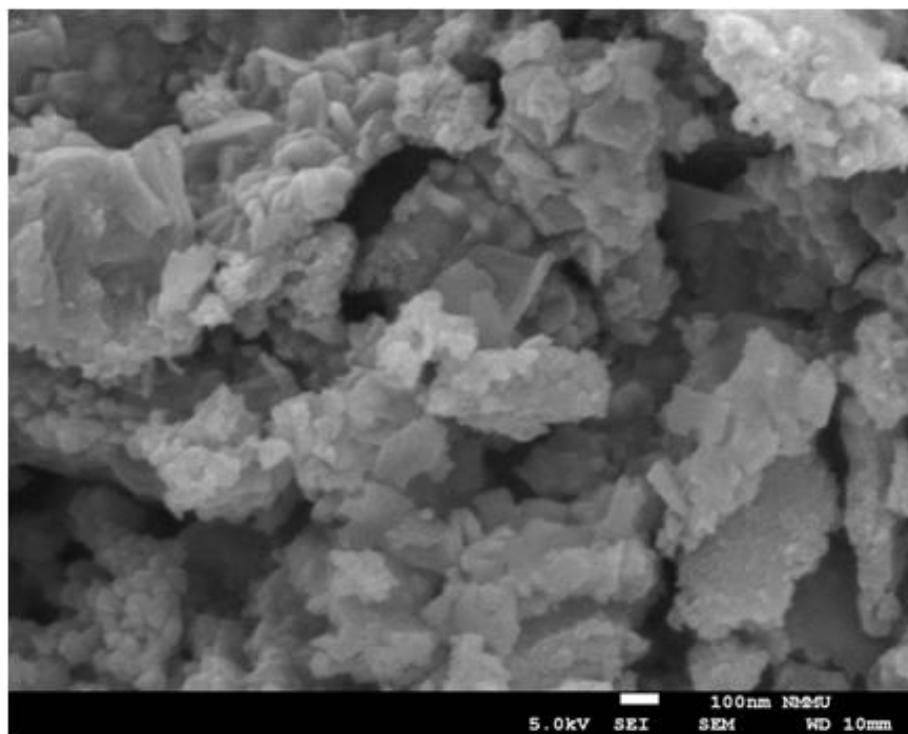**Figure 4.68 (a): LiAl$_{0.4}$Mn$_{1.6}$O$_4$ by batch sol-gel at 800 °C**

Figure 4.68 (b): LiAl$_{0.4}$Mn$_{1.6}$O$_4$ by spray-drying at 400 °C
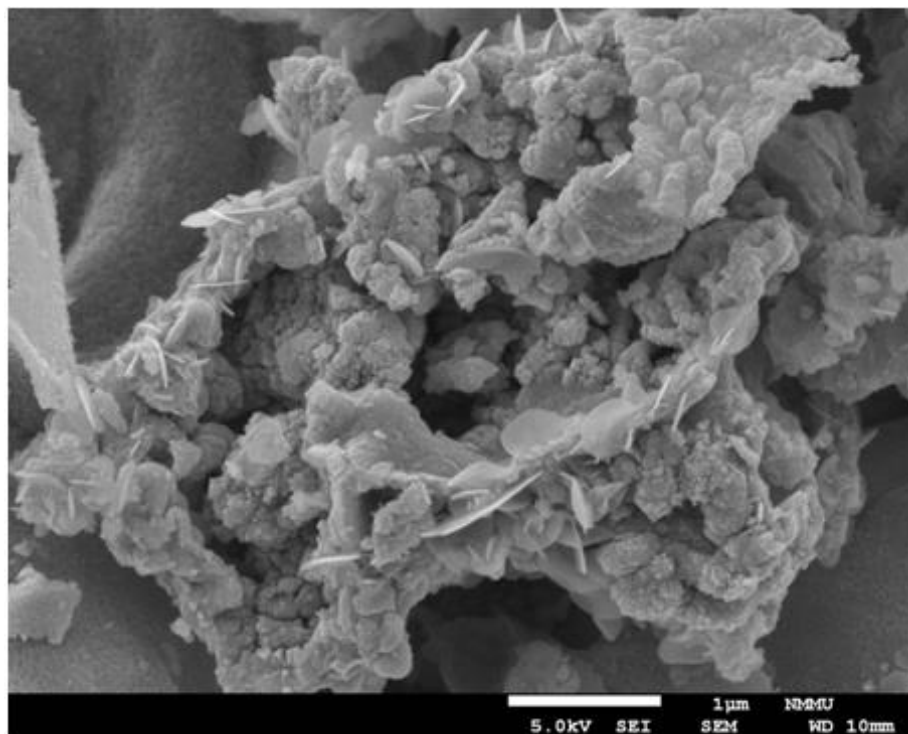
Figure 4.68 (c): LiAl$_{0.4}$Mn$_{1.6}$O$_4$ by batch sol-gel at 800 °C
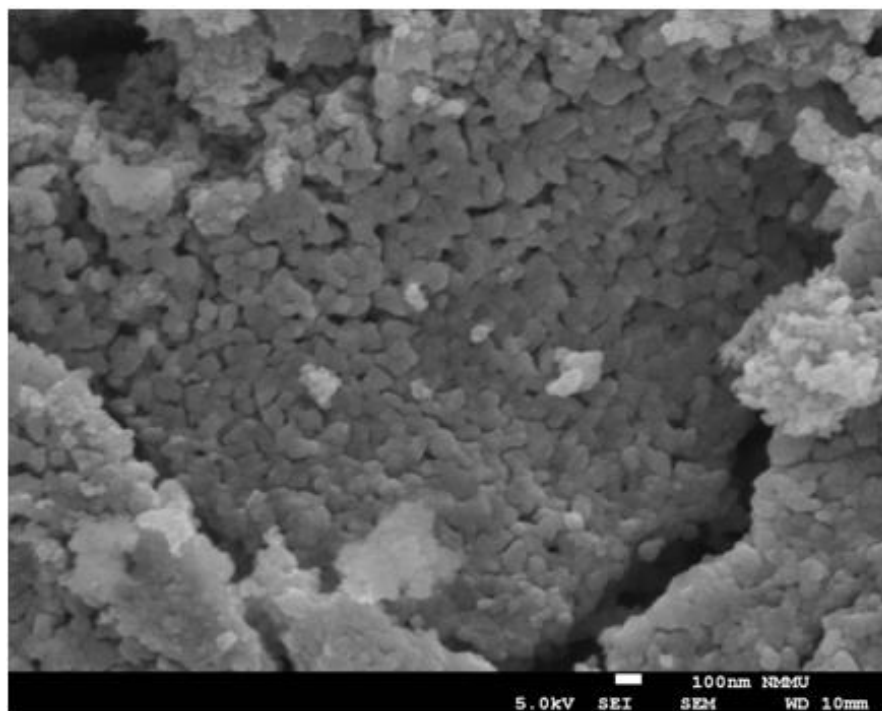
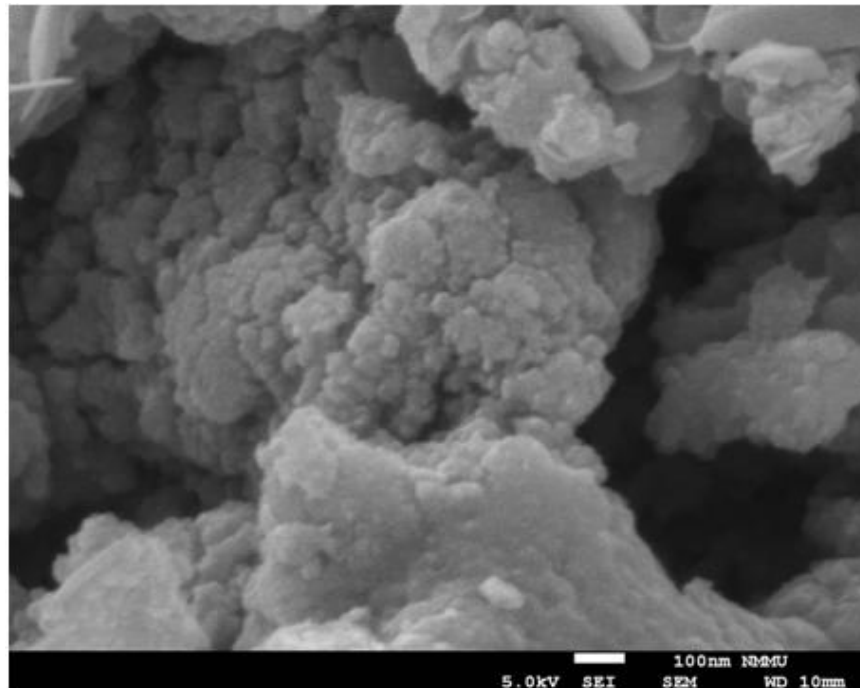**Figure 4.68 (d): LiAl$_{0.4}$Mn$_{1.6}$O$_4$ by spray-drying at 400 °C**

Figure 4.68: SEM micrographs of LiAl$_{0.4}$Mn$_{16}$O$_4$ synthesized by the batch sol-gel and spray-drying techniques at various magnifications.

LiAl$_{0.4}$Mn$_{1.6}$O$_4$ prepared by batch sol-gel at 800 °C	LiAl$_{0.4}$Mn$_{1.6}$O$_4$ prepared by spray-drying at 400 °C
(a)	**(d)**
3.0 µm scale	3.0 µm scale
(b)	**(e)**
1.0 µm scale	1.0 µm scale

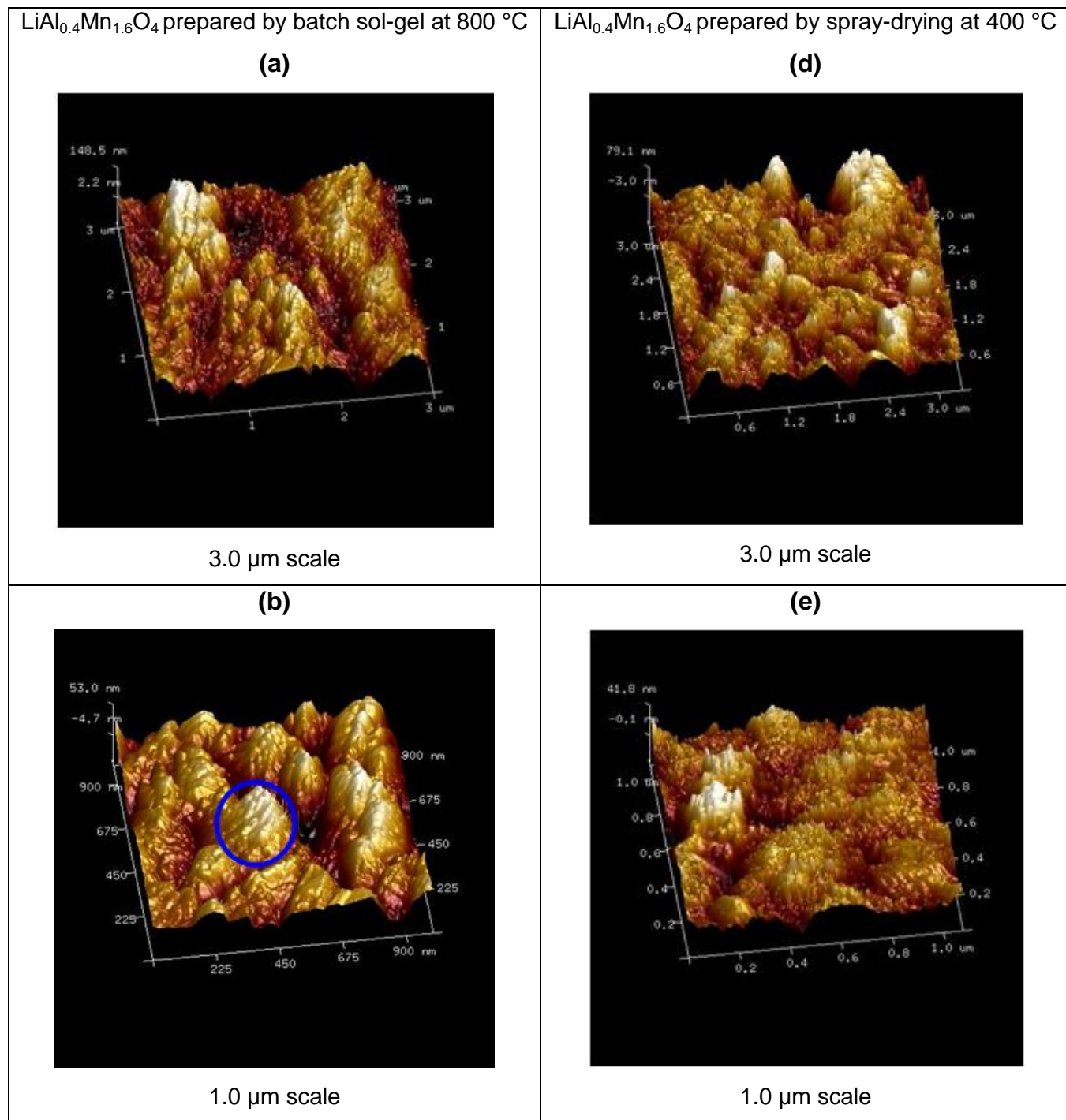*Figure 4.69: AFM scans of LiAl$_{0.4}$Mn$_{1.6}$O$_4$ synthesized by batch sol-gel (a and b) and spray-drying (d and e) techniques at various magnifications.*
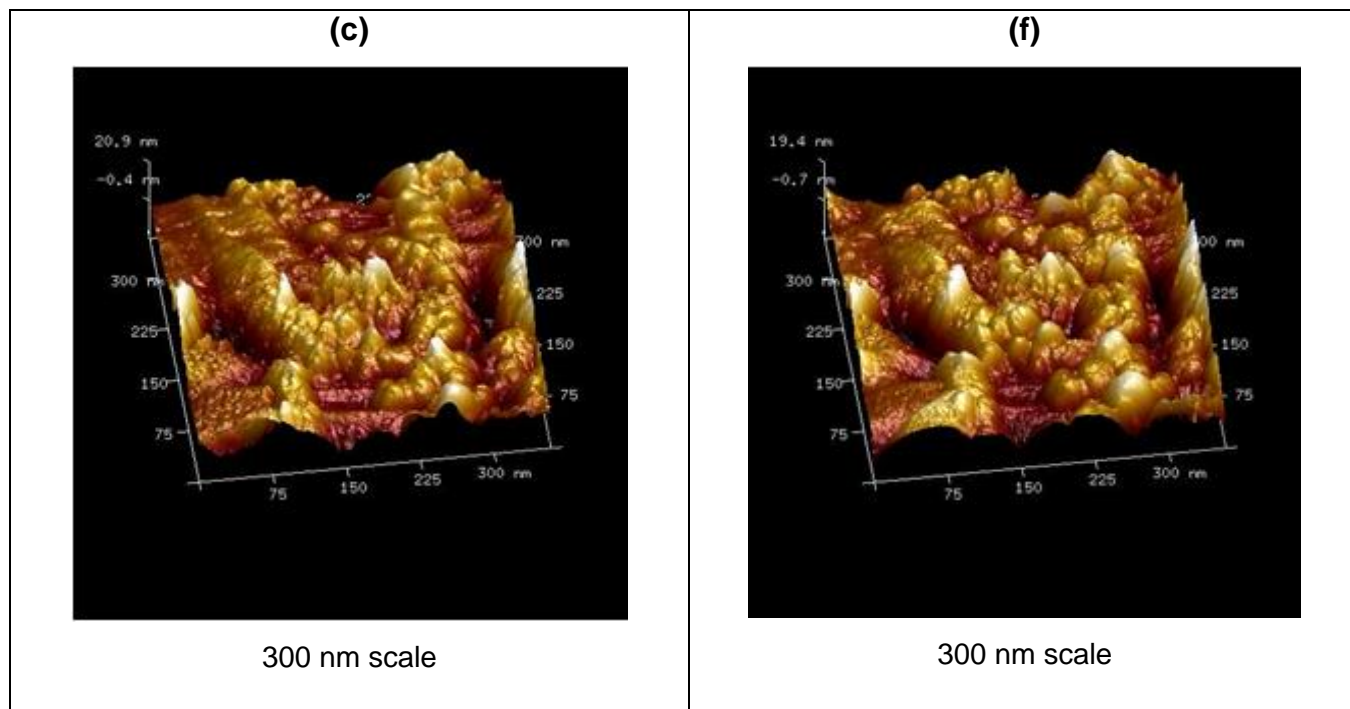
(c)	(f)
300 nm scale	300 nm scale

Figure 4.69 continued: AFM scans of LiAl$_{0.4}$Mn$_{1.6}$O$_4$ synthesized by batch sol-gel (c) and spray-drying (f) techniques at various magnifications.

The AFM images of material made by the spray-dry technique showed again the smaller particles that were typically between 5-10 nm (f in Figure 4.69).

4.4.3 Li$_{1.03}$Mg$_{0.2}$Mn$_{1.77}$O$_4$

SEM micrographs a to f in Figure 4.70 represent Li$_{1.03}$Mg$_{0.2}$Mn$_{1.77}$O$_4$ made by the batch sol-gel and spray-drying synthesis techniques.

The particles of the Li$_{1.03}$Mg$_{0.2}$Mn$_{1.77}$O$_4$ material synthesized by the batch method showed similar jiggered and "flaky" type particles (a, c and e Figure 4.70). The SEM images of the material that was made by the spray-drying process (b, d and f in Figure 4.70) showed an unusual coating on the particles that were in some places conglomerated into small clusters. This conglomeration effect of the finer particles was also observed when analyzing the samples by AFM (e and f in Figure 4.71).

Figure 4.70 (a): Li$_{1.03}$Mg$_{0.2}$Mn$_{1.77}$O$_4$ by batch sol-gel at 800 °C
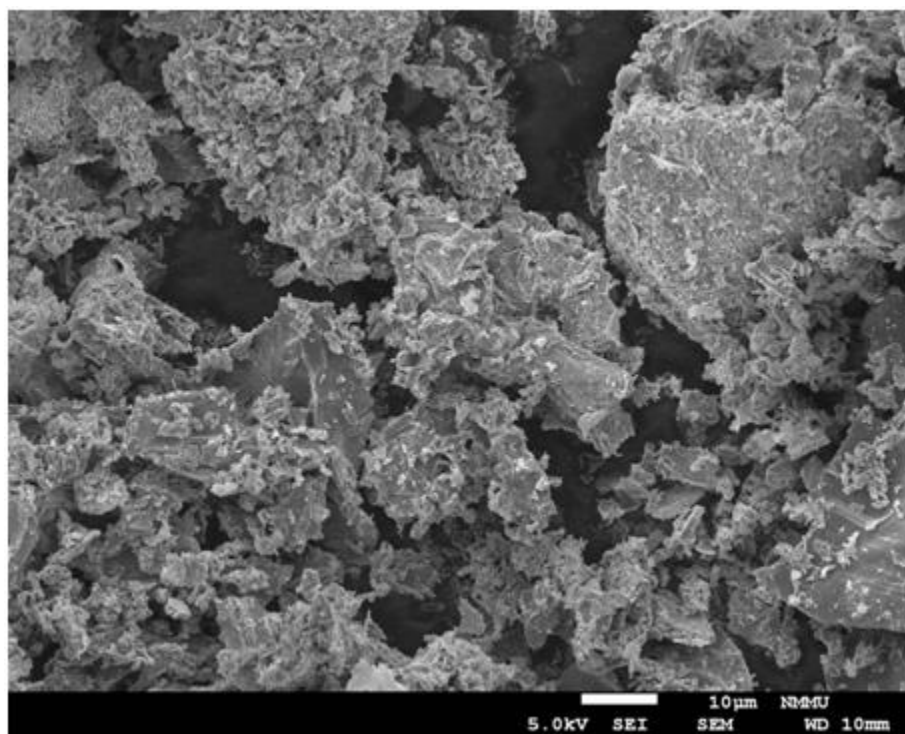
Figure 4.70 (b): Li$_{1.03}$Mg$_{0.2}$Mn$_{1.77}$O$_4$ by spray-drying at 400 °C
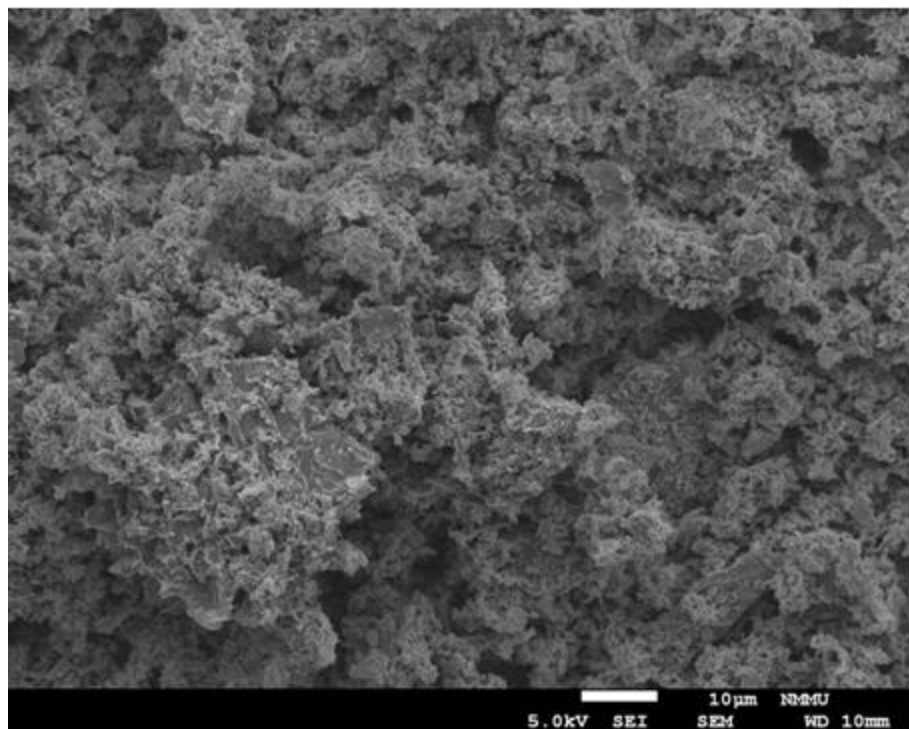
Figure 4.70 (c): $Li_{1.03}Mg_{0.2}Mn_{1.77}O_4$ by batch sol-gel at 800 °C
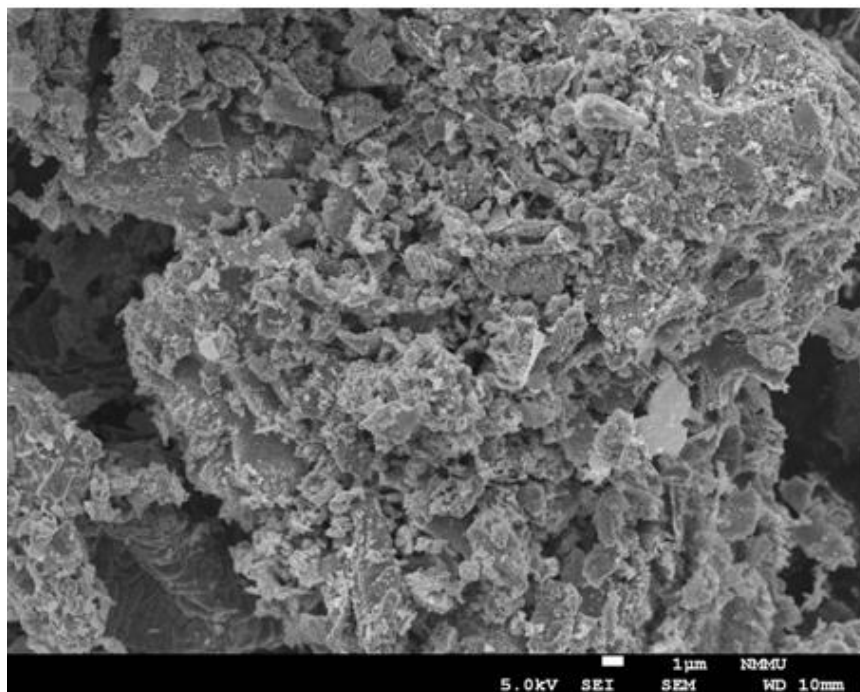
Figure 4.70 (d): $Li_{1.03}Mg_{0.2}Mn_{1.77}O_4$ by spray-drying at 400 °C
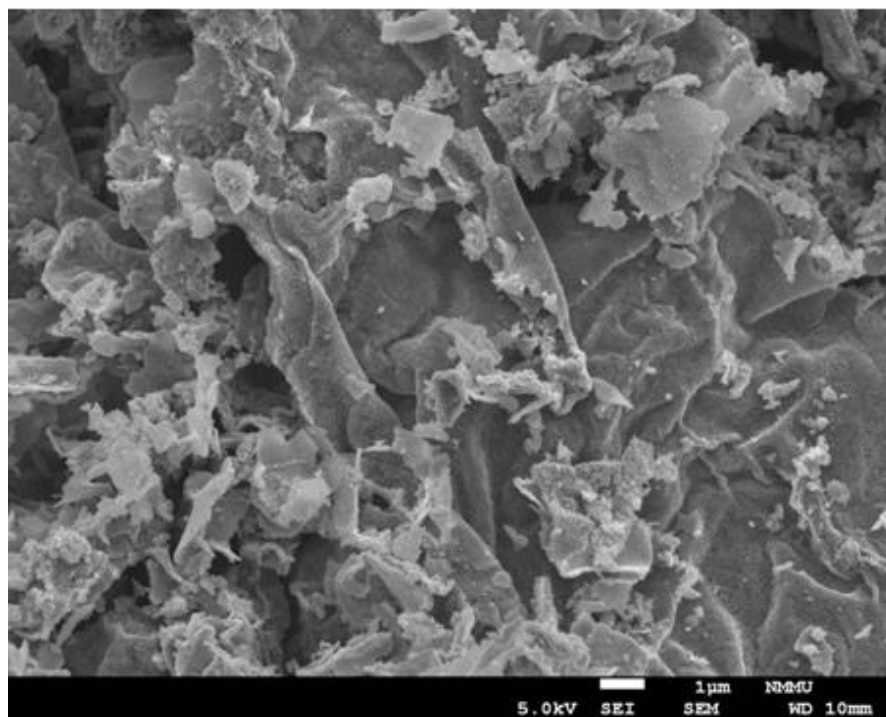
Figure 4.70 (e): Li$_{1.03}$Mg$_{0.2}$Mn$_{1.77}$O$_4$ by batch sol-gel at 800 °C
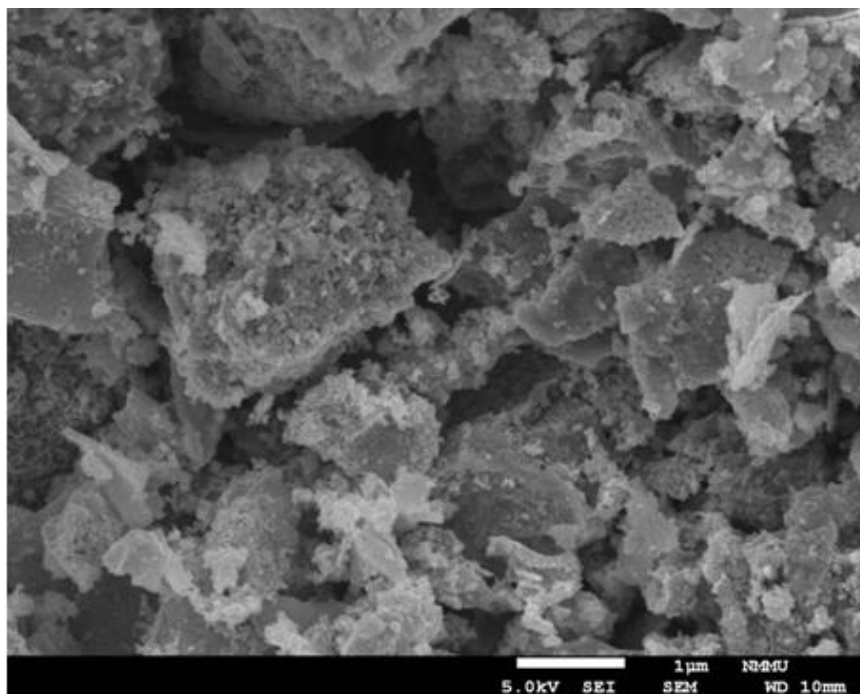
Figure 4.70 (f): Li$_{1.03}$Mg$_{0.2}$Mn$_{1.77}$O$_4$ by spray-drying at 400 °C
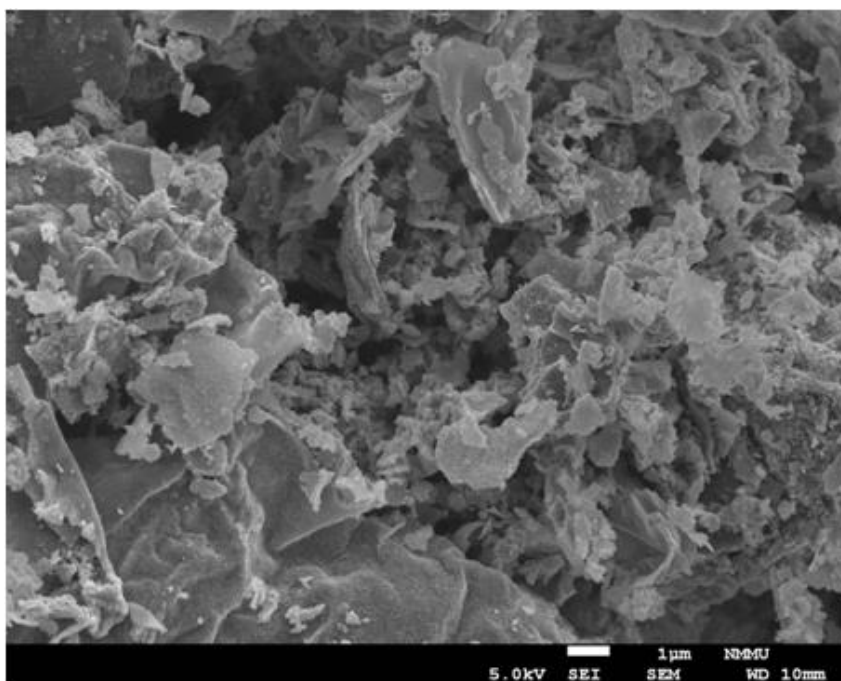
Figure 4.70: SEM micrographs of Li$_{1.03}$Mg$_{0.2}$Mn$_{1.77}$O$_4$ synthesized by the batch sol-gel and spray-drying techniques at various magnifications.

$Li_{1.03}Mg_{0.2}Mn_{1.77}O_4$ prepared by batch sol-gel at 800 °C	$Li_{1.03}Mg_{0.2}Mn_{1.77}O_4$ prepared by spray-drying at 400 °C
(a)	**(d)**

3.0 µm scale

3.0 µm scale

(b)	**(e)**

1.0 µm scale

1.0 µm scale
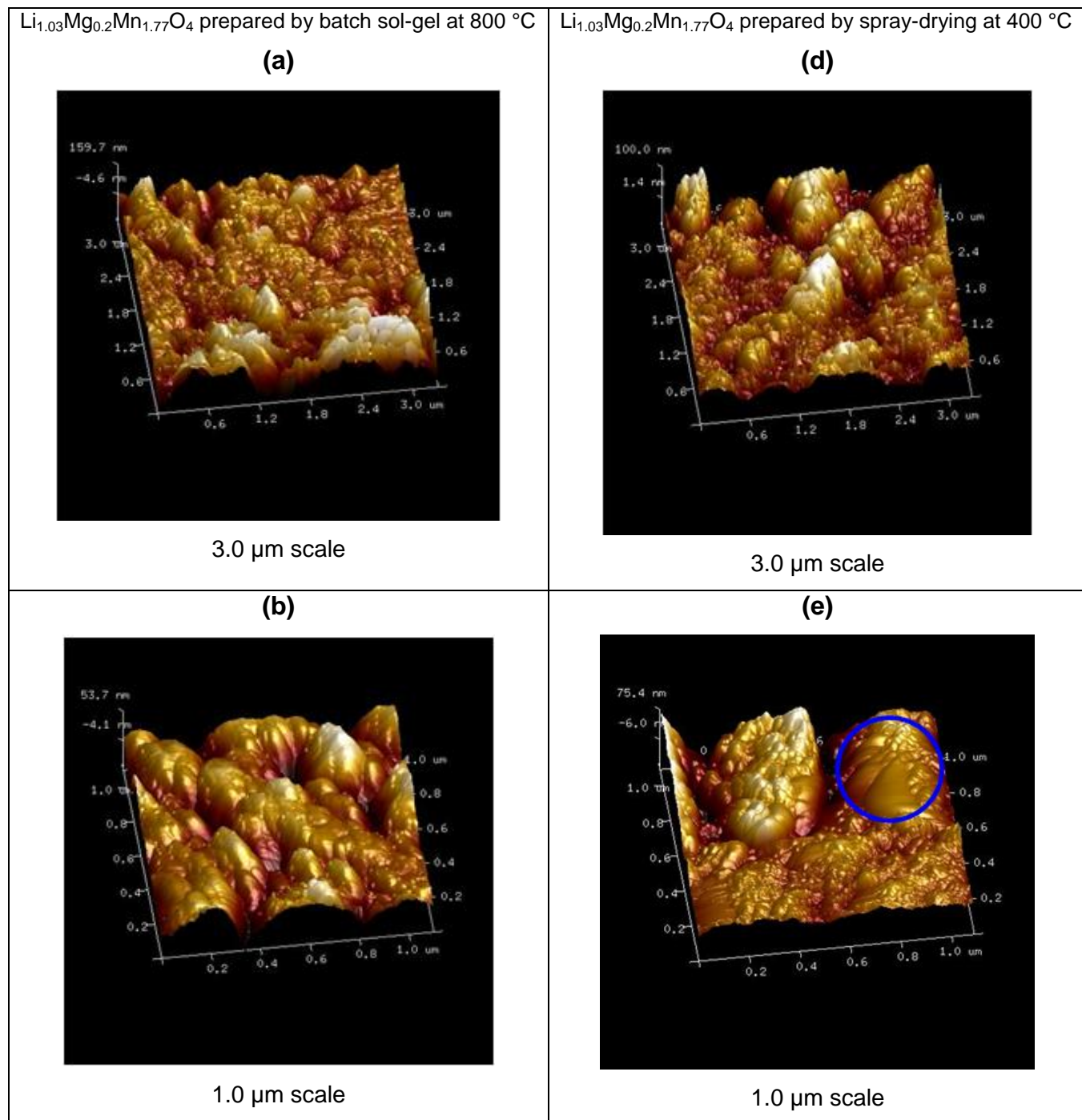
Figure 4.71: AFM scans of $Li_{1.03}Mg_{0.2}Mn_{1.77}O_4$ synthesized by batch sol-gel (a and b) and spray-drying (d and e) techniques at various magnifications.

(c)	(f)
300 nm scale	300 nm scale

Figure 4.71 continued: AFM scans of Li$_{1.03}$Mg$_{0.2}$Mn$_{1.77}$O$_4$ synthesized by batch sol-gel (c) and spray-drying (f) techniques at lowest magnification.

The AFM images of the spray-dried material showed the conglomerated particles at low magnifications to be between 5 to 15 nm (f in Figure 4.71).

4.4.4 LiCo$_{1.09}$Mn$_{0.91}$O$_4$

The SEM micrographs and AFM images for LiCo$_{1.09}$Mn$_{0.91}$O$_4$ synthesized by the batch sol-gel at 800 °C (a, c and e) and spray-drying at 400 °C (b, d and f) techniques are represented in Figures 4.72 and 4.73 respectively.

The results in Figure 4.72 showed an unusual "leaf" shaped morphology of the material at the higher magnification of the batch synthesized oxide (Figure 4.72 image a), that when looking at the lower magnification, the images showed that the regions comprised of small closely packed spherical particles (image c in Figure 4.72). Similar morphology was observed for the oxide material synthesized by the spray-drying material (images b, d and f in Figure 4.72), with some of the particles showing slightly jiggered edges (f in Figure 4.72).

The AFM images of the material were similar to the materials made by the two synthesis methods (images a to f in Figure 4.73).

Figure 4.72 (a): LiCo$_{1.09}$Mn$_{0.91}$O$_4$ by batch sol-gel at 800 °C
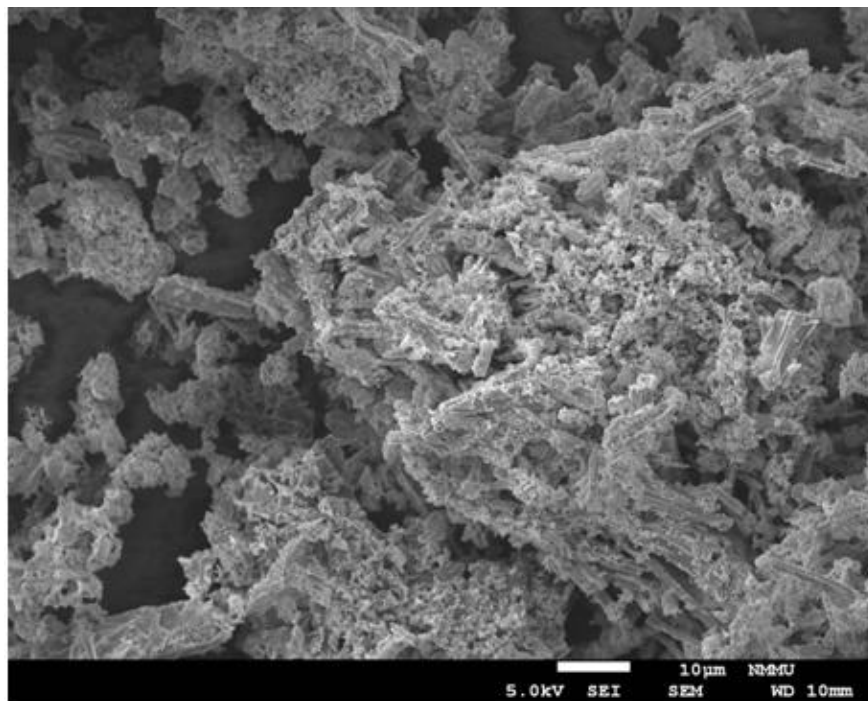
Figure 4.72 (b): LiCo$_{1.09}$Mn$_{0.91}$O$_4$ by spray-drying at 400 °C
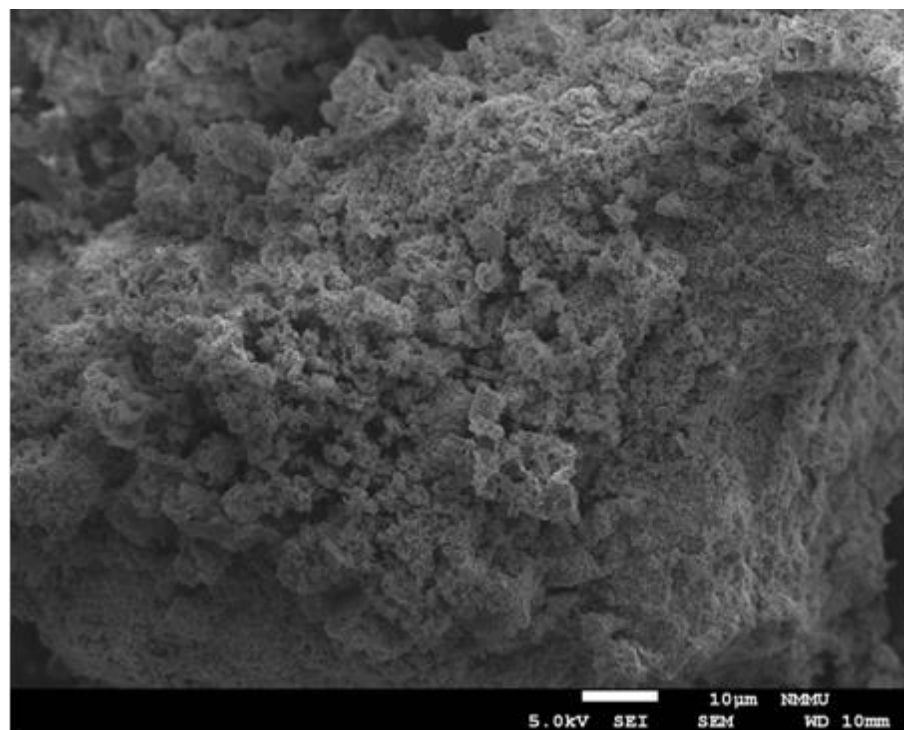
Figure 4.72 (c): LiCo$_{1.09}$Mn$_{0.91}$O$_4$ by batch sol-gel at 800 °C
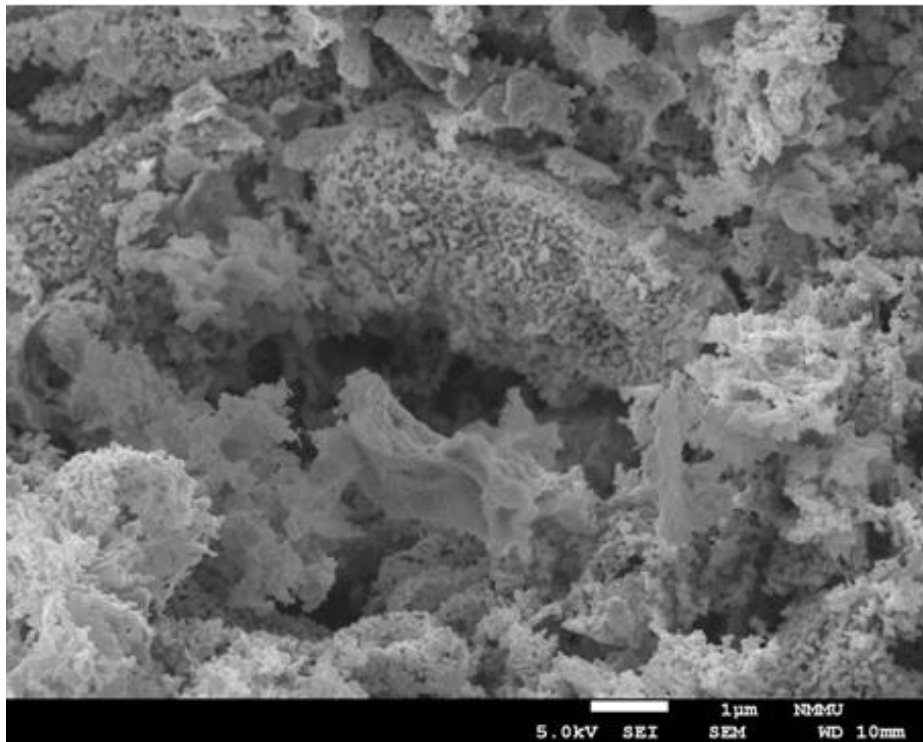
Figure 4.72 (d): LiCo$_{1.09}$Mn$_{0.91}$O$_4$ by spray-drying at 400 °C
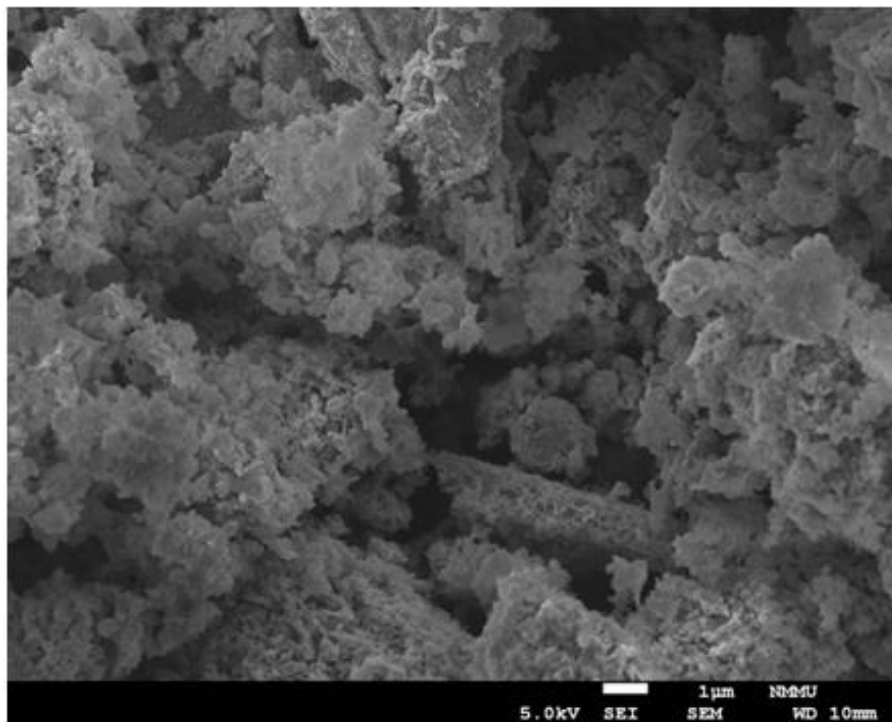
Figure 4.72 (e): LiCo$_{1.09}$Mn$_{0.91}$O$_4$ by batch sol-gel at 800 °C
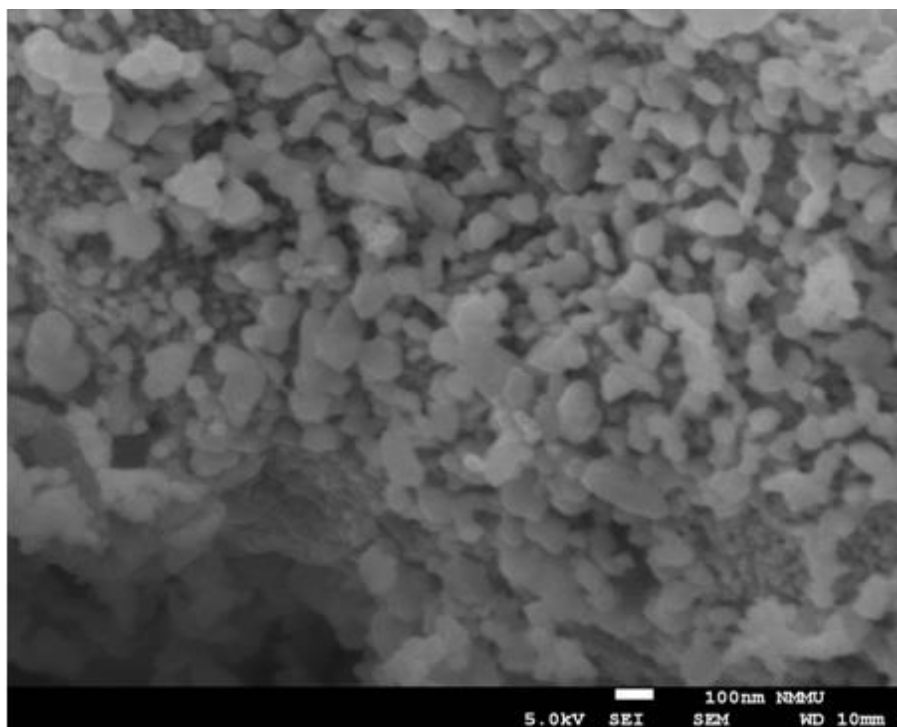
Figure 4.72 (f): LiCo$_{1.09}$Mn$_{0.91}$O$_4$ by spray-drying at 400 °C
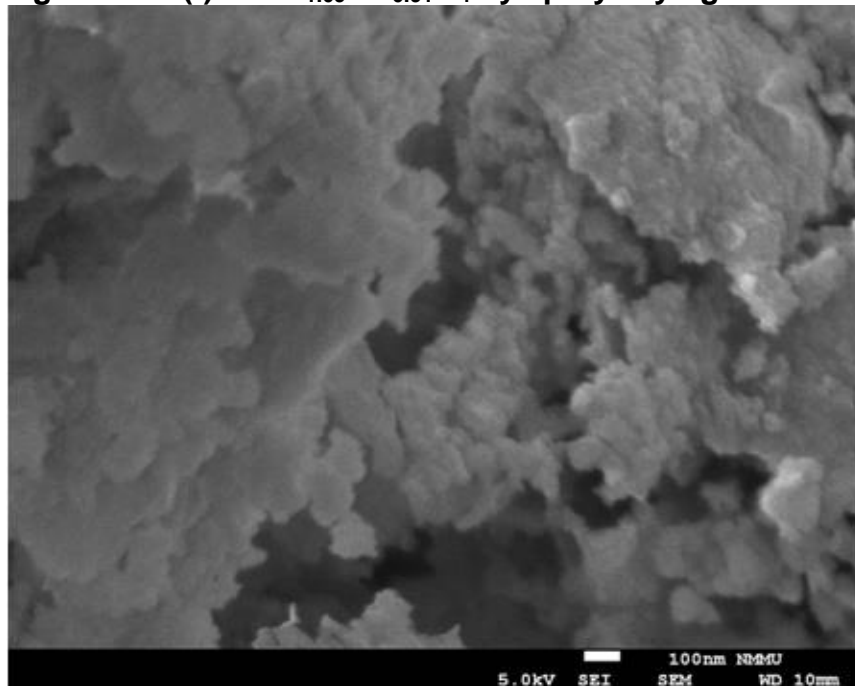
Figure 4.72: SEM micrographs of LiCo$_{1.09}$Mn$_{0.91}$O$_4$ synthesized by the batch sol-gel and spray-drying techniques at various magnifications.

LiCo$_{1.09}$Mn$_{0.91}$O$_4$ prepared by batch sol-gel at 800 °C	LiCo$_{1.09}$Mn$_{0.91}$O$_4$ prepared by spray-drying at 400 °C
(a) 3.0 µm scale	**(d)** 3.0 µm scale
(b) 1.0 µm scale	**(e)** 1.0 µm scale

Figure 4.73: AFM scans of LiCo$_{1.09}$Mn$_{0.91}$O$_4$ synthesized by batch sol-gel (a and b) and spray-drying (d and e) techniques at various magnifications.
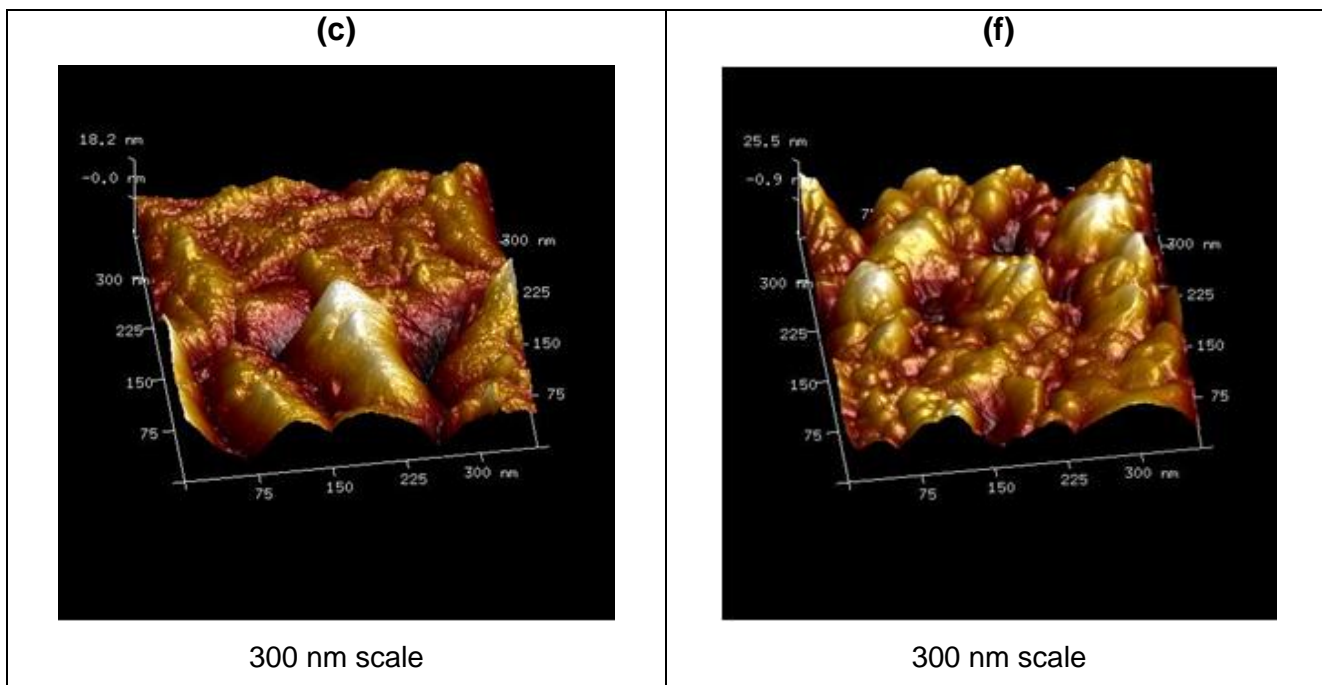
(c)	(f)
300 nm scale	300 nm scale

Figure 4.73 continued: AFM scans of LiCo$_{1.09}$Mn$_{0.91}$O$_4$ synthesized by batch sol-gel (c) and spray-drying (f) techniques at various magnifications.

4.4.5 LiNi$_{0.5}$Mn$_{1.5}$O$_4$

The SEM micrographs and AFM images of LiNi$_{0.5}$Mn$_{1.5}$O$_4$ synthesized by the batch sol-gel at 800 °C (a, c and e) and spray-drying at 400 °C (b, d and f) techniques are represented in Figures 4.74 and 4.75 respectively.

The results in Figure 4.74 showed that the material formed large conglomeration of particles (a and c), which upon higher magnification (e) showed the finer particles in the nano-meter range. The material made by the spray-drying technique showed to have a type of coating on certain parts of the material on some sections (d in Figure 4.74), whereas some regions showed to comprise of very small particles (f in Figure 4.74).

Figure 4.74 (a): LiNi$_{0.5}$Mn$_{1.5}$O$_4$ by batch sol-gel at 800 °C
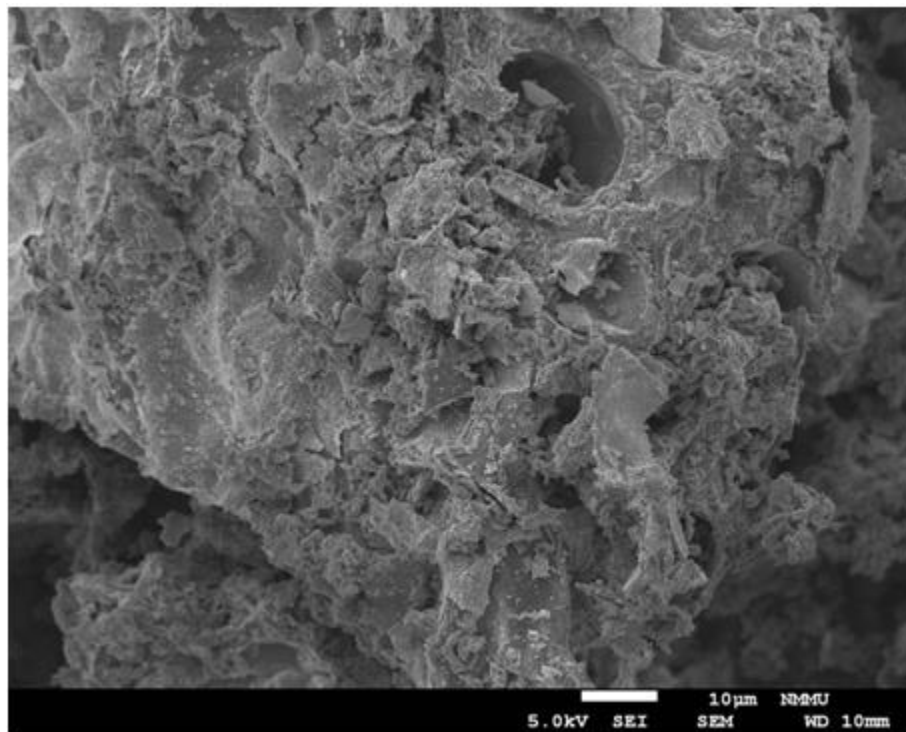
Figure 4.74 (b): LiNi$_{0.5}$Mn$_{1.5}$O$_4$ by spray-drying at 400 °C
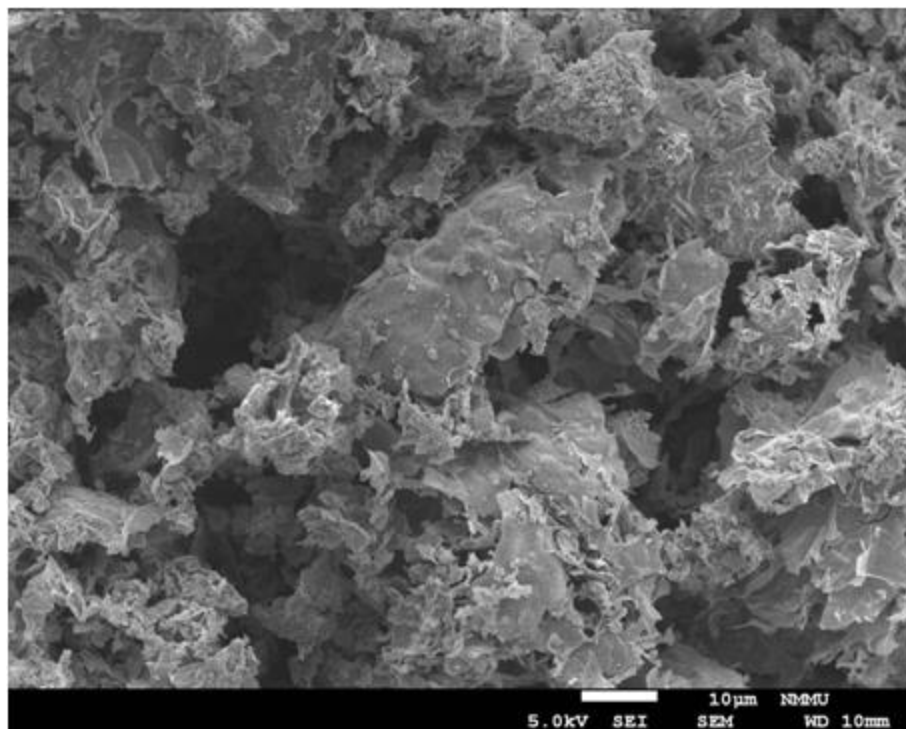
Figure 4.74 (c): LiNi$_{0.5}$Mn$_{1.5}$O$_4$ by batch sol-gel at 800 °C
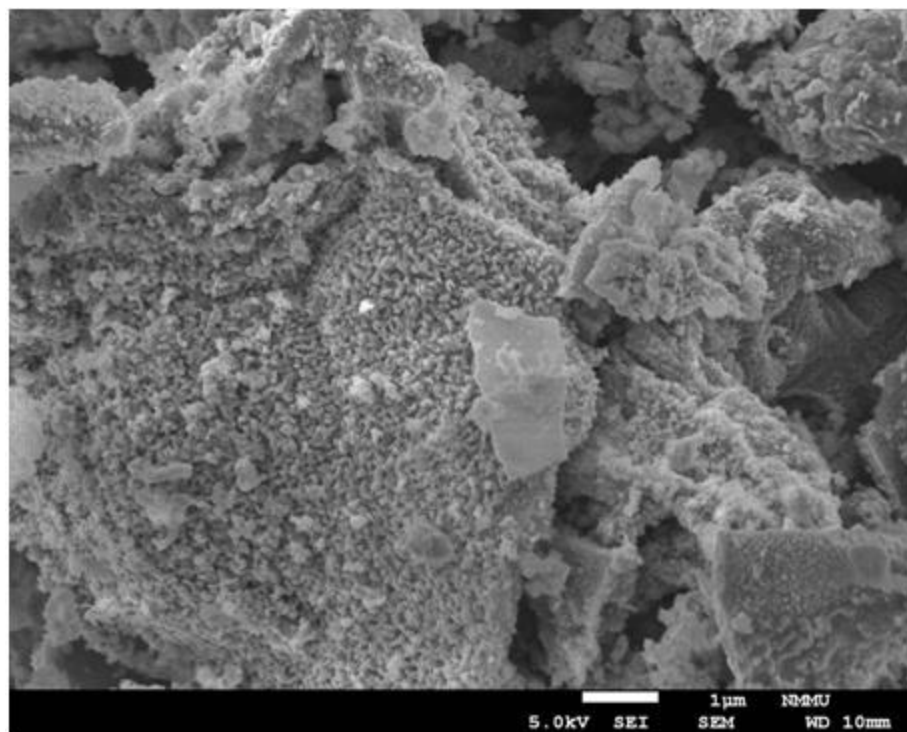
Figure 4.74 (d): LiNi$_{0.5}$Mn$_{1.5}$O$_4$ by spray-drying at 400 °C
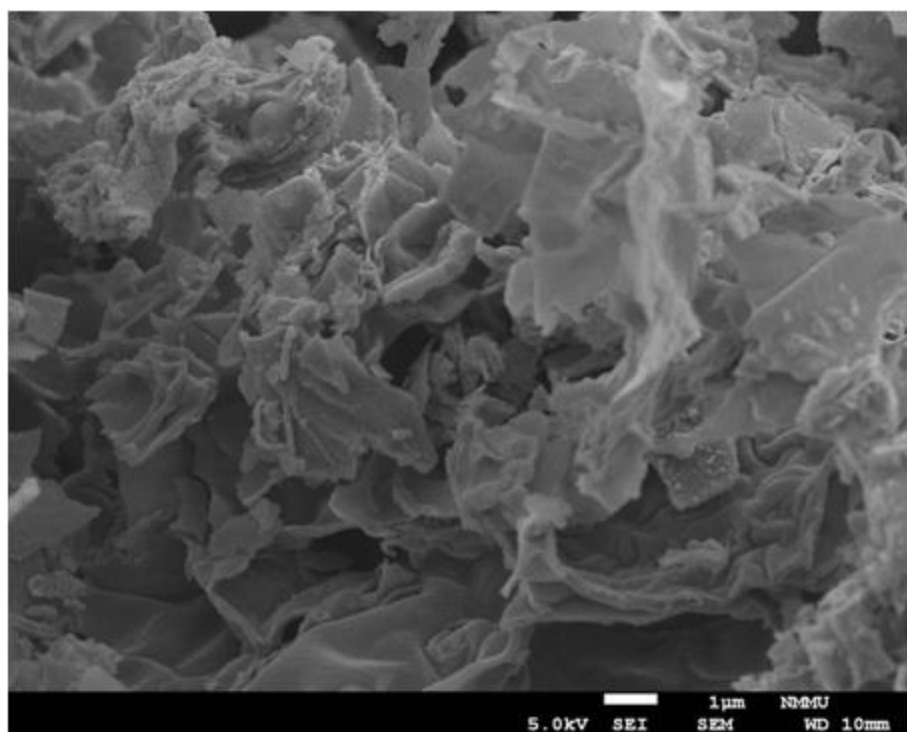
Figure 4.74 (e): LiNi$_{0.5}$Mn$_{1.5}$O$_4$ by batch sol-gel at 800 °C
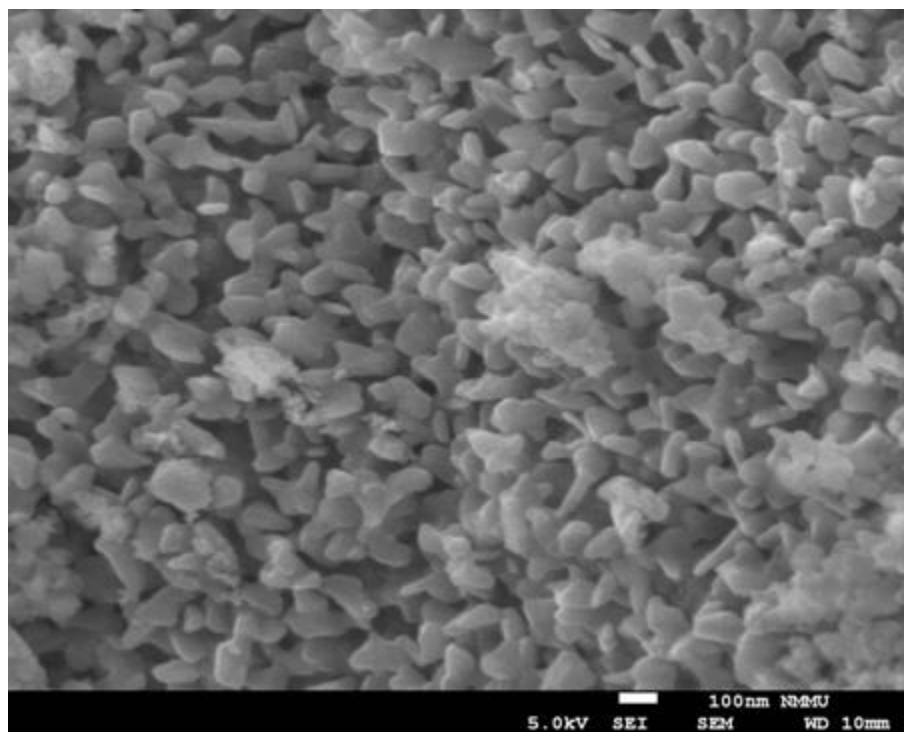
Figure 4.74 (f): LiNi$_{0.5}$Mn$_{1.5}$O$_4$ by spray-drying at 400 °C
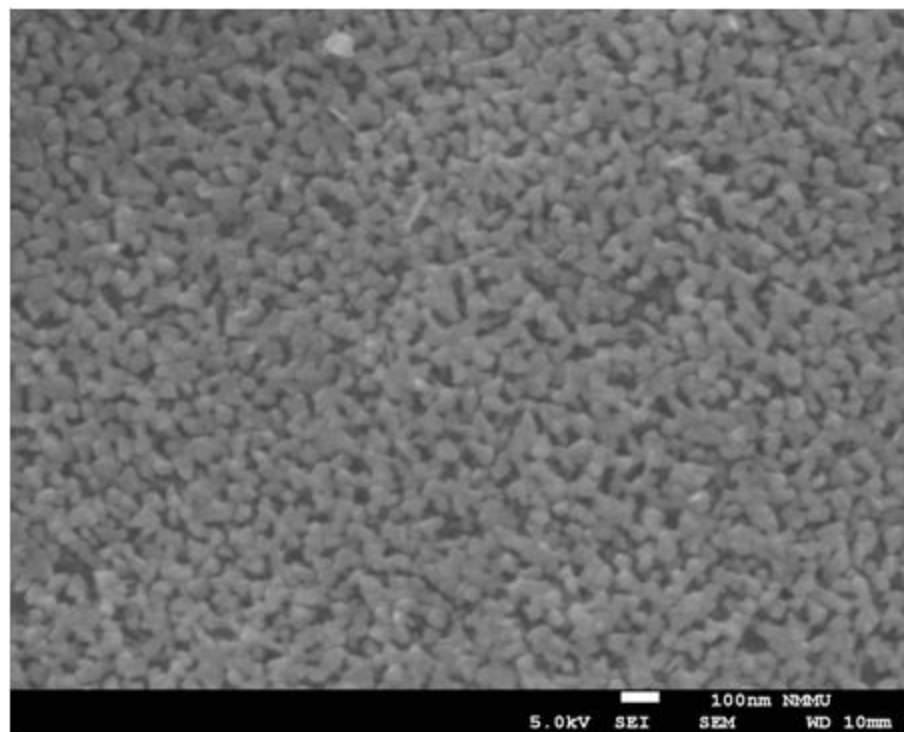
Figure 4.74: SEM micrographs of LiNi$_{0.5}$Mn$_{1.5}$O$_4$ synthesized by the batch sol-gel and spray-drying techniques at various magnifications.

These observations were confirmed by the AFM analysis that showed at low magnification (images a and d in Figure 4.75) to have particles that were closely staggered or packed together. Images c and f showed the particles to be spherical in shape with similar sized particles from both synthesis techniques.

$LiNi_{0.5}Mn_{1.5}O_4$ prepared by batch sol-gel at 800 °C	$LiNi_{0.5}Mn_{1.5}O_4$ prepared by spray-drying at 400 °C
(a)	**(d)**
3.0 µm scale	3.0 µm scale
(b)	**(e)**
1.0 µm scale	1.0 µm scale
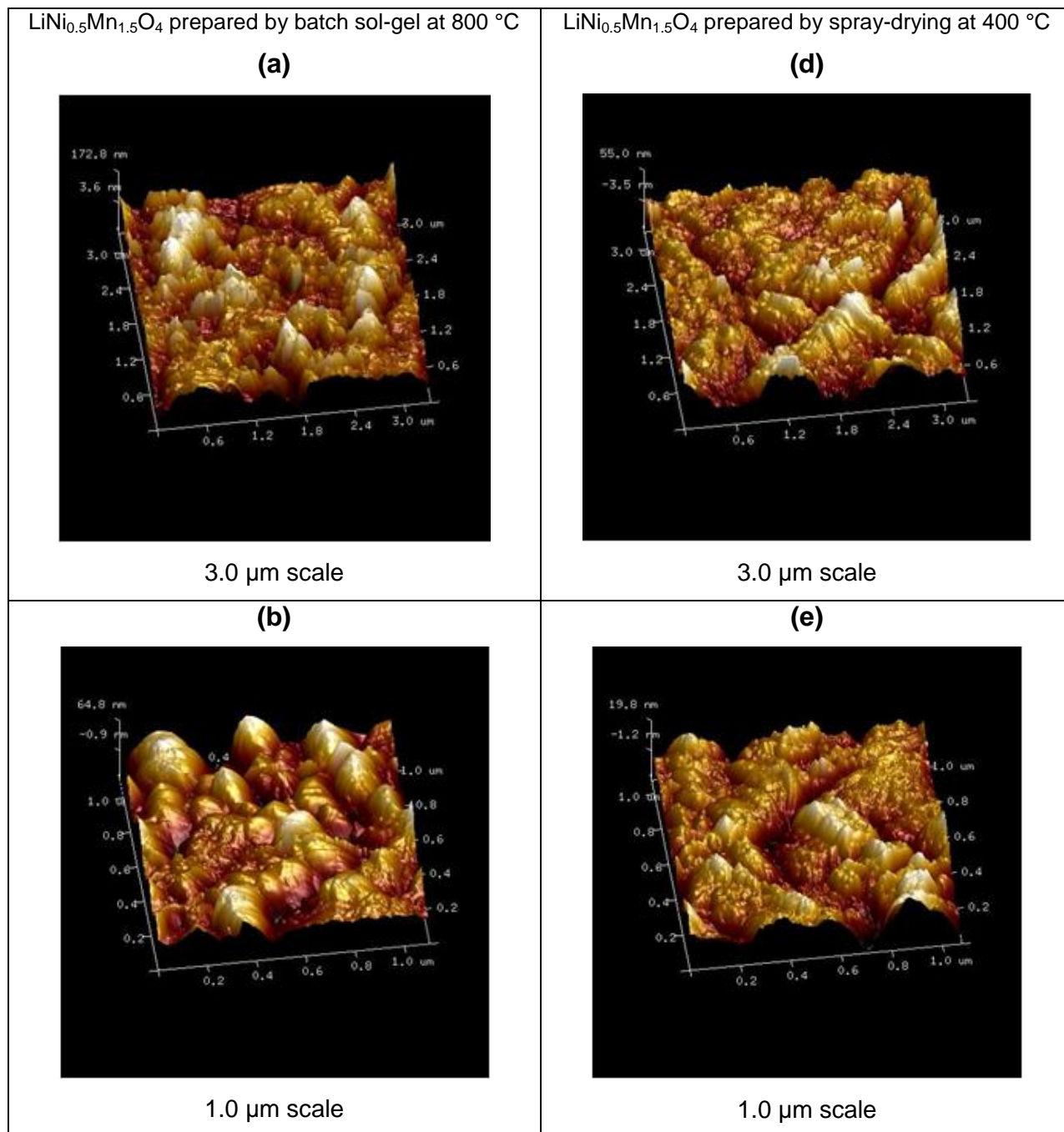
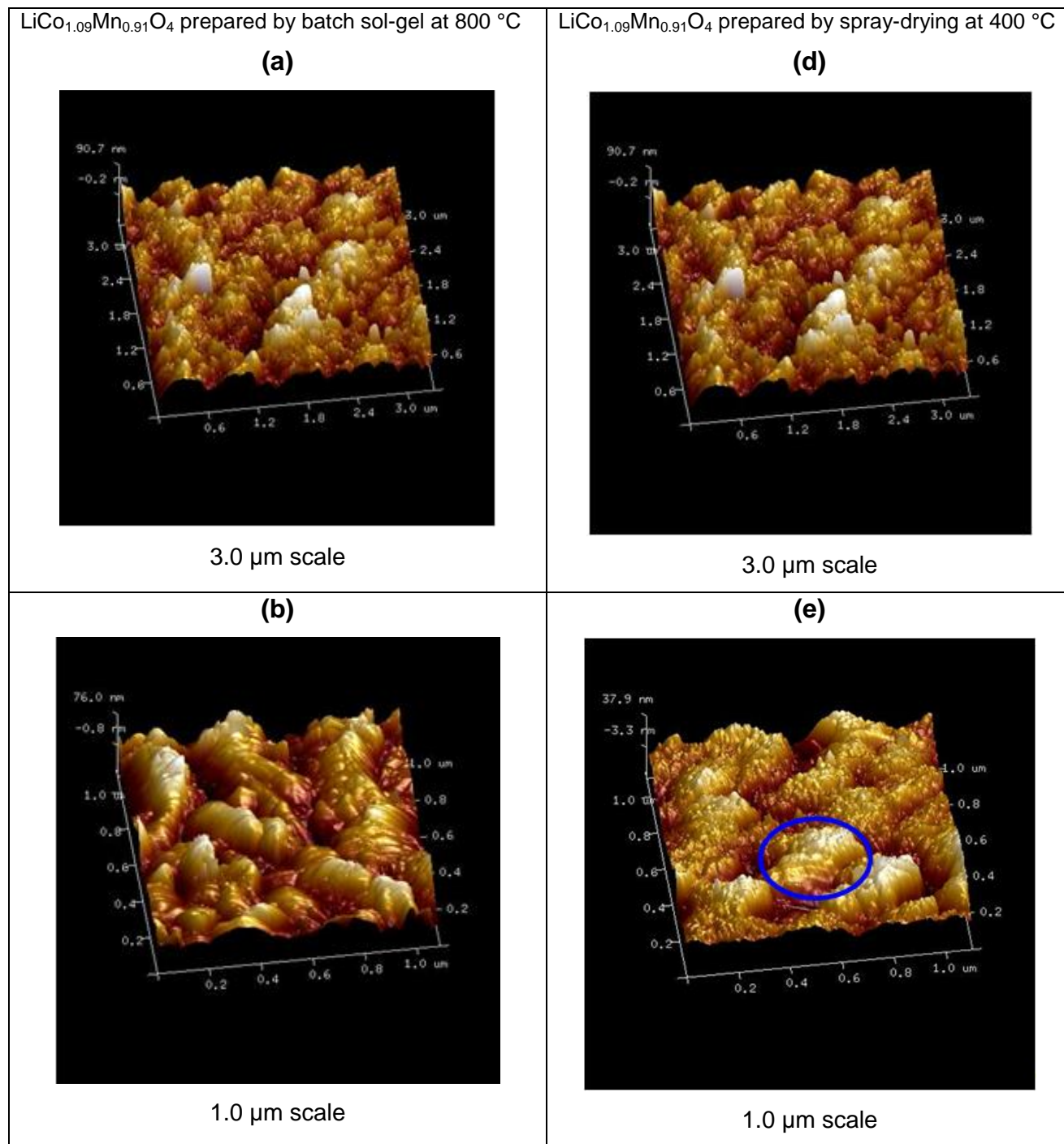*Figure 4.75: AFM scans of $LiNi_{0.5}Mn_{1.5}O_4$ synthesized by batch sol-gel (a and b) and spray-drying (d and e) techniques at various magnifications.*

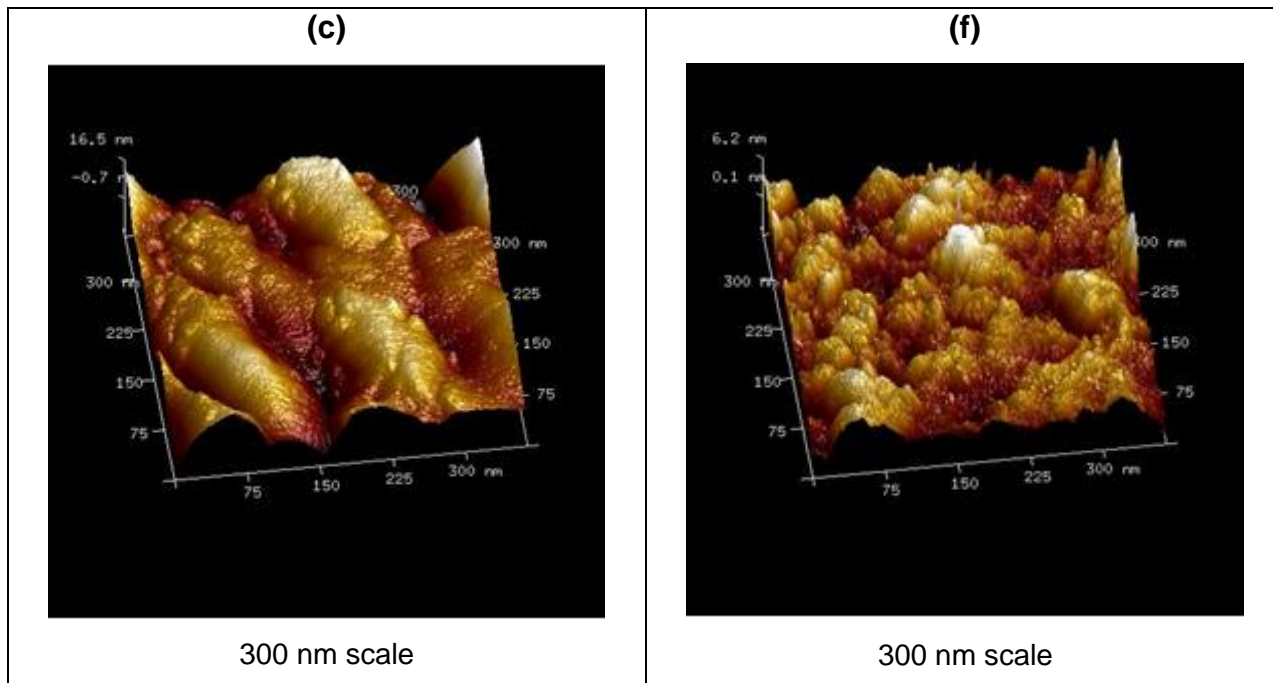| (c)	(f)
300 nm scale	300 nm scale
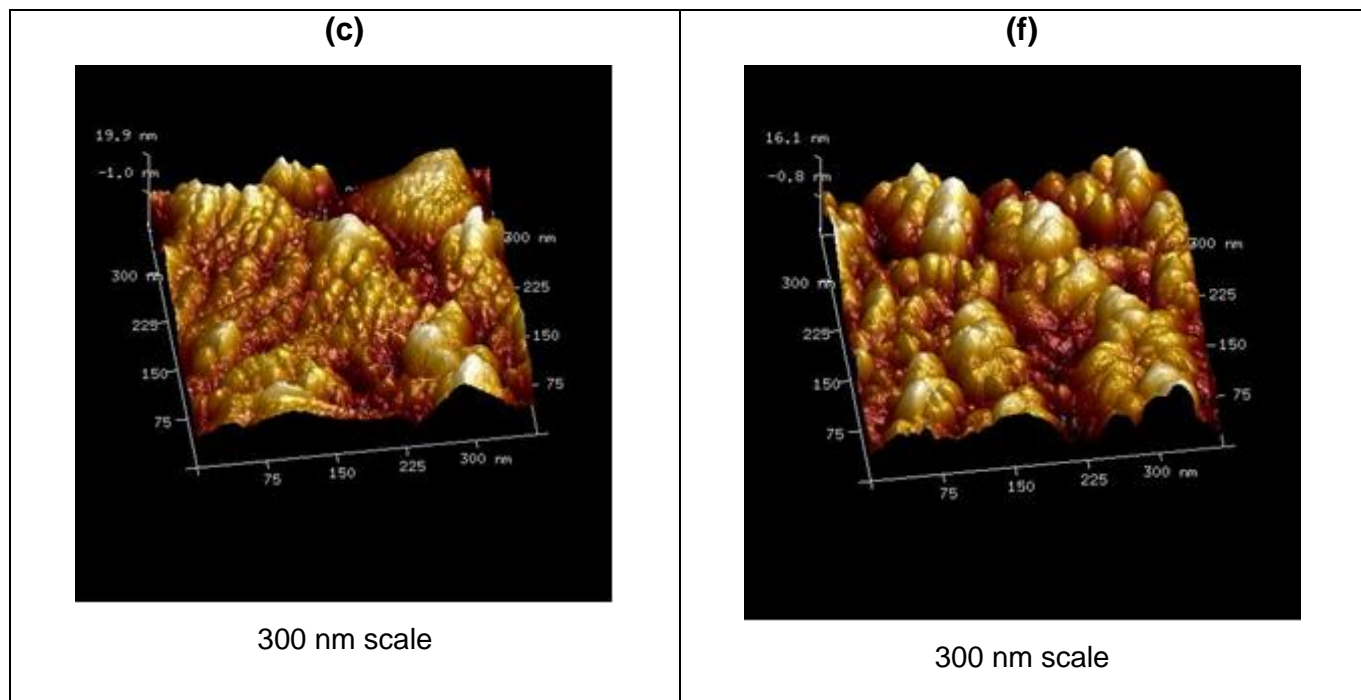
Figure 4.75 continued: AFM scans of LiNi$_{0.5}$Mn$_{1.5}$O$_4$ synthesized by batch sol-gel (c) and spray-drying (f) techniques at highest magnification.

In summary the results supported the findings from the powder X-ray diffraction crystallite size and the BET surface area analysis in that the materials synthesized by the spray-drying process do produce materials with a small particle size. However, the results also showed that some materials were not necessarily homogenous in their particle distribution across the samples selected for analysis.

REFERENCES

1. Y.S. Lee, Y.K. Sun and K.S. Nahm, *Solid State Ionics*, 1998, **109**, 285-294.

2. Y.K. Sun, *Solid State Ionics*, 1997, **100**, 115-125.

3. L.J. Fu, H. Liu, C. Li, Y.P. Wu, E. Rahm, R. Holze, H.Q. Wu, *Progress in Materials Science*, 2005, **50**, 881-928.

4. P. Singh, A. Sil, M. Nath, S. Ray, *Physica B*, 2010, **405**, 649-654.

5. R. Thirunakaran, A. Sivashanmugam, S. Gopukumar, C.W. Dunnill, D.H. Gregory, *Journal of Materials Processing Technology*, 2008, **208**, 520-531.

6. X. Huang, M. Lin, Q. Tong, X. Li, Y. Ruan, Y. Yang, *Journal of Power Sources*, 2012, **202**, 352-356.

7. S.T. Myung, S. Komaba and N. Kumagai, *Journal of Electrochemical Society*, 2001, **145 (5)**, A482-A489.

8. J. Xiao, X.Chen, P.V. Sushko, M.L. Sushko, L. Kovarik, J. Feng, Z. Deng, J. Zheng, G.L. Graff, Z. Nie, D. Choi, J. Lui, J. Zhang, M.S. Wittingham, *Advance Materials*, 2012, **24**, 2109.

9. S.J. Bao, Y.Y. Liang and H.L. Li, *Materials Letters*, 2005, **59**, 3761-3765.

10. R. Thirunakaran, G.H. Lew and W.S. Yoon, *Journal of Nano Science and Engineering*, 2016, **6**, 1-19.

11. K. Suryakala, G.P. Kalaignan and T. Vasudevan, *International Journal of Electrochemical Science*, 2006, **1**, 372-378.

12. L.H. Chi, N.N. Dinh, S. Brutti, B. Scrosati, *ElectrochimicaActa*, 2010, **55**, 5110-5116.

13. Y. Huang, J. Li and D. Jia, *Journal of Colloid and Interface Science*, 2005, **286**, 263-267.

14. N. Amdouni, F. Gendron, A. Mauger, H. Zarrouk and C.M. Julien, *Materials Science and Engineering B*, 2006, **129**, 64-75.

15. S.J. Bao, Y.Y. Liang, W.J. Zhou, B.L. He and H.L. Li, *Journal of Power Sources*, 2006, **154**, 239-245.

16. Y.K. Sun, I.H. Oh and K.Y. Kim, *Industrial. Engineering Chemistry. Research*, 1997, **36**, 4839-4846.

17. C. Julien, S. Ziolkiewicz, M. Lemal and M. Massot, *Journal of Materials Chemistry*, 2001, **11**, 1837-1842.

18. N. Amdouni, K. Zaghib, F. Gendron, A. Mauger and C.M. Julien, *Ionics*, 2006, **12**, 117-126.

19. M. Hu, Y. Tian, L. Su, J. Wei and Z. Zhou, *Applied Materials and Interfaces*, 2013, **5**, 12185-12189.

CHAPTER 5

RESULTS AND DISCUSSION

Electrochemical studies

5.1 <u>Cell Capacities</u>

Capacity studies were done on assembled 2032 coin cells that were charged and discharged in a voltage range of 3.0 V to 4.5 V at 0.1 C respectively; all units of capacity are expressed as mAh.g^{-1} of the active cathode material. The positive electrode of these coin cells consisted of the synthesized $LiM_xMn_{1-x}O_4$ (whereby M=Al, Co, Mg, Ni) with a lithium foil as the negative electrode. This section will discuss the electrochemical results of the various positive electrode materials that were synthesized by the conventional batch sol-gel process (at 800 °C) and compare them to the electrode materials prepared by the spray-drying process (at 400 °C).

For comparison purposes, the undoped $Li_{1.03}Mn_{1.97}O_4$ that was synthesized by both the spray-drying and batch process was compared to cells that were made with commercial cathode material purchased from Aldrich (0.5 μm >99 %). This was then also compared to the doped $LiM_xMn_{1-x}O_4$ (whereby M=Al, Co, Mg, Ni) materials synthesized by both techniques (spray-drying and batch sol-gel processes) and its charge and discharge capacities are graphically shown in Figures 5.1 to 5.5 respectively.
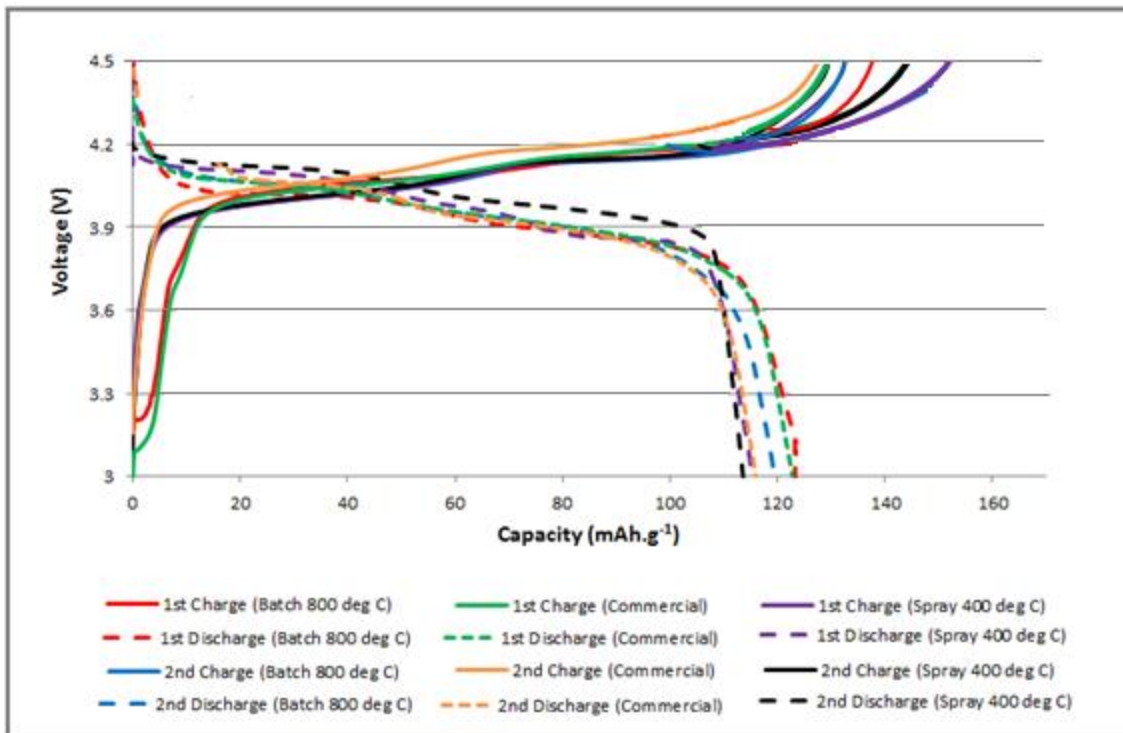
Figure 5.1: Capacity results of $Li_{1.03}Mn_{1.97}O_4$ by various synthesis techniques.

Figure 5.1 showed the charge and discharge capacity (at 0.1 C) curves for $Li_{1.03}Mn_{1.97}O_4$ synthesized at 800 °C (batch sol-gel method), 400 °C (spray-dried method) and the commercially available material in a voltage range of 3.0 to 4.5 V. During charge, potential plateaus were observed between 3.9 to 4.1 V and at approximately 4.2 V however, upon discharge, potential plateaus were observed approximately within the region between the 4.2 to 4.0 V and at about 4.1 to 3.9 V. A voltage step (at about 4.1 V) was also noted for $Li_{1.03}Mn_{1.97}O_4$ regardless of the synthesis method which was similar to the work reported by Singh *et al.*[1]. This voltage step was explained by Singh *et al.*[1] as the transition from two cubic phases "fusing" into one cubic phase. This in turn resulted into a higher amount of Li^+ to be removed from the cathode material (below the 4.1 V barrier), therefore allowing the de-intercalation process to be more efficient. Both synthesis routes used in this study showed similar voltage profiles for this particular material, which were similar to those reported in literature[1-4].
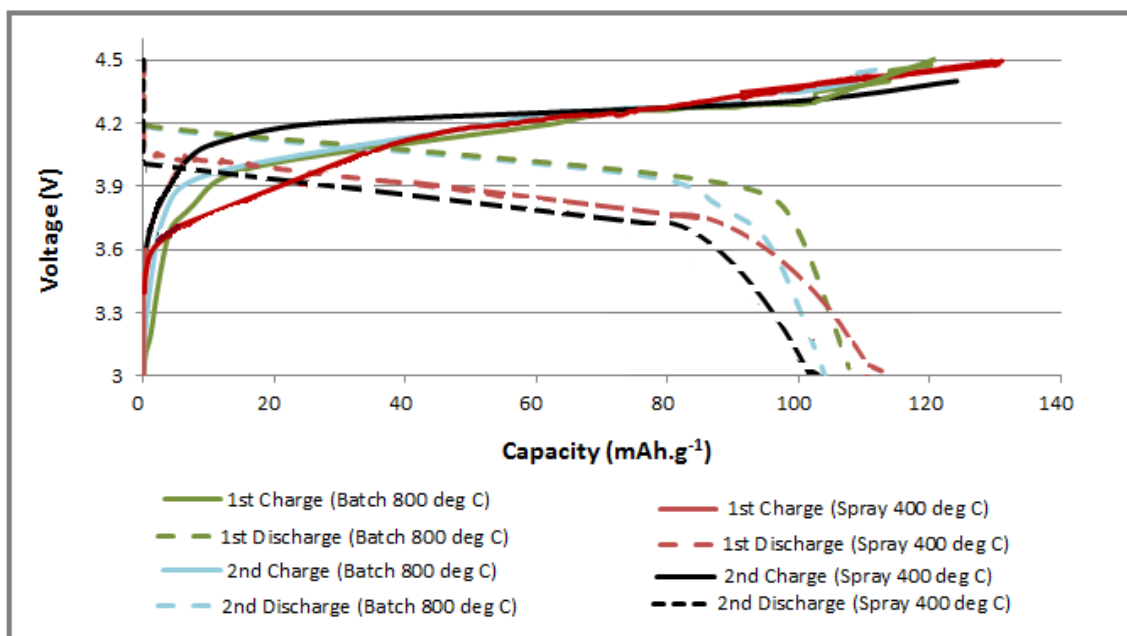
Figure 5.2: Capacity results of $LiAl_{0.4}Mn_{1.6}O_4$ by various synthesis techniques.

The charge and discharge capacity (at 0.1 C) curves for $LiAl_{0.4}Mn_{1.6}O_4$ synthesized at 800 °C (batch sol-gel method) and 400 °C (spray-dried method) is displayed in Figure 5.2. A slight voltage plateau was observed at 4.2 V during charging and between 4.1 to 3.9 V during the discharge step. These observed voltage plateaus within the materials charge or discharge profiles were compared to literature reported results[5-8]. Literature gave slightly different results, Wang *et al.*[5] and Bao *et al.*[6] done a study on $LiAl_{0.1}Mn_{1.9}O_4$ whereby two voltage plateaus were observed at approximately 4.0 and 4.2 V (for both charge and discharge) with a voltage step at 4.1 V. Song *et al.*[7] also obtained two voltage plateaus (for $LiAl_{1/6}Mn_{11/6}O_4$) at 4.0 V and between 4.1 to 4.2 V during charging however, during discharging voltage plateaus were at about 4.1 V and between 4.0 to 3.9 V. Xiao *et al.*[8] studied various Al doping concentrations (x=0.02-0.08) and displayed voltage plateaus at 4.0 and 4.2 V (upon charging and discharging) with a voltage step at 4.1 V. The absence in the distinct plateaus at 4.0 V (during charge) and 4.2 V (during discharge) in this study could be explained by the variation in metal to Mn ratio, where literature reported results had a range of different ratios (as previously mentioned). The absence of the voltage step and voltage plateau observation could also be observed by the results of the cyclic voltammetry studies that showed single broad peaks instead of double peaks for both its anodic and cathodic reactions (explained in Section 5.4).
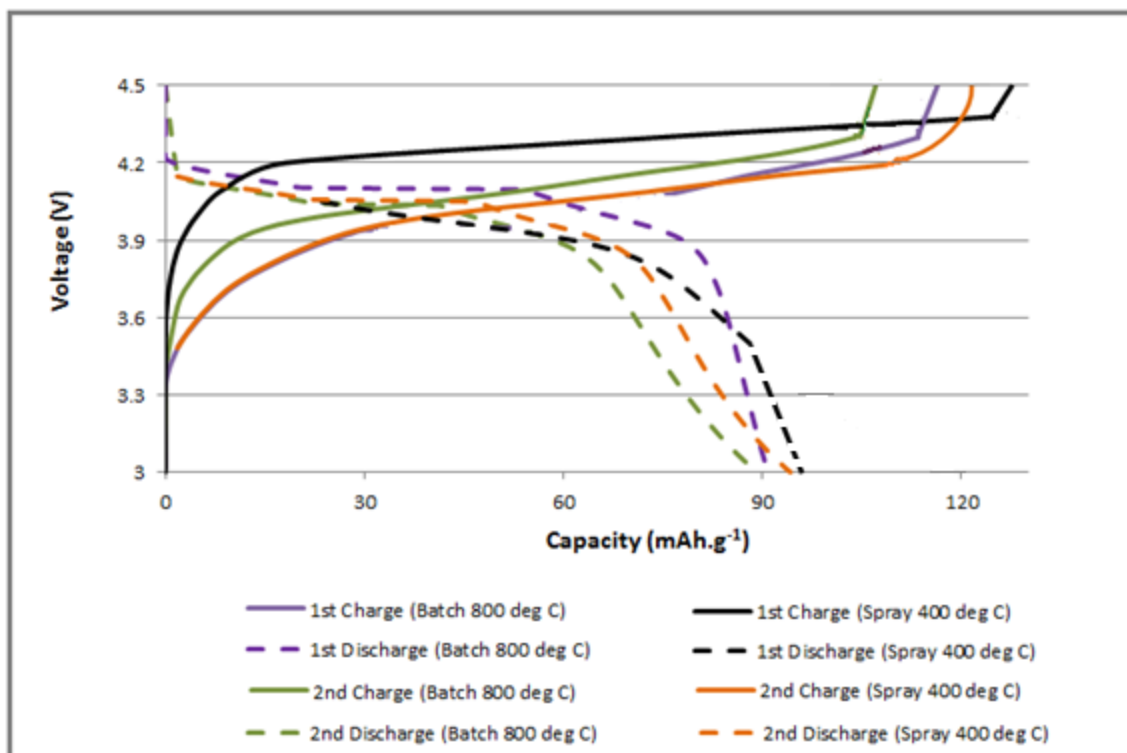
Figure 5.3: Capacity results of $Li_{1.03}Mg_{0.2}Mn_{1.77}O_4$ by various synthesis techniques.

The charge and discharge voltage profiles for the $Li_{1.03}Mg_{0.2}Mn_{1.77}O_4$ cathode material were similar for both synthesis techniques and were in agreement to the results reported by Singh *et al.*[1] and Aikiyo *et al.*[9]. For both charge and discharge profiles the spray-dried material showed a slightly higher discharge capacity than the batch sol-gel synthesized material. The typical voltage step that was observed for the undoped material (at approximately 4.1 V) was again not observed for this particular spinel oxide material ($Li_{1.03}Mg_{0.2}Mn_{1.77}O_4$), whereby the "splitting and fusing" phenomena was neglected (discussed in Figure 5.1). In part this could be explained by, Mg doping suppresses the "fusing" (during charge at 4.1 V) and splitting (during discharge at 4.1 V) occurrence, which would result into a decrease in Li^+ content removal and in turn leaded to a lower discharge capacity relative to the undoped material.
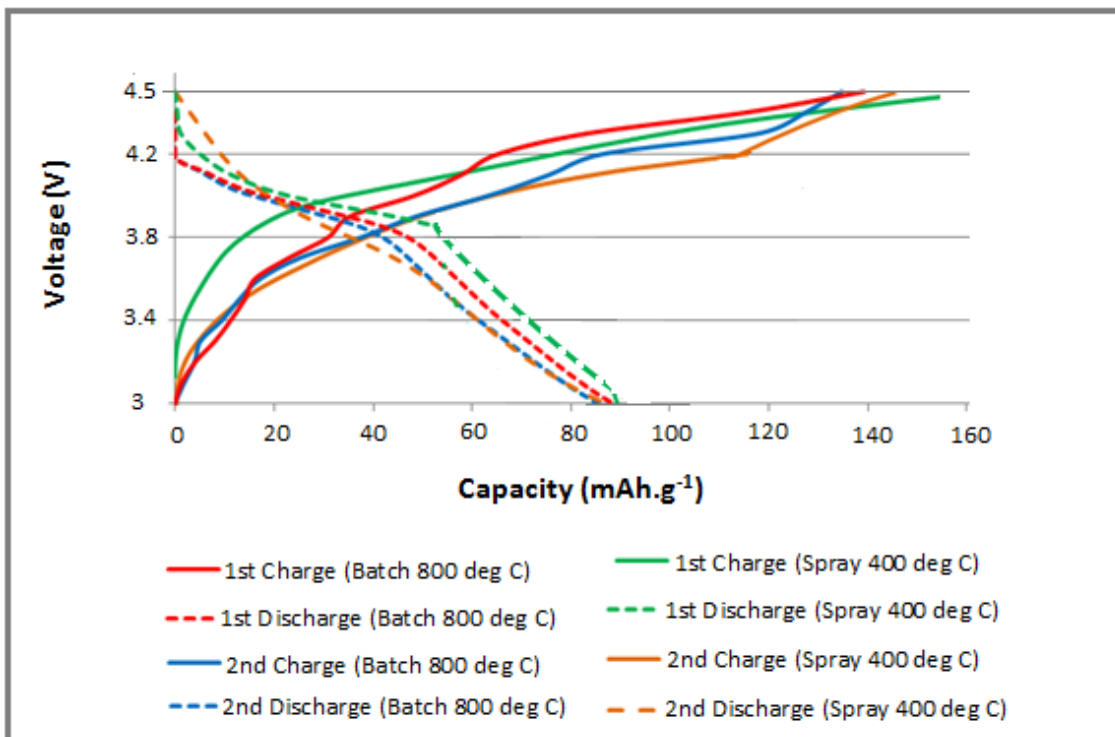
Figure 5.4: Capacity results of LiCo$_{1.09}$Mn$_{0.91}$O$_4$ by various synthesis techniques.

Figure 5.4 showed the voltage profile for LiCo$_{1.09}$Mn$_{0.91}$O$_4$ prepared by sol-gel and spray-dried methods. The voltage profile for this oxide material had slight differences in comparison to literature report results[10-12]. Huang *et al.*[10] and Amdouni *et al.*[12] showed that two voltage plateaus appeared at 3.9 and 4.1 V for both charge and discharge curves. Whereas in this study single plateaus were obtained at higher voltages (compared to literature) of about 4.0 to 4.2 V and about 4.0 to 3.9 V during charging and discharging respectively. These differences included the absence of a distinct volatge plateau around the 3.9 and 4.0 V region upon charge and dischage respectively. The differences could be accounted for variations in metal to Mn ratio (0.16:1.84, in literature)[10-12].
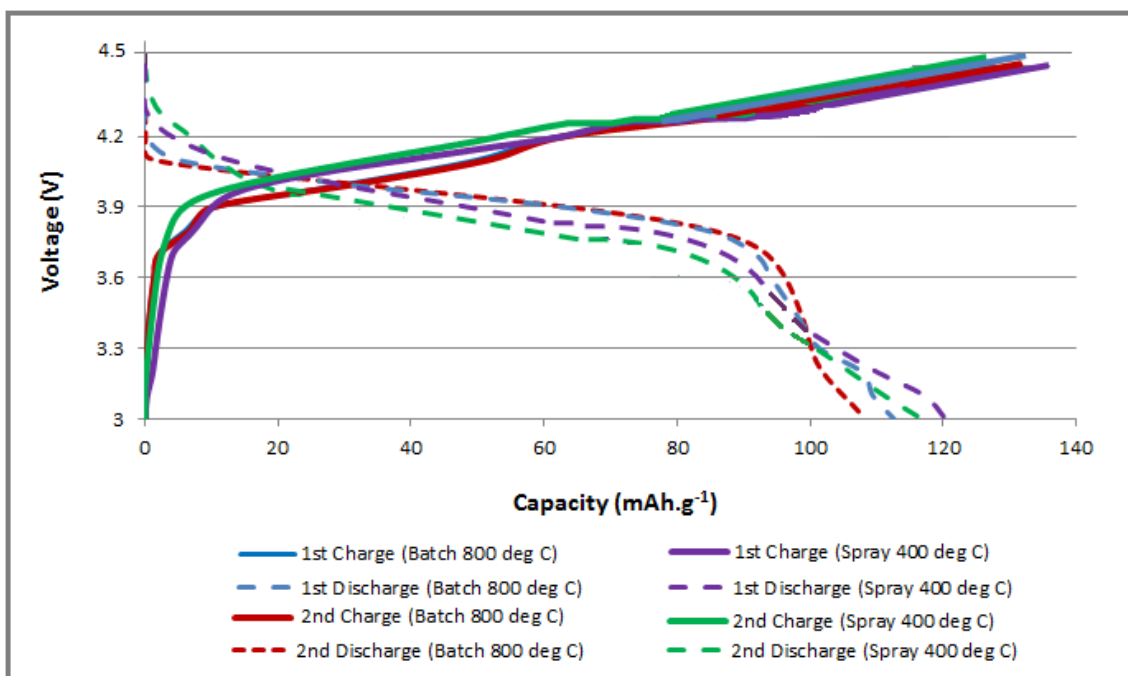
Figure 5.5: Capacity results of $LiNi_{0.5}Mn_{1.5}O_4$ by various synthesis techniques.

The voltage profile in Figure 5.5 showed no distinct voltage plateaus and voltage steps during charge or discharge regardless of the synthesis method used as obtained for certain oxides in literature[13]. Sun *et al.*[13] studied $LiNi_{0.05}Mn_{1.95}O_4$ and showed two voltage plateaus at about 4.0 and 4.2 V (during charging) and also at about 3.9 and 4.1 V (during discharging) together with a voltage step at about 4.2 V. The voltage profile observed in Figure 5.5 was different to that reported by Sun *et al.*[13] due to variation in metal to manganese ratio (0.05:1.95). However, the voltage profile observed in Figure 5.5 was slightly similar to the results reported by Xu *et al.*[14]. Xu *et al.*[14] presented two voltage plateaus in their study, a short plateau at 4 V (associated with redox Mn^{3+}/Mn^{4+} reactions) and a long plateau at 4.7 V (associated with redox Ni^{2+}/Ni^{4+} reactions). In this study (Figure 5.5) the results showed slightly lower voltage plateaus with a short plateau at 3.8 V and a plateau at 4.3 V during charging. During subsequent discharging a single plateau was observed at 4.0 V. However it would have been worthwhile to operate this material at a cut off or end voltage of 5.0 V (during charge) for direct or exact comparison to literature as most Ni-doped oxides produced results based on a 5.0 V profile[15-18].

Table 5.1 summarizes the initial discharge capacities obtained within this study for the various oxide materials which were then compared to the discharge capacities achieved by various authors from literature (using a batch sol-gel process) together with its theoretical capacities. In this study, the batch and spray-dried materials were synthesized at 800 °C and 400 °C respectively.

Table 5.1: Summary on the cathode oxide materials initial discharge capacities.

Sample	Discharge capacity (experimental) mAh.g^{-1}		Discharge capacity (literature) mAh.g^{-1}	Theoretical capacity (mAh.g^{-1})
$Li_{1.03}Mn_{1.97}O_4$	Batch	125	126 [1]	148
	Spray	116		
	Commercial	123		
$LiAl_{0.4}Mn_{1.6}O_4$	Batch	108	125 [19, 20]	158
	Spray	114		
$Li_{1.03}Mg_{0.2}Mn_{1.77}O_4$	Batch	94	88 [1, 21]	154
	Spray	95		
$LiCo_{1.09}Mn_{0.91}O_4$	Batch	89	87.1 – 90 [22]	144
	Spray	91		
$LiNi_{0.5}Mn_{1.5}O_4$	Batch	113	126 [20]	146
	Spray	120		

The results showed that the initial discharge capacity for the undoped material synthesized by the spray-drying process was lower than the batch sol-gel synthesized material that was made at 800 °C. Both the batch synthesized and commercial $Li_{1.03}Mn_{1.97}O_4$ capacities were in agreement with literature reported values and about 15 % less than the theoretical achievable capacity. The cells made with Al and Ni doped spinel cathode material showed to have comparatively lower initial capacities for both the batch and spray-drying technique when compared to the results reported in literature however, the spray-dried materials produced a higher capacity than the batch sol-gel materials (both Al and Ni doped). Whereas the cells made with the Mg and Co doped spinel cathode material gave capacities that were comparatively similar. It is not clear from these initial studies why some of the cells with doped cathode materials gave slightly lower initial capacities.

Based on the X-ray diffraction results reported in Chapter 4 (Section 4.3) that showed an increase in the crystallite size of the spinel material above 600 °C following batch synthesis, cells were then also made with these respective cathode materials (synthesized at 600 °C) and their voltage profiles are reported in Figure 5.6. It was of interest to see if the lowering of the synthesis temperature resulting in a material with lower crystallite sizes would have an influence on the initial capacity of the respective Li-ion cells made with different manganese doped spinel cathode materials.
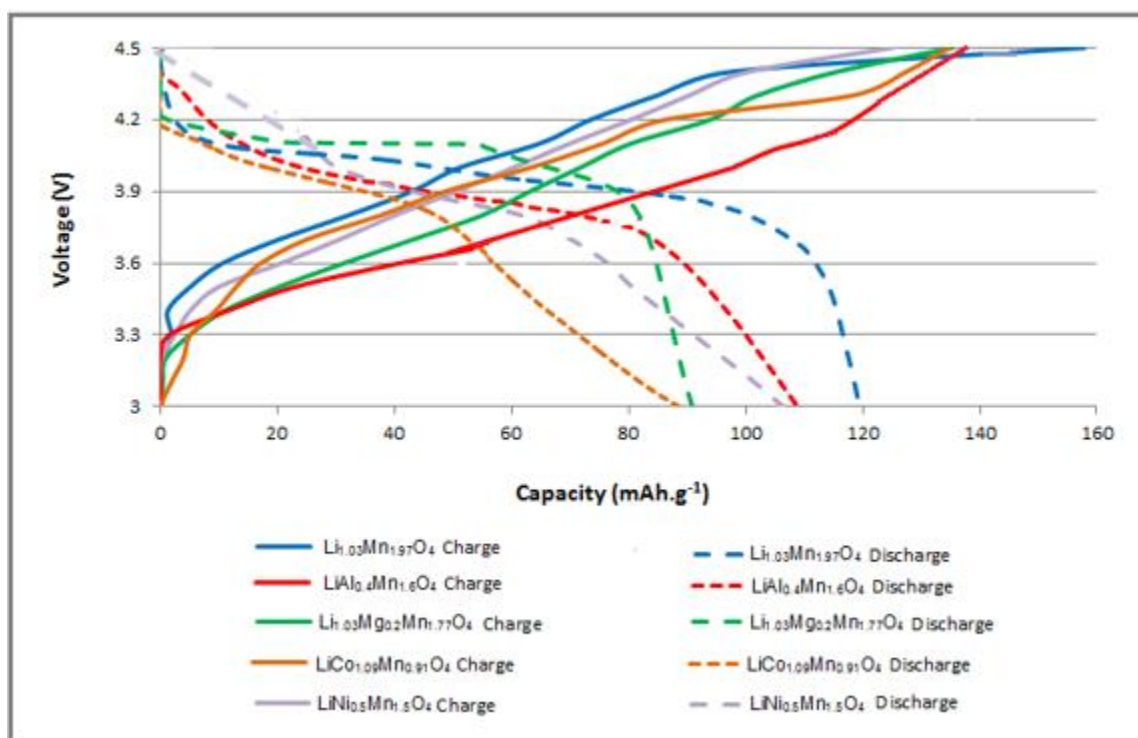
Figure 5.6: Capacity results of the various oxide materials at 600 °C.

The results showed upon discharge, that the observed voltage plateaus were within the 4.2 to 4.0 V region (for undoped and Mg doped oxides) and between 4.0 to 3.9 V region (for all the spinel oxide materials) respectively.

In summary, there was a good comparison of the initial discharge capacities obtained within this study for the various oxide materials synthesized by the batch sol-gel (800 and 600 °C) and spray-dried methods 400 °C (Table 5.2). These results (Table 5.2) showed that the initial discharge capacities of the cells were relatively similar between the materials synthesized at 600 and 800 °C and that there was no noticeable difference on

the first 0.1 C discharge cycles. There might have been differences in other electrochemical properties such as cycle life or high rate discharges, which were not considered in this study.

Table 5.2: Summary on the cathode oxide materials initial discharge capacities at different synthesis temperatures.

Sample	Discharge capacity by batch process (800 °C) mAh.g^{-1}	Discharge capacity by batch process (600 °C) mAh.g^{-1}	Discharge capacity by spray-drying (400 °C) mAh.g^{-1}
$Li_{1.03}Mn_{1.97}O_4$	125	121	116
$LiAl_{0.4}Mn_{1.6}O_4$	108	109	114
$Li_{1.03}Mg_{0.2}Mn_{1.77}O_4$	94	89	95
$LiCo_{1.09}Mn_{0.91}O_4$	89	90	91
$LiNi_{0.5}Mn_{1.5}O_4$	113	106	120

On average the cells made with the material that was spray-dried at 400 °C required a higher charging capacity on its first charge step when compared to the cells made with the cathode material synthesized at 600 and 800 °C. The undoped manganese spinel, $Li_{1.03}Mn_{1.97}O_4$, obtained a discharge capacity similar to the results that are reported in literature except for the spray-dried material that showed comparatively a slightly lower discharge capacity (Tables 5.1 and 5.2). Similarly, the first 0.1 C discharge capacities of the materials synthesized at 600 °C showed similar results to the material made at 800 °C. On average, the cells made with the doped lithium manganese materials obtained discharge capacities that were slightly lower when compared to the undoped manganese spinel synthesized materials. There was a slightly higher first discharge capacity of the doped manganese oxide materials that had larger active material that were made by the spray-drying method. This could be due to the slightly larger surface areas and smaller crystallite sizes of the active material when compared to the material made by the batch process (Section 4.2, Table 4.6). The overall electrochemical performance of these cells will have to be studied further, that includes the construction of larger type cells with more active cathode material and subjecting them to a variable discharge rate test and a

comparatively deep capacity life cycle test at various temperatures. This would require careful synthesis of a larger amount of material that is uniform in its particle size, morphology and surface area.

In order to understand the materials' electrochemical performance, apart from its capacity performance (made on a small scale), the variation of their impedance properties was also investigated that could give possible insight into the materials' electrochemical characteristics as it relates to its synthesis and material characteristics. The obtained results would then give insight into the ability to synthesize homogenous cathode active materials on a larger scale and could be used as a quality control check for large scale active cathode material synthesis. Small amounts could then be taken from the larger batches that were obtained by the manufacturing processes and built into suitable button cells and analyzed using a relatively quick impedance profile test giving insight into the electrochemical characteristics of the material.

5.2 <u>Electrochemical Impedance Spectroscopy (EIS)</u>

EIS analysis was done to investigate the variation in certain electrochemical impedance characteristics that included the materials' Li-ion diffusion ability upon the charging process of the cells. The EIS profile consisted of applying a frequency range of 100 kHz to 10 mHz at various predetermined charge voltages. The test procedure involved charging the cell to a specific voltage (3.5, 3.9, 4.2 and 4.5 V) at 0.1 C respectively and potentiostatically holding the potential until the current dropped to 0.001 mA. This was followed by an EIS measurement at each of the particular voltages similar to that reported by Gamry application notes[23]. The experiments were done in duplicate and the results averaged. After each EIS test at a particular voltage, the cells were discharged to 3.0 V before recharging to the next voltage limit, followed by another EIS scan (Figure 5.6). This was done in order to ensure that a full recharge (Li-ion extraction) at a particular voltage was achieved. This was in line with the work that was reported by Erol[24] where they studied the cell's impedance in the nominal operating voltage together with their impedance responses to overcharging, over-discharging and temperature extremes[24].

This study was done on all the synthesized cathode oxide materials (the doped and undoped materials) prepared by both the batch and spray-drying techniques. A typical

charge profile is shown in Figure 5.6 and a typical range of EIS spectra with the fitted equivalent circuit model at each charge step is shown in Figure 5.7. The electrical equivalent circuit (EEC) used in this study was shown in Figure 3.16 and was typically used to describe the impedance performance of Li-ion cells[25]. The results were graphically similar for all types of cells studied and their results are summarized in Appendix A.
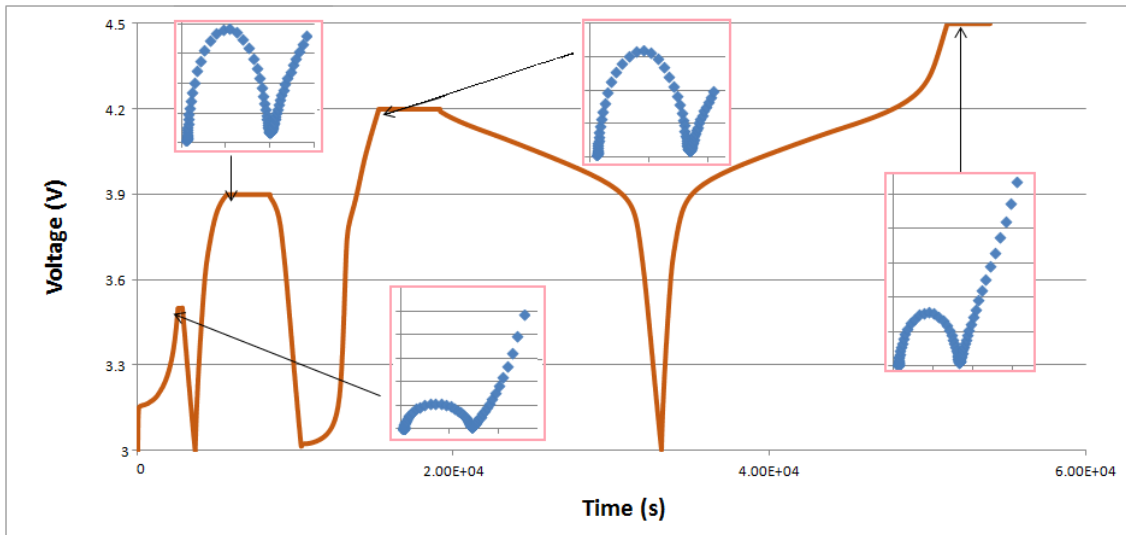
Figure 5.6: Typical charge – discharge curve with inserted EIS measurements at various voltages.
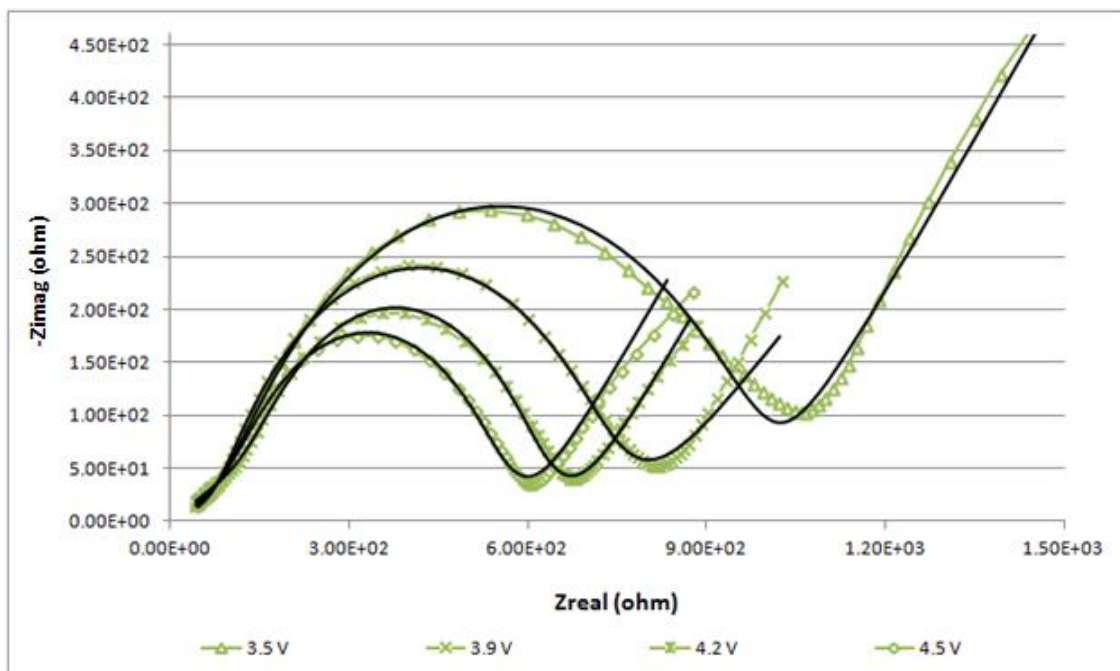
Figure 5.7: Typical Nyquist plots of $LiCo_{1.09}Mn_{0.91}O_4$ (by spray-drying) at various voltages whereby the solid line indicates the fitted model to the experimental data.

The EIS spectra consisted typically of a semicircle in the high frequency region and a straight sloping line in the low frequency region. The semicircle relates to the charge-transfer process that occurs at the electrode's surface and the straight line at about an angle of 45° to the diffusion limiting effect of lithium ions in the cathode material. These observations are in line with many other authors that describe the impedance spectra of Li-ion cells[25-27]. These results showed that the observed semicircles decreased as the charge voltages increased implying that the charge or capacitance contribution decreased proportionally as the cell approached full state of charge and that there was a significant influence on the lithium ion's mobility at different voltage limits.

Some values of interest from the results of the EEC model fitting for all the various cells studied are compared graphically in Figures 5.8 to 5.13 and the tabulated results are shown in Appendix A.
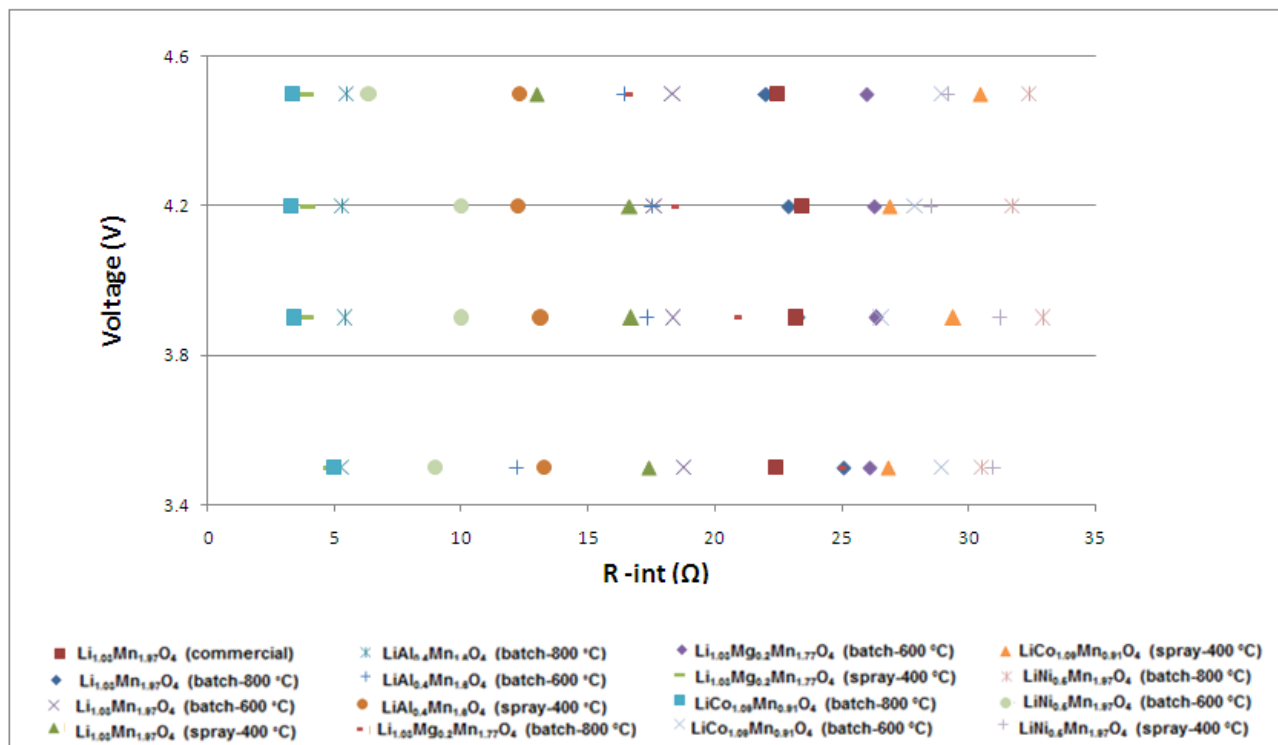
Figure 5.8: Plot of the change in the cells internal resistance over the various charge voltage ranges.

The results showed that the internal cell resistance (R-int) would typically vary between 4 to 34 Ω for the various oxide materials at the different voltages studied. On average, the cells made with the undoped Mn spinel material showed a slightly higher internal resistance throughout the voltage ranges. There was little variation between the internal resistances of a particular cell analyzed at the various voltages. The internal resistance contribution of the cells would be typically influenced by the cell assembling, electrolyte wetting of the electrode materials and separators. These values in this study were relatively low between the different cells with the different cathode materials.
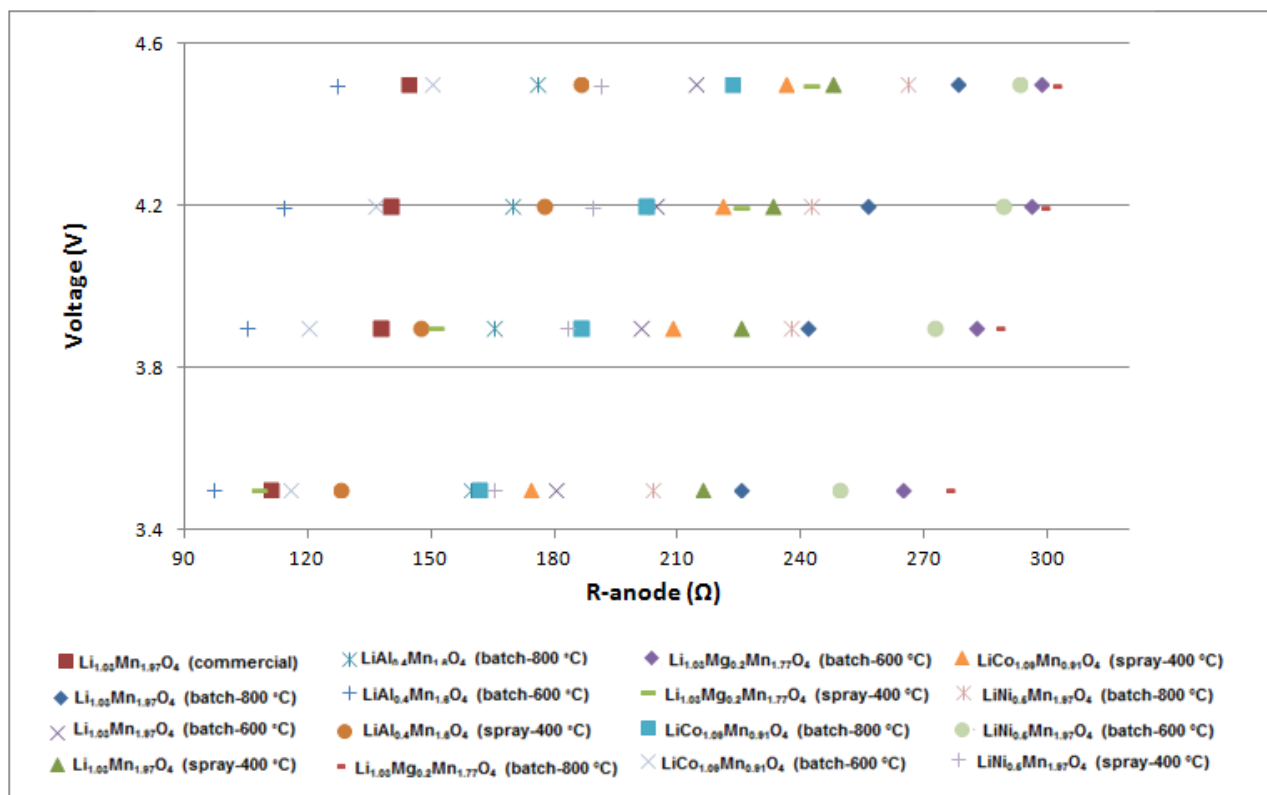
Figure 5.9: Plot of the cell's anode resistance over the various voltage ranges.

The results showed that the resistance was relatively small at low voltages (irrespective of the material or synthesis process). As the cell was charged, the resistance would then increase. This implies that at low voltages there was enough space or cavities for the Li-ion to deposit into the anode. As the Li-ions deposits are accumulating at the anode resulting into a decrease in rate deposition (constant rate or plateau) at the higher voltages, the electrode resistance would then increase slightly.
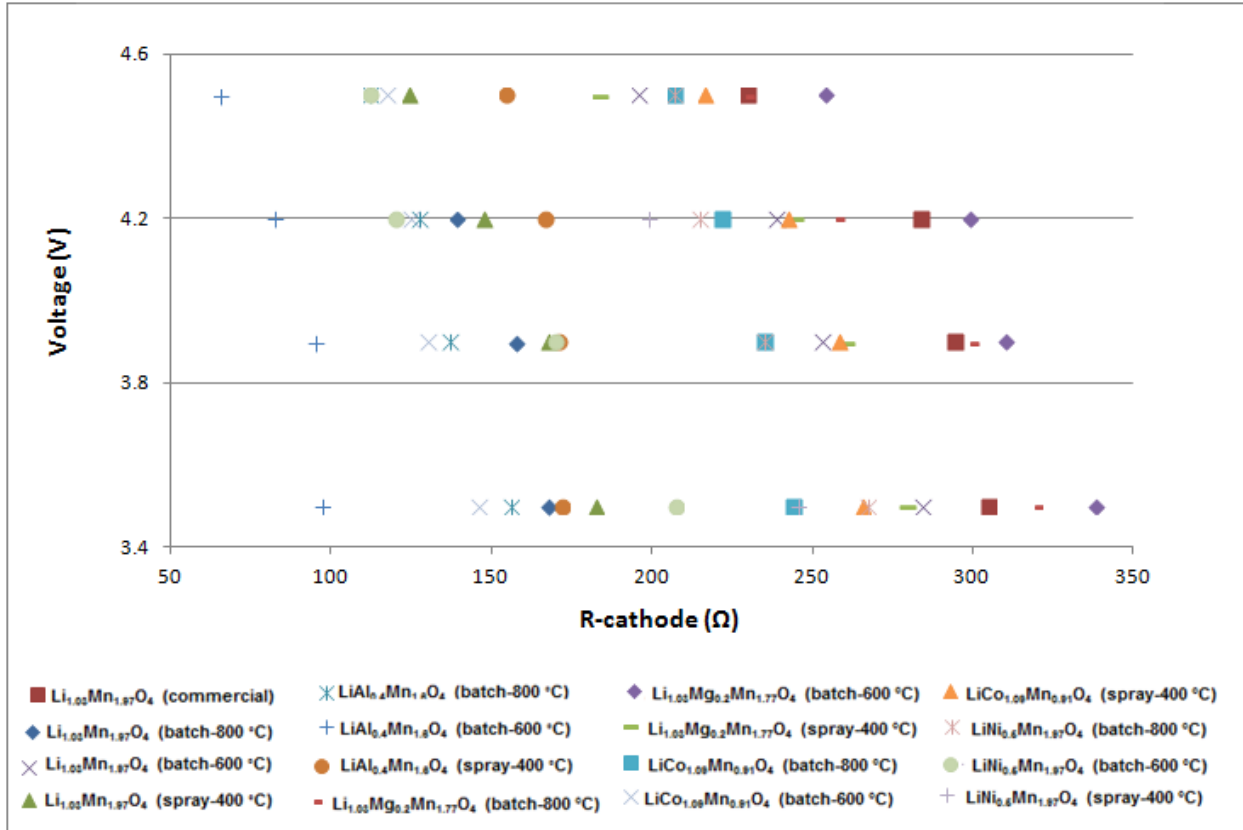
Figure 5.10: Plot of the cell's cathode resistance over the various voltage ranges.

The results showed an opposite effect to that observed by the anode resistance (Figure 5.9). At low voltages the cathode resistance was comparatively higher and as the cell reached its fully charged state, the electrode resistance would then decrease. This implies there was more electron diffusion taking place in the cathode material as the cell was charged thereby lowering the cathode resistance. This decrease in resistance as the charge voltage increased was observed throughout the various oxide materials irrespective of the cathode synthesis technique used.

The results of plotting the Warburg function (W) observed for the various cells made by the different synthesis techniques and dopants at the various charge voltages are shown in Figure 5.11. The results varied over a relatively wide range with no clear trends between the various cathode oxide materials at various charge voltages.
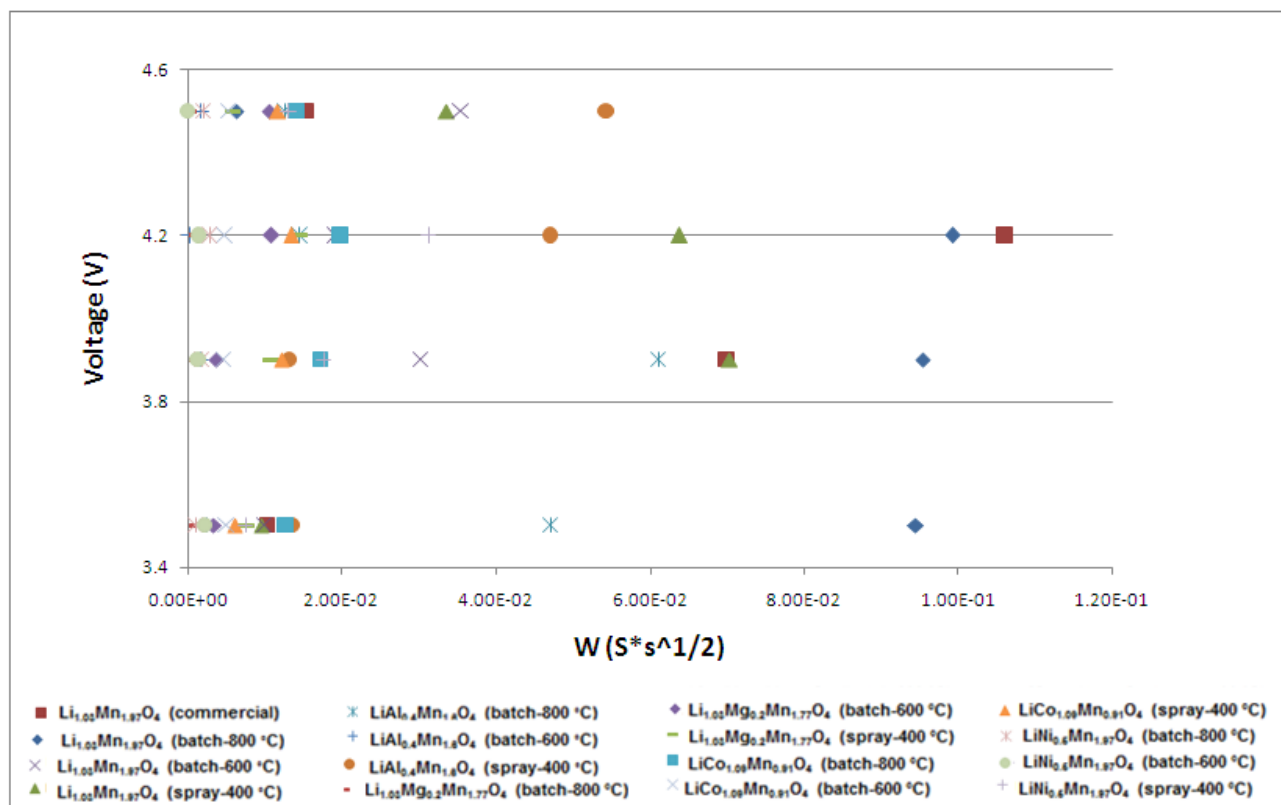
Figure 5.11: Plot of the cells Warburg function over the various charge voltage ranges.

The results of the comparative study of the various cells' anode and cathode capacitance are shown in Figures 5.12 and 5.13 respectively.
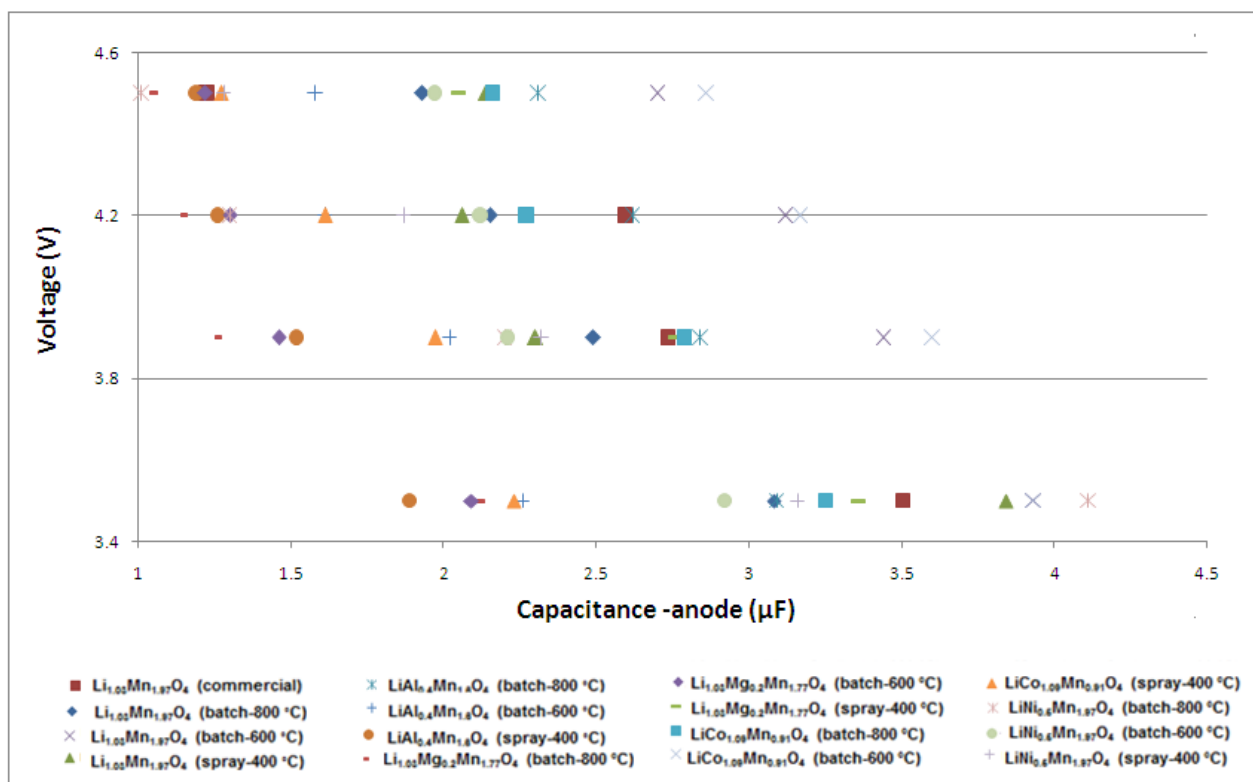
Figure 5.12: Plot of the cell's anode capacitance over the various voltage ranges.
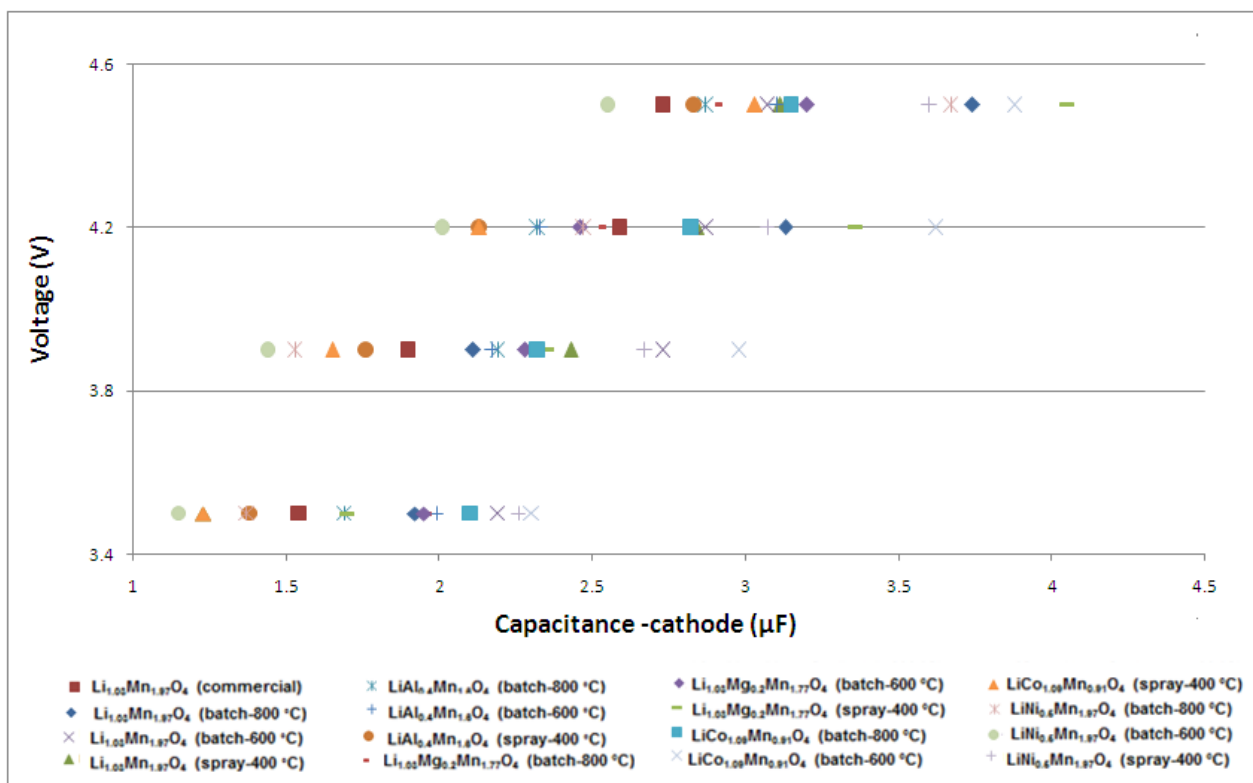
Figure 5.13: Plot of the cell's cathode capacitance over the various voltage ranges.

The results showed that as the charge voltage of the various cells increased, the respective anode capacitance decreased for all the various cathode oxide materials studied. Whereas the relative capacitance of the cathode would increase as the charge voltage increased. This implied that as the cell was recharged (increase in voltage) the Li^+ migrate out of the spinel structure to the anode allowing the surface to be charged and thus increasing the capacitance. Proportionality, the charge on the anode would then decrease, taking into consideration that the anode (Li metal foil) would be in excess in the cell used in this study. There are notable differences observed in the respective cells that are charged at different charge voltages with regards to the Li-ion mobility from the cathode material that are made with different dopants. The goodness of fit (GoF) observed during model fitting would also provide a good estimation if the EEC model was appropriate for the particular data. On average, for these materials a goodness of fit was obtained to be 10^{-4} or lower (Appendix A). This is in agreement as recommended by Gamry[23]. From these results, parameters such as Li-ion diffusion, electron diffusion and the diffusing rate can be obtained to give insight into the electrochemical behaviour of the various doped cathode materials. In this study, the Li-ion diffusion will be considered.

5.3 <u>Lithium-ion diffusion</u>

The lithium-ion diffusion ability between the electrodes and electrolyte is of importance in understanding the ability for the host cathode material to provide the "speed" or rate at which the intercalated Li-ion electron couple can move. This relates to the materials' ability in a cell to deliver the high rates of charge or discharge that has become important in typical consumer electronics and EV applications[28]. In literature the diffusion coefficient can be determined by using potentiostatic and galvanostatic intermittent titration technique (PITT and GITT respectively), cyclic voltammetry (CV) or by electrochemical impedance spectroscopy (EIS)[29-32]. In this study the EIS technique was used to determine the lithium diffusion coefficient (D_{Li}).

Within this study the diffusion coefficient was determined and compared for the various cathode oxide materials using different synthesis techniques at the various charge voltage limits. The diffusion coefficient in equation 3.4 considers the surface area of the electrode. In some literature, the area used in the calculation was usually the geometrical electrode

surface area[33]. However, this study showed that there were significant differences in the measured BET surface areas (when used to calculate D_{Li}) of the various cathode oxide materials prepared by the different synthesis techniques. However, if literature considered mainly the geometrical electrode surface area or area of the cathode electrode/electrolyte interface[33-36], it can be an over simplification when considering the movement of the Li-ion in a cathode active material. The diffusion of the Li-ion in the active material would be dependent on the materials particle size and its active surface area that is in contact with the electrolyte across a 3D electrode active surface. The available surface area of the active material to the electrolyte interface is not only the macroscopic measured electrode disc area, which in this case was that of a typical button cell of 2.01 cm^2. The electrolyte would typically permeate throughout the actively prepared cathode material, allowing for a significantly larger area to be available at the electrolyte/active-material interface. Also, using only the geometrical electrodes surface area does not take the active materials mass into consideration thereby having a significant influence on equation 3.4. Hence, since BET surface area measurements are a good representation of the amount of surface area[37, 38] of the active materials that can be in contact with the electrolyte, it would be a better measurement to use in its contribution to the Li-ion diffusability from equation 3.4. The equation shows that the D_{Li} is inversely proportional to the square of the area and the value used for the active area can influence the results significantly. In this study, both the geometrical area of the electrode and the BET active material surface area were used in the calculations and compared (Appendix B).

The calculated molar ratio of lithium in the active material was plotted for each of the different charge voltages in order to calculate the lithium concentration within the active material (Figure 5.14). This calculated concentration would then contribute toward the diffusion coefficient calculation (equation 3.4).
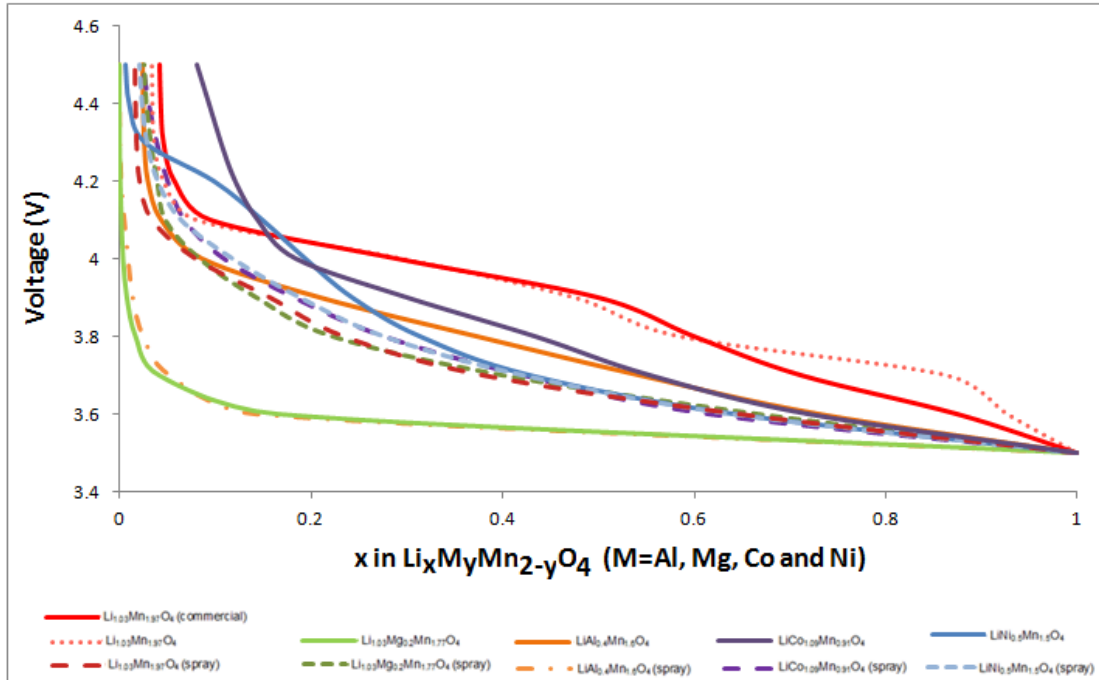
Figure 5.14: Plot of the lithium molar concentration ratio for each active material at the different charge voltages.

The Warburg factor (σ) for each of the cells studied at the various charge voltages was determined from the slope of the straight line by plotting Z (Ω) versus the $\omega^{-1/2}$ (Figures 5.15 to 5.25).
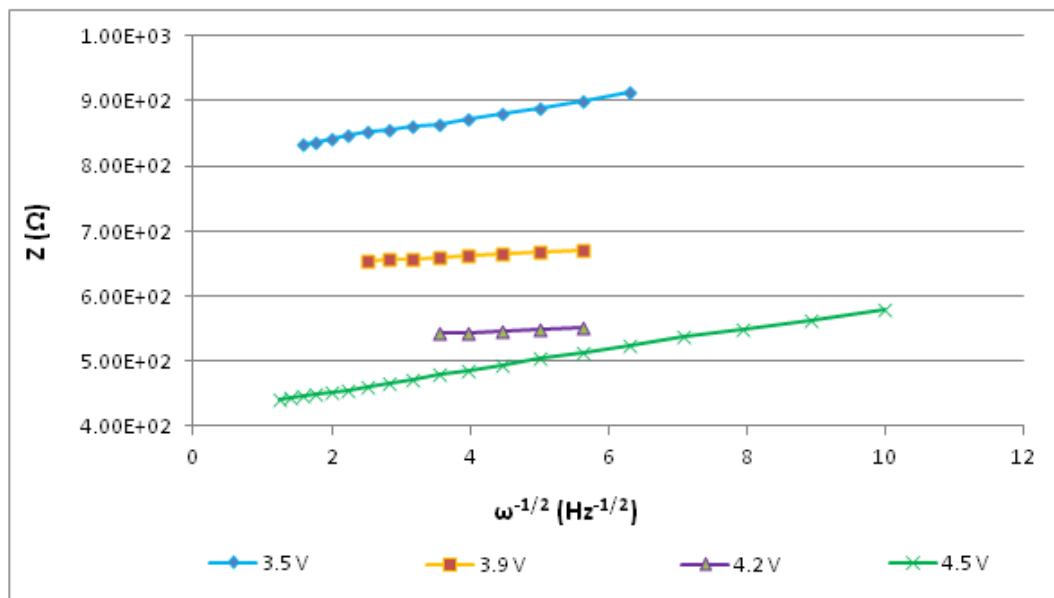
Figure 5.15: The relationship between Z (real impedance) and $\omega^{-1/2}$ in the low frequency region for commercial $Li_{1.03}Mn_{1.97}O_4$.
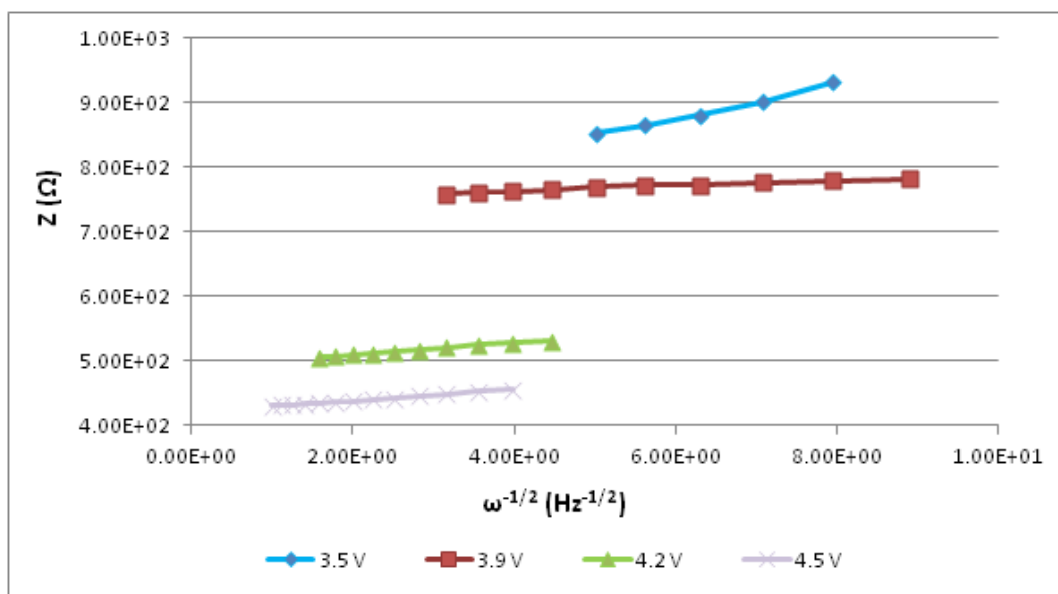
Figure 5.16: The relationship between Z (real impedance) and ω$^{-1/2}$ in the low frequency region for Li$_{1.03}$Mn$_{1.97}$O$_4$ (synthesized batch process).
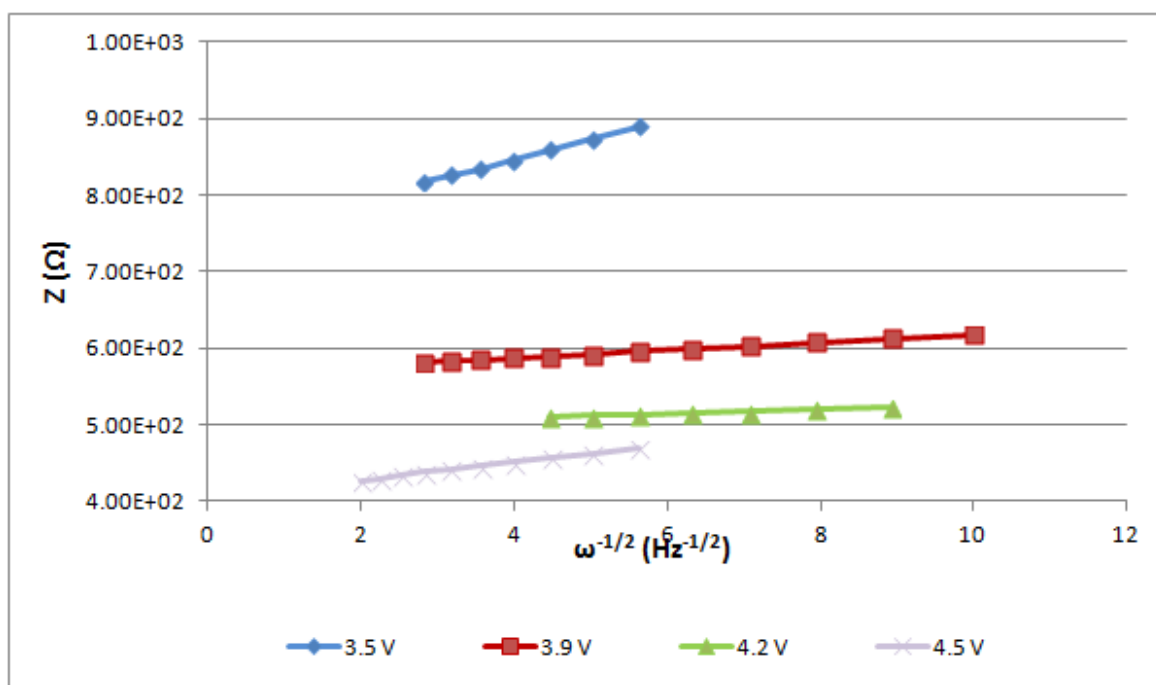
Figure 5.17: The relationship between Z (real impedance) and ω$^{-1/2}$ in the low frequency region for Li$_{1.03}$Mn$_{1.97}$O$_4$ (spray process).
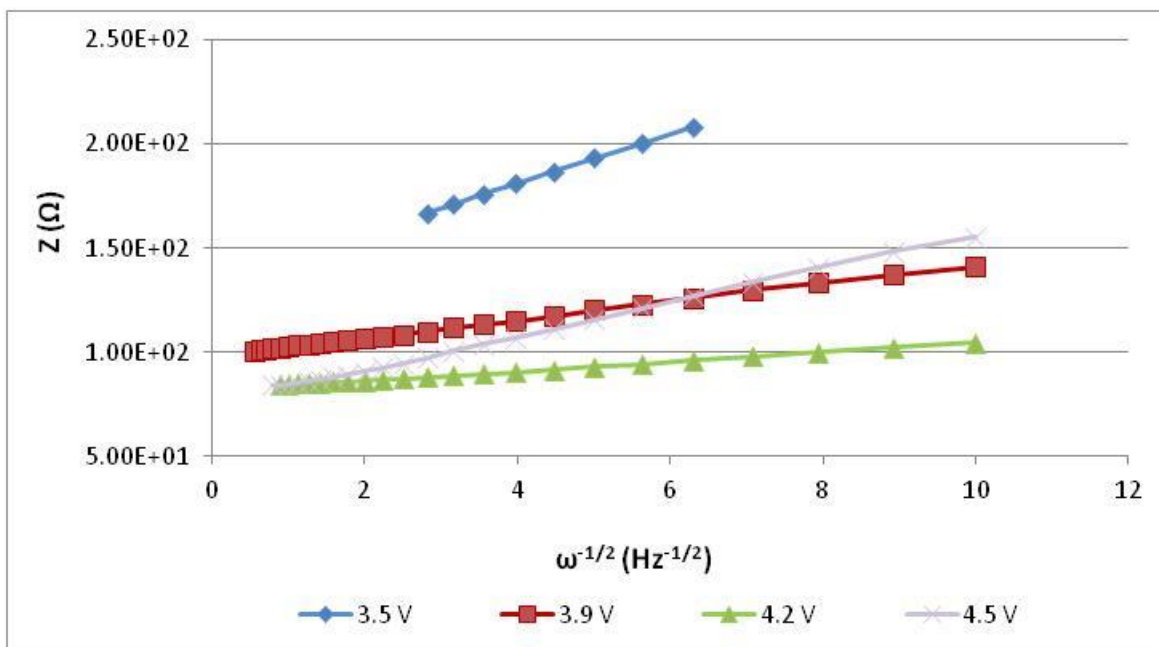
Figure 5.18: The relationship between Z (real impedance) and $\omega^{-1/2}$ in the low frequency region for LiAl$_{0.4}$Mn$_{1.6}$O$_4$ (batch process).
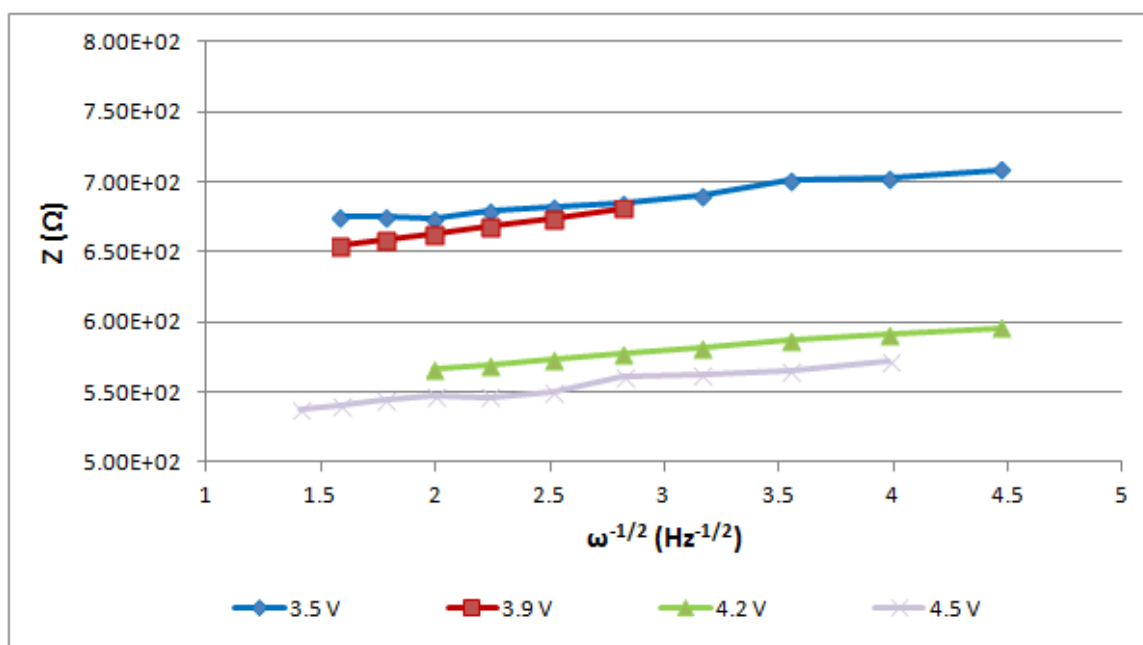
Figure 5.19: The relationship between Z (real impedance) and $\omega^{-1/2}$ in the low frequency region for LiAl$_{0.4}$Mn$_{1.6}$O$_4$ (spray process).
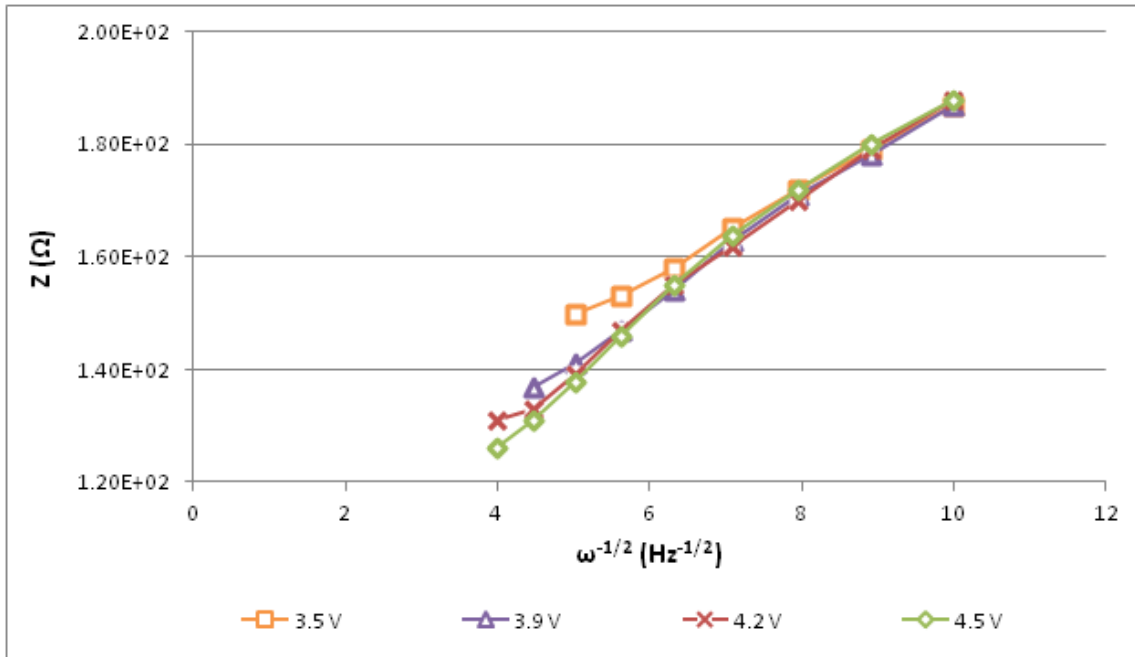
Figure 5.20: The relationship between Z (real impedance) and $\omega^{-1/2}$ in the low frequency region for $Li_{1.03}Mg_{0.2}Mn_{1.77}O_4$ (batch process).
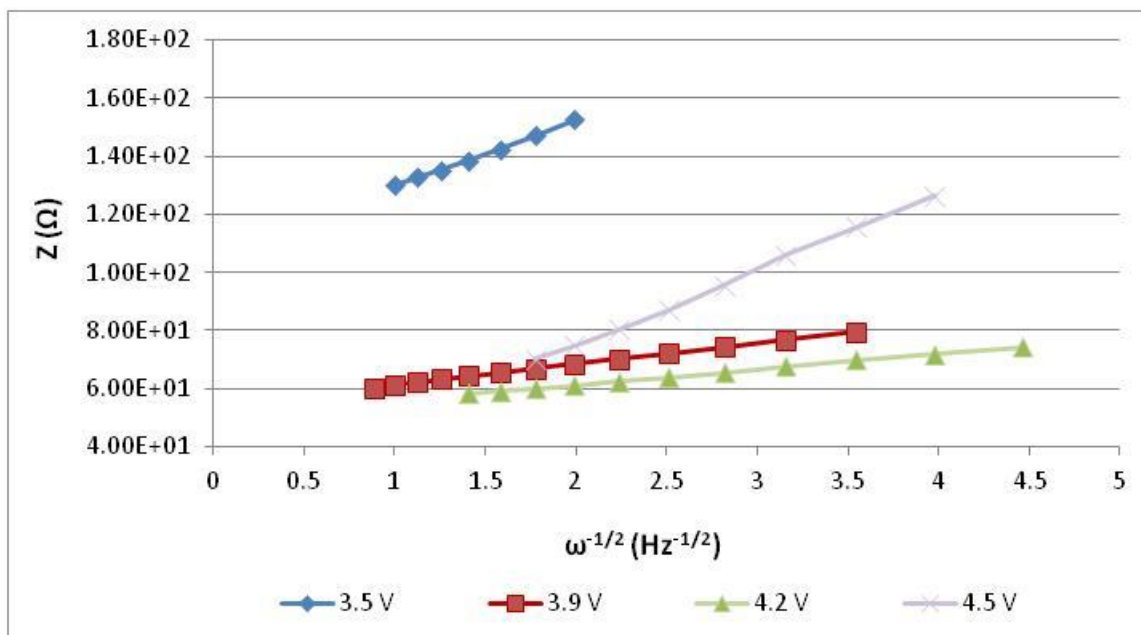
Figure 5.21: The relationship between Z (real impedance) and $\omega^{-1/2}$ in the low frequency region for $Li_{1.03}Mg_{0.2}Mn_{1.77}O_4$ (spray process).
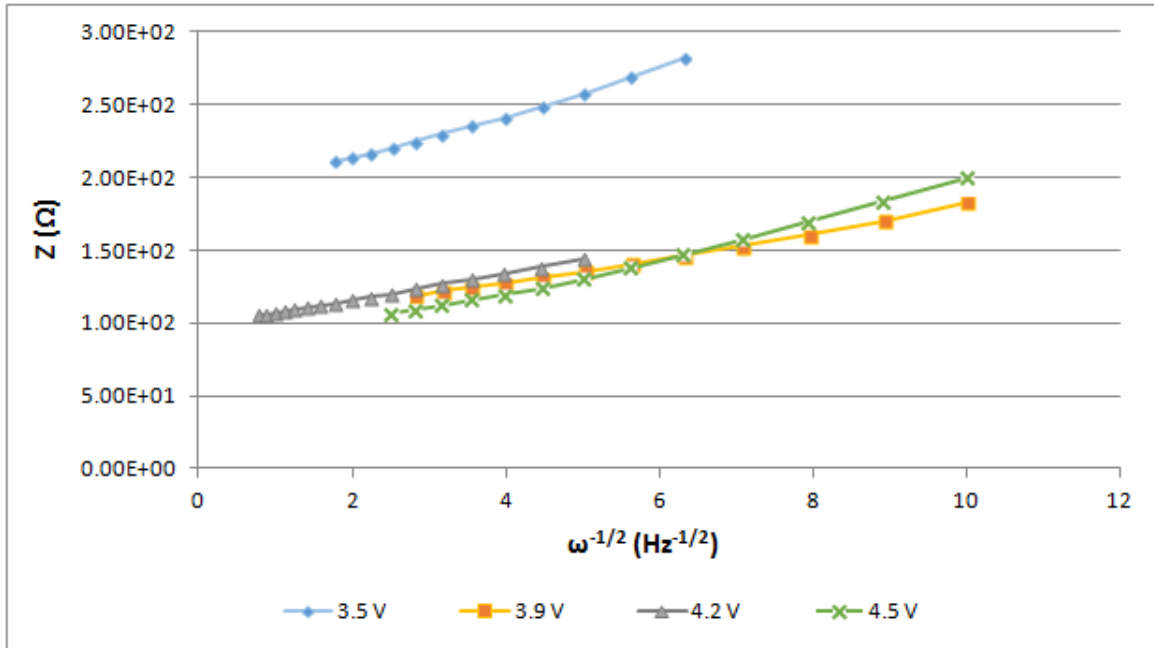
Figure 5.22: The relationship between Z (real impedance) and $\omega^{-1/2}$ in the low frequency region for $LiCo_{1.09}Mn_{0.91}O_4$ (batch process).
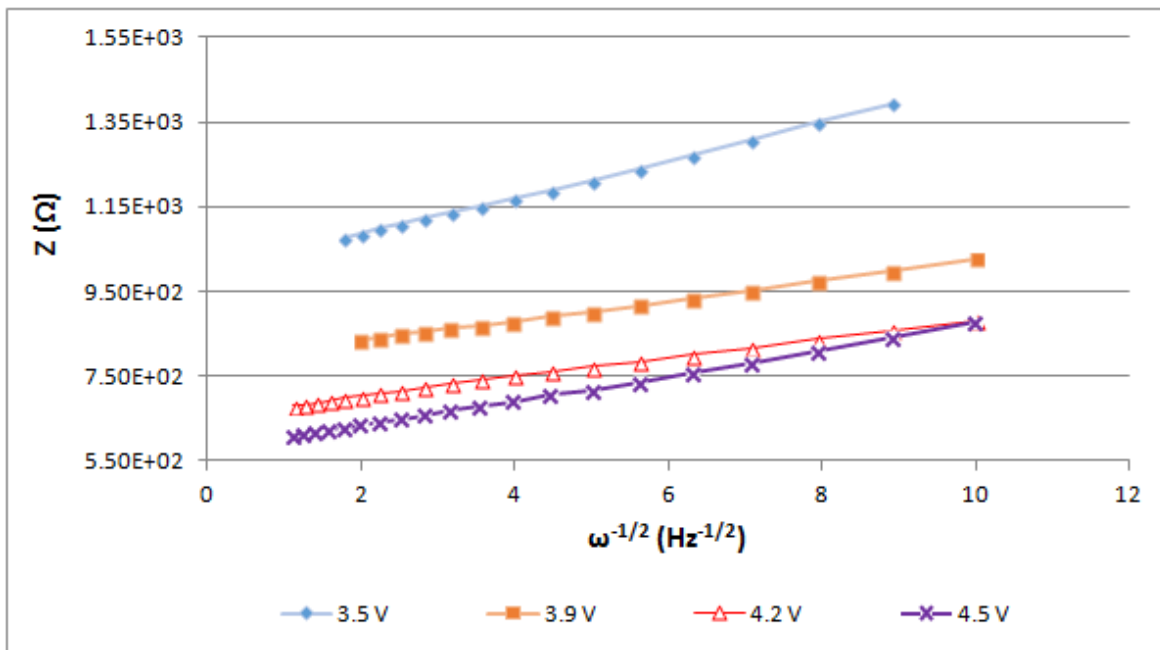
Figure 5.23: The relationship between Z (real impedance) and $\omega^{-1/2}$ in the low frequency region for $LiCo_{1.09}Mn_{0.91}O_4$ (spray process).
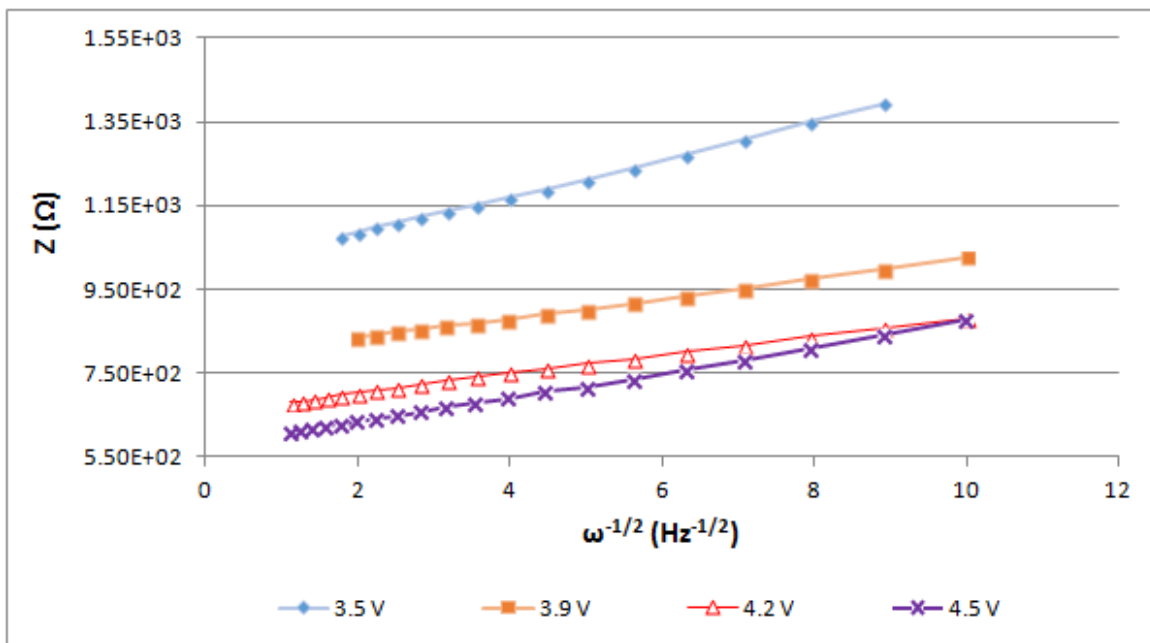
Figure 5.24: The relationship between Z (real impedance) and ω$^{-1/2}$ in the low frequency region for LiNi$_{0.5}$Mn$_{1.5}$O$_4$ (batch process).
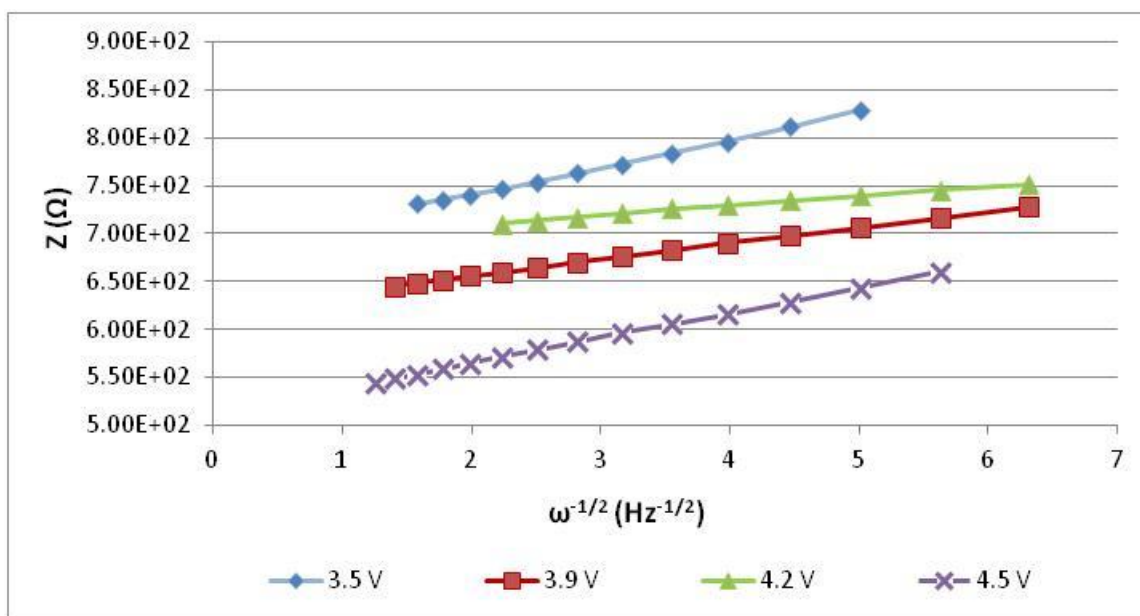
Figure 5.25: The relationship between Z (real impedance) and ω$^{-1/2}$ in the low frequency region for LiNi$_{0.5}$Mn$_{1.5}$O$_4$ (spray process).

The results (Figures 5.15 to 5.25) showed that there was a linear relationship for all the samples studied in terms of their respective Z$_{real}$ vs ω$^{-1/2}$ values and that in most cases the

values at the 3.5 V charge voltage had comparatively higher real impedance values. The slope from these graphs were then used as the σ ($\Omega.s^{-1/2}$) value in equation 3.4 in order to determine the Li-ion diffusion coefficient at the specified charge voltages for the different cathode materials synthesized. Both the slope of the graphs (σ) and their respective y-intercepts with the BET surface area for the cells made with the different cathode materials are shown in Appendix B.

The BET surface area ($m^2.g^{-1}$ of active material) and the geometrical electrode area (2.01 cm^2) of the various synthesized cathode materials were used in equation 3.4 to calculate the D_{Li} coefficient. These calculated D_{Li} coefficient results were compared for the different cathode oxide materials at their specific charge voltages (3.5, 3.9. 4.2 and 4.5 V) and summarized in Table 5.3. Within Table 5.3 the highlighted sections represented the D_{Li} coefficient based on using the materials' BET surface area. The results showed that materials synthesized by the spray-drying method produced a material with a higher surface area when compared to the batch sol-gel process and in turn would have an influence on how the D_{Li} was then calculated.

As a result of the findings from the in-situ PXRD material study (Chapter 4, Table 4.12 to 4.16), for comparison purposes, samples that were synthesized at 600 °C are included throughout this study.

Table 5.3: Summary of the calculated diffusion coefficients

Voltage (V)	Batch sol-gel process D_{Li} (cm^2.sec^{-1}) at 800 °C		D_{Li} (cm^2.sec^{-1}) at 600 °C		Spray-drying process D_{Li} (cm^2.sec^{-1}) at 400 °C	
Li$_{1.03}$Mn$_{1.97}$O$_4$ (Commercial)						
3.5	2.6E-13	1.99E-18				
3.9	1E-11	7.68E-17				
4.2	1.32E-09	1.01E-14				
4.5	1.62E-09	1.24E-13				
Li$_{1.03}$Mn$_{1.97}$O$_4$						
3.5	9.65E-14	5.57E-17	7.65E-14	1.19E-16	1.05E-13	7.01E-17
3.9	1.05E-11	1.16E-15	5.85E-11	3.3E-14	5.53E-12	3.68E-15
4.2	4.20E-10	8.14E-14	1.80E-10	8.38E-14	5.54E-11	3.69E-14
4.5	8.32E-10	1.56E-13	3.32E-09	1.31E-13	3.17E-10	2.11E-13
LiAl$_{0.4}$Mn$_{1.6}$O$_4$						
3.5	4.45E-13	1.24E-17	3.19E-13	2.07E-17	3.58E-13	6.08E-17
3.9	2.81E-11	1.12E-16	1.02E-11	6.58E-16	1.25E-11	2.11E-16
4.2	4.35E-10	6.85E-16	3.34E-11	1.16E-15	9.82E-11	1.49E-15
4.5	7.50E-10	2.2E-15	3.40E-11	1.67E-15	2.76E-10	3.30E-15
Li$_{1.03}$Mg$_{0.2}$Mn$_{1.77}$O$_4$						
3.5	1.07E-12	1.39E-17	6.58E-12	4.81E-17	1.23E-13	1.64E-17
3.9	1.13E-12	1.47E-16	1.95E-11	7.03E-16	2.47E-12	3.28E-16
4.2	1.24E-11	8.39E-15	1.84E-10	3.74E-15	8.97E-12	1.19E-15
4.5	1.39E-11	1.81E-14	2.14E-10	1.74E-14	5.75E-11	7.63E-15
LiCo$_{1.09}$Mn$_{0.91}$O$_4$						
3.5	3.07E-13	6.43E-17	1.45E-14	4.43E-17	3.70E-14	5.32E-17
3.9	1.05E-11	4.88E-16	1.61E-14	1.40E-16	3.19E-12	4.59E-16
4.2	2.14E-11	9.92E-16	2.63E-14	8.06E-16	5.60E-11	8.04E-16
4.5	4.66E-11	3.16E-15	4.20E-14	2.97E-15	2.05E-10	2.94E-15
LiNi$_{0.5}$Mn$_{1.5}$O$_4$						
3.5	1.30E-14	1.70E-16	1.50E-14	8.21E-17	7.09E-14	9.24E-17
3.9	2.56E-14	1.26E-15	3.07E-13	4.68E-16	5.27E-13	6.87E-16
4.2	9.64E-14	3.34E-15	6.57E-13	3.59E-15	2.92E-12	3.81E-15
4.5	2.96E-13	7.38E-15	1.59E-12	3.86E-15	5.66E-11	8.67E-15

(Annotations: green arrow → BET surface area; red arrow → geometrical electrode area)

The results showed that by using the different surface areas based on either the cathode geometrical electrode area or the actual BET active material surface area (SA), significant differences were observed in the calculated D_{Li} coefficient. The D_{Li} coefficient calculated with the BET SA gave a range of values from 10^{-13} to 10^{-18}, that was significantly lower when compared to the calculated D_{Li} by using the geometrical electrode surface area which was from 10^{-9} to 10^{-14} respectively. The calculated D_{Li} coefficient values was however in most cases within range to literature reported results (summarized in Table 5.4) at the various charge voltages (3.9, 4.2 and 4.5 V) for both synthesis techniques, by using the estimated geometrical electrode area except for the 3.5 V regions (D_{Li} was lower). It should also be observed that the calculated D_{Li} coefficient for the doped oxide materials was lower than the undoped oxide material (at 4.5 V) regardless of the synthesis techniques and surface areas used.

Table 5.4: Summary of the literature reported diffusion coefficients

Spinel oxide material	D_{Li} (cm^2.sec^{-1})
$Li_{1.03}Mn_{1.97}O_4$	$[10^{-9} - 10^{-13}]$ [39-48]
$LiAl_{0.4}Mn_{1.6}O_4$	$[10^{-9} - 10^{-12}]$ [45, 46, 48]
$LiCo_{1.09}Mn_{0.91}O_4$	$[10^{-8} - 10^{-12}]$ [41, 44, 48]
$LiNi_{0.5}Mn_{1.5}O_4$	$[10^{-9} - 10^{-16}]$ [49-51]

It should be noted that the assumption was made that these literature D_{Li} coefficient results was on fully charged cells, as it was not always specified under which potential conditions (fully charged/discharged or partially charged/discharged) these values were calculated. The only condition which was fully discussed was the techniques (example PITT, GITT, CV or EIS) used to calculate the D_{Li} coefficient. The D_{Li} coefficient results for $LiMg_{0.2}Mn_{1.77}O_4$ was not available or provided in literature therefore, it was assumed that the D_{Li} coefficient for this material would also be within range to the other doped oxide materials (Al, Co and Ni) as their D_{Li} values are relatively similar.

This study made use of the BET surface area of the active materials in all the subsequent D_{Li} discussions and are summarized in Figures 5.26 to 5.30 respectively. In a state of full discharge, Li-ions are situated within the host cathode, whereby the Li-ions are closely

staggered together. Thereafter at the beginning of charge (low voltage), the de-intercalation of the Li-ion from the spinel oxide material results in a de-shielding of the electrostatic repulsion between the oxygen atoms of two adjacent layers in the unit cell. As the cell potential increases, there is an increase in site vacancies within the crystal structure thereby increasing the ease at which the ions can move through the material. These results are similar to the work done by Wang *et al.*[52] and Croce *et al.*[53]. The results are shown graphically using the active materials' BET surface area per active mass of material in the cell (Figures 5.26 to 5.30).
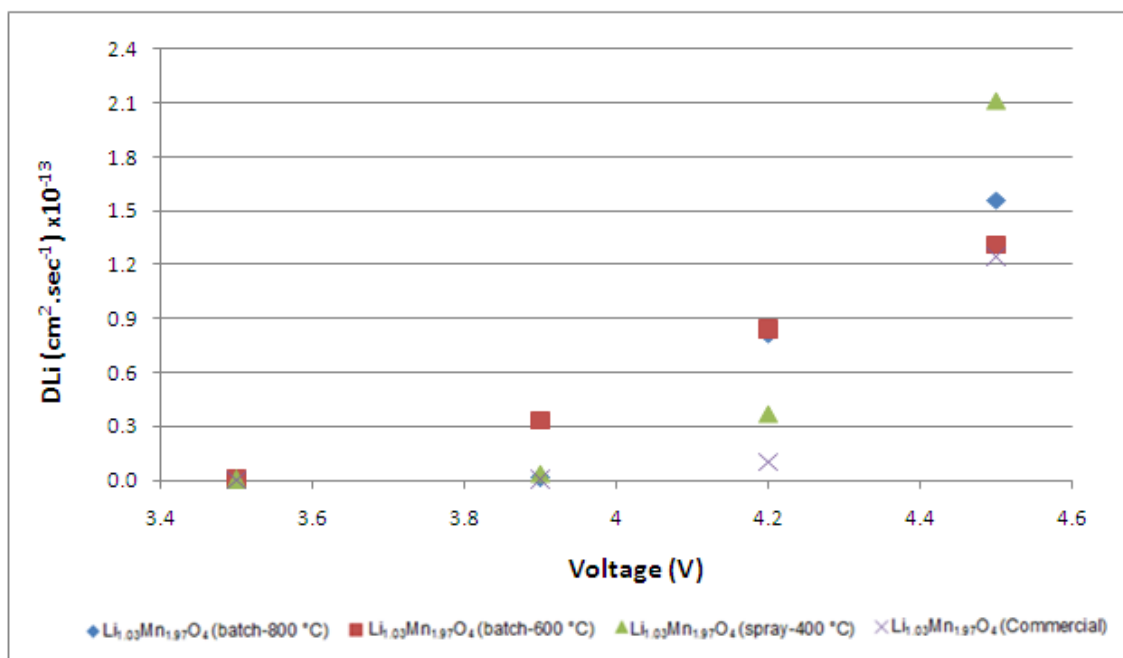
Figure 5.26: Graphical display of the lithium diffusion coefficient based on the BET surface area for $Li_{1.03}Mn_{1.97}O_4$.
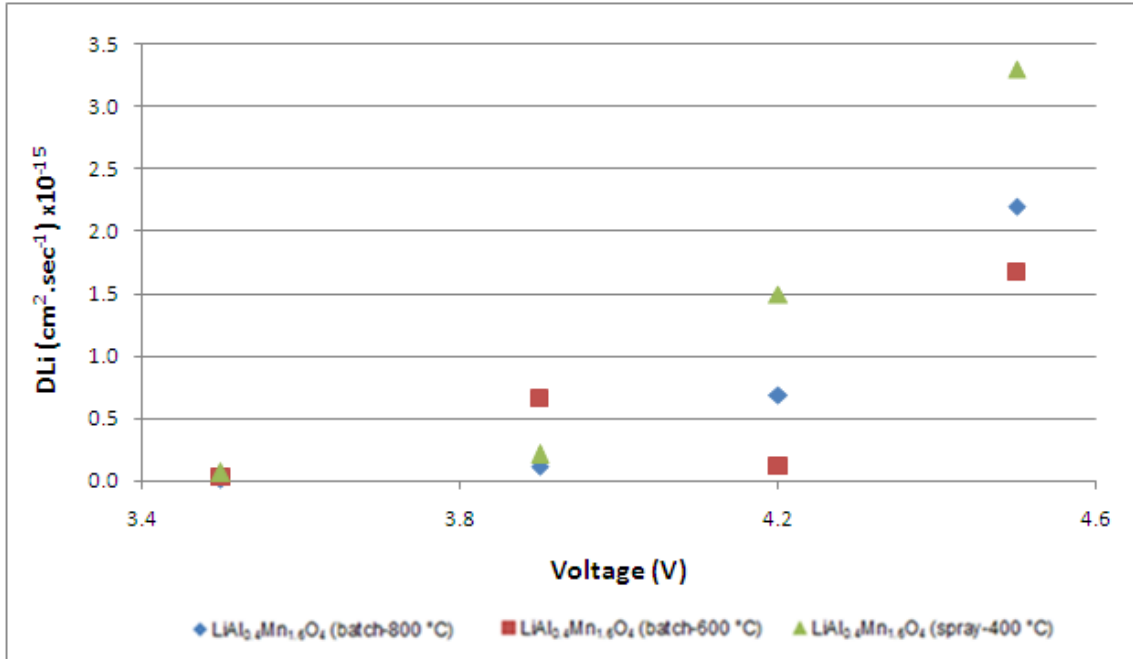
Figure 5.27: Graphical display of the lithium diffusion coefficient based on the BET surface area for LiAl$_{0.4}$Mn$_{1.6}$O$_4$.
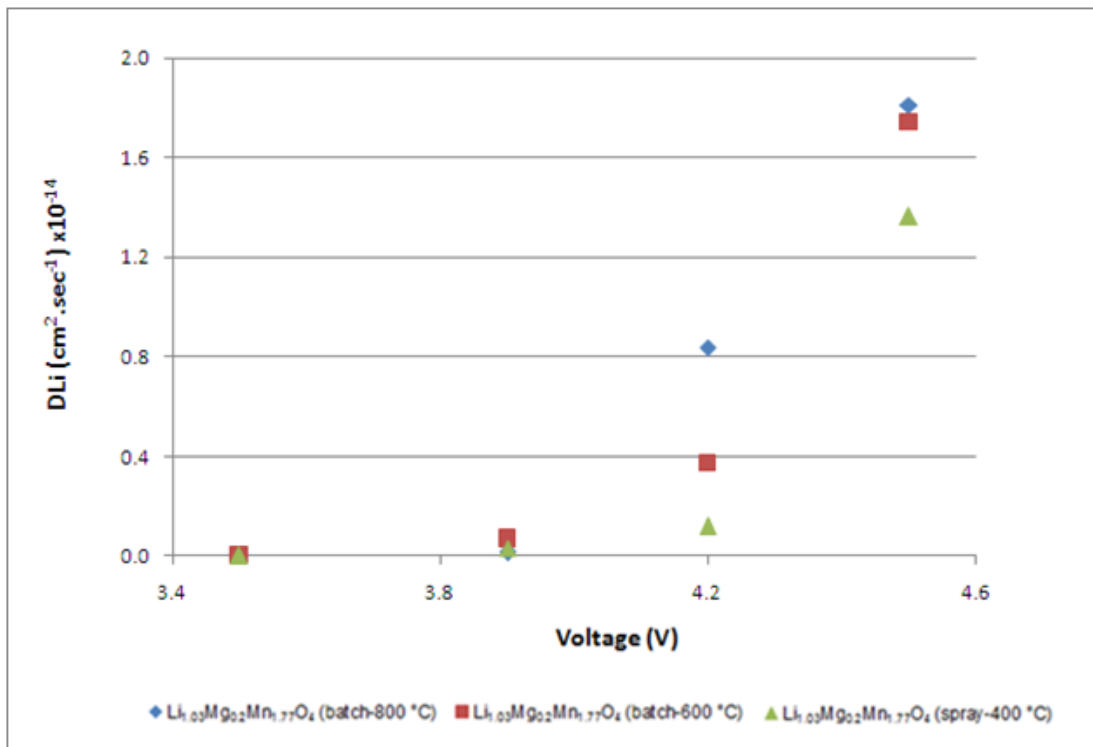
Figure 5.28: Graphical display of the lithium diffusion coefficient based on the BET surface area for Li$_{1.03}$Mg$_{0.2}$Mn$_{1.77}$O$_4$.
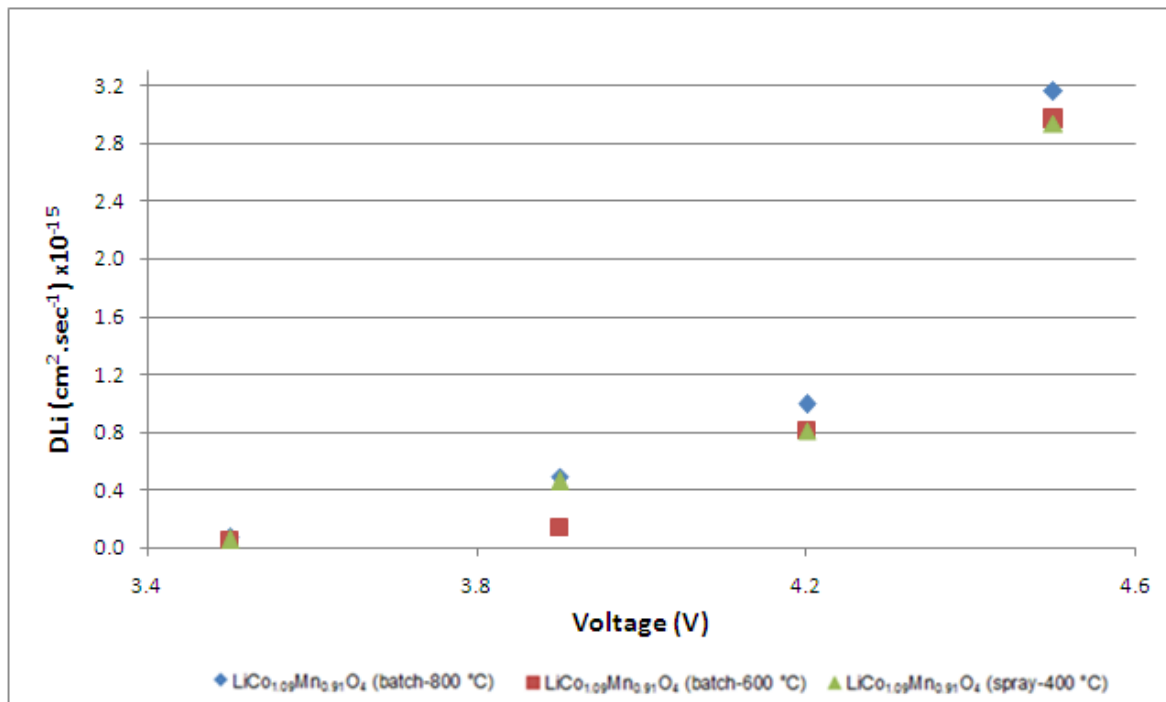
Figure 5.29: Graphical display of the lithium diffusion coefficient based on the BET surface area for LiCo$_{1.09}$Mn$_{0.91}$O$_4$.
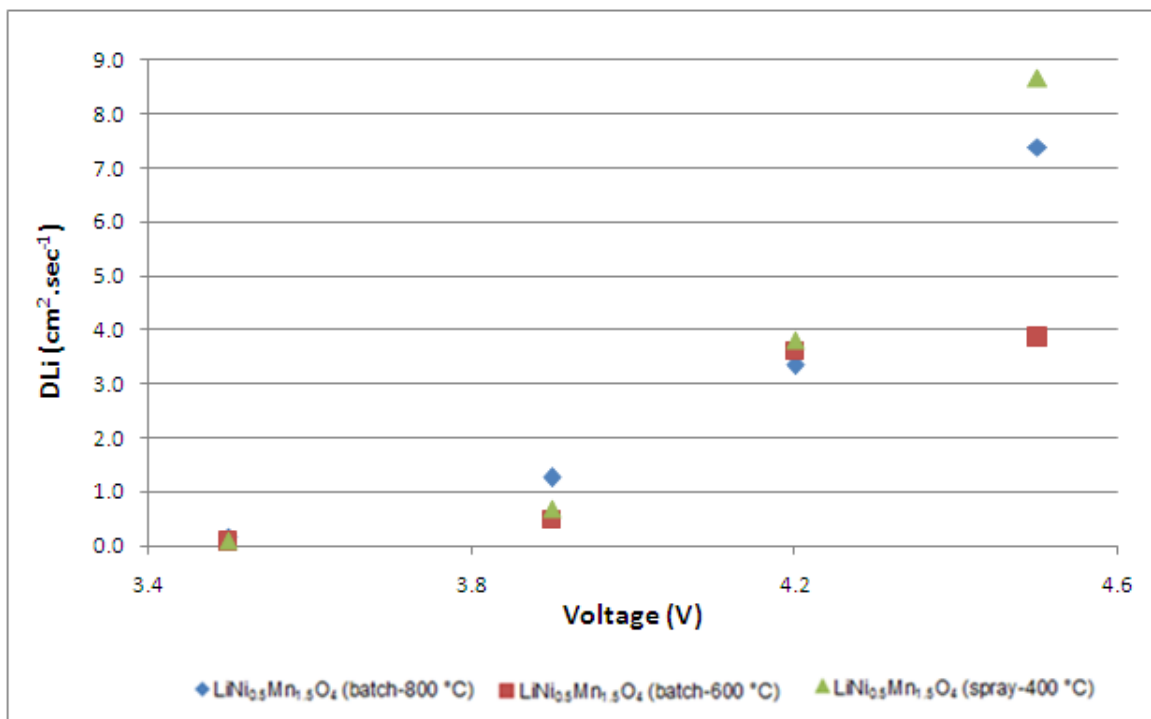
Figure 5.30: Graphical display of the lithium diffusion coefficient based on the BET surface area for LiNi$_{0.5}$Mn$_{1.5}$O$_4$.

The results showed that the D_{Li} coefficients followed similar trends (D_{Li} increases as voltage increase) between the different oxide materials regardless of the different synthesis techniques used (Figures 5.26 to 5.30). Referring to the diffusion calculation (equation 3.4) it should be noted that both the σ and Li-ion concentration (C) values vary over the different charge voltages. As σ increases with increase in the charge voltage, the diffusion coefficient should decrease. However the slope values obtained within this study showed no significantly large difference to offset the change in the Li-ion concentration. The D_{Li} results observed slight differences in the various materials synthesized by different techniques. For some materials synthesized at 400 °C the diffusion coefficient was slightly lower than others (example $LiMg_{0.2}Mn_{1.77}O_4$, Figure 5.27 and $LiCo_{1.09}Mn_{0.91}O_4$, Figure 5.29). This could in part be explained by the comparatively larger (or smaller) σ values and could also relate to the fact that these doped oxides produced lower discharge capacities from the spray-dried technique when compared to the oxides made by the batch sol-gel technique.

In conclusion, a larger D_{Li} value implies a faster rate at which the Li^+ moves or diffuses through the bulk material. Materials made by the spray-drying technique did not always give a material with a higher D_{Li} value for all the synthesized materials, once the cell reached full state of charge.

For comparison purposes, the slope (σ) and the y-intercept (Z-real) obtained from Figures 5.15 to 5.25 were graphically plotted against the different cell's charge voltages.

Figure 5.31: Graphical display of the slope obtained from the relationship between Z (real impedance) vs ω$^{-1/2}$ in the low frequency region for Li$_{1.03}$Mn$_{1.97}$O$_4$.

Figure 5.32: Graphical display of the slope obtained from the relationship between Z (real impedance) vs ω$^{-1/2}$ in the low frequency region for LiAl$_{0.4}$Mn$_{1.6}$O$_4$.

Figure 5.33: Graphical display of the slope obtained from the relationship between Z (real impedance) vs $\omega^{-1/2}$ in the low frequency region for $Li_{1.03}Mg_{0.2}Mn_{1.77}O_4$.

Figure 5.34: Graphical display of the slope obtained from the relationship between Z (real impedance) vs $\omega^{-1/2}$ in the low frequency region for $LiCo_{1.09}Mn_{0.91}O_4$.
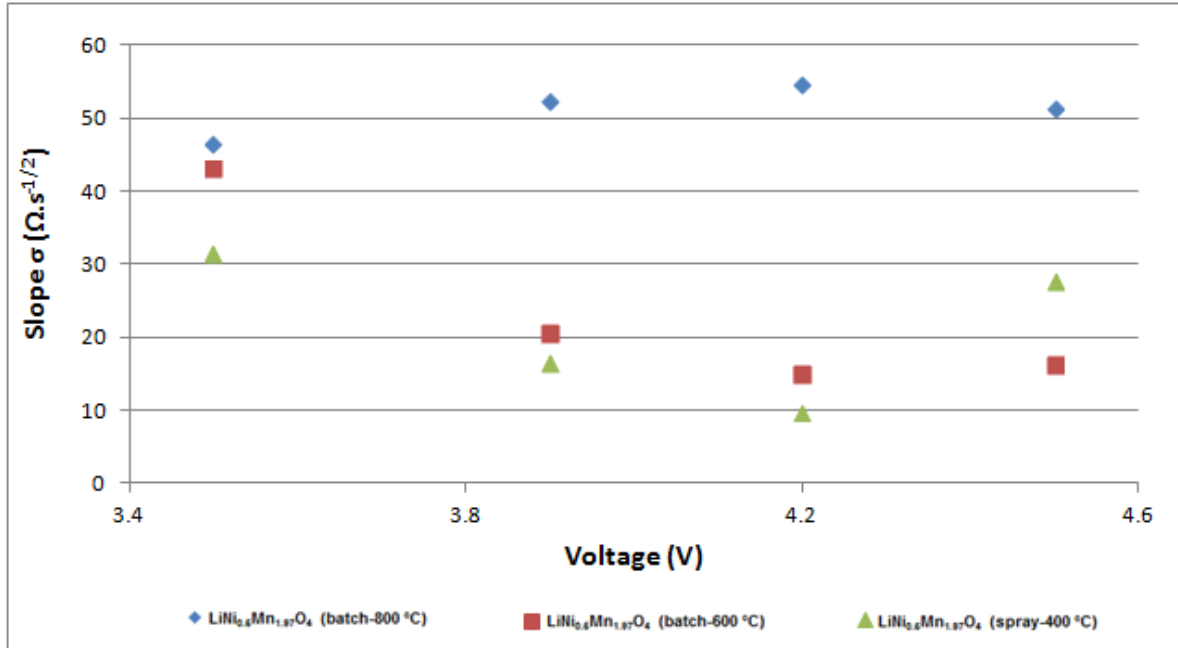
Figure 5.35: Graphical display of the slope obtained from the relationship between Z (real impedance) vs $\omega^{-1/2}$ in the low frequency region for $LiNi_{0.5}Mn_{1.5}O_4$.

The diffusion coefficient of ions in solution is referred to the Warburg coefficient (σ). This factor can be found from equation 3.6. The results when comparing the Warburg factor, σ, of the various oxide materials over the different charge voltage ranges (Figures 5.31 to 5.35) showed that there were no significant trends for the different oxide materials studied. This implied that the charge voltage of a particular cell has only little influence on the Warburg diffusion coefficient (slope, σ) of the ions as they move through the cathode material at the different charge voltages.

However, the y-intercept obtained from plotting the Z (real impedance) with $\omega^{-1/2}$ for the different charge voltages showed a definite linear trend for the various cathode materials studied at the different charge voltages (Figures 5.36 to 5.40). The y-intercept from the Z versus $\omega^{-1/2}$ relationship can be considered as the charge transfer resistance (R_{ct})[54].

The relationship between R_{ct} and Warburg are referred to as part of the faradaic impedance, whereby the cells reaction was kinetically controlled. A low R_{ct} would imply faster kinetics of the faradaic reaction[55, 56]. The charge transfer resistance also relates to the materials electronic conductivity. A higher R_{ct} would imply a lower electronic

conductivity. Charge transfer would be associated with the speed of the electron transfer to the electroactive species near the electrode surface[56]. The speed is dependent on the following parameters or variables; temperature, type of reaction, concentration of the reaction products, pressure, surface area and voltage[55, 56]. The effect of these variables on the R_{ct} was partially studied by Zhang *et al.*[55] and came to the conclusion that R_{ct} varies significantly with cell voltage and showed an increase in R_{ct} as temperature decreases. The R_{ct} would be the point whereby the semicircle observed on the impedance Nyquist plot would intercept with the start of the Warburg straight line. The R_{ct} values obtained throughout this study followed a similar trend to the results reported by Zhang *et al.*[55] where the R_{ct} would decrease with an increase in the charge voltage. What was evident in this study was that a good linear correlation for all the samples was observed.
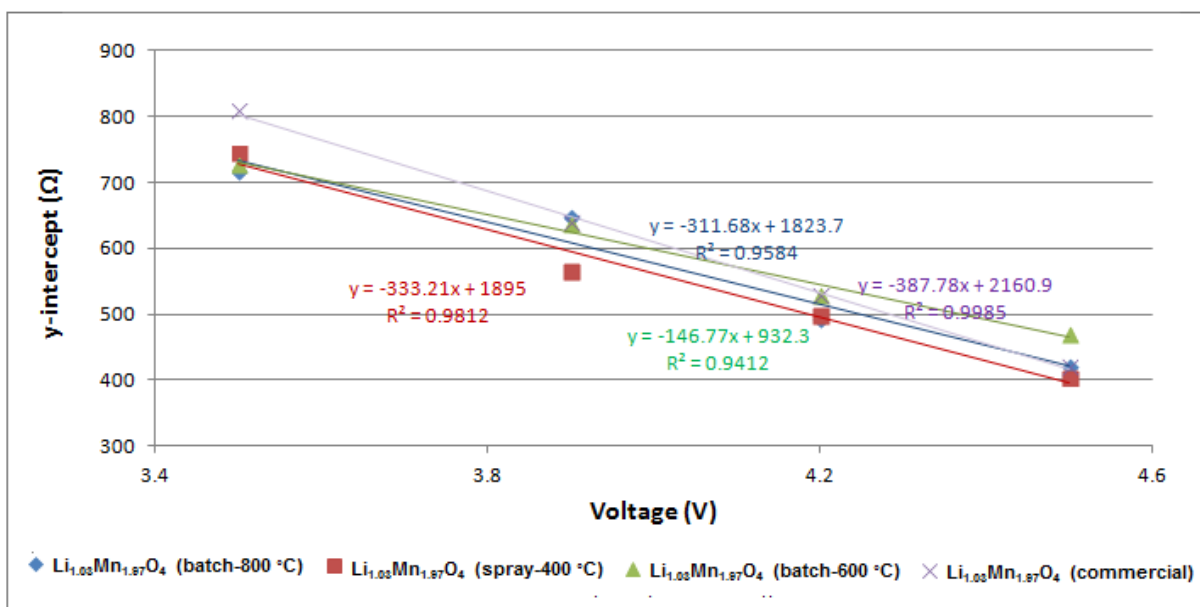
Figure 5.36: Graphical display of the y-intercept obtained from the relationship between Z (real impedance) vs ω$^{-1/2}$ in the low frequency region for Li$_{1.03}$Mn$_{1.97}$O$_4$.

The results showed that for the comparative study of the undoped Mn spinel cathode materials, the change in the y-intercept (R_{ct}) would vary similarly with the increase in voltage. The slight variation could be due to differences in cell construction and slight differences in surface area and crystallite sizes (Table 4.18). However, there were significant differences in the correlations between the various synthesis batches made with

the dopants (Figures 5.37 to 5.40). Of interest would be the slope of the straight line graph or to consider the change of the R_{ct} with increase in charge voltage.
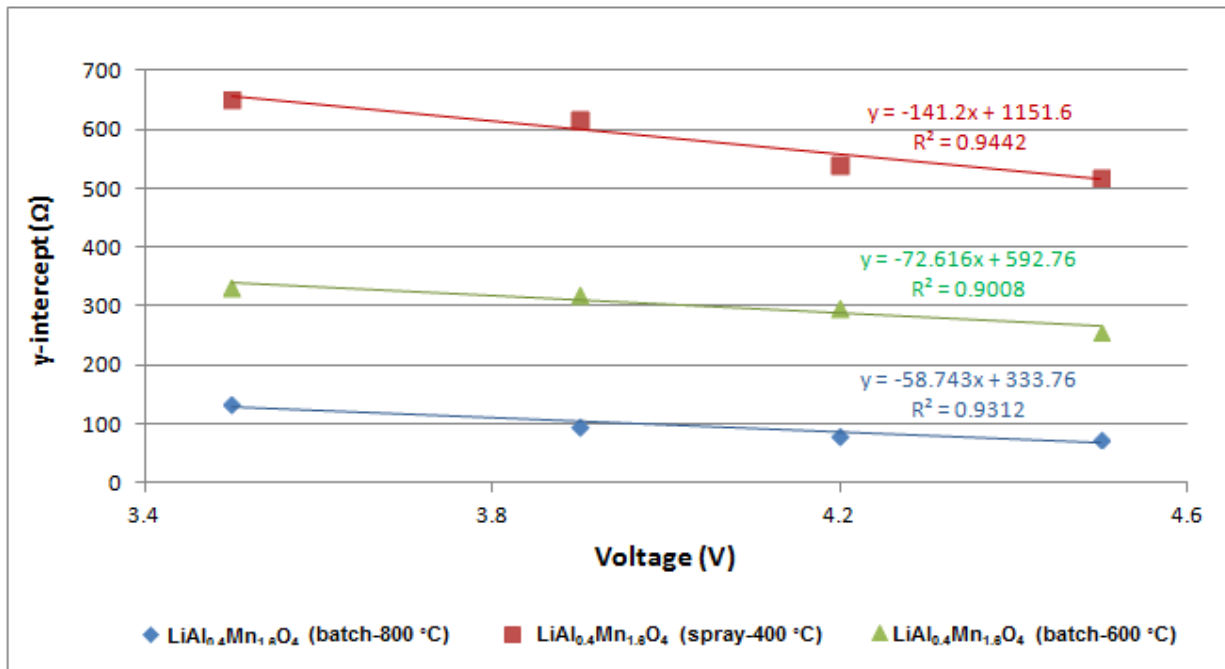
Figure 5.37: Graphical display of the y-intercept obtained from the relationship between Z (real impedance) vs $\omega^{-1/2}$ in the low frequency region for $LiAl_{0.4}Mn_{1.6}O_4$.
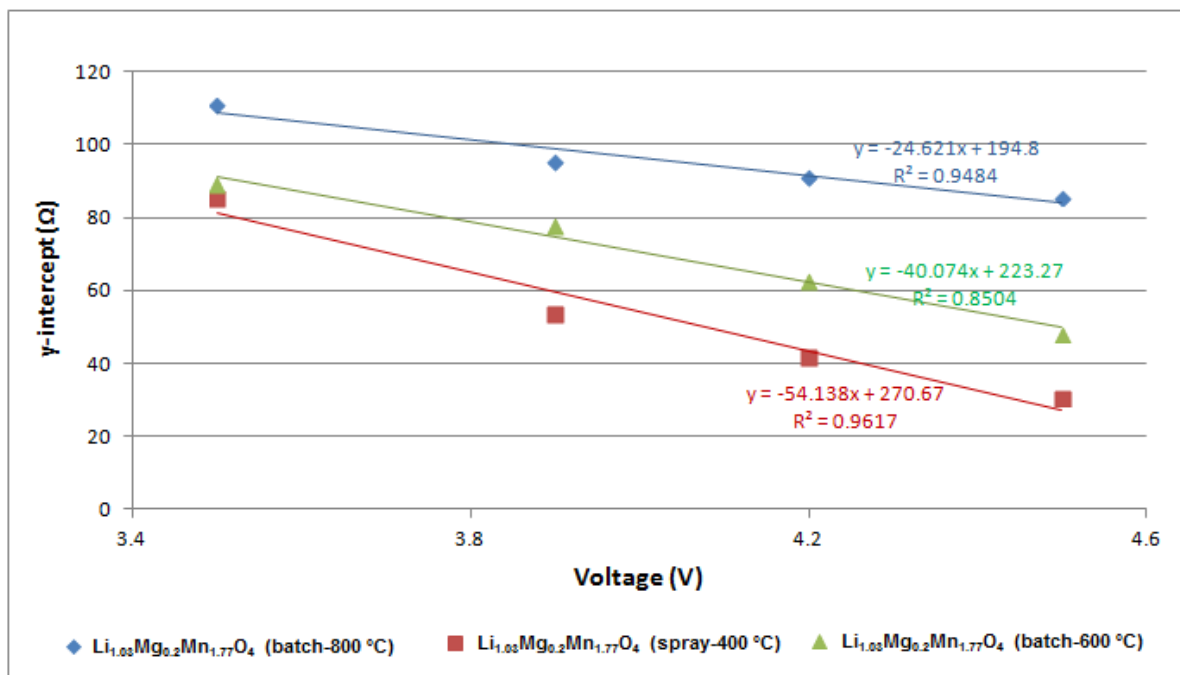
Figure 5.38: Graphical display of the y-intercept obtained from the relationship between Z (real impedance) vs $\omega^{-1/2}$ in the low frequency region for $Li_{1.03}Mg_{0.2}Mn_{1.77}O_4$.
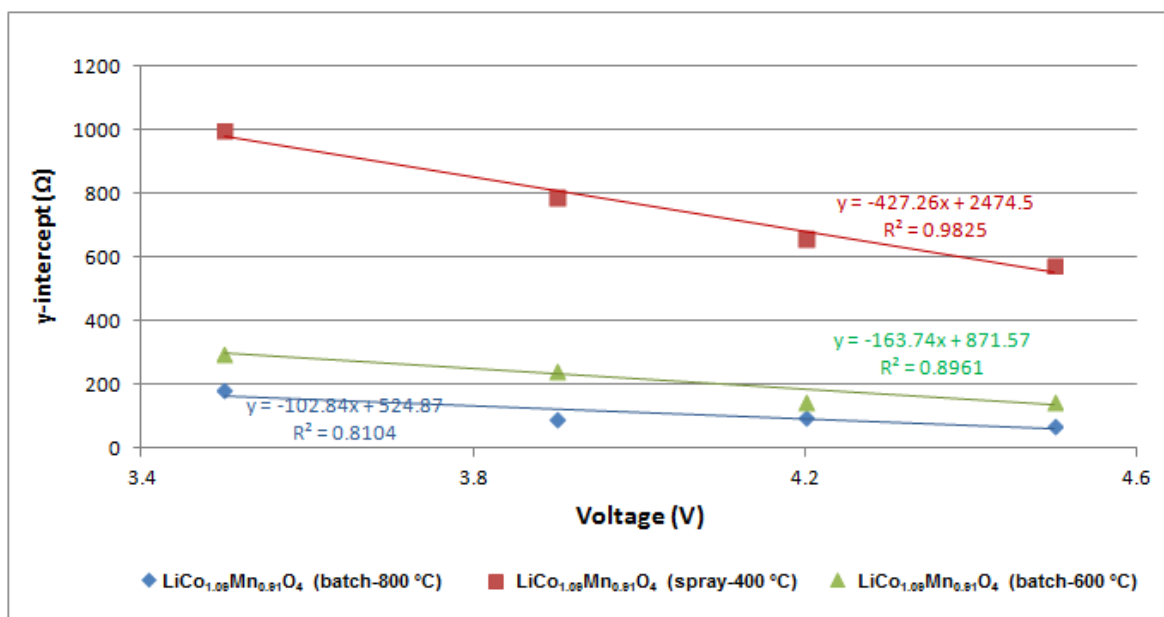
Figure 5.39: Graphical display of the y-intercept obtained from the relationship between Z (real impedance) vs $\omega^{-1/2}$ in the low frequency region for $LiCo_{1.09}Mn_{0.91}O_4$.
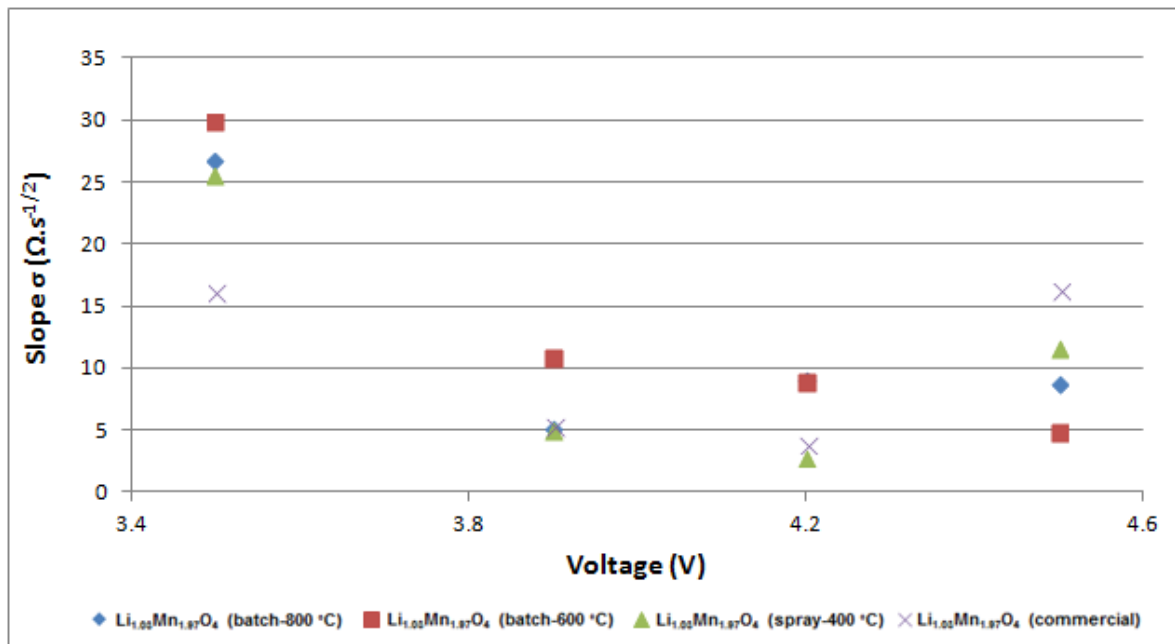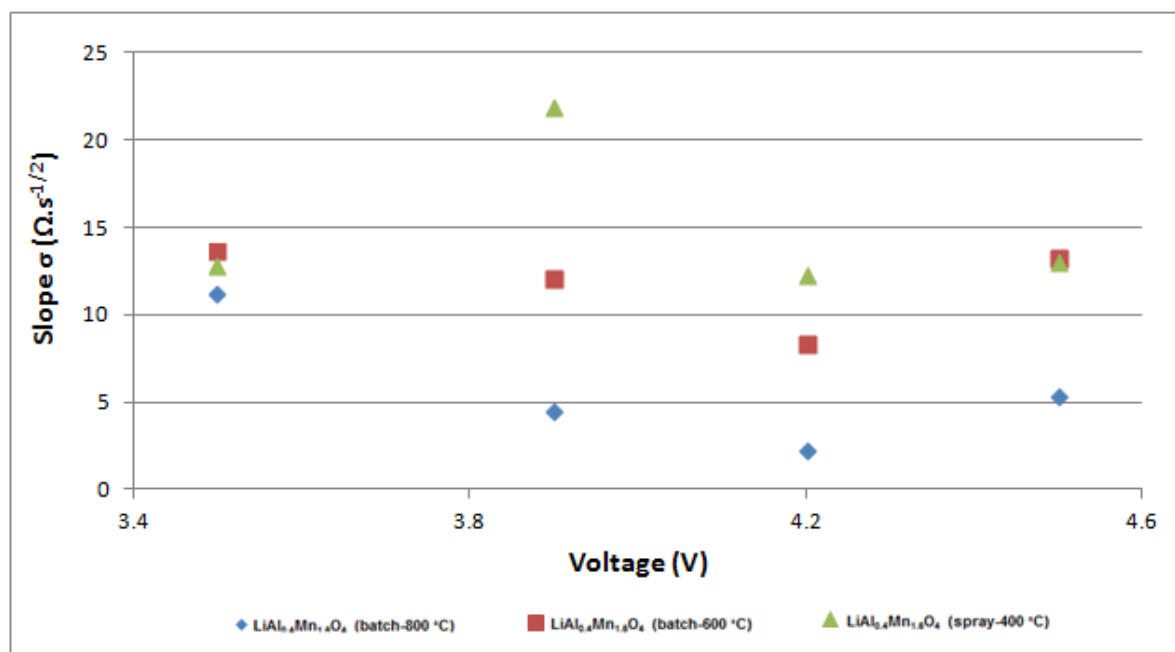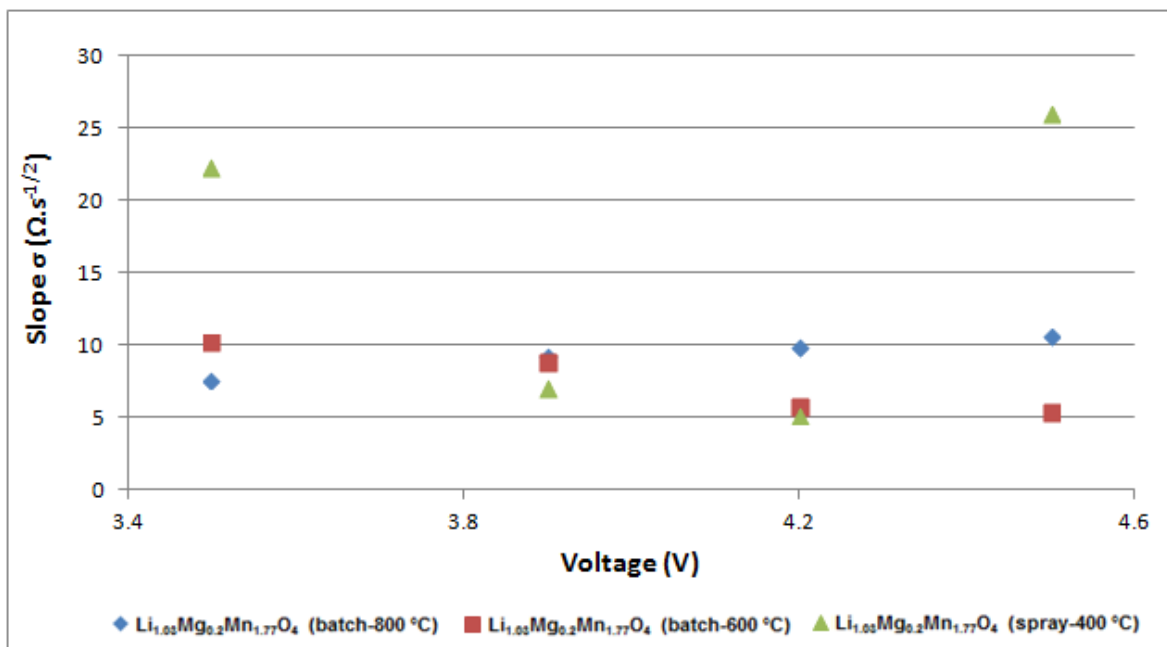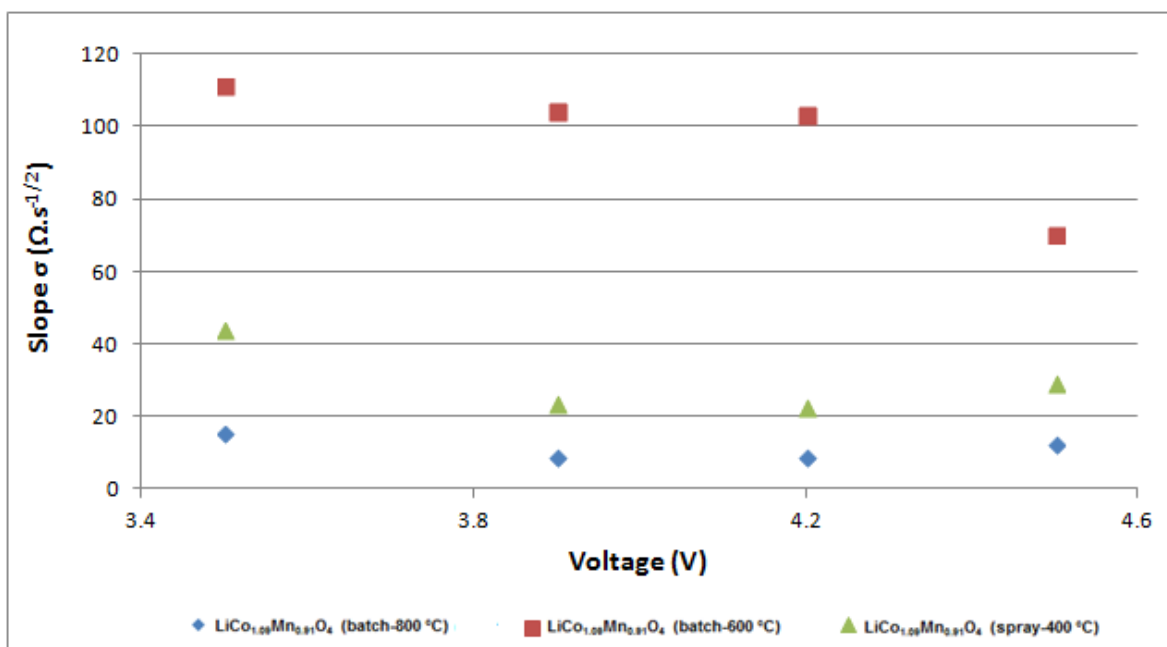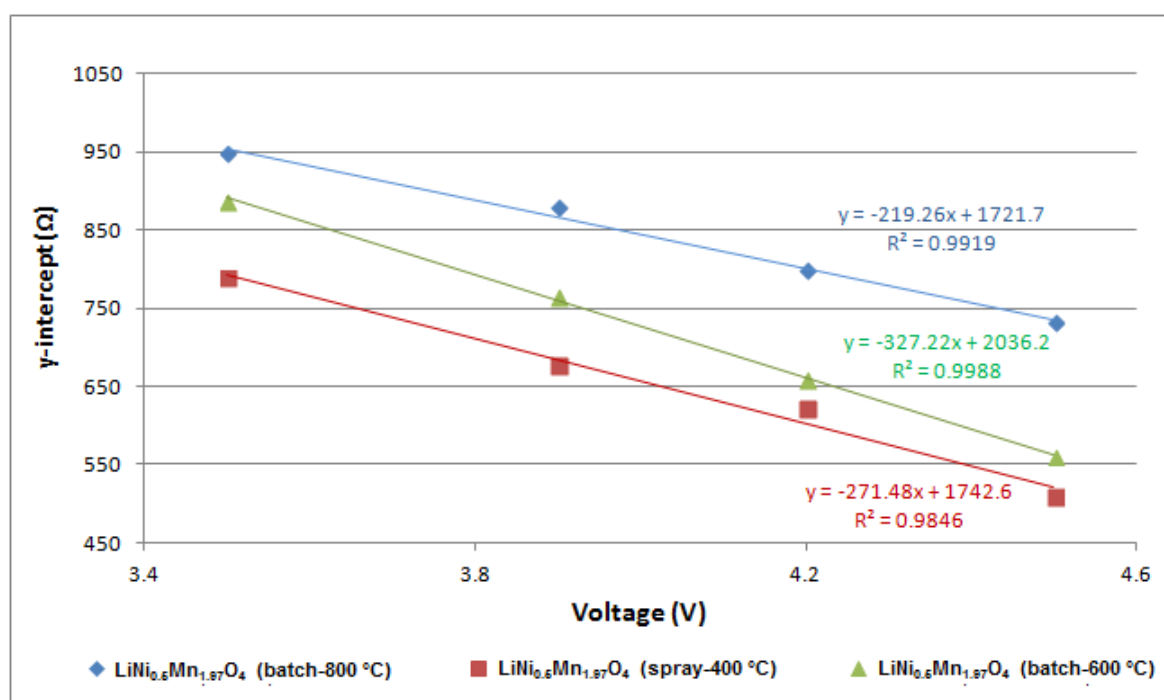

Figure 5.40: Graphical display of the y-intercept obtained from the relationship between Z (real impedance) vs $\omega^{-1/2}$ in the low frequency region for $LiNi_{0.5}Mn_{1.5}O_4$.

The results (Figures 5.36 to 5.40) showed that as the voltage increased the R_{ct} decreased. The lower R_{ct} value would correspond to a fast kinetics of the faradaic reaction, thereby

implying that at high voltages (low R_{ct}) the ions would move at a faster rate into the electrolyte. When looking at the y-intercept vs voltage plots (Figures 5.36 to 5.40) and considering the slopes within these plots, the larger slope of the straight line would relate to a larger decrease in R_{ct} over the increasing charge voltage range. This would imply that a faster recharge could be achieved and that the kinetics of the Li-ion movement through the materials was comparatively faster. The Al and Mg doped spinel material had a comparatively smaller slope (about 65 on average) in comparison to the undoped spinel oxide. This would imply that the kinetics of the Li-ion movement through the material was comparatively slower. However the slopes for the Co and Ni doped spinel oxides were comparatively similar to the undoped spinel oxide, implying a similar kinetic rate. The y-intercept in Figures 5.36 to 5.40 could also be referred to the R_{ct} at the start of the charge process where the materials' electronic conductivity would be comparatively lower.

5.4 <u>Cyclic voltammetry</u>

Cyclic voltammetric analysis were done on the cells made with the synthesized $LiM_xMn_{1-x}O_4$ (whereby M=Al, Co, Mg, Ni) electrode materials by batch process at 800 °C and compared to the cells made with the electrode materials prepared by the spray-drying process. The voltammograms (Figures 5.41 to 5.45) were obtained in the potential range of 3.5 to 5 V at a scan rate of 0.1 mV.s^{-1} using Li as reference and counter electrode.
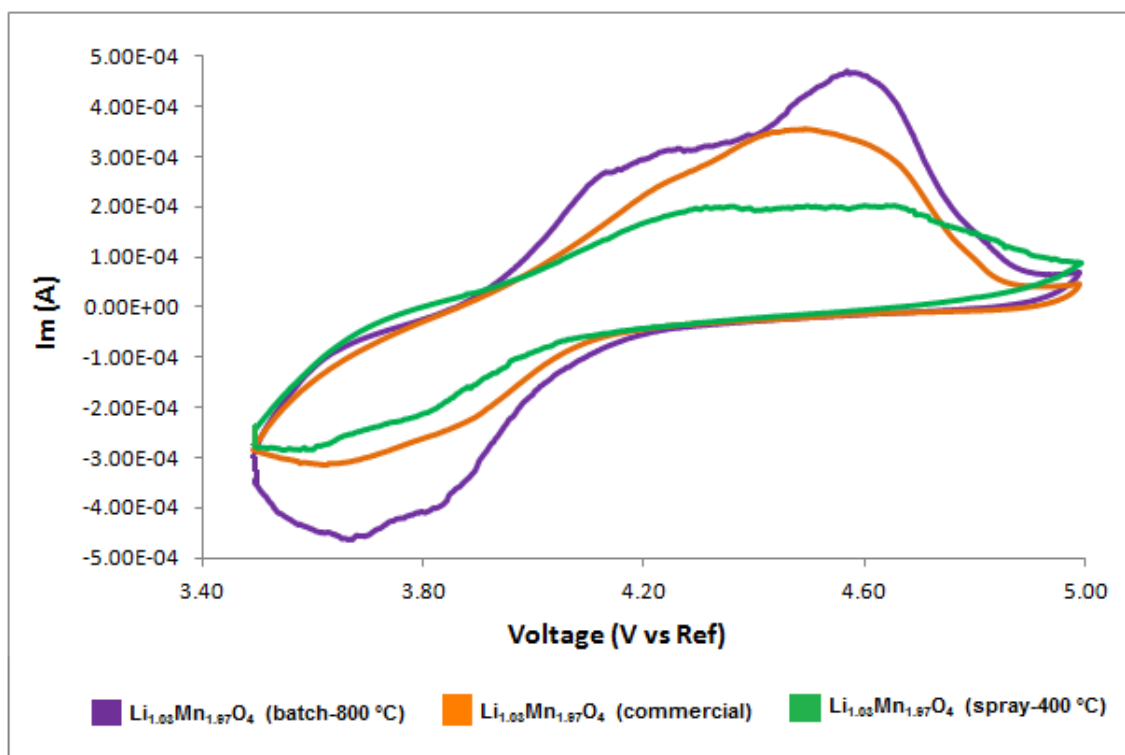
Figure 5.41: Cyclic voltammograms of the cell made with cathode Li$_{1.03}$Mn$_{1.97}$O$_4$ material.

The results represented the standard undoped Li$_{1.03}$Mn$_{1.97}$O$_4$ prepared by various synthesis processes. The CV scans showed two pairs of reversible redox peaks approximately between 3.7 and 4.4 V. The commercial material obtained a distinct anodic peak around 4.3 V with a smaller shoulder peak around 4.2 V and two cathodic peaks around the 3.7 to 3.9 V region (although they were not distinct peaks). The spray-dried oxide materials again showed no distinct two pairs of reversible redox peaks however, double anodic and cathodic peaks were approximately between 3.7 and 4.3 V. These observations could be due to one peak being swamped by the other therefore, showing no distinct double peaks and the sensitivity in scan rates could also possibly be considered. Although these peaks were not distinctly separated in comparison to the results reported by Hwang *et al.*[57] and other researchers[58-64], the double redox peaks were an indication of a typical stoichiometric spinel phase. The two peaks are a representation of the insertion or extraction of Li-ions into or from the spinel structure. These CV scans showed shifts within its anodic (4.1 and 4.4 V, corresponding to Mn^{3+}/Mn^{4+} couple) and cathodic peaks (3.7 and 3.9 V, associated to the Mn^{4+}/Mn^{3+} couple)[65] compared to literature[57-64]. To

mention or discuss only a few literature results, Hwang *et al.*[57] and Wang *et al.*[61] reported anodic peaks at 4.05 and 4.18 V and cathodic peaks at 3.95 and 4.07 V. Even though the cells made with the spray-dried cathode material showed no distinct peaks within the CV scans, this does not imply that there was no oxidation or reduction reversible reactions taking place, but rather within the broader potential range of the regions shown in Figure 5.41. These shifts in peak positions could have resulted from changes in reference electrodes (e.g. SCE), difference in scan rate (e.g. 0.02 $V.s^{-1}$, 0.05 $mV.s^{-1}$) or slight differences in sample or material synthesis methods provided from literature studies.
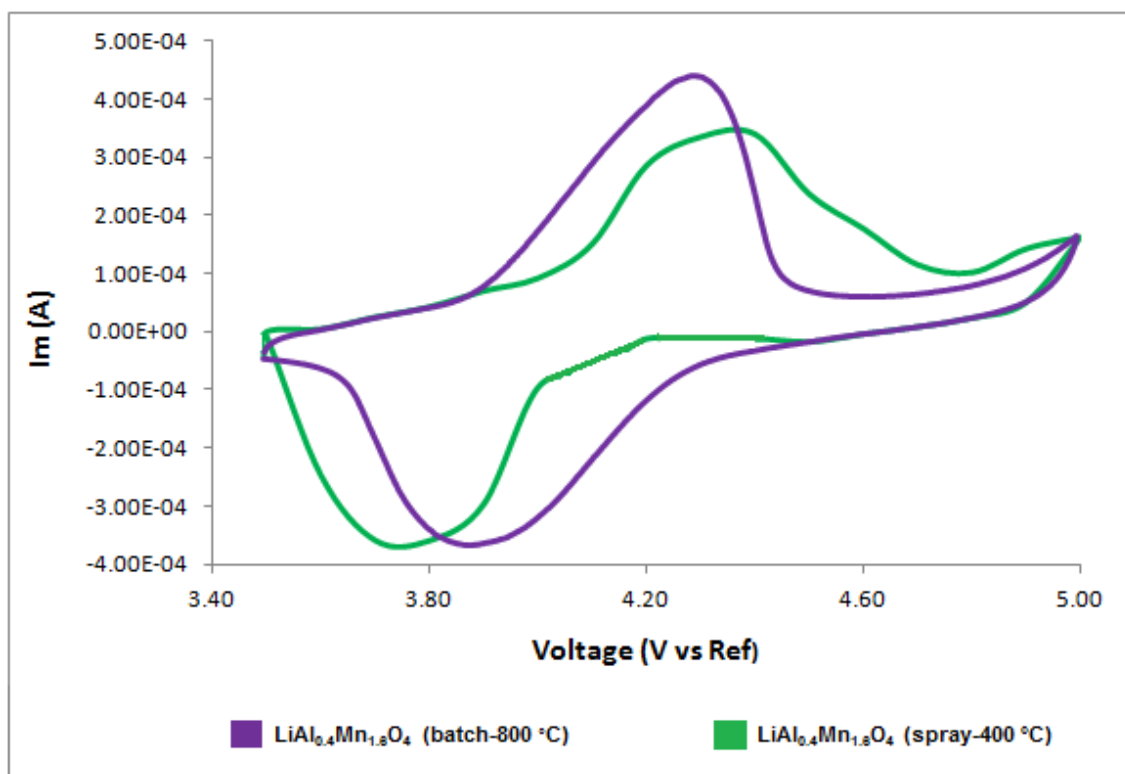
Figure 5.42: Cyclic voltammograms of the cell made with cathode $LiAl_{0.4}Mn_{1.6}O_4$ materials.

The CV scans (Figure 5.42) for the Al doped spinel oxide showed a single anodic (at about 4.2 V) and cathodic peak (at about 3.9 V) which was in agreement to the voltage profile (Figure 5.2) that observed slight voltage plateaus at these potentials (4.2 and 3.9 V). The results showed that there were no secondary peaks at the lower potentials when compared to the undoped manganese spinel (Figure 5.41). Also, the Al doped oxide material that was synthesized by the spray-drying technique showed similar curves and

peak intensities with a slight shift to a higher potential for the oxidizing potential and a slightly lower reducing potential when compared to batch synthesized material. The results differed from those reported by Hwang *et al.*[58] and other researchers[66-69], where they reported double anodic (4.09/4.22 V) and cathodic peaks (3.93/4.10 V) respectively however, on average (for these pair of peaks) the peak positions correlated to the results reported in this study. These differences (results in this study compared to literature) could be due to variations in Al to Mn synthesis ratio (0.1:1.9, 0.05:1.95 or 0.15:1.85), difference in synthesis methods (ultrasonic-assisted sol-gel, microwave assisted sol-gel, polymer-pyrolysis), variations in scan rates (0.02, 0.2, 0.5, 0.7 or 1 mV.s^{-1}) and difference in chelating reagent (adipic or acrylic acid)[66-69]. However, the symmetry of the anodic and cathodic peaks reflects the reversibility of the oxidation and reduction reactions that correspond to lithium extraction and insertion.
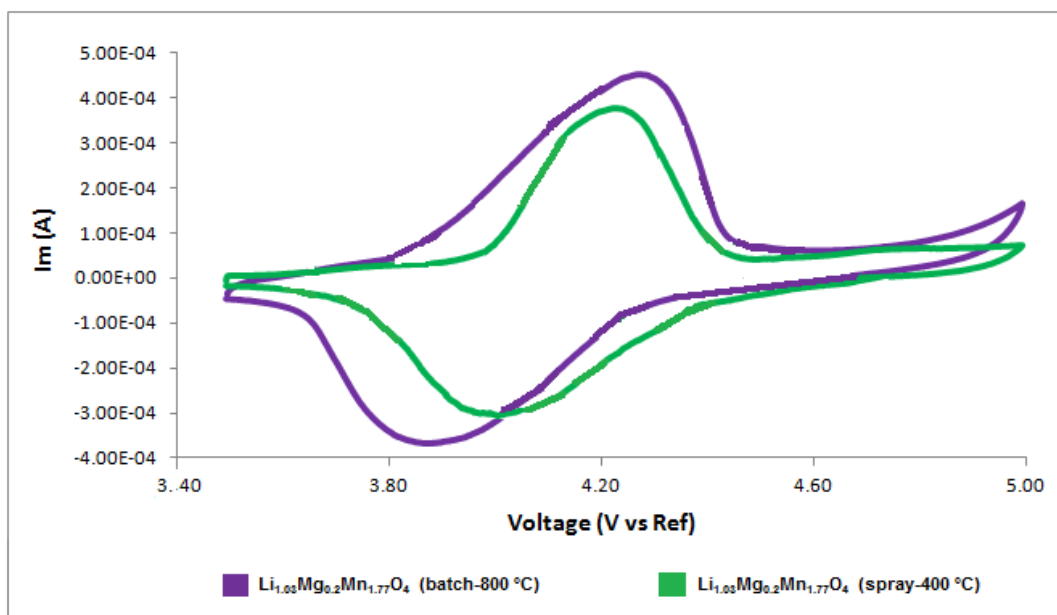
Figure 5.43: Cyclic voltammograms of the cell made with cathode Li$_{1.03}$Mg$_{0.2}$Mn$_{1.77}$O$_4$ materials.

Figure 5.43 showed the CV scans for Mg doped manganese spinel oxide material. These obtained results were similar to those reported by Suryakala *et al.*[65]. Similar single anodic peaks were observed within this study and in literature, at 4.2 V and between 4.25-4.75 V respectively. A single reverse cathodic peak was again provided in Figure 5.43 and by

Suryakala *et al.*[65] with peak positions at 4.0 and 4.25 V respectively. A slight shift in the peak positions were observed for cells made with the material that was spray-dried when compared to cells made with the batch synthesized material.
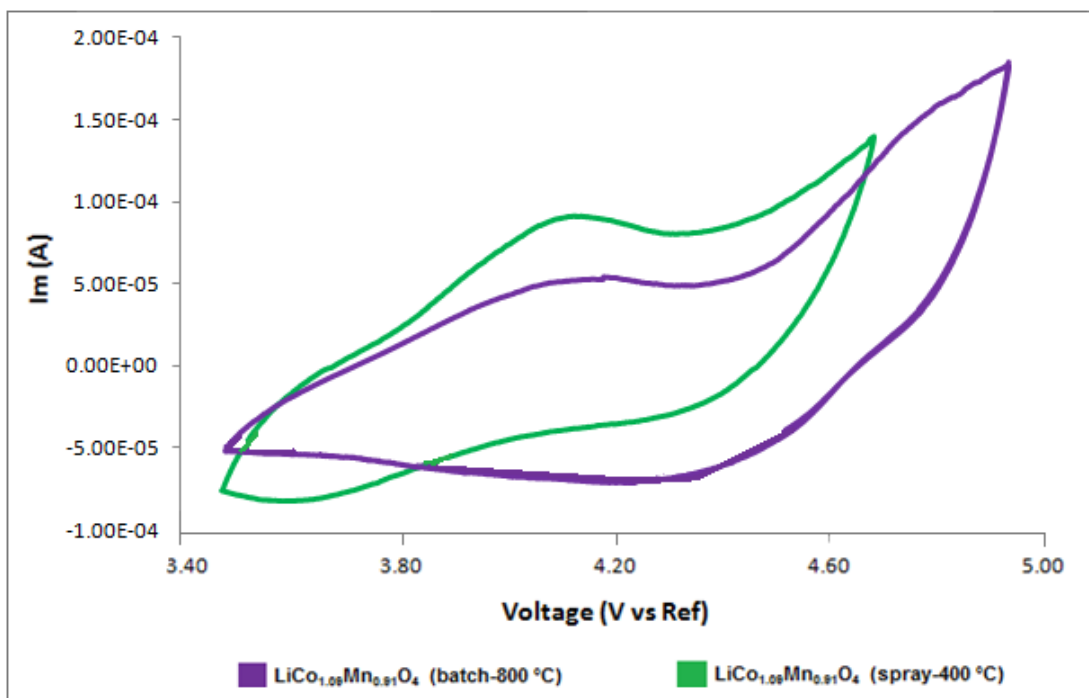
Figure 5.44: Cyclic voltammograms of the cell made with cathode $LiCo_{1.09}Mn_{0.91}O_4$ materials.

The results showed that the cell with the cobalt doped manganese spinel cathode produced a single broad peak for both the oxidation and reduction. The CV scan of the cell made with the material that was spray-dried was similar except for a slight shift in the oxidation peaks. These observed results were different to literature reported results, whereby literature reported double anodic (4.0/4.2 V) and double cathodic (4.1/3.9 V) peaks[10, 12]. However on average the broad peak potentials observed for this study was comparatively similar to literature potentials. The differences could be due to variation in metal to Mn ratio (0.16:1.84, in literature)[10, 12]. The results reflected the reversibility of the oxidation and reduction reactions that correspond to lithium extraction and insertion respectively.
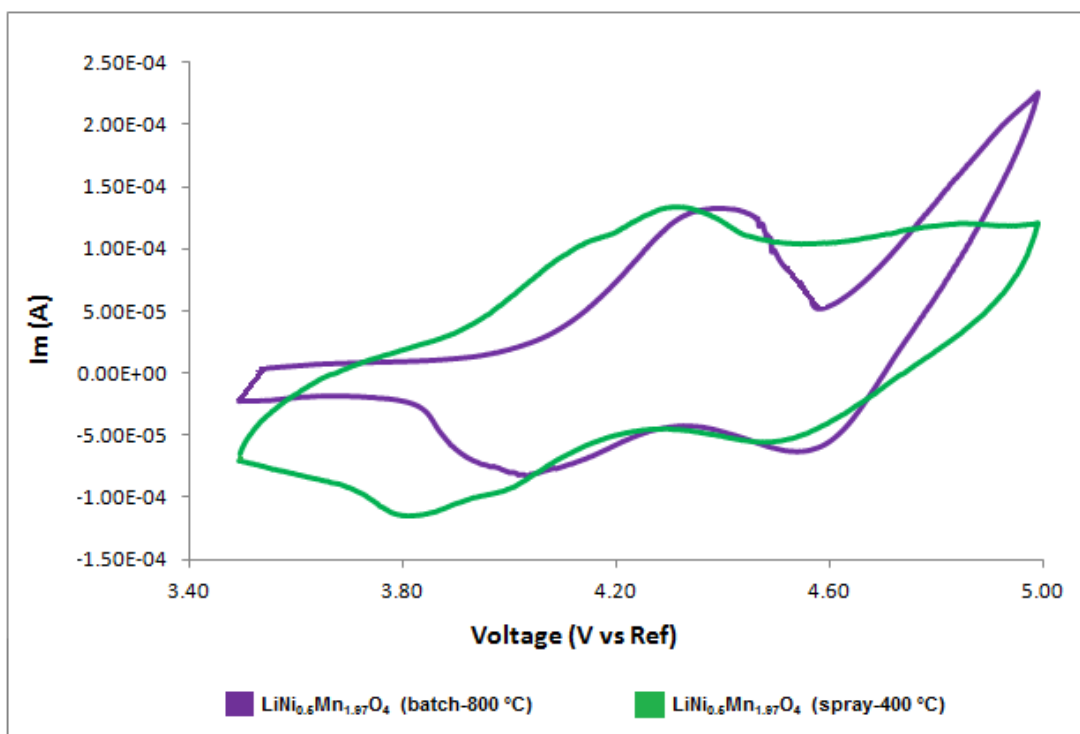
Figure 5.45: Cyclic voltammograms of the cell made with cathode LiNi$_{0.5}$Mn$_{1.5}$O$_4$ materials.

The results showed that the CV scans of the cells made with the Ni doped spinel cathode materials had one distinctive oxidizing peak at 4.4 V for the batch synthesized oxide with a slight shift in peak position when compared to the spray-dried synthesized oxide. The scan also showed two reducing peaks near 4.6 and 4.0 V respectively. From literature, the 4.5 to 5.0 V region corresponded to the redox couple Ni^{2+}/Ni^{4+} whereas the 3.9 to 4.2 V region corresponded to the Mn^{3+}/Mn^{4+} redox couple[64]. It should be noted that the 4.5 to 5.0 V regions did not show distinct peaks in this study compared to literature. However, the oxidation/reduction reversible reactions are shown and are slightly different to those reported in the literature[64-71].

In summary the results showed that the CV analysis indicated that the cells made with the various spinel oxide materials were able to reversibly undergo the oxidation and reduction reactions that correspond to lithium extraction and insertion respectively.

C . S n y d e r s

REFERENCES

1   P. Singh, A. Sil, M. Nath, S. Ray, *Physica B*, 2010, **405**, 649-654.

2   M.M. Thackery, *Progress in Solid State Chemistry*, 1997, **25**, 1-71.

3   H. Liu, Y.P. Wu, E. Rahm, R. Holze, H.Q. Wu, *Journal of Solid State Electrochemistry*, 2004, **8**, 450-466.

4   Y.K. Sun, I.H. Oh, K.Y. Kim, *Industrial and Engineering Chemistry Research*, 1997, **36**, 4839-4846.

5   J.L. Wang, Z.H. Li, J. Yang, J.J. Tang, J.J. Yu, W.B. Nie, G.T. Lei, Q.Z. Xiao, *Electrochimica Acta*, 2012, **75**, 115-122.

6   S.J. Bao, Y.Y. Liang, W.J. Zhou, B.L. He, H.L. Li, *Journal of Power Sources*, 2006, **15**4, 239-245.

7   D. Song, H. Ikuta, Y. Uchida, M. Wakihara, *Solid State Ionics*, 1999, **117**, 151-156.

8   L. Xiao, Y. Zhao, Y. Yang, Y. Cao, X. Ai, H. Yang, *Electrochimica Acta*, 2008, **54**, 545-550.

9   H. Aikiyo, K. Nakane, N. Ogata, T. Ogihara, *Key Engineering Materials*, 2002, **216**, 131-134.

10 Y. Huang J. Li, D. Jia, *Journal of Colloid and Interface Science*, 2005, **286**, 263-267.

11 M. Hu, Y. Tian, L. Su, J. Wei, Z. Zhou, *Applied Materials and Interfaces*, 2013, **5**, 12185-12189.

12 N. Amdouni, F. Gendron, A. Mauger, H. Zarrouk, C.M. Julien, *Materials Science and Engineering B*, 2006, **129**, 64-75.

13 Y.K. Sun, D.W. Kim, Y.M. Choi, *Journal of Power Sources*, 1999, **79**, 231-237.

14 H.Y. Xu, S. Xie, N. Ding, B.L. Liu, Y. Shang, C.H. Chen, *Electrochimica Acta*, 2006, **51**, 4352-4357.

15 L.H. Chi, N.N. Dinh, S. Brutti, B. Scrosati, *Electrochimica Acta*, 2010, **55**, 5110-5116.

16 Y. Fan, J. Wang, X. Ye, J. Zhang, *Materials Chemistry and Physics*, 2007, **103**, 19-23.

17 Q. Zhong, A. Bonakdarpour, M. Zhang, Y. Gao, J.R. Dahn, *Journal of Electrochemical Society*, 1997, **144**, 205-213.

18 N. Amdouni, K. Zaghib, F. Gendron, A. Mauger, C.M. Julien, *Ionics*, 2006, **12**, 117-126.

19 R. Thirunakaran, A. Sivashanmugam, S. Gopukumar, C.W. Dunnill, D.H. Gregory, *Journal of Materials Processing Technology*, 2008, **208**, 520-531.

20 M. Kebede, K. Ozoemena, M. Mathe, "Synthesis and electrochemical properties of cation doped spinel $LiM_{0.5}Mn_{1.5}O_4$ (M=Mn, Ni, Al) cathode materials for Li-ion battery", Energy Materials and Manufacturing, Council for Scientific and Industrial Research.

21 A. Subramania, N. Angayarkanni, A.R.S. Priya, T. Vasudevan, R. Gangadharan, *Bulletin Material Science*, 2005, **28**, 663-667.

22 X. Huang, M. Lin, Q. Tong, X. Li, Y. Ruan, Y. Yang, *Journal of Power Sources*, 2012, **202**, 352-356.

23 Gamry Instruments Application notes, Testing Lithium-Ion Batteries, 2015.

24 S. Erol, *Electrochemical Impedance Spectroscopy analysis and modelling of lithium cobalt oxide/carbon batteries*, Dissertation from the University of Florida, 2015.

25 C. Heubner, M. Schneider, A. Michaelis, *Journal of Power Sources*, 2015, **288**, 115-120.

26 J. Zhao, L. Wang, X. He, C. Wan, C. Jiang, *International Journal of Electrochemical Science*, 2010, **5**, 478-488.

27 D. Andre, M. Meiler, K. Steiner, Ch. Wimmer, T. Soczka-Guth, D.U. Sauer, *Journal of Power Sources*, 2011, **196**, 5334-5341.

28 L.I. Yun-Jiao, X.U. Hu, K. Long, L.I. Hua-Cheng, L.I. Chun-Xia, Z. Xian-Zhen, H. Qiang, *Journal of Inorganic Materials*, 2014, **29**, 661-666.

29 M. Kebede, N. Kunjuzwa, K. Ozoemena, M. Mathe, *ECS Transactions*, 2013, **50**, 1-14.

30 P. Yu, B.N. Popov, J.A. Ritter, R.E. White, *Journal of The Electrochemical Society*, 1999, **146**, 8-14.

31 Q. Guo, V.R. Subramanian, J.W. Weidner, R.E. White, *Journal of The Electrochemical Society*, 2002, **149**, A307-A318.

32 M.D. Levi, D. Aurbach, *Journal of Physical Chemistry B*, 1997, **101**, 4641-4647.

33 H. Liu, C. Li, H.P. Zhang, L.J. Fu, Y.P.Wu, H.Q. Wu, *Journal of Power Sources*, 2006, **159**, 717-720.

34 Y. Zhou, J. Wang, Y. Hu, R. O'Hayre, Z. Shao, *Chemistry Communication*, 2010, **46**, 7151.

35 X. Zhang, A. Mauger, Q. Lu, H. Groult, L. Perrigaud, F. Gendron, C.M. Julien, *Electrochimica Acta*, 2010, **55**, 6440-6449.

36 Y.K. Sun, D.W. Kim, Y.M. Choi, *Journal of Power Sources*, 1999, **79**, 231-237.

37 Y. Zhu, Y. Xu, Y. Liu, C. Luo, C. Wang, *Nanoscale*, 2013, **5**, 780-787.

38 M.V. Reddy, R. Jose, A. Le Viet. K.I. Ozoemena, B.V.R. Chowdari, S. Ramakrishma, *Studies on the lithium ion diffusion coefficients of electrospun Nb_2O_5 nanostructures using galvanostatic intermediate titration and electrochemical impedance spectroscopy*, Report from Department of Physics, National University of Singapore.

39 D. Guyomard, J.M. Tarascon, *Journal of Electrochemical Society*, 1992, **139**, 937-948.

40 H. Kanoh, Q. Feng, T. Hirotsu, K. Ooi, *Journal of Electrochemical Society*, 1996, **143**, 2610-2615.

41 P.Arora, B.N. Popov, R.E. White, *Journal of Electrochemical Society*, 1998, **145**, 807-815.

42 D. Aurbach, M.D. Levi, E. Levi, H. Teller, B. Markovsky, G. Salitra, *Journal of Electrochemical Society*, 1998, **145**, 3024-3034.

43 K.A. Striebel, C.Z. Deng, S.J. Wen, E.J. Cairns, *Journal of Electrochemical Society*, 1996, **143**, 1821-1827.

44 K.M. Shaju, G.V. SubbaRao, B.V.R. Chowdari, *Journal of Materials Chemistry*, 2003, **13**, 106-113.

45 D. Song, H. Ikuta, T. Uchida, M. Wakihara, *Solid State Ionics*, 1999, **117**, 151-156.

46 B.J. Johnson, D.H. Doughty, J.A. Voigt, T.J. Boyle, *Journal of Power Sources*, 1997, **68**, 634-636.

47 B.M. Hwang, S.J. Kim, Y.W. Lee, B. Han, S.B. Kim, W.S. Kim, K.W. Park, *International Journal of Electrochemical Science*, 2013, **8**, 9449-9458.

48 M. Park, X. Zhang, M. Chung, G.B. Less, A.M. Sastry, *Journal of Power Sources*, 2010, **195**, 7904-7929.

49 T.F. Yi, Y. Xie, M.F. Ye, L.J. Jiang, R.S. Zhu, Y.R. Zhu, *Ionics*, 2011, **17**, 383-389.

50 H. Liu, J. Wang, X. Zhang, D. Zhou, X. Qi, B. Qiu, J. Fang. R. Kloepsch, G. Schumacher, Z. Liu, J. Li, *Applied Materials and Interfaces*, 2016, **8**, 4661-4675.

51 B. Xu, D. Qian, Z. Wang, Y.S. Meng, *Materials Science and Engineering R*, 2012, **73**, 51-65.

52 L. Wang, J. Zhao, X. He, J. Gao, J. Li, C. Wan, C. Jiang, *International Journal of Electrochemical Science*, 2012, **7**, 345-353.

53 F. Croce, F. Nobili, A. Deptula, W. Lada, R. Tossici, A. D'Epifanio, B. Scrosati, R. Marassi, *Electrochemistry Communications*, 1999, **1**, 605.

54 Identifying a Warburg Impedance, <http://www.consultrsr.net/resources/eis/warburg1.htm#wplot> (accessed on 8 April 2015).

55 S.S. Zhang, K. Xu, T.R. Jow, *Electrochimica Acta*, 2004, **49**, 1057-1061.

56 V.F. Lvovich, *Impedance Spectroscopy, Applications to Electrochemical and Dielectric Phenomena*, John Wiley and Sons Inc. Publications, Hoboken, New Jersey, 2012.

57 B.J. Hwang, R. Santhanam, D.G. Liu, *Journal of Power Sources*, 2001, **97-98**, 443-446.

58 B.J. Hwang, R. Santhanam, D.G. Liu, Y.W. Tsai, *Journal of Power Sources*, 2001, **102**, 326-331.

59 S. Ma, H. Noguchi, M. Yoshio, *Journal of Power Sources*, 2001, **97-98**, 385-388.

60 M.A. Kiani, M.F. Mousavi, M.S. Rahmanifar, *International Journal of Electrochemical Science*, 2011, **6**, 2581-2595.

61 G.G. Wang, J.M. Wang, W.Q. Mao, H.B. Shao, JQ. Zhang, C.N. Cao, *Journal of Solid State Electrochemistry*, 2005, **9**, 524-530.

62 X. Zhang, M. Yang, X. Zhao, Y. Wang, M. Wang, L. Ma, *Journal of Materials Science: Materials in Electronics*, 2015, **26**, 6366-6372.

63 Q. Li, C. Peng, J. Huang, W. Xu, F. Yang, H. Bai, C. Su, J. Guo, *International Journal of Electrochemical Science*, 2015, **10**, 7513-7520.

64 S. Qiang, L.I. Xin-hai, W. Zhi-xing, J.I. Yong, *Transactions of Nonferrous Metals Society of China*, 2009, **19**, 176-181.

65 K. Suryakala, G.P. Kalaignan, T. Vasudevan, *International Journal of Electrochemical Science*, 2006, **1**, 372-378.

66 L. Xiao, Y. Zhao, Y. Yang, Y. Cao, X. Ai, H. Yang, *Electrochimica Acta*, 2008, **54**, 545-550.

67 S.J. Bao, Y.Y. Liang, W.J. Zhou, B.L. He, H.L. Li, *Journal of Power Sources*, 2006, **154**, 239-245.

68 T. Yi, X. Hu, K. Gao, *Journal of Power Sources*, 2006, **162**, 636-643.

69 B. Cheng, X. Chen, X. Li, H. Xu, J. Yang, Y. Qian, *International Journal of Electrochemical Science*, 2012, **7**, 6453-6464.

70 X.Y. Feng, C. Shen, X. Fang, C.H. Chen, *Chinese Science Bulletin*, 2012, **57**, 4176-4180.

71 O. Sha, S. Wang, Z. Qiao, W. Yuan, Z. Tang, Q. Xu, Y. Su, *Materials Letters*, 2012, **89**, 251-253.

CHAPTER 6

CONCLUSION

The study considered the physical and electrochemical properties of the cathode spinel lithium manganese oxide materials used in rechargeable Li-ion cells.

In summary the findings of the study showed:

- Differences in the various material characteristics induced by two different synthesis techniques (batch sol-gel and spray-dry).
- The effect on the synthesis route and final product of doping the spinel lithium manganese oxide with various metals, namely; Al, Mg, Co and Ni respectively.
- Electrochemical capacity performance and its Li-ion mobility as determined by EIS of various cells made with the doped and undoped cathode oxide materials.

The study focused on the characterization of the thermal synthesis process of making doped and undoped lithium manganese oxide. Based on these summarized findings; the following points can be considered as some of the important results from this study:

1. Metal doping of the lithium manganese spinel material showed that multiple decomposition steps or regions (resulting in intermediate phases) were observed in their thermal reaction process using TG analysis, when compared to the undoped material. These doped precursors or materials completed their final decomposition step at slightly higher temperatures than the undoped $Li_{1.03}Mn_{1.97}O_4$ precursor. At heating temperatures of about 400 °C and higher, the study showed that the precursor materials would no longer decompose, even though it might not have formed the final active phase. As a result of the multiple decomposition steps, it could be concluded that metal doping resulted into a more complex process to make the final spinel active material when compared to the undoped lithium manganese oxide material. The study also highlighted that the organic and chelating reagents or acids would degrade completely around 400 °C, (regardless of the metal dopant or

chelating reagents used) resulting in the remainder of only the inorganic matrix (such as $Li_{1.03}Mn_{1.97}O_4$ and other complexes). The study also showed that at the operating temperature of the spray-drying method (at 400 °C and higher) the TGA results showed that the inorganic matrix had formed which was partially crystalline showing the formation of the spinel phase similar to what was reported in literature.

2. The study also looked at the use of various chelating reagents that could influence the formation of the undoped oxide material ($Li_{1.03}Mn_{1.97}O_4$). The synthesized material in using citric acid as additional reagent was the only one that showed the occurrence of a single decomposition step in the respective TG analysis. The final decomposition step where there was no further mass loss was at a slightly lower temperature than the other chelating reagents or acids studied (ascorbic, succinic and poly-acrylic acids). The citrate precursor was shown to be the better suited material that formed a low hydrated precursor, cost-effective when compared to the others, was less sensitive to moisture during the synthesis process and more suitable for the spray drying process.

3. In-situ phase analysis with changes in heating temperature of the precursor doped and undoped materials prepared in citric acid were done by using PXRD. The in-situ PXRD technique gave insight into the various phase transitions that occurred when heating the precursor material up to 850 °C in air. The results showed that most precursor materials would undergo in some cases a number of phase transitions in order to form or obtain the final pure spinel oxide material. In general the materials would go through an amorphous phase, where the respective crystal structure would collapse before the formation of the final spinel structure (Mg and Co dopants followed this trend). In some cases, the precursor material also showed to be already amorphous, collapsing into an intermediate crystalline phase (Mn_2O_3), which would then form the crystalline spinel structure (Ni dopant and undoped $Li_{1.03}Mn_{1.97}O_4$). These results were in agreement with the TGA studies done on the same materials. The Co doped crystalline precursor showed a transition to form an amorphous phase around 250 °C where the spinel type structure around 300 °C was observed. At higher temperatures (around 850 °C) secondary phases were formed, which would

then transition back to the spinel structure at lower temperatures. Further investigation will be required to see if the intermediate high temperature phase formation has any influence on the electrochemical properties such as capacity and cycle life.

4. Rietveld refinement analysis of the in-situ PXRD data showed that once the spinel oxide material started to form around 400 °C; their lattice parameters would increase with increase in temperature (up to 800 °C). In turn the crystallite size as determined by PXRD would remain relatively constant up to 600 °C, thereafter it would increase with increasing temperature up to 800 °C. Samples of the materials made at 400, 600 and 800 °C were analyzed for their respective surface area by BET analysis. The results correlated well in comparing the calculated increase in crystallite size from 400 to 800 °C with a decrease in BET surface area for the spinel oxides over the same temperature range of selected samples. These observations could in turn have an effect on the electrochemical performance of the material in a cell.

5. SEM and AFM analysis of the final spinel oxide materials were done in order to obtain visual microscopy images of the respective particle shapes and sizes. The results confirmed that the materials synthesized by the spray-drying technique produced particles that were smaller in size. However, the results also showed some of the materials were not necessarily homogenous in their particle shape and distribution across the samples selected for analysis.

6. The study looked at the electrochemical properties or performance of the spinel oxide materials synthesized at 400, 600 and 800 °C respectively. The cells made with spinel materials synthesized at 600 and 800 °C showed a consistently lower initial charge capacity relative to the oxide materials synthesized at 400 °C. When considering the materials first discharge capacity, the cells made with the spinel oxide materials synthesized at 400 °C gave a slightly higher initial discharge capacity (except for the undoped material) compared to the materials synthesized at 600 and 800 °C. On average all materials showed slightly lower capacities than those reported in literature regardless of the synthesis temperatures. Further studies would however

be necessary that would include different charge and discharge rates and the ability to capacity cycle.

7. Of interest in this study was to consider electrochemical activity of the oxide materials surface (at the cathode). This was done by looking at the Li-ion mobility during the charging process using electrochemical impedance spectroscopy (EIS). In general, for the cells studied, the results showed an increase in relative capacitance of the various cathode materials as the voltage increased. The study also showed that as the charge voltage increased the charge transfer resistance (R_{ct}) would comparatively decrease. This implied that a faster recharge was achieved and that the kinetics of the Li-ion movement through the materials was comparatively faster.

8. By using the results from the EIS study, the Li-ion diffusion ability (D_{Li}) was determined and based on the literature review done, there were some inconsistencies in applying the formula to determine the D_{Li}. The difference was between either using the cell electrode's physical geometrical surface area or the materials surface area as determined by BET. Although the determined D_{Li} coefficient was for some samples similar to those reported in literature (using geometrical area or BET surface area), the use of BET surface area would generality give a smaller D_{Li} coefficient. The inconsistency in using only the geometric surface area was particularly noticeable, when the same material was synthesized at different temperatures giving different BET surface areas. Future work would involve the understanding of which would be the proper or best way of determining the D_{Li} coefficient. This study showed similar trends within the determined D_{Li} coefficient could be seen, where an increase in D_{Li} coefficient was obtained with increase in voltage, but on a different scale based on having either used BET surface area and electrode geometrical surface area. There would also be difficulty in comparing absolute values to reported literature values that are not always clear on their determination and use of the surface area of the electrode.

The study showed that by carefully controlling the spray-drying process at relatively low temperatures a relatively good performing active cathode material can be made with a relatively high surface area. This type of process is scalable to produce higher quantities of material that would be comparable in its initial electrochemical performance with material that is made by the traditional batch process. The study also showed that by using higher temperatures of 800 °C and higher many of the doped and undoped cathode materials would result in having comparatively larger crystallites and in some cases (Co doped) have different high temperature phases occurring. Further studies will have to be done in order to investigate if any of these higher temperature phases have an effect on the capacity performance of the cells made with such materials. The spray-drying method that can work at these relatively low temperatures can also be expanded to manufacture the material in a continuous flow process. This would in turn possibly reduce processing time and produce a uniform homogenous material without the need for post synthesis grinding or heating thereby reduce the manufacturing costs. The spray-drying process also allows for the relative ease of introducing selective dopants or additives within the process such as carbons or metal ions. The continuous spray process looked at in this study might not lend itself to the traditional scaling up process within traditional industries, but can be accommodated within the typical "numbering up" process used in considering micro flow manufacturing systems.

APPENDIX A: Summary of the EIS results obtained from the fitted EEC

Voltage (V)	R - int (Ω)	R - anode (Ω)	Yo - anode (S*s^a)	a - anode	Cap-anode (µF)	Cap-cathode (µF)	Rf - cathode (Ω)	Yo - cathode (S*s^a)	a - cathode	W (S*s^1/2)	Goodness of fit
$Li_{1.03}Mn_{1.97}O_4$ (synthesized)											
at 3.5	65.05	225.5	5.55E-06	0.919	3.08	1.92	167.8	2.40E-05	0.686	9.44E-02	1.06E-03
at 3.9	63.24	241.5	5.26E-06	0.899	2.49	2.11	195.0	4.61E-06	0.9	9.53E-02	1.80E-04
at 4.2	37.89	256.2	6.54E-06	0.852	2.15	3.13	157.9	8.82E-06	0.864	9.92E-02	2.89E-04
at 4.5	51.99	277.9	6.53E-06	0.838	1.93	3.74	139.42	5.42E-06	0.851	6.25E-03	8.14E-04
$Li_{1.03}Mn_{1.97}O_4$ (commercial)											
at 3.5 V	93.38	111.1	1.20E-05	0.966	3.506	1.54	294.3	3.77E-06	0.884	1.04E-02	9.29E-04
at 3.9 V	79.18	137.7	1.06E-05	0.914	2.734	1.9	304.6	1.75E-05	0.702	6.99E-02	1.76E-04
at 4.2 V	66.42	140.1	1.31E-05	0.881	2.593	2.59	283.4	2.74E-05	0.673	1.06E-01	1.31E-04
at 4.5 V	54.46	144.5	1.84E-05	0.773	1.225	2.73	229.7	2.30E-05	0.711	1.54E-02	1.10E-04
$Li_{1.03}Mn_{1.97}O_4$ (spray dry)											
at 3.5 V	67.367	216	7.81E-06	0.9	3.84	1.23	182.1	1.71E-05	0.687	9.59E-03	5.15E-04
at 3.9 V	76.669	225.3	4.34E-06	0.916	2.3	2.43	167.2	5.70E-06	0.891	7.03E-02	4.36E-04
at 4.2 V	56.625	232.8	5.23E-06	0.878	2.06	2.84	147.1	7.94E-06	0.868	6.38E-02	2.95E-04
at 4.5 V	62.949	247.5	3.32E-06	0.942	2.14	3.11	124.2	8.25E-06	0.876	3.36E-02	1.46E-04
$Li_{1.03}Mn_{1.97}O_4$ (600 °C)											
at 3.5 V	18.76	180.3	5.63E-03	0.633	3.93	2.19	284.4	3.24E-05	0.635	9.95E-03	9.79E-05
at 3.9 V	18.32	201	2.90E-05	0.707	3.44	2.73	253.1	2.78E-05	0.681	3.02E-02	6.79E-05
at 4.2 V	17.58	204.6	6.37E-05	0.59	3.12	2.87	238.6	2.34E-05	0.712	1.91E-02	6.44E-04
at 4.5 V	18.3	214.2	2.08E-05	0.726	2.7	3.07	195.9	4.18E-05	0.648	3.54E-02	9.83E-05
$LiAl_{0.4}Mn_{1.6}O_4$ (synthesized)											
at 3.5 V	5.245	59.8	6.76E-06	0.909	3.09	1.69	40.71	2.25E-06	0.97	4.71E-02	3.03E-05
at 3.9 V	5.384	65.2	6.88E-06	0.897	2.84	2.19	36.97	6.06E-06	0.892	6.10E-02	5.71E-05
at 4.2 V	5.27	69.8	5.54E-06	0.913	2.62	2.32	27.32	7.12E-06	0.884	1.45E-02	2.34E-05
at 4.5 V	5.482	76.1	5.53E-06	0.899	2.31	2.87	12.16	5.63E-05	0.71	1.26E-02	1.37E-04
$LiAl_{0.4}Mn_{1.6}O_4$ (spray dry)											
at 3.5 V	13.26	127.9	1.20E-05	0.778	1.889	1.38	71.71	3.91E-06	0.887	1.36E-02	1.80E-04
at 3.9 V	13.11	147	1.05E-05	0.77	1.52	1.76	70.67	9.55E-06	0.812	1.32E-02	7.85E-04
at 4.2 V	12.25	177.2	1.12E-05	0.74	1.26	2.13	56.63	3.77E-06	0.937	4.71E-02	2.05E-04
at 4.5 V	12.29	186.1	1.33E-05	0.793	1.19	2.83	44.5	3.36E-06	0.981	5.43E-02	1.27E-04
$LiAl_{0.4}Mn_{1.6}O_4$ (600 °C)											
at 3.5 V	42.19	97	3.00E-05	0.693	2.26	1.99	97.2	2.97E-05	0.684	2.57E-03	9.91E-04
at 3.9 V	47.32	105	2.87E-05	0.709	2.02	2.17	95.1	1.94E-05	0.742	1.72E-03	1.40E-03
at 4.2 V	47.53	114	2.52E-05	0.739	1.61	2.33	82.4	2.37E-05	0.729	1.87E-04	6.81E-04
at 4.5 V	46.41	127	2.38E-04	0.411	1.58	3.1	65.5	2.60E-05	0.75	1.77E-03	1.38E-03
$Li_{1.03}Mg_{0.2}Mn_{1.77}O_4$ (synthesized)											
at 3.5 V	84.87	275	2.16E-06	0.997	2.11	1.95	379	2.33E-05	0.656	2.37E-04	8.09E-04
at 3.9 V	80.77	287	4.04E-05	0.785	1.25	2.35	299	2.54E-05	0.672	2.49E-04	1.41E-03
at 4.2 V	78.26	298	1.02E-05	0.717	1.14	2.52	257	4.35E-05	0.612	2.41E-04	3.90E-03
at 4.5 V	76.45	301	1.12E-05	0.692	1.04	2.9	229	2.80E-05	0.69	2.21E-04	8.16E-03
$Li_{1.03}Mg_{0.2}Mn_{1.77}O_4$ (spray dry)											
at 3.5 V	4.861	108.2	3.84E-05	0.82	3.36	1.7	379.4	2.38E-05	0.767	7.66E-03	9.74E-04

at 3.9 V	3.855	151.1	1.71E-05	0.899	2.76	2.35	260.29	3.74E-05	0.74	1.09E-02	6.80E-04
at 4.2 V	3.941	225.2	1.62E-05	0.875	2.27	3.36	244.44	4.34E-05	0.734	1.45E-02	2.55E-04
at 4.5 V	3.881	242.6	5.21E-05	0.67	2.05	4.05	183.6	2.52E-05	0.84	5.84E-03	1.76E-03
Li$_{1.03}$Mg$_{0.2}$Mn$_{1.77}$O$_4$ (600 °C)											
at 3.5 V	56.06	265	8.94E-06	0.806	2.09	1.95	459.9	2.18E-05	0.656	3.40E-03	2.46E-04
at 3.9 V	56.32	282.8	1.76E-06	0.976	1.46	2.28	410	2.04E-05	0.686	3.63E-03	6.51E-05
at 4.2 V	56.26	295.9	1.22E-05	0.71	1.3	2.46	354	2.80E-05	0.655	1.09E-02	6.79E-05
at 4.5 V	55.97	298.4	1.16E-05	0.71	1.22	3.2	299	1.77E-05	0.754	1.06E-02	5.73E-05
LiCo$_{1.09}$Mn$_{0.91}$O$_4$ (synthesized)											
at 3.5 V	4.99	161.6	7.13E-06	0.896	3.25	2.1	13.82	2.35E-05	0.769	1.27E-02	4.08E-03
at 3.9 V	3.407	186	7.19E-06	0.875	2.79	2.32	14.47	2.33E-05	0.776	1.72E-02	2.75E-04
at 4.2 V	3.295	202.2	5.13E-06	0.894	2.27	2.82	11.51	4.45E-05	0.733	1.98E-02	3.11E-04
at 4.5 V	3.327	223.11	5.30E-06	0.91	2.16	3.15	6.88	2.88E-05	0.794	1.41E-02	2.38E-03
LiCo$_{1.09}$Mn$_{0.91}$O$_4$ (spray dry)											
at 3.5 V	26.81	174.4	2.80E-05	0.733	2.23	1.23	30.29	2.03E-05	0.725	6.12E-03	2.03E-04
at 3.9 V	29.37	208.6	1.22E-05	0.766	1.97	1.65	27.99	4.45E-05	0.67	1.22E-02	2.18E-04
at 4.2 V	26.86	220.7	1.23E-05	0.744	1.61	2.13	22.18	5.93E-05	0.666	1.34E-02	1.99E-04
at 4.5 V	30.42	236.2	1.19E-05	0.724	1.27	3.03	16.5	8.87E-05	0.659	1.17E-02	2.18E-04
LiCo$_{1.09}$Mn$_{0.91}$O$_4$ (at 600 °C)											
at 3.5 V	28.91	115.6	2.17E-05	0.822	3.93	2.3	36.1	4.24E-05	0.69	5.00E-03	1.45E-03
at 3.9 V	32.54	120	1.08E-05	0.91	3.6	2.98	40.1	4.94E-05	0.689	4.63E-03	1.59E-04
at 4.2 V	27.86	136.3	2.25E-05	0.747	3.17	3.62	34.7	7.19E-05	0.677	4.79E-03	8.56E-04
at 4.5 V	28.93	150	1.48E-05	0.788	2.86	3.88	27.5	5.23E-05	0.734	5.24E-03	2.42E-04
LiNi$_{0.5}$Mn$_{1.97}$O$_4$ (synthesized)											
at 3.5 V	107.5	204	1.14E-05	0.856	4.11	1.37	215	1.88E-05	0.678	1.07E-03	2.81E-04
at 3.9 V	102.9	266	1.19E-05	0.773	2.2	1.53	235	1.31E-05	0.729	1.88E-03	2.82E-04
at 4.2 V	93.68	242.6	1.22E-05	0.722	1.3	2.47	267	1.67E-05	0.739	2.82E-03	4.53E-04
at 4.5 V	92.37	237.6	6.25E-05	0.698	1.01	3.67	207	2.76E-05	0.719	2.12E-03	3.15E-04
LiNi$_{0.5}$Mn$_{1.97}$O$_4$ (spray dry)											
at 3.5 V	40.94	209.5	3.85E-06	0.973	3.16	2.26	207.3	8.58E-06	0.808	7.49E-03	7.37E-04
at 3.9 V	32.22	272.6	1.36E-05	0.76	2.32	2.67	170	9.58E-06	0.834	1.77E-02	2.38E-04
at 4.2 V	44.5	293	1.41E-05	0.731	1.87	3.07	120.1	1.15E-05	0.833	3.13E-02	7.65E-05
at 4.5 V	28.17	289.2	2.40E-05	0.629	1.28	3.6	112.4	2.56E-05	0.749	1.31E-02	4.58E-04
LiNi$_{0.5}$Mn$_{1.97}$O$_4$ (at 600 °C)											
at 3.5 V	8.98	191	1.89E-05	0.731	2.92	1.15	245.6	2.30E-06	0.915	2.19E-03	2.16E-03
at 3.9 V	9.99	183	4.37E-06	0.913	2.21	1.44	198.9	2.16E-05	0.668	1.31E-03	1.06E-03
at 4.2 V	10	189	5.02E-06	0.89	2.12	2.01	169.9	2.35E-05	0.692	1.38E-03	1.18E-03
at 4.5 V	6.35	165.1	2.28E-06	0.982	1.97	2.55	139.3	2.49E-05	0.713	1.07E-05	9.42E-04

APPENDIX B: Summary of the BET surface area at different synthesis temperatures

Sample	BET Surface area ($m^2.g^{-1}$)	Slope of Z_{real} vs $\omega^{-1/2}$		y-intercept of Z_{real} vs $\omega^{-1/2}$	
$Li_{1.03}Mn_{1.97}O_4$ (commercial)	13.73	3.5 V	16.18	3.5 V	809.16
		3.9 V	5.23	3.9 V	640.60
		4.2 V	3.79	4.2 V	529.89
		4.5 V	16.21	4.5 V	420.72
$Li_{1.03}Mn_{1.97}O_4$ (batch synthesized at 800°C)	8.67	3.5 V	26.65	3.5 V	716.08
		3.9 V	4.11	3.9 V	747.19
		4.2 V	8.95	4.2 V	492.16
		4.5 V	8.66	4.5 V	421.20
$Li_{1.03}Mn_{1.97}O_4$ (spray-drying at 400°C)	14.11	3.5 V	25.52	3.5 V	744.93
		3.9 V	5.04	3.9 V	567.08
		4.2 V	2.78	4.2 V	498.32
		4.5 V	11.61	4.5 V	404.91
$Li_{1.03}Mn_{1.97}O_4$ (batch synthesized at 600 °C)	13.75	3.5 V	29.80	3.5 V	427.21
		3.9 V	10.78	3.9 V	338.48
		4.2 V	8.88	4.2 V	330.07
		4.5 V	4.78	4.5 V	270.48
$LiAl_{0.4}Mn_{1.6}O_4$ (batch synthesized at 800°C)	18.15	3.5 V	11.85	3.5 V	133.68
		3.9 V	4.39	3.9 V	98.02
		4.2 V	2.23	4.2 V	81.92
		4.5 V	8.06	4.5 V	75.66
$LiAl_{0.4}Mn_{1.6}O_4$ (spray-drying at 400°C)	29.80	3.5 V	12.92	3.5 V	651.18
		3.9 V	21.91	3.9 V	619.16
		4.2 V	12.34	4.2 V	542.47
		4.5 V	13.06	4.5 V	520.02

$LiAl_{0.4}Mn_{1.6}O_4$ (batch synthesized at 600 °C)	23.64	3.5 V	13.68	3.5 V	330.36
		3.9 V	12.13	3.9 V	319.28
		4.2 V	8.36	4.2 V	295.82
		4.5 V	13.26	4.5 V	256.47
$Li_{1.03}Mg_{0.2}Mn_{1.77}O_4$ (batch synthesized at 800°C)	9.68	3.5 V	7.65	3.5 V	110.72
		3.9 V	9.30	3.9 V	95.45
		4.2 V	9.86	4.2 V	91.04
		4.5 V	10.62	4.5 V	85.57
$Li_{1.03}Mg_{0.2}Mn_{1.77}O_4$ (spray-drying at 400°C)	19.91	3.5 V	22.47	3.5 V	85.15
		3.9 V	7.17	3.9 V	53.73
		4.2 V	5.29	4.2 V	41.68
		4.5 V	26.06	4.5 V	30.50
$Li_{1.03}Mg_{0.2}Mn_{1.77}O_4$ (batch synthesized at 600 °C)	11.85	3.5 V	10.26	3.5 V	60.18
		3.9 V	8.95	3.9 V	52.82
		4.2 V	5.82	4.2 V	52.69
		4.5 V	5.39	4.5 V	48.18
$LiCo_{1.09}Mn_{0.91}O_4$ (batch synthesized at 800°C)	12.25	3.5 V	15.28	3.5 V	182.09
		3.9 V	8.70	3.9 V	92.88
		4.2 V	9.14	4.2 V	97.63
		4.5 V	12.41	4.5 V	71.20
$LiCo_{1.09}Mn_{0.91}O_4$ (spray-drying at 400°C)	26.15	3.5 V	43.81	3.5 V	997.93
		3.9 V	23.58	3.9 V	787.39
		4.2 V	22.53	4.2 V	658.63
		4.5 V	29.45	4.5 V	575.06
$LiCo_{1.09}Mn_{0.91}O_4$ (batch synthesized at 600 °C)	22.46	3.5 V	70	3.5 V	299
		3.9 V	111	3.9 V	249
		4.2 V	104	4.2 V	150

		4.5 V	103	4.5 V	152
LiNi$_{0.5}$Mn$_{1.5}$O$_4$ (batch synthesized at 800°C)	6.12	3.5 V	46.47	3.5 V	947.36
		3.9 V	52.30	3.9 V	878.85
		4.2 V	54.54	4.2 V	799.61
		4.5 V	51.29	4.5 V	731.04
LiNi$_{0.5}$Mn$_{1.5}$O$_4$ (spray-drying at 400°C)	19.48	3.5 V	31.38	3.5 V	789.50
		3.9 V	16.42	3.9 V	678.25
		4.2 V	9.78	4.2 V	623.27
		4.5 V	27.70	4.5 V	508.55
LiNi$_{0.5}$Mn$_{1.5}$O$_4$ (batch synthesized at 600 °C)	17.72	3.5 V		3.5 V	
		3.9 V		3.9 V	
		4.2 V		4.2 V	
		4.5 V		4.5 V	

APPENDIX C: Results on using the initial spray pyrolysis method

Following the initial continuous spray pyrolysis method, the resulting powder's diffraction pattern, particle shape and size are shown in Figures 1 and 2.
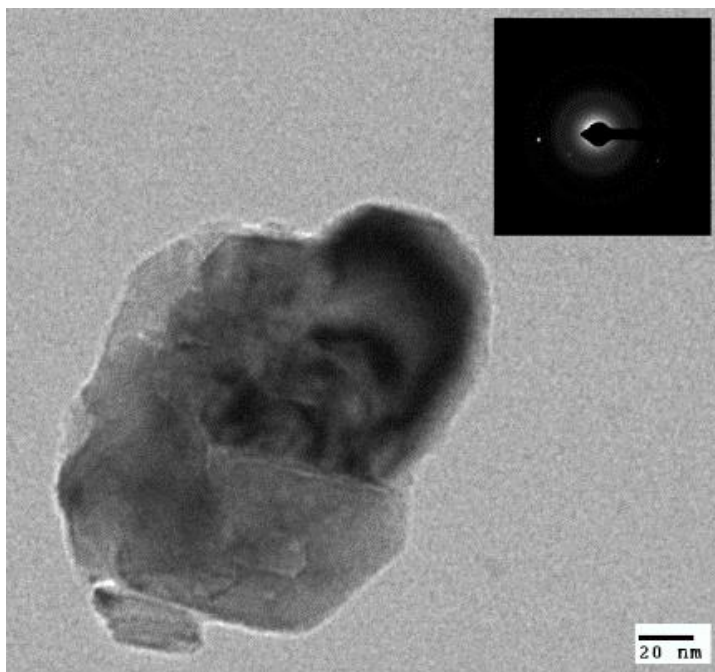
Figure 1: TEM image on $Li_{1.03}Mn_{1.97}O_4$ by continuous spray pyrolysis method.

The TEM image results (Figure 1) showed that the crystal sizes ranged between 100 nm to 700 nm with a majority of them around 100 nm particles. However the impurities observed within this analysis setup resulted from possible contamination from the quartz glass rod and the steel screw.
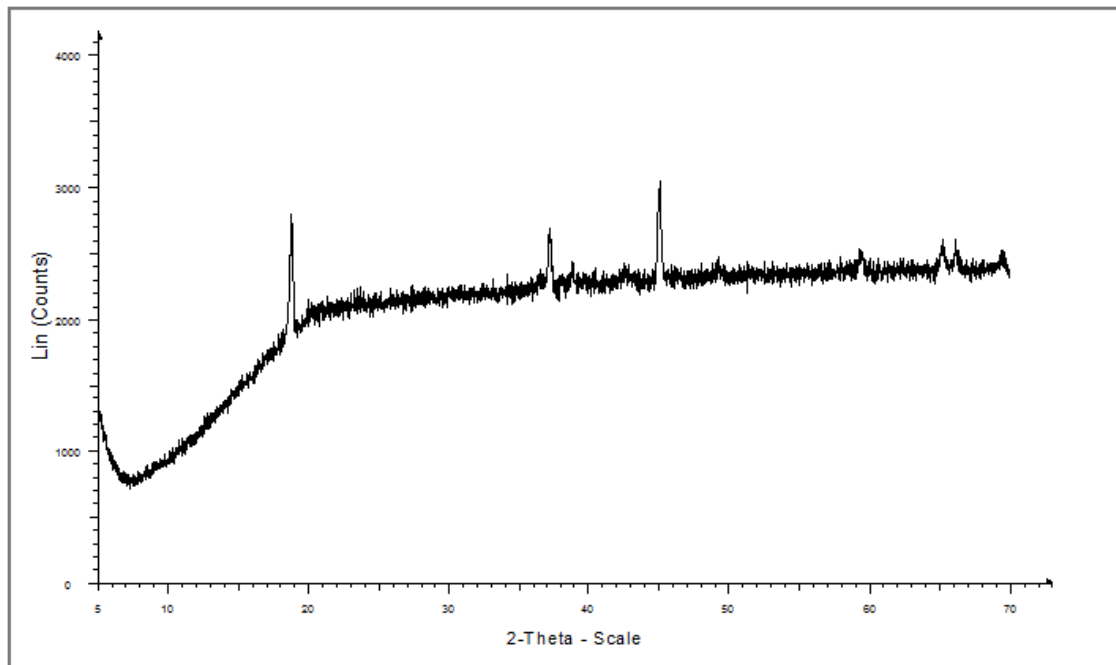
Figure 2: PXRD pattern on Li$_{1.03}$Mn$_{1.97}$O$_4$ by continuous spray pyrolysis method.

The PXRD pattern, Figure 2, showed a crystalline material was produced that corresponded to the typical spinel material. There were some impurities present, which were noted on the diffraction pattern to be between 35 and 45 °2θ and no distinct separation between the two peaks at 65 °2θ.

APPENDIX D: Published review article in South African Journal of Chemistry

A review of using spray pyrolysis through sol-gel materials in the synthesis of cathode materials for lithium-ion batteries

Charmelle D. Snyders[1], Ernst E. Ferg[a], Julian. Schuelein[b,c] and Holger. Loewe[b]

[a]*Department of Chemistry, Nelson Mandela Metropolitan University, P.O. Box 77000, Port Elizabeth 6031, South Africa*

[b]*Institute of Organic Chemistry, Johannes Gutenberg University, Duesbergweg 10-14, 55128 Mainz, Germany*

[c]*Fraunhofer ICT-IMM, Carl-Zeiss-Str. 18-20, 55129 Mainz, Germany*

ABSTRACT

Over the years, new synthesis routes of the cathode electrochemical active material for lithium-ion batteries have improved remarkably to optimize their capacity and cycle life performance. This review study focused on the use of some techniques to synthesize the common cathode materials ($LiCoO_2$, $LiMn_2O_4$, $LiFePO_4$). The most common and simplest synthesis method was the mixing of powders in their solid-state form and heating them at relatively high temperatures over long periods. Other methods included the formation of sol-gel products that could be either heat-treated more or could be used directly by means of a spray pyrolysis method producing the desired active material. The spray pyrolysis method showed that suitable cathode oxide materials formed in shorter periods, resulting in small homogenous particles with narrow particle size distribution. The spray pyrolysis method allowed for making doped or coated cathode materials easily of the various base forms $LiCoO_2$, $LiMn_2O_4$ and $LiFePO_4$, with doping elements such as Zr, Mn, Ni, Co, B or Mg. Coating of

[a]To whom correspondence should be addressed: E-mail address: Charmelle.Snyders@nmmu.ac.za

the particles could also be done with materials such as glassy lithium boride oxide, TiO_2 or carbon. These additives to the cathode material improved the active material's physical morphology and electrochemical properties.

Keywords: $LiCoO_2$, $LiMn_2O_4$, $LiFePO_4$, sol-gel, spray pyrolysis method

---

Table of contents

---

1.   Introduction

The large scale commercialization of lithium-ion cells can be dated back to the early 1990s with the development of modern portable consumer equipment, from wireless communications to mobile computing.[1] The lithium-ion cell consists of an anode electrode (such as lithium metal or lithiated carbon supported onto a copper current collector), a cathode electrode (for example $LiCoO_2$, $LiMn_2O_4$ or $LiFePO_4$ supported onto an aluminium current collector)[1] immersed in non-aqueous or aprotic electrolytes consisting of lithium salts (such as $LiPF_6$, $LiBF_4$ or $LiClO_4$) dissolved in an organicsolvent (for example ethylene carbonate, dimethyl carbonate, or diethyl carbonate or a mixture of them)[2]. The anode and cathode electrodes are separated by a separator which was made of a porous membrane (such as cellulose, glass fiber, inorganic composite membranes and microporous polymer membranes) to allow the ionic flow or transport of lithium-ions between the electrodes.[3, 4] Lithium-ion cells are manufactured and assembled in the discharge state (the lithium-

ions are in the cathode's active material structure). The cell was first charged before it is sealed and packaged for commercial use. During the charging process lithium-ions are extracted from the lithium metal oxide structure and migrate through a porous separator with the aid of an electrolyte, into the anode active material (known as intercalation). Whereas upon discharge the lithium-ions are extracted from the anode and embedded back into the vacant sites of the lithiummetal oxide material's crystal structure (known as de-intercalation). Fig. 1 demonstrated the intercalation and de-intercalation processes taking place in a lithium-ion cell.
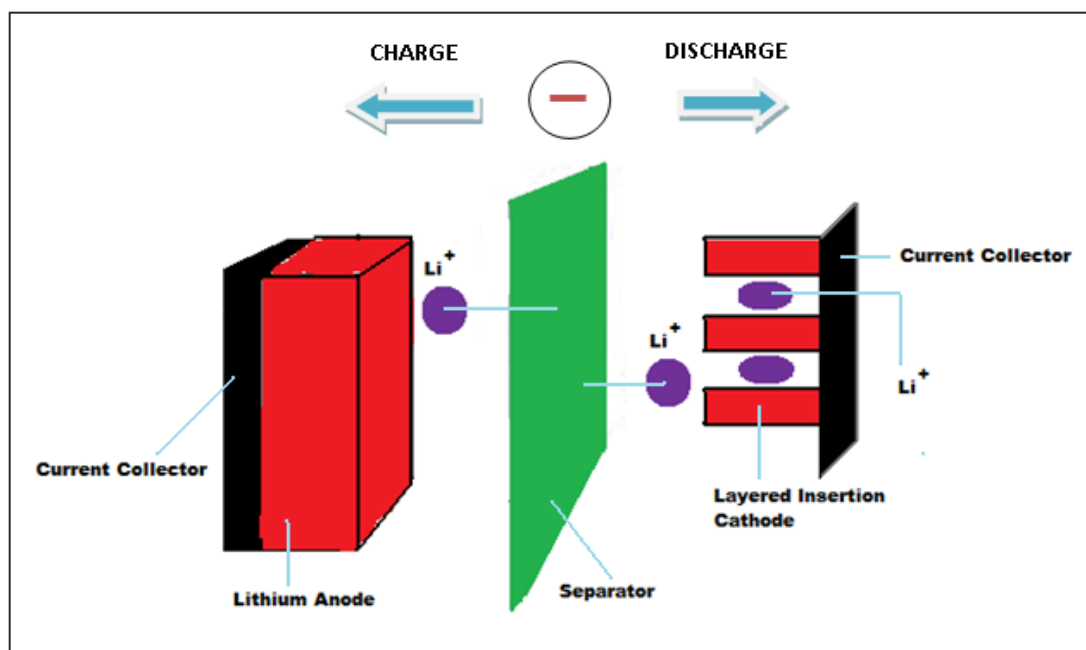
Figure 1. A schematic diagram on the insertion and extraction in lithium-ion cells

The synthesis process used to make the cathode oxide material for lithium-ion batteries has undergone a variety of changes in techniques that ranged from solid-state to sol-gel, co-precipitation, combustion, spray pyrolysis, microwave and hydrothermal methods.[5] Even though many of these methods have proved to be useful at laboratory-scale synthesis, the complexity and cost implications of scaling such methods to industrial manufacturing often proved to be unfeasible. Over the years one method, the spray pyrolysis method, proved to be successful at both laboratory scale and industrial level of synthesising. The spray pyrolysis method showed versatility in its approach to incorporate a variety of chemical compositions and techniques that canbe scaled to industrial feasible processeswith relative ease.

The presentstudy reviewed the historical and current uses of the spray pyrolysis method on the synthesis of cathode oxide materials in lithium-ion (Li-ion) batteries. The traditional synthesis methods used at laboratory scale to make cathode materials for Li-ion batteries mainly comprised of solid-state reaction methods. The solid-state methods were applied by a relatively simple process of mixing the right ratios of solid powders containing the lithium-ion (usually Li_2CO_3) with a transition metal oxide such as Mn, Co or Ni. These elements were typically heated in an oxidising atmosphere at high temperatures for a few hours. The processes were scaledwith relative ease to industrial batch-size processes to obtain a relatively consistent product that met the requirements in application. These reaction processes were divided into two methods/categories (the dry solid-state and wet-milling methods), depending on the difference in pre-treatment.[6] However, these methods had a number of disadvantages in both the cost of scaling and the consistency of the final prepared product. The disadvantages included a relatively large particle size distribution, long synthesis times at elevated temperatures, several mechanical mixing and grinding steps and calcinations temperatures.[6]

2   Various synthesis methods

The different cathode oxide materials (such as $LiCoO_2$, $LiMn_2O_4$ and $LiFePO_4$) were synthesised following various synthesis techniques (including the solid-state, sol-gel and spray pyrolysis method), which are discussed in the sections that follow.

2.1   Synthesis by solid-state method

The well-known cobalt-based cathode material, $LiCoO_2$, was synthesised by the solid-state method by mechanical mixingthe right stoichiometric ratios of Li_2CO_3 and Co_3O_4, followed by heating the product at 850 °C for 24 hours. Thereafter the product underwent further calcination at 650 °C for 12 hours in an air atmosphere. The final crystalline reaction product was ground and stored in a desiccator.[7]

The typical synthesis of $LiMn_2O_4$ by solid-state reaction involved stoichiometric amounts of Li_2CO_3 and MnO_2 as starting materials. These starting materials were ball milled and heated at 750 °C for 24 hours in an air atmosphere. The final product was ground at ambient temperature.[8]

For the synthesis of $LiFePO_4$ by solid-state method, LiF, Li_2CO_3, $LiOH \cdot 2H_2O$ or CH_3COOLi were used as the lithium source, $FeC_2O_4 \cdot 2H_2O$, $Fe(CH_3COO_2)_2$ or $FePO_4(H_2O)_2$ were used as the Fe source, and $NH_4H_2PO_4$ or $(NH_4)_2HPO_4$ was used as the PO_4 source.[9] The method typically involved complete mixing of Li_2CO_3, $FeC_6H_5O_7 \cdot H_2O$ and $NH_4H_2PO_4$ as starting materials in the right proportionate amounts in an acetone medium using a ball mill for 24 hours. The product was preheated in air at various temperatures: 200, 300 and 400 °C for threehours. The samples werefurther calcined at 700 °C in Ar gas for sixhours, producing the final product.[10] However, Kim et al.[11] prepared this material slightly different using an acetone solution of $FeC_2O_4 \cdot 2H_2O$, Li_2CO_3 and $NH_4H_2PO_4$ that was ball milled for 24 hours followed by drying at 100 °C for 12 hours. The product was decomposed by heating it at 350 °C for 10 hours in an Ar atmosphere. The dried product was pelletised and calcined at 600 °C for 10 hours under Ar producing the final crystalline $LiFePO_4$.[11] These four examples showed that the solid-state synthesis procedures were high in time and energy consumption.

2.2   Synthesis by sol-gel method

Over the years various synthesis methods were developed not only to improve the performance of the material but also to reduce the energy required and the time involved in solid-state synthesis methods. The use of sol-gel chemistry was originally studied in 1846 by Ebelenen[12] when he discovered that SiO_2 gels could be formed through hydrolysing $Si(OEt)_4$. However, it was only in 1930 that the sol-gel method developed further for commercial applications.[12] The synthesis of silica by sol-gel method involved the hydrolysis and condensation of silicon alkoxides. The synthesis method could be explained as follows[13] and summarized in Fig.2.

Si - OR + H_2O $\Longrightarrow$ Si - OH + ROH (hydrolysis)

Si - OH + RO – Si $\Longrightarrow$ Si - O -Si + ROH (alcohol condensation)

Si - OH + Si - OH $\Longrightarrow$ Si - O - Si+ HOH (water condensation)

Si (OR) $_4$ + $2H_2O$ $\Longrightarrow$ SiO_2 + 4ROH (overall reaction)
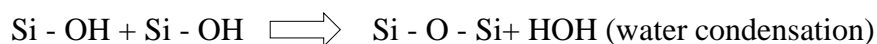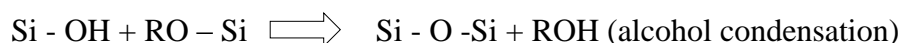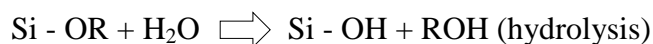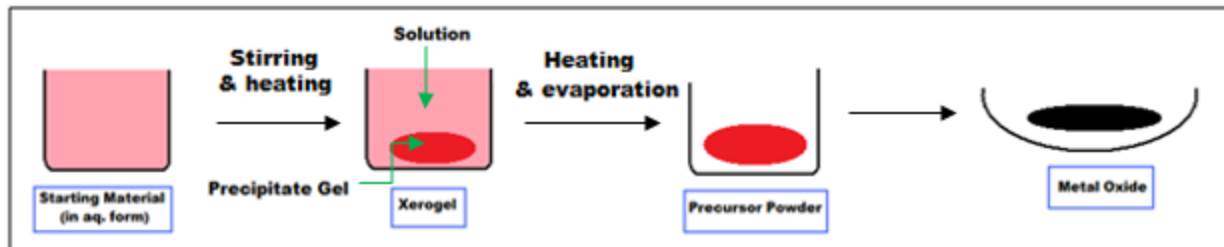
Figure 2. Schematic flow diagram of a typical sol-gel process

The sol-gel method was developed even more for the synthesis of a variety of glasses, ceramics, inorganic fillers and coatings.[12] In some industrial applications, the coatings were used for chemical protection (such as corrosion inhibitors) and mechanical protection (such as abrasion resistance).[14] The technology was also used in biomedical applications (such as biomedical sensors and coatings for metal implants)[15, 16] and is still used daily in various chemistries such as cosmetics (including sunscreen lotion and makeup with UV absorbers).[16] The uniqueness of the sol-gel method was that it produced a homogeneous mixture in a solution that was almost at the atomic/molecular level. The stoichiometric amount could be controlled and the synthesis temperatures were relatively low in comparison to the solid-state method. Short heating rates by the sol-gel process could produce a good crystalline material with uniform particle sizes that had relatively smaller diameters.[12] However, there were a number of disadvantages in using sol-gel methods that included the high cost of the raw material and a comparatively large volume shrinkage as a result of drying and sintering the material.

A number of cathode materials for Li-ion batteries were made by using the sol-gel method. The methods included the layered ($LiCoO_2$) structured material that was prepared by dissolving a cobalt salt (nitrate or acetate) in a suitable solvent such as water or ethanol. The carrier used to control the particle size and uniformity for dispensing ions in the solution was typically made of an organic compound that acted as a chelating agent (such as citric acid, polyacrylic acid, malic acid or oxalic acid) producing an aqueous solution. At this point, the pH of the solution had to be maintained producing an acidic solution (at about pH 4 to pH 5.5) by the addition of an aqueous LiOH or ammonium solution.[12, 17] The solvent evaporated at about 70 to 100 °C, producing a viscous gel that was completely dried at about 140 to 400 °C, producing a precursor powder. The precursor powder was heated between 500 and 800 °C in air with a 12-hour plateau producing the final metal oxide product.[12, 17, 18] There have been recent developments in making the layered structured materials

with new synthesis routes by doping the final material with various transition metal elements that included Mg, Cu, Eu or Co.[19-22]. In addition, the method was used to coat the active layered oxide with carbon and various metal oxides that included Al_2O_3, MgO, Li_2CO_3, $AlPO_4$, SnO_2.[12, 23]These new developments have shown improvements in reducing the manufacturing cost, increasing the active material's capacity and cycling ability, improving structural stability and improving the overall electrochemical properties of the batteries.[12, 23]

The sol-gel synthesis process of the well-knownspinel-type $LiMn_2O_4$materials was typically made by dissolving the manganese and lithium salts (acetates) in stoichiometric amounts with a carrier (citric acid, ethylene glycol, polyacrylic acid, adipic acid or glycolic acid)[24, 25, 26] in water. The result was an aqueous solution where the pH was sometimes adjusted to a slightly basic form by adding ammonium hydroxide.[12, 27, 28, 29] The aqueous solution was then heated to 120 °C with continuous stirring to form the gel-solid precipitate. Further heating resulted in the solid powder precursor which was completely dried at 140 °C for about fivehours. The dried precursor was calcined at 750 °C for about 15 hours in an air atmosphere producing the final Li-metal oxide spinel cathode material.[27] Modifications of the spinel material weredone by doping the spinel material with various transition elements (only a few are mentioned such as Mg, Al, Cr, Co and Ni)[27, 30, 31, 32] and by surface coating (such as nano-SiO_2, Al_2O_3 and carbon coating).[33] These modifications helped to increase the electrochemical properties of the material, such as improvement in capacity retention and cycleability, improved interfacial properties between electrolyte and electrode, enhanced electrical conductivity and protecting the metal oxide from chemical corrosion.[33]

The sol-gel synthesis method for synthesising the olivine-type structure materials, of which the $LiFePO_4$ is a typical example, consisted of various starting materials. For the Li component, the following salts could be used: Li $(OH) \cdot H_2O$, $LiNO_3$, $LiCO_3$, Li (CH_3COO) or $Li_2C_2O_4$.[34, 35, 36, 37] For the Fe complex, $FeC_2O_4 \cdot 2H_2O$, Fe $(C_2H_3O_2)$ or $C_6H_5FeO_7$[34, 35, 36, 37]could be used, whereas the phosphate used$NH_4 \cdot H_2PO_4$.[34, 35] Two synthesis routes following the sol-gel process were discussed to show that the pure olivine structure could be formed regardless of the different starting materials. The first method involved dissolving stoichiometric amounts of Li $(OH) \cdot H_2O$, $FeC_2O_4 \cdot 2H_2O$ and $NH_4 \cdot H_2PO_4$ reagents in deionised water with polyacrylic or citric acid.[34] Another synthesis procedure involveddissolving stoichiometric amounts of $NH_4 \cdot H_2PO_4$, Fe_3NO_3 and $LiNO_3$ in a polyvinyl alcohol and ethanol–water (50:50 v/v) solution.[35] Both these procedures resultedin a sol-

gel at 80–85 °C with vigorous stirring. The first procedure required drying the gel at about 500 °C under Ar gas, decomposing all the organics present and heating the precursor more at 700 °C under a reducing gas mixture (10% H_2 in Ar) resulting in the pure olivine structure. The second procedure however, required the gel to dry under a reducing atmosphere of a H_2/N_2 (10/90) mixture until the gel dried completely. Thereafter, the precursor was heated at 675 °C for four hours under the same atmospheric environment resulting in the olivine-structured material. The olivine-structured material was pyrolised or sintered in a controlled gas environment to prevent the formation of Fe^{2+} resulting in an increased yield of the olivine structure. Dopants were introduced to the material to improve the conductivity and cycle life by using ascorbic acid as the carrier with dissolved metals such as Cu or Ag. The metals were added in very low concentrations to improve the kinetics and conductivity of the final structured material.[12]

Other cathode materials for lithium-ion batteries were also prepared and studied using the sol-gel methods. The materials included a range of lithium vanadium oxides and lithium nickel oxides. The Li-ion intercalation into V_2O_5 was already recorded in 1976.[38] V_2O_5 was considered a cathode material because of its low cost, abundance and its ability to synthesise easily with a relatively high energy density. V_2O_5 had a layered crystal structure and therefore, it was a typical intercalation compound. However, due to the material's poor structural stability during the intercalation process, low electronic and ionic conductivity and slow electrochemical kinetics, the development of V_2O_5 as cathode in rechargeable lithium-ion batteries was limited.[38] Using the solid-state method, lithium vanadium phosphate ($Li_3V_2(PO_4)_3$) was synthesised by mixing appropriate amounts of $NH_4H_2PO_4$, V_2O_5 and Li_2CO_3. The prepared mixture was heated at 300 °C in air for four hours, allowing water and NH_3 to evolve. The obtained product was ground, pelletised and heated at 850 °C in an H_2 atmosphere for eight hours. After furnace cooling, the product was ground, pelletised and heated again for another 16 hours (at 850 °C) to ensure complete final metal oxide formation.[39] $Li_3V_2(PO_4)_3$ prepared by the sol-gel method involved dissolving $LiOH \cdot H_2O$, NH_4VO_3, H_3PO_4 and citric acid in distilled water while stirring continuously and maintaining the pH around 9 by adding $NH_3 \cdot H_2O$.[40] The gel formed by means of vacuum drying at 120 °C for eight hours. The dried gel was heated at 300 °C for three hours in air to remove water, NH_3 and CO_2 completely. The obtained product was calcined for eight hours at 700–900 °C in a reducing atmosphere (8% H_2 in Ar).[40] The electrochemical performances of this material showed an increase in cycling capacity with reasonably good capacity retention of about 95%.[40]

$LiNiO_2$was also used as a cathode material for Li-ion batteries. The cost of $LiNiO_2$was relatively lower than the cost of $LiCoO_2$ and had a higher reversible capacity. The layered structure made it difficult to prepare the material on a large scale because of the Ni^{2+} to Ni^{3+} oxidation.[12] $LiNiO_2$had a lower degree of ordering (when compared to $LiCoO_2$) when the nickel-ions occupiedthe sites in the lithium crystal planes causing difficulties to form the appropriate composition.[41] The problems were solved by adding cobalt upon which the nickel-ion positions were occupied by the nickel/cobalt crystal plane, resulting in an increased degree of ordering.[41] Following a sol-gel synthesis route, this cathode material was synthesised by making an aqueous solution consisting of lithium hydroxide, ammonium hydroxide, a nickel salt (such as nickel nitrate) and citric acid. The solution was stirred and the solvent was removed at a temperature below 100 °C to form a xero-gel. Crystalline $LiNiO_2$ was formed by heating the obtained dry powder at above 400 °C.[12] The sol-gel synthesis method produced a good capacity retention material. Cobalt-doped $LiNiO_2$ by means of sol-gel methods was prepared as follows: Stoichiometric nitrate amounts of lithium, cobalt and nickel were dissolved in a suitable solvent (such as water or ethanol) with chelating carrier agents (such as ascorbic acid, citric acid, maleic acid, oxalic acid or triethanolamine)[12, 42] The resulting solution was stirred at 80 °C. The obtained solution was heated further at 100 °C, producing a gel. The gel was dried at 100–200 °C for twohours and at 240 °C for fivehours.[42] The dried precursor was calcined further for 12 hours at 800 °C.[12] The doped material stabilised $LiNiO_2$ and improvedthe electrochemical properties.

2.3   Synthesis by Spray Pyrolysis method

Spray pyrolysis combined with the development of sol-gel chemistry processes proved that it is necessary to synthesise powders of good quality, low moisture and a narrow particle size distribution. The technique was used for a variety of chemistry synthesesand could be adapted for either continuous or single-step preparation methods. The use of spray pyrolysis as a route for thermal synthesis of chemical materials was used in many industries for a variety of applications such as fuel cells (Pt active material), foods (milk powder, cereal, coffee, tea), pharmaceuticals (antibiotics, medical active ingredients) and consumer goods (paint pigments, ceramic materials, catalyst supports).[43, 44] Besides the large number of advantages this technique displayed, it also had a few disadvantages. The technique was well suited for the synthesis of micro- or even nano-sized particles. However, an efficient separation technique was required for the production of these fine powders in order to avoid the loss of products and environmental pollution.[44] These processes often

required high evaporation rates and usually took place within short residence times. The spray pyrolysismethod was ideal for drying heat-sensitive materials but it was not suitable for materials that could conglomerate easily. The powders of the desired material wereproduced from a liquid or slurry mixture that was pumped through a set of nozzles after which it was dried rapidly with the aid of hot gases. Air was the preferred gas to use during the drying process.However, if the solvent or liquid was flammable and if the produced product was oxygen-sensitive, nitrogen gas was often used. The technique used spray nozzles or atomisers that could disperse the liquid into very finely controlled droplets. The gas used during the process, acted as a carrier, enabling the particles that were formed to undergo a significantly faster and uniform thermal reaction. The flow of the precursor solution was pumped, usually by a peristaltic pump, with a constant gas flow through a nozzle into a pre-heated heating apparatus. At this point, solvent evaporation took place rapidly and the dried mixed precursor powder was passed through a filtering system that collected the final desired active material. The final product of this process produced amorphous, semi crystalline or crystalline powders.[45] A schematic diagram of the spraying process was shown in Fig. 3.
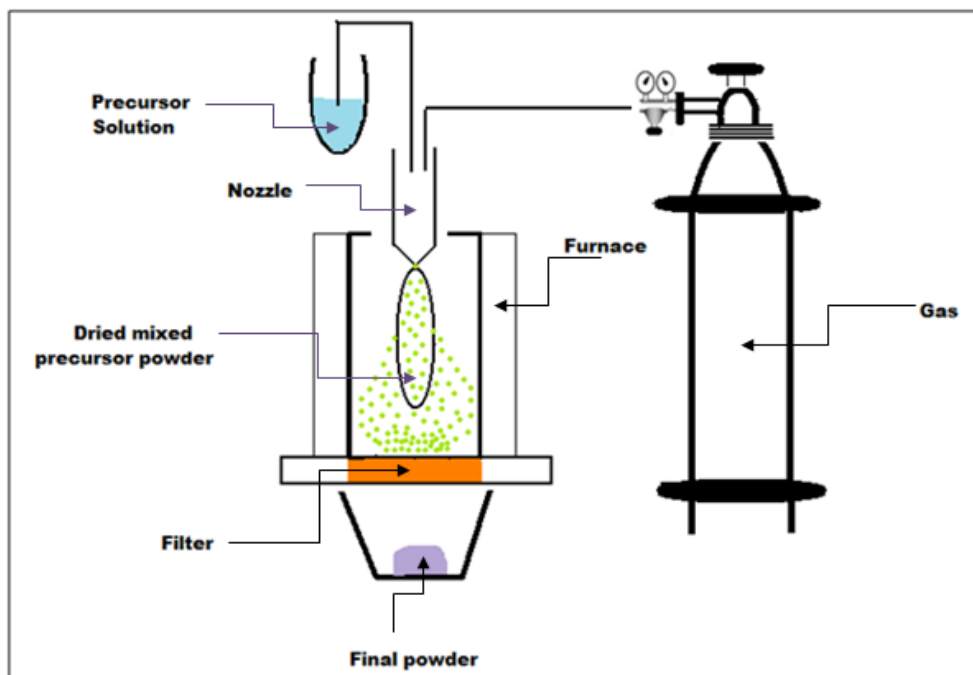

Figure 3: Schematic diagram on a typical spray drying process

Using the spray pyrolysis process, ultrafine $LiCoO_2$ could be synthesised in a short period. The method involved the use of an aqueous solution containing acetates of Li and Co with polyethylene glycol. The solution was pumped through a nozzle with pressurised hot air (at 0.1 MPa, a gas flow

rate of 6.6 L.min^{-1} and a residence time of 6 sec) into a heated apparatus at about 300 °C.[46] The dried precursor material was formed followed by further calcining at 800°C in air for fourhours, producing the pure LiCoO$_2$.[46]

Spray pyrolysis techniques were used successfully to make pure cubic spinel LiMn$_2$O$_4$ hollow structures with a spherical shaped nanostructured particlewith improvements to the electrochemical properties.[47] The method involved the use of an aqueous reaction solution of LiNO$_3$ and Mn(NO$_3$)$_2$·6H$_2$O in stoichiometric ratios that went through an ultrasonic atomiser (at 100 kHz with a gas flow rate of 20 dm^3.min^{-1} and residence time of 60 sec) into a heated ceramic furnace at 800 °C for fourhours in an air atmosphere.[47]

Gomez et al.[48] recorded the preparation of LiFePO$_4$ material by means of the spray pyrolysis method. The method used a 0.01M precursor solution of LiNO$_3$, Fe$_2$C$_2$O$_4$·H$_2$O and NH$_4$H$_2$PO$_4$ in nitric acid (pH 1.5). An aerosol ultrasonic generator atomised the solution, with Ar as the carrier gas (with a flow rate of 1.5 L.min^{-1}) into fine droplets at 2.1 MHz. The droplets passed through a tubular flow reactor and thermally decomposed at 400 to 700 °C. The obtained powders were further heated for sixhours in an Ar atmosphere at 600 to 800 °C, obtaining the pure LiFePO$_4$ phase.[48]

Companies such as Argonne National Laboratory (USA), who made nanoparticles of lithium titanates and spinel oxides, made active cathode materials for Li-ion batteries by means of the commercially process of spray drying. They had a license agreement with BASF to produce and market these materials.[49]

3   Characterisation of materials made by spray pyrolysis method

Li et al.[46] followed the spray pyrolysis technique for the LiCoO$_2$ synthesis route and thescanning electron microscopy (SEM) analysis,showed the formation of a relatively good distribution of homogeneous particles with a small grain size, with no agglomeration and an average particle size of between 200 and 700 nm. During their electrochemical testing, when a constant charge/discharge current was applied, an initial charge capacity of 148 mAh.g^{-1} and a discharge capacity of 135 mAh.g^{-1} were observed with a good cycle life without any distinct capacity loss over 10 cycles.[46] The synthesis process for this material (in comparison to other synthesis techniques) was shortened

to a period of eight hours. This process improved the preparation of the materials in comparison to the normally batch synthesis, positively contributing to time efficiency and improved cycle life.

Further investigations were performed on the cathode material using doping and coating to improve the material's electrochemical behaviour further. One ofthese investigations was doping with Zr using ultrasonic spray pyrolysis.[50] $LiCo_{1-x}Zr_xO_2$ was prepared by making a 0.5 mol.L^{-1} solution consisting of Li, Co and Zr nitric salts. The produced solution was atomised at 1.67 MHz into a two-stage heating zone (at 400 and 800 °C) quartz reactor. The product was calcined at 900 °C for 20 hours in a furnace using air.[50] A 1 mol% Zr-doped material produced a pure spinel layered structure. Increasing the Zr-doped concentration showed a decrease in the 1C discharge capacity.These results were summarized in Table 1. As the discharge rate was increased, the capacity typically decreased (summarized in Table 2).

Table 1. Summary of results of the materials' capacity compared to the change in Zr-doped concentration

Zr-concentration	Capacity (mAh.g^{-1})
x= 0.005	143
x= 0.01	139
x= 0.05	135

Table 2. Summary of results of the materials' capacity compared to the change in discharge rate.

C-rate	Capacity (mAh.g^{-1})
0.2C	176
0.5C	161
1C	148
3C	100

From these results, it was concluded that Zr doping improved both cycling stability and rate performance comparatively. The expansion of the unit cell's lattice distance to allow the extraction/insertion of the Li^+ ion upon discharge/charge respectively explained the

improvements.[50] The only shortfall in this study was adding and increasing the Zr content by more than 1 mol %, as it developed into a secondary phase (Li_2O_3).[50]

The preparation of a lithium cobalt oxide material with both Mn and Ni as dopants to form $Li_{1.2}Mn_{0.54}Ni_{0.13}Co_{0.13}O_2$ showed the versatility of the spray pyrolysis method in synthesising cathode oxides.[51] The Mn and Ni doped lithium cobalt oxide material was synthesised by making a 2.5 M aqueous nitrate solution that contained $LiNO_3$, $Mn(NO_3)_2\cdot4H_2O$, $Ni(NO_3)_2\cdot6H_2O$ and $Co(NO_3)_2\cdot6H_2O$ in the right proportions. The prepared solution was sprayed (with the aid of an ultrasonic nebuliser) at 2.4 MHz into a preheater (at 200 °C) with a water-saturated air carrier gas (at a flow rate of 6.6 $L.min^{-1}$ with a residence time of 6 sec). The precursor powder was placed in a temperature-controllable 3-zone vertical furnace reactor where the reactor wall temperatures were kept at 350, 575 or 650 °C respectively. The cooled powder was collected on a porous polycarbonate membrane filter for further analysis and cell preparation.[51] A robust synthesis method was required to prepare the cathode oxide materials for lithium-ion batteries. Most synthesis methods (such as solid-state combustion and freeze drying) were challenging as they required long reaction times, they contained material impurities and batch-to-batch inconsistencies which caused obstructions in the large-scale implementation. The synthesis technique used for this material showed that the variable reactor temperature effect was important, as the primary particle's size influenced the electrochemical performance significantly. A material with a decrease in its primary particle stimulated the electrochemical activation as well as an increase in capacity. In this study, the reactor temperature varied between 350, 575 and 800 °C respectively. At 350 °C, a large particle size was observed because the material was hygroscopic with traces of unreacted $LiNO_3$. Above 575 °C, the nitrate salts reactedcompletely during the synthesis process.However, the crystallinity of the material increased with improved primary particle growth by increasing the heat of the material from 800 to 900 °C at shorter time intervals. For cycling and rate capability tests, a discharge capacity that ranged between 162 and 206 $mAh.g^{-1}$ was observed after 100 cycles at a C/3 rate.[51] This study (following spray pyrolysis) showed improvements in the batch-to-batch consistency, phase pure materials and cathode materials that produced excellent electrochemical performance.

The electrochemical properties of $LiCoO_2$ could improve by coating the particles with glassy lithium boron oxide (LBO) during the flame spray pyrolysis process.[52] This type of coating was

used in the current study because it hada high Li^+ content and conductivity. The wetting properties of the coating were good with a relatively low viscosity. The synthesis process consisted of a 1.5 M aqueous nitrate solution that contained $LiNO_3$ and $Co(NO_3)_2 \cdot 6H_2O$ dissolved in distilled water, $LiNO_3$ and boric acid (H_3BO_3) were used for the $Li_2O-2B_2O_3$ glass coating material. This solution was pumped (at a 5 L.min^{-1} flow rate) with an O_2 carrier gas (at a 10 L.min^{-1} flow rate) into a high-temperature diffusion flame. The produced precursor droplets evaporated, decomposed and melted in the diffusion flame. The produced precursor particles were calcined at 500, 600 and 700 °C respectively for threehours in air. The LBO glass-coated $LiCoO_2$ produced a particle size with a mean of about 54 nm, which was slightly larger than the pure $LiCoO_2$ of about 42 nm. The coated material and the pure $LiCoO_2$ showed lower charge and discharge capacities before calcination (Table 3).

Table 3. The initial capacities of $LiCoO_2$and LBO glass modified $LiCoO_2$ (10 wt%)

	$LiCoO_2$	LBO glass modified $LiCoO_2$
Initial charge capacity (mAh.g^{-1})	97	83
Initial discharge capacity (mAh.g^{-1})	79	74
Discharge capacity after 10 cycles (mAh.g^{-1})	62	66

These materials' crystallinity and electrochemistry improved by post-treating the pure $LiCoO_2$ and the LBO glass modified $LiCoO_2$ at temperatures between 500 and 700 °C. When the pure $LiCoO_2$ and the LBO glass modified $LiCoO_2$ materials were calcined at 600 °C, an improvement was observed in the material's discharge capacity, decreasing from 119 to 85 mAh.g^{-1} (for pure $LiCoO_2$) and 122 to 109 mAh.g^{-1} (for the LBO glass modified $LiCoO_2$) upon cycling (55 cycles). From the results, it was concluded that coating the active material's particles increased the mean particle size, showing an improvement in the material's electrochemical properties (such as improved charge/discharge capacities and good cycle properties) and decreasing the material's reactivity in an acidic electrolyte.[52]

The spray pyrolysis synthesis method was also applied successfully to make manganese spinel cathode material.[53] A big advantage of the technique was that a small particle size could be

achieved when the final dried solid $LiMn_2O_4$ powder, made from the spray technique, obtained particles that ranged between 75 and 1250 nm.[54] Taniguchi et al.[47] also studied the synthesis of $LiMn_2O_4$ by the spray pyrolysis and drying system. According to their study, the X-ray diffraction analysis showed a pure crystalline material that was cubic spinel in structure, and the SEM analysis showed that the particles were spherical and in some cases, hollow. The charge/discharge curves showed distinct plateaus corresponding to well-defined $LiMn_2O_4$ structures, indicating the characteristics of a spinel manganese oxide structure. Their electrochemical analysis results were summarized in Table 4.

Table 4.$LiMn_2O_4$ capacity results after continuous cycling and at various discharge rates.

	Discharge capacity (mAh.g^{-1})
1st cycle at 0.1C	126
after 99 cycles at 0.1C	100
at 10C	74

After 99 capacity cyclesan irreversible capacity of 12% was produced.[47] An increase in rate also produced a slight change in discharge capacity, which was a resultof slow lithium-ion diffusion, but it was still producing a relatively high discharge capacity. Following this method showed good cycle and high rate performances.

The manganese spinel cathode material, $LiMn_2O_4$, experienced capacity fading during cycling, therefore doping contributed to the improvement of cycling performance. These doping elements included B, Co, Fe, Cu, Al and Cr to mention only a few.[55, 56, 57, 58, 59] The doped $LiM_xMn_{2-x}O_4$ material was made by using an aqueous solution that contained nitric salts of the respective dopants with an approximately 0.9 M total metal-ion concentration with tartaric acid for a pH control between 1 and 1.7.[55, 59] The prepared precursor solution was atomised by an ultrasonic nebuliser (frequency ranging from 1.3 to 1.75 MHz). The solution was sprayed into air (at a flow rate of 500 ml.min^{-1}) in an electric furnace that waspreheated to 800 °C. Solvent evaporation took place within the heating reactor and produced the final oxide particles with a residence time of about 9.4 sec.[55, 56, 57, 58, 59]

The boron doped, $LiB_xMn_{2-x}O_4$, phases were studied at different concentration ranges where x=0.1–0.4. When X-ray diffraction occurred, pure crystalline spherical morphology was observed, whereby these spherical morphologies decreased as the boron concentration increased.[55] However, SEM analysis showed porous and hollow particles except for the high boron concentration materials contributing to the submicron size of mainly all the materials. Having these small particle sized materials for lithium batteries would result into higher charge/discharge rates and short diffusion paths. Electrochemical analysis results showed a significant decrease in the first discharge capacity as provided in Table 5.

Table 5. Summarized electrochemical analysis for $LiB_xMn_{2-x}O_4$

Substitution levels	Discharge capacities at 0.5C $(mAh.g^{-1})$
0.1	53
0.2	62
0.3	92
0.4	50

The boron-doped material, $LiB_{0.3}Mn_{1.77}O_4$, retained up to 82 % of its capacity after 50 cycles at the 0.5C rate.[55] Although the material showed a decrease in the first discharge capacity, an improvement in the material's structural stability was observed upon capacity cycling. The results obtained in this study met the industry requirements because the materials produced good cycling performance and capacity.

Cobalt-substituted $LiMn_2O_4$ samples were studied by heating the sample at 750 °C for various time intervals (1, 4 and 8 hours) by the ultrasonic spray pyrolysis process. Their structural analysis showed spherical single spinel-phase particles that ranged in crystallite sizes (summarized in Table 6).[56] This structural behaviour (crystallinity increase) resulted in an increase in the first discharge capacity (refer to Table 6) with a decrease in irreversible capacity loss over the first cycles (below 10 %).

Table 6. Crystallite sizes and first discharge capacities of cobalt-substituted $LiMn_2O_4$ at various time intervals.

	1 hour	4 hours	8 hours
Crystallite size (nm)	39.6	52	58.9
1st discharge capacity (mAh.g^{-1})	107	108	113

The cobalt-substituted $LiMn_2O_4$ material was also studied at various C-rates ranging from 1 C to 60 C. At higher rates (60 C), the sample that was prepared at fourhour time intervals resulted in better capacity retention (87 %) compared to the capacity at 0.1 C rate. The spray pyrolysis process was followed forthis material at four hour time intervals which showed an improvement in the electrochemical performance at high rates, whereby the crystallinity was well controlled.[56]

Taniguchi et al. [60] studied $LiMn_2O_4$ with its substituted form $LiM_{1/6}Mn_{11/6}O_4$ (M= Co, Al and Ni) synthesised by ultrasonic spray pyrolysis. The ultrasonic spray pyrolysis synthesis method involved making an aqueous nitrate solution (0.45 mol.dm^{-3} in concentration). The solution was generated into a mist by an ultrasonic vibrator with a flow of air (flow rate of 2 dm^{-3}.min^{-1}) into an electric furnace, (the mist was keptin the furnace for 4.8 min) to dry and complete the pyrolysis process. The produced materials' crystallite sizes with its specific area were summarized in Table 7. The spray pyrolysis synthesis route was followed and $LiAl_{1/6}Mn_{11/6}O_4$ and $LiMn_2O_4$ porous microstructure particles developed whereas $LiCo_{1/6}Mn_{11/6}O_4$ and $LiNi_{1/6}Mn_{11/6}O_4$ showed a smooth surface.

Table 7. Morphology and electrochemical properties of the metal substituted $LiMn_2O_4$ materials.

Crystallite size (nm)	28-33
Surface area (m^2.g^{-1})	5.7-12.7
Initial capacity (mAh.g^{-1})	101-117

The electrochemistry results of these materials showed two voltage plateaus at approximately 4.05 and 4.1 V. However, the substituted metal-ions showed lower initial capacities (refer to Table 7)

compared to the pure $LiMn_2O_4$ (129mAh.g^{-1}) due to the decrease in Mn^{3+}ions in $LiMn_2O_4$. An improvement in the capacity retention was observed whereby $LiMn_2O_4$ had an 85 % increase in capacity retention by following the spray pyrolysis process compared to a 75 % capacity retention by following the solid-state process[60].

Over the years, $LiMn_2O_4$ was used as a suitable cathode material for lithium-ion batteries. However, this material also experienced a few disadvantages of which capacity fading was one of the main drawbacks especially at elevated temperatures. Capacity fading was suppressed by the addition of $AlPO_4$ to the electrolyte. Bakenov et al.[61]studied this electrolyte's alteration by following the spray pyrolysis technique. They prepared the spinel material by atomizing the precursor solution (an aqueous 0.9 mol.dm^{-3} total cation solution) at 1.7 MHz withan ultrasonic nebulizer. The sprayed droplets with airflow were carried into the reactor (at 800 °C) where the solvent evaporated, dried and pyrolysed forming the solid oxide particles. Thereafter, the particles were collected by means of an electrostatic precipitator at 150 °C. $AlPO_4$wasadded to the electrolyte (1:1), stirred for 24 hours and thereafter the solid $AlPO_4$ phase was separated from the electrolyte by means of the centrifuge technique. The PXRD analysis showed pure single-cubic spinel structures. From the electrochemical results it was observed that the materials' capacity fade decreases with an increase in temperature. At 60 °C, 50 % of the materials capacity was lost (after 50 cycles). However, with the addition of $AlPO_4$a capacity loss of 28 % was observed at 60 °C.[61] An improvement in the materials' capacity fading was observed by adding $AlPO_4$ especially at high temperatures.

Another new development in this spinel structure was that $LiMn_2O_4$ particles were coated to improve the electrochemical performance in the cathode oxide material. The effects included the dissolution of the electrode material that was in contact with the electrolyte, with side reactions on the electrode's surface and the crystal structure's instability contributing to shortening the battery's capacity life. The particles of $LiMn_2O_4$ (LMO) could be coated with lithium boron oxide glass (LMO-LBO) and TiO_2 (LMO-TiO_2) by a spray pyrolysis process.[62] The spray pyrolysis process involveddissolving Li, Mn and boron precursors and atomising them into droplets. These droplets were exposed to a heated reactor where the Li reacted with the Mn to form $LiMn_2O_4$ and upon evaporating the solvent, a reaction between Li and B occurred to produce the LBO glass phase. The preparation of a core-shell structure by the one-step spray pyrolysis method occurred where the

substance, with a higher melting point, tended to bond at the core, while the substance with a lower melting point would be "pushed" outwardly forming the coating layer[62] as illustrated in Fig. 4.
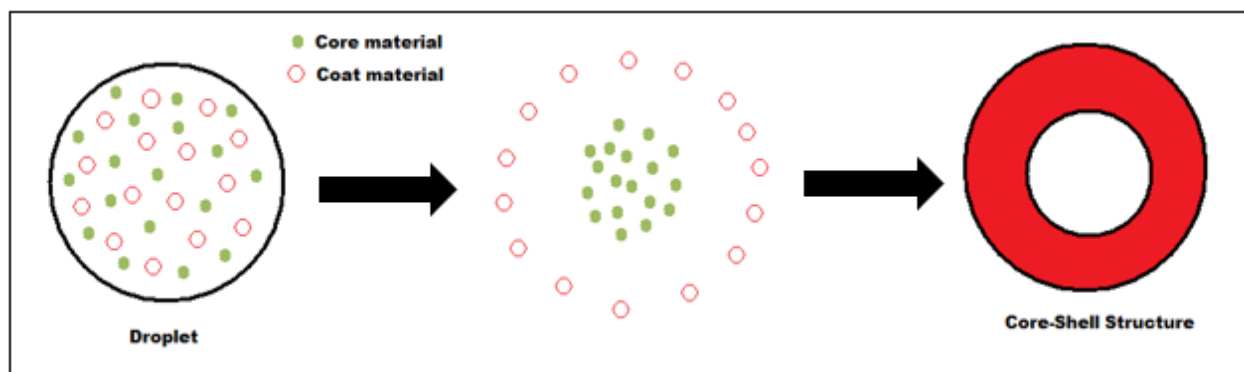

Figure 4: Schematic diagram on the formation of a core-shell structure

The cathode material $LiMn_2O_4$ coated with Li_2O-$2B_2O_3$ glass showed an improvement in its initial capacity of 131 mAh.g^{-1} with an 86 % retention after 100 cycles at the 1 C rate, in comparison to the uncoated $LiMn_2O_4$ producing a 80% capacity retention (after 100 cycles at 1C).[62] $LiMn_2O_4$ coated with TiO_2 had an initial capacity of 126. mAh.g^{-1} with an 86% retention after 170 cycles at the 1C rate.[62] The coated synthesis route enhanced or improved the materials' structural stability and prevented the active materials' dissolution during cycling.

$LiFePO_4$ prepared by spray pyrolysis[48], produced spherical, hollow, non-agglomerated, narrow particle sizes of 200 to 400 nm (at 500 °C) according to the SEM analysis. However, X-ray diffraction analysis showed a mixed amorphous/crystalline sample (at 500 °C with traces of $Li_3Fe_2(PO_4)_3$, Fe_2O_3 and SiO_2 [from the quartz tube of the reactor] phases) resulting in heating the sample more at 600 to 800 °C for six hours. This annealed heat-treated material produced non-spherical hollow particles with a foam-like appearance and larger particle sizes.[48] Nanostructured particles prepared by spray pyrolysis (which was achieved in this study) resulted into shorter Li^+ ion diffusion lengths and a reduced ohmic drop, enhancing the electrochemical performance (higher capacities at higher rates).[48]

The structural, morphological and electrochemical performance of $LiFePO_4$ cathode materials was improved by doping and coating them using similar spray pyrolysis.[62, 63, 64, 65] The material was doped with transition metals such as Ni, Co, Mg and other metals that are still being investigated.[9, 63]Mg-doped $LiFePO_4$synthesised by the spray pyrolysis method involved using diluted nitric acid

where Li_2CO_3, $NH_4 \cdot H_2PO_4$, $FeC_2O_4 \cdot 4H_2O$ and $Mg(C_2H_3O_2)_2 \cdot 4H_2O$ were dissolved to make up the precursor solution.[63] The solution was pumped into a furnace (at 400°C) with the aid of Ar as the carrier gas. A cyclone collected the produced precursor powder, which was further calcined at 750 °C for 10 hours.[63] Wang et al.[63] studied the effect of Mg-doped $Li_{1-x}Mg_yFePO_4$ at various stoichiometric amounts (x=0.97, 0.98, 0.99 and y=0.005, 0.01, 0.02). X-ray diffraction analysis showed a pure single olivine-doped structure and the SEM analysis showed the crystallised powders with an average particle size of between 1 and 2 μm. The result was a material that had a higher electronic conductivity by four orders of magnitude when compared to the undoped $LiFePO_4$ material.[63] The initial charging capacity was higher than its discharge capacity, which could be due to $LiFePO_4$ producing a large surface area by the spray pyrolysis synthesis. Further investigations were done on this material due to its poor electrochemical results which could be improved by optimizing the sintering procedure which could lead to obtaining optimal crystals and improved electrochemical performance[63].

A two-step carbon coating and spray pyrolysis process prepared LiFe0.6Mn0.4PO4/C.[65] Firstly carbon coating was prepared by dissolving the appropriate starting materials with sucrose in ethanol. The mixture was ball milled for three hours, dried under vacuum at 100 °C for two hours and heated in a furnace for threehours at 550 °C under N_2. The second process involved ball milling in the water of the pre-sintered product, polyethylene glycol (PEG400 as a dispersant), sucrose and multiwall carbon nanotubes (MWCNT) for fivehours producing a suitable slurry. The slurry was sprayed to form an aerosol, resulting in the formation of spherical powdered particles after the moisture had evaporated. The spray-dried product was annealed at 650 °C for 10 hours under N_2, forming pure $LiFe_{0.6}Mn_{0.4}PO_4/C$. The characterisation of the product showed pure spherical oxide particles (5–20 μm in size) and a carbon layer of about 3 nm. This was a comparative study of $LiFe_{0.6}Mn_{0.4}PO_4/C$ and $LiFe_{0.6}Mn_{0.4}PO_4/C$ with MWCNT. The surface area of the material was 22.36 $m^2.g^{-1}$ and the electrochemical tests showed a discharge capacity of 163.3 $mAh.g^{-1}$ at 0.1C rate ($LiFe_{0.6}Mn_{0.4}PO_4/C$ with MWCNT). This result was an improvement of the electrochemical performance, whereby bare $LiFe_{0.6}Mn_{0.4}PO_4/C$ could still deliver a capacity of 12.8 $mAh.g^{-1}$ at 50 C, and $LiFe_{0.6}Mn_{0.4}PO_4/C$ with MWCNT could deliver a capacity of 64.23 $mAh.g^{-1}$. Furthermore, $LiFe_{0.6}Mn_{0.4}PO_4/C$ with MWCNT microspheres was promising in large-scale applications (such as electric vehicles).[65]

4   Conclusion

This brief review of the spray pyrolysis through sol-gel materials for Li-ion cathode materials showed the versatility of the ability to prepare a number of doped and coated materials that could range in particle size, crystalline characteristics and material properties. In this study, it was observed that a spray pyrolysis method produced micro to submicrometer particles effectively, as well as particles with narrow particle size distributions and homogeneous particles in a continuous step, which was controllable in a short time period. These parameters contributed to optimise the electrochemical properties (making it possible to still obtain reasonable capacity at high rates) in terms of the achievable discharge capacities and capacity cycle durability. The use of a spray pyrolysis method resulted in a decreased use of expensive reagents/compounds (cost effective), it lowered solvent use, improved temperature control, and workplace safety because of the decreasein harmful materials to which workers could be exposed. The spray pyrolysis synthesis process could be considered as a suitable technique for large-scale pilot plant cathode materials, concluding that the technique met the industrial requirements or specifications. In this study, the spray pyrolysis through sol-gel materials was followed to obtain the materials' best results.

References

1. Energizer Report, *Nickel Metal Hydride (NiMH), Handbook and Application Manual*, (2010).
2. B.C.H. Steele (eds.), *Fast ion transport in solids: solid-state batteries and devices*, North-Holland/American Elsevier Inc., Amsterdam-London/New York, 1973.
3. J. Yamaki, *Advances in Lithium-Ion Batteries*, W.A. van Schalkwijk (ed) and B. Scrosati, Kluwer Academic/Plenum Publishers, New York, 2002, Chapter 5 pp. 155-183.
4. S.S. Zhang, A review on the separators of liquid electrolyte Li-ion batteries, *J. Power Sources*, 2007, **164**, 351-364.

5. V. Palomares, T. Rojo, *Synthesis Process for Li-ion battery electrodes-from solid state reaction to solvothermal self-assembly methods, Lithium ion batteries-New developments,*I. Belharouak (Ed), InTech, Croatia Europe,2012.

6. Q. Lui, S. Wang, H. Tan, Z. Yang andJ. Zeng, Preparation and Doping Mode of Doped $LiMn_2O_4$ for Li-ion Batteries, *Energies,*2013, **6,** 1718–1730.

7. T. Ohzuku andA. Ueda, Solid-State Redox Reactions of $LiCoO_2$ (R3m) for 4 Volt Secondary Lithium Cells, *J. Electrochem. Soc.,* 1994, **141**,2972–2977.

8. T. Cui, N. Hua, Y. Han andX. Kang, Preparation and Electrochemical Properties of $LiMn_2O_4$ by a Rheological-Phase-Assisted Microwave Synthesis Method, *Inorg. Mater.,* 2008, **44,**542–548.

9. Y. Zhang, Q. Huo, P. Du, L. Wang, A. Zhang, Y. Song, Y. Lv andG. Li, Advances in new cathode material $LiFePO_4$ for lithium-ion batteries, *Synth. Met.*, 2012, **162,** 1315–1326.

10. J. Gim, J. Song, D. Nguyen, M.H. Alfaruqi, S. Kim, J. Kang, A.K. Rai, V. Mathew V andnJ. Kim, A two-step solid state synthesis of $LiFePO_4$/C cathode with varying carbon contents for Li-ion batteries, *Ceram. Int.*,2014, **40**,1561–1567.

11. H.S. Kim, D.W. Kam andW.S. Kim, Synthesis of $LiFePO_4$ by a solid-state reaction using organic acids as a reducing agent, *Ionics*,2011, **17,**293–297.

12. L.J. Fu, H. Liu, C. Li, Y.P. Wu, E. Rahm, R. Holze andH.Q. Wu, Electrode materials for lithium secondary batteries prepared by sol-gel methods, *Prog. Mater Sci.*,2005, **50,**881–928.

13. M.A. Aegerter andM. Mennig,(eds.),*Sol-Gel Technologies for Glass Producers and Users*Springer Science & Business Media, New York, 2004.

14. G.G. Avci andD. Abanoz, Corrosion Protection of Steel by Hybrid Sol-Gel Coating, *Eng. Mater.*,2004, **264–268,**387–390.

15. A.U. Jarza, D. Andrzejewski, K. Maruszewski, H. Podbielska andW. Strek, Advantages of sol-gel technologies for biomedical applications, *P. Soc. Photo-opt. Ins.*, 1999, **50**.

16. PRNewswire Report, *Sol-Gel Processing of Ceramics and Glass*,New York,July (2014).

17. L. Predoana, A. Barau, M. Zaharescu, H. Vasilchina, N. Velinova, B. Banov andA. Momchilov, Advanced Techniques for $LiCoO_2$ Preparation and Testing, International Workshop, *Advanced Techniques for Energy Sources Investigation and Testing,* September **P4**, 2004, 1-7.

18. I.H. Oh, S.A. Hong andY.K. Sun, Low-temperature preparation of ultrafine $LiCoO_2$ powders by sol-gel method, *J. Mater. Sci.*, 1997, **32,**3177–3182.

19. M.V. Reddy, T.W. Jie, C.J. Jafta, K.I. Ozoemena, M.K. Mathe, A.S. Nair, S.S. Peng, M.S. Idris, G. Balakrishna, F.I. Ezema andBVR. Chowdari, Studies on Bare and Mg-doped $LiCoO_2$ as a cathode material for Lithium ion Batteries, *Electrochim. Acta*, 2014, **128,**192–197.

20. P. Prahasini, M. Sivakumar, R. Subadevi andF.M. Wang, Synthesis and characterization of Cu doped $LiCoO_2$ Cathode material for Lithium Batteries using Microwave assisted Sol-gel synthesis, *Adv. Mater. Res.*, 2012, **584,**345–349.

21. S. Valanarasu, R. Chandramohan, R.M. Somasundaram andS.R. Srikumar, Structural and electrochemical properties of Eu-doped $LiCoO_2$, *J. Mater. Sci.*, 2011, **22,**151–157.

22. C. Julien, L. El-Farh, S. Rangan and M. Massot, Studies of LiNi0.6Co0.4O2 cathode material prepared by the citric acid-assisted sol-gel method for lithium batteries, *J. Sol-Gel Sci. Technol.,* 1999, **15,** 63-72.

23. C. Li, H.P. Zhang, L.J. Fu, H. Lui, Y.P. Wu, E. Rahm, R. Holze and H.Q. Wu, Cathode materials modified by surface coating for lithium ion batteries, *Electrochim. Acta*, 2006, **51,** 3872–3883.

24. B.J. Hwang, R. Santhanam and D.G. Liu, Characterization of nanoparticles of $LiMn_2O_4$ synthesized by citric acid sol-gel method, *J. Power Sources,* 2001, **97-98,** 443-446.

25. Y.K. Sun, Synthesis and electrochemical studies of spinel $Li_{1.03}Mn_2O_4$ cathode materials prepared by a sol-gel method for lithium secondary batteries, *Solid State Ionics,* 1997, **100,** 115-125.

26. Y. Lee, Y. Sun and K. Nahm, Synthesis of spinel $LiMn_2O_4$ cathode material prepared by an adipic acid-assisted sol-gel method for lithium secondary batteries, *Solid State Ionics,* 1998, **109,** 285-294.

27. P. Singh, A. Sil, M. Nath andS. Ray, Preparation and characterization of lithium manganese oxide cubic spinel $Li_{1.03}Mn_{1.97}O_4$ doped with Mg and Fe, *Physica B,*2010, **405,**649–654.

28. Y. Lee, Y. Sun andK. Nahm, Synthesis of spinel $LiMn_2O_4$ cathode material prepared by an adipic acid-assisted sol-gel method for lithium secondary batteries, *Solid State Ionics,*1998, **109,**285–294.

29. X. He, L. Wang, W. Pu, G. Zhang, C. Jiang and C. Wan, Synthesis of spinel $LiMn_2O_4$ for Li-Ion Batteries via Sol-gel, *Inter. J. Electrochem. Sci.*, 2006, **1,** 12–16.

30. R. Thirunakaran, A. Sivashanmugam, S. Gopukumar, C.W. Dunnill and D.H. Gregory, Studies on chromium/aluminium-doped manganese spinel as cathode materials for lithium-ion batteries – A novel chelated sol-gel synthesis *J. Mater. Process. Technol.*, 2008, **208,** 520–531.

31. X. Huang, M. Lin, Q. Tong, X. Li, Y. Ruan and Y. Yang, Synthesis of $LiCoMnO_4$ via a sol-gel method and its application in high power $LiCoMnO_4/Li_4Ti_5O_{12}$ lithium-ion batteries, *J. Power Sources*, 2012, **202,** 352–356.

32. C.Y. Li, B.W. Sing, Y. Zheng, Z.Q. Chao and S. Zhi, Electrochemical Performance Ni doped Spinel $LiMn_2O_4$ Cathode for Lithium Ion Batteries, *Adv. Mater. Res.*, 2012, **347–353,** 290–300.

33. T.F. Yi, Y.R. Zhu, X.D. Zhu, J. Shu, C.B. Yue and A.N. Zhou, A review of recent developments in the surface modification of $LiMn_2O_4$ as cathode material of power lithium-ion battery, *Ionics*, 2009, **15,** 779–784.

34. G.X. Wang, S. Needham, J. Yao, J.Z. Wang, R.S. Liu and H.K. Liu, A study on $LiFePO_4$ and its doped derivatives as cathode material for lithium-ion batteries, *J. Power Sources*, 2006, **159,** 282–286.

35. H. Karami and F. Taala, Synthesis, characterization and application of $Li_3Fe_2(PO_4)_3$ nanoparticles as cathode of lithium-ion rechargeable batteries, *J. Power Sources*, 2011, **196,** 6400–6411.

36. J.K. Kim, J.W. Choi, G.S. Chauhan, J.H. Ahn, G.C. Hwang, J.B. Choi and H.J. Ahn, Enhancement of electrochemical performance of lithium iron phosphate by controlled sol-gel synthesis, *Electrochim. Acta*, 2008, **53,** 858–8264.

37. D. Jugovic and D. Uskokovic, A review of recent developments in the synthesis procedure of lithium iron phosphate powders, *J. Power Sources*, 2009, **190,** 538–544.

38. M.C. Rao, Vanadium Pentoxide Cathode Material for Fabrication of All Solid State Lithium-Ion Batteries, *Res J Recent Sci.*, 2013, **2,** 67–73.

39. M.Y. Saidi, J. Barker, H. Huang, J.L. Swoyer and G. Adamson, Performance characteristics of lithium vanadium phosphate as a cathode material for lithium-ion batteries, *J. Power Sources*, 2003, **119–121,** 266–272.

40. X.J. Zhu, Y.X. Liu, L.M. Geng andL.B. Chen, Synthesis and performance of lithium vanadium phosphate as cathode materials for lithium ion batteries by a sol-gel method, *J. Power Sources*, 2008, **184,**578–582.

41. J.W. Fergus, Recent developments in cathode materials for lithium ion batteries, *J. Power Sources*, 2010, **195,**939–954.

42. Y.H. Jouybari andS. Asgari ,Synthesis and electrochemical properties of $LiNi_{0.8}Co_{0.2}O_2$ nanopowders for lithium ion battery applications, *J. Power Sources*, 2011, **196,** 337–342.

43. C. Arpagaus, N. Schafroth andM. Meuri, Buchi Report, *Laboratory Scale Spray Drying of Lactose*, best@buchi,2010, **57**.

44. A. Gharsallaoui, G. Roudaut, O. Chambin, A. Voilley andR. Saurel, Applications of spray-drying in microencapsulation of food ingredients, *Food Res Int.*, 2007, **40,** 1107–1121.

45. T. Penovic, A. Sander andV. Grozdanic, Spray Drying of Aqueous Solutions of Inorganic and Organic Materials, *Part. Sci. Technol.*, 2013, **31.5,** 458–465.

46. Y. Li, N.P. Haigh, C. Wan, Y. Wu, C. Jiang and Y. Zhu, Synthesis and characterization of ultrafine $LiCoO_2$ powders by a spray-drying method, *J. Power Sources*, 2000, **85,** 294–298.

47. I. Taniguchi, N. Fukuda andM. Konarova, Synthesis of spherical $LiMn_2O_4$ microparticles by a combination of spray pyrolysis and drying method, *J. Power Sources*, 2008, **181,** 228–236.

48. L.S. Gomez, I. de Meatza, M.I. Martin, M. Bengoechea, I. Cantero and M.E. Rabanal, Morphological, structural and electrochemical properties of lithium iron phosphate synthesized by Spray Pyrolysis, *Electrochim. Acta*, 2010, **55,** 2805–2809.

49. K. Amine, S. Ban andR.M. Nault, *News from Argonne's Transportation Technology R&D Center*, 2 009, Report **9**.

50. S.H. Kim andC.S. Kim, Improving the rate performance of $LiCoO_2$ by Zr doping, *J. Electroceram*, 2009, **23,** 254–257.

51. M. Lengyel, G. Atlas, D. Elhassid, P.Y. Luo, X. Zhang, I. Belharouak andR.L. Axelbaum, Effects of synthesis conditions on the physical and electrochemical properties of $Li_{1.2}Mn_{0.54}Ni_{0.13}Co_{0.13}O_2$ prepared by spray pyrolysis, *J.Power Sources*, 2014, **626,** 286–296.

52. S.H. Choi, J.H. Kim, Y.N. Ko, K.M. Yang and Y.C. Kang, Preparation and electrochemical properties of glass-modified LiCoO2 cathode powders, *J. Power Sources*, 2013, **244,** 129–135.

53. S. Hirose, T. Kodera andT. Ogihara, Synthesis and electrochemical properties of Li-rich spinel type $LiMn_2O_4$ powders by spray pyrolysis using aqueous solution of manganese carbonate, *J. Alloys Compd.*, 2010, **506,** 883–887.

54. B. Ebin, V. Battaglia andS. Gurmen, Comparison of 4V and 3V electrochemical properties of nanocrystalline $LiMn_2O_4$ cathode particles in lithium ion batteries prepared by ultrasonic spray pyrolysis, *Ceram. Int.*, 2014, **40,** 7029–7035.

55. B. Ebin, G. Lindbergh andS. Gurmen, Preparation and electrochemical properties of nanocrystalline $LiB_xMn_{2-x}O_4$ cathode particles for Li-ion batteries by ultrasonic spray pyrolysis method, *J. Alloys Compd.*, 2015, **620,** 399–406.

56. C.H. Lu, T.Y. Wu, H.C. Wu, M.H. Yang, Z.Z. Gua andI. Taaniguchi, Preparation and electrochemical characteristics of spherical spinel cathode powders via an ultrasonic spray pyrolysis process, *Mater. Chem. Phys.*, 2008, **112,** 115–119.

57. I. Taniguchi andZ. Bakenov, Spray pyrolysis synthesis of nanostructured $LiFe_xMn_{2-x}O_4$ cathode materials for lithium-ion batteries, *Powder Technol.*, 2005, **159,** 55–62.

58. B. Ebin, S. Gurmen andG. Lindbergh, Preparation and electrochemical properties of spinel $LiFe_xCu_yMn_{1.2}O_4$ by ultrasonic spray pyrolysis, *Ceram. Int.*, 2014, **40,** 1019–1027.

59. I. Taniguchi, Powder properties of partially substituted $LiM_xMn_{2-x}O_4$ (M= Al, Cr, Fe and Co) synthesized by ultrasonic spray pyrolysis, *Mater. Chem. Phys.*, 2005, **92,**172–179.

60. I. Taniguchi, D. Song and M. Wakihara, Electrochemical properties of $LiM_{1/6}Mn_{11/6}O_4$ (M= Mn, Co, Al and Ni) as cathode materials for Li-ion batteries prepared by ultrasonic spray pyrolysis method, *J. Power Sources*, 2002, **109,** 333-339.

61. Z. Bakenov, M. Wakihara andI. Taniguchi, Battery performance of nanostructured lithium manganese oxide synthesized by ultrasonic spray pyrolysis at elevated temperature, *J. Solid State Electrochem.*, 2008, **12,** 57-62.

62. D. Jung, Y. Ko, Y. Kang andS. Park, Recent progress in electrode materials produced by spray pyrolysis for next-generation lithium ion batteries,*Adv. Powder Technol.*, 2014, **25, -** 18–31.

63. G.X. Wang, S.L. Bewlay, K. Konstantinov, H.K. Liu, S.X. Dou andJ.H. Ahn, Physical and electrochemical properties of doped lithium iron phosphate electrodes, *Electrochim.Acta*, 2004, **50,**443–447.

64. J. Wang and X. Sun, Understanding and recent development of carbon coating on LiFePO$_4$ cathode materials for lithium-ion batteries, *Energy Environ Sci.*, 2012, **5,** 5163-5185.

65. Y. Mi, P. Gao, W. Liu, W. Zhang and H. Zhou, Carbon nanotube-loaded mesoporous LiFe$_{0.6}$Mn$_{0.4}$PO$_4$/C microspheres as high performance cathodes for lithium-ion batteries, *J. Power Sources*, 2014, **267,** 459–468.